Long Term Assessment of Dams Suffering from Alkali Aggregate Reaction;

Analyses Results

Final Report

Cooperative Agreement No. R18AC00055

December 12, 2023

Golsa Mahdavi

Victor E. Saouma

University of Colorado, Boulder

Contents

List of Figures

List of Tables

Acknowledgments

The authors would like to thank Dr. M.Amin Hariri-Ardebili and Dr. Jerzy Salamon for their helpful comments and contribution throughout this report.

Chapter 1

Introduction

Abstract

This introductory chapter will provide contextual reference for this work, along with a brief outline of individual chapters.

1.1 Motivation

Mutliple dams, worldwide, are known to have been suffering from alkali silica reaction (ASR) (also known as alkali aggregate reaction, AAR) for many years. Many of them exhibit concerning cracking, and increased irreversible displacements.

As such, after many years of observations, regulators are increasingly confronted with critical decisions: a) Shall we wait, and continue to observe? or b) shall we initiate dismateling and possible replacement plans?

Thise are not easy questions, and they can be addressed by economic considerations backed by reliable scientific prediction as to the future damage to the dam.

In here, two approaches are confronted. A "simplistic" traditional one based on the State of the Practice (in many countries, but not in France, Canada or other European countries); or a "State of the Art" one that has proven most valuable for those (few) regulators who have embraced it.

Grant it, the approach is not simple to understand for the novice, and require a good understanding of AAR.

Another complicating factor is that a deterministic analysis is hardly credible. There are too many parameters impacting analysis results that at best have a probability distribution which can be categorized as normal, or log-normal.

As a result, at best, one can make a risk assessment, and provide regulators with a qualified assessment based on what is commonly known as a "Monte-Carlo" simulation.

1.2 Ultimate Goal

Ultimately, this report could assist Reclamation in performing its own safety risk assessment. In such a study, a Probable Failure Mode would have to be identified, and the resulting uncontrolled release of water

quantified, prior to the ultimate assessment of financial consequences.

As one would expect, there is not, and neither could there be, a clear-cut answer to many of the questions related to the dam safety. However this study provided as quantitative assessment as can be using modern analytical tools based on the State of the Art.

1.3 Objective

As such, this document will report on a comprehensive investigation of Seminoe dam under a cooperative agreement between the Bureau of Reclamation and the University of Colorado.

It should be noted that whereas the work was supervised by the second author, it constitutes the Ph.D. dissertation of the first one (who will further perform a seismic analysis of the dam), and it should be published in 2023.

Prior to this study, the University of Colorado has submitted the following reports

1. Hariri-Ardebili and Saouma, V.E. (2021), *Long Term Assessment of Dams Suffering from Alkali Aggregate Reaction;State of the Art Review* , (**saoumaborreport1**).
2. Saouma, V.E. and M.Amin Hariri-Ardebili (2021), *Road Map for the Probabilistic Static and Dynamic Assessment of Concrete Dams Suffering from AAR*, (**saoumaborreport2**)
3. This report was supposed to address AAR testing, however it was deemed not necessary by Reclamation.
4. Saouma, V.E. and Mahdavi, G. (2022), *Long Term Assessment of Dams Suffering from Alkali Aggregate Reaction; Procedure*, (**saoumaborreport5**)

1.4 Procedure

The investigation is best described through Fig. 1.1 which calls for the following clarification

- Dam instrumentation and recorded data constitute the starting point.
- Dam geometry provide an insight on how to generate a finite element model. For a seimic investigation, natrually additional information would be needed.
- A finite element program (Merlin in our case) is then used, it should have the proper constitutive models for joint, concrete, and most importantly for AAR.
- A system identification (or parameter identification) process will be used to indirectly determine the AAR properties of the dam.
- Though not performed in this ivestigation, a sensitivity analysis could isolate those parameters likely to highly influence results through small variation.
- AAR will have temporal uncertainties associated with them, and will be accounted for.
- Spatial distribution of AAR properties could be accounted for, however this was not performed in this study.
- Again, for seismic investigation, one would study available (or synthetic) ground motion records.
- A monte-Carlo simulation (or uncertainty quantification) will complete the investigation. It would necesitates limit states (not easily defined for dams with AAR), and this will ultimately yield “fragility curves”.

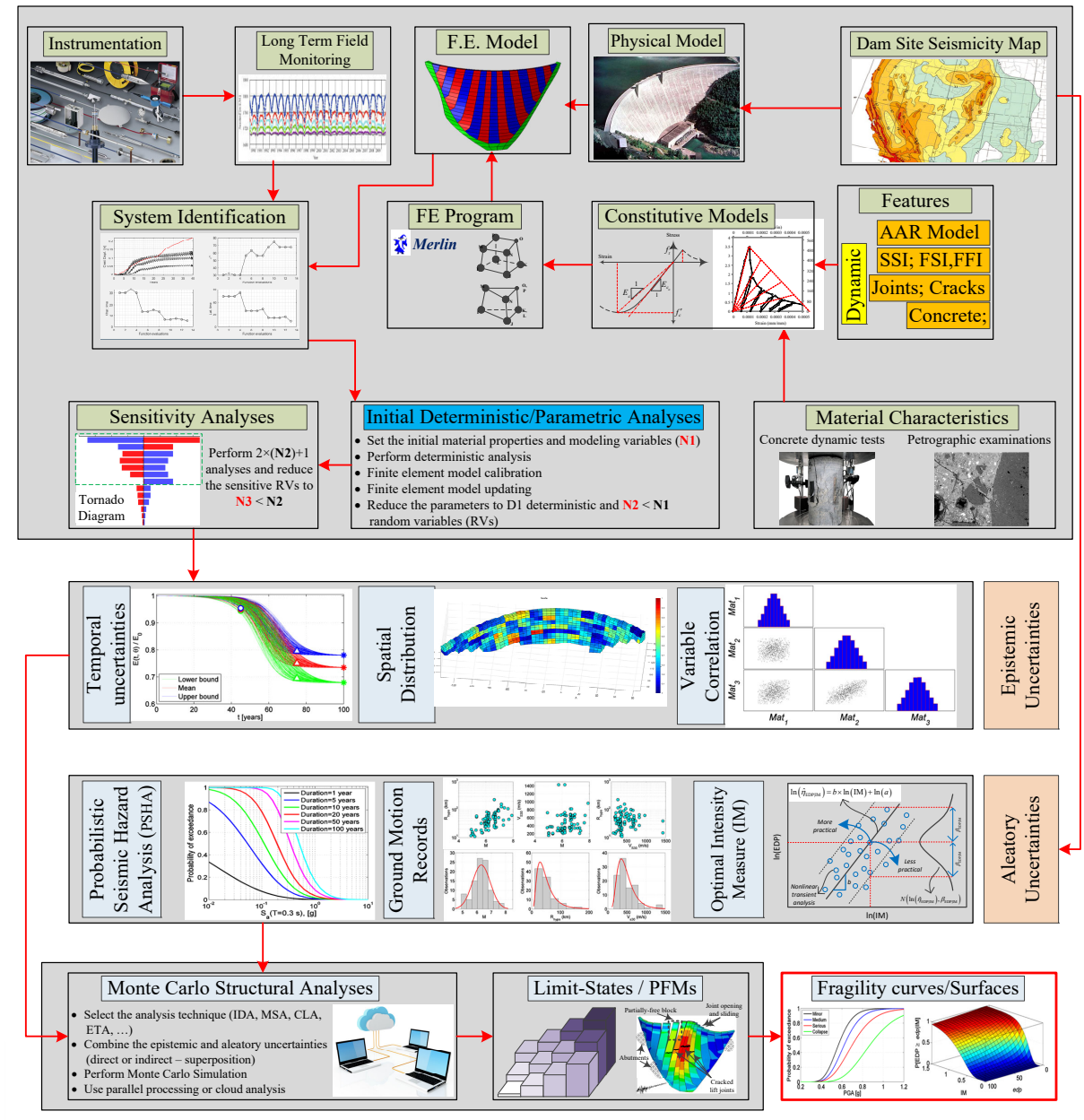

Figure 1.1: Outline of a comprehensive analysis

1.5 Report outline

This report will be subdivided into three main parts, and accompanying chapters.

I Theory to provide a good explanation of the methods used in the analysis. The corresponding chapters are

Chap. 1. will covers the fundamentals of AAR, focusing on the model used in this study.

Chap. 2. will address the often ignored modeling of solar radiation in the thermal analysis of concrete dams.

Chap. 3. describes the theory behind parameter identification that will be used later.

Chap. 4. will provide a verification of the thermal analysis

II Analysis of Seminoe Dam

Chap. 5. will provide all the physical properties of the dam specifically needed for the subsequent analyses.

Chap. 6. will describe the numerical (finite element) modeling of the dam.

Chap. 7. will cover the thermal analysis necessary for the subsequent AAR stress analysis.

Chap. 8. constitutes the first major chapter of this study, it will first report on the parameter identification using a linear concrete model, and then nonlinear deterministic analyses results.

Chap. 9. is the other most important chapter of the report, it is the uncertainty quantification of both thermal and stress analysis.

Chap. 10. Concludes the study with summaries, and recommendations for future work.

III Appendices are critical to provide a full explanation of the analyses without encumbering the report body.

App. A will summarizes the all the available field data associated with Seminoe.

App. B. will provide a verification of the thermal analysis.

App. C. will summarize pool and concrete temperatures.

App. D. will describe RILEM benchmark problems to (quasi) validate a finite element code for AAR analysis.

App. E. is the validation of the code Merlin used in this study.

App. F. will provide some of the secondary figures generated by this investigation.

App. G. will tabulate some of the key input filed data required by the analysis.

App. H. will provide some of the additional results associated with the Uncertainty Quantification study.

App. I will provide initial observations made when the first massive concrete placement had been ignored.

App. J. is a verification study for pool and concrete temperatures.

Part I

THEORY

Chapter 2

Alkali Aggregate Reaction

Abstract

The underlying mechanisms causing Alkali Aggregate Reactions (AAR) are by now well known. This chapter will limit itself to describe AAR in the context of the constitutive model developed by **saouma-aar-1empty citation** *and implemented in the computer program Merlin used in the analyses. Validation of the model is given in Appendix E.*

2.1 Finite element modeling of AAR in dams

`Section Adapted from (saoumaborreport2)`

Prognosis of hydraulic structures suffering from AAR is notoriously difficult and for some impossible.

For the most part, current approach relies on one or more investigative tools, Fig. 2.1. Unfortunately those methodologies tend to be disjointed and difficult to directly relate to others. For example a petrographer may find the DRI (or other measure microscopically determined) too elevated, and hence consider the structure unfit. Expansion tests may be performed, but results are seldom fed into the finite element study. Finite element studies themselves may be conducted with invalidated codes.

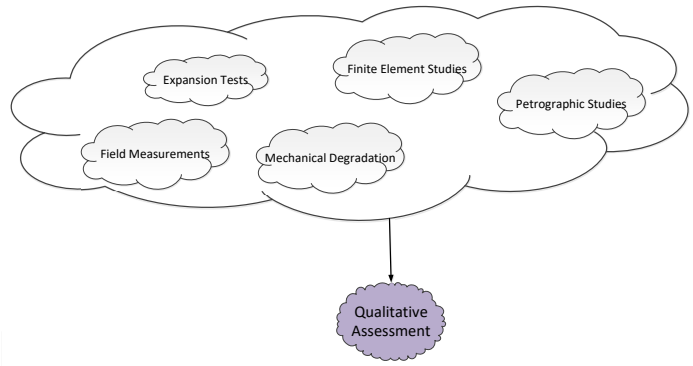

Figure 2.1: A clouded approach

There are essentially two possible approaches to model AAR, Fig. 2.2. The first is representative of thee State of the Practice, while the second captures the State of the Art in AAR,

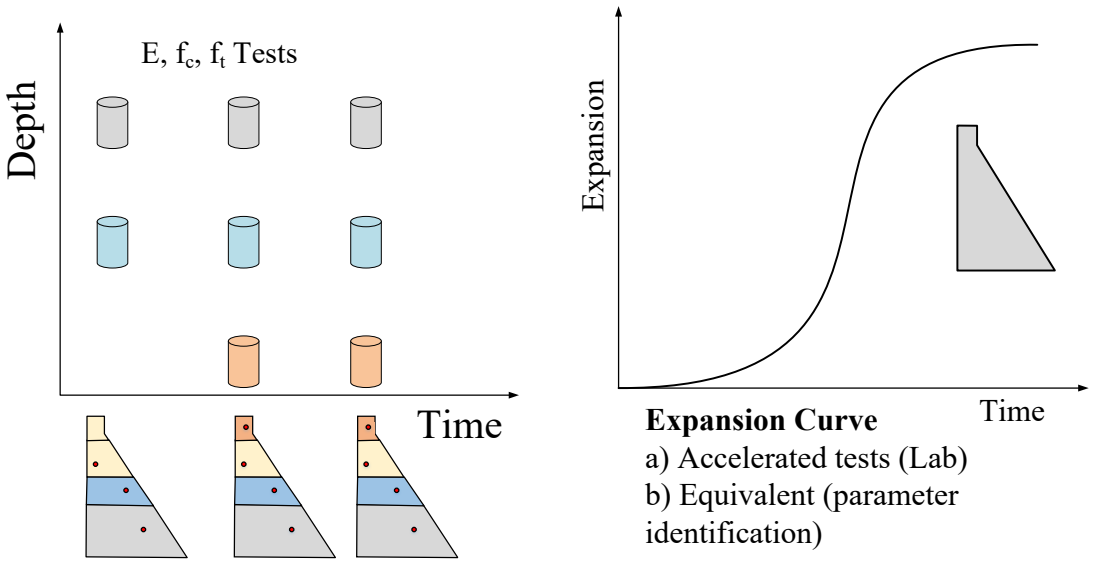

(a) State of the practice

(b) Proposed

Figure 2.2: AAR FEA models

A brief summary of the two methods is shown in Table 2.1.

Table 2.1: Side-b-Side Comparison of the State-of-the-Practice and the State-of-the-Arth methodologies to analyze dams with AAR

Methods	**State of the Practice (e.g. Hatch)**	**State of the Art (e.g. Merlin)**
# of Analyses	Multiple, one for each year we are interested in	Single analysis that starts at time 0 (dam construction) up till desired year
	Input data	
Parameters	Topological distribution of damaged concrete properties over the dam at the time of analysis	Characteristics of the concrete expansion to capture its kinetics (3 parameters)

How do we obtain them	Subdivide the dam in multiple regions; Extract sufficient representative cores from each one of them; perform tests (E and f_c primarily)	1. Perform expansion and appropriate petrographic tests (Katayama), determine the 3 parameters that characterize the concrete since time of construction 2. Same as above, without petrographic tests, characterization since date of core extraction 3. Perform a parameter identification based on the historical record of crest deflections
	Analysis	
Advantage	Easier to perform the analysis if one does not have a finite element code that can track the expansion with time.	Single analysis that capture the entire response (displacements and internal deterioration of concrete); Requires only three parameters that capture the cause of the expansion (as opposed to multiple tests that reflect the consequences of the reaction); Truly captures the complex response of a structure subjected to AAR (listed as disadvantage for Method 1 below).
Disadvantage	Approximate as we have to assign material properties over large zones, many input data coming from tests. May not be representative enough as it does not capture: 1) interaction of temperature with expansion; 2) effect of confinement on the anisotropic expansion;	Some numerical instability may occur in a nonlinear time history analysis
	Analysis Output	
Dislacements stresses	Yes, a snapshot at time t (of analysis), i.e. one single scalar quantity at time t	Yes, a "movie" that captures the evolution of the dam response, i.e. a vector for each response in terms of time)
Concrete deterioration	No, that was part of the input	Yes as computed by the AAR model
	Future Prediction	
Possible	Will have to be based on the time dependent concrete deterioration	By just letting the analysis go beyond present date.

Reliability	Low would rely on the extrapolation of concrete damage measured in the laboratory and inputted in the mesh	High, embedded in the analysis are the expansion characteristics measured in the lab (or extracted from a parameter identification based on historical record of crest displacement)

2.1.1 State of the practice

The simplest approach, and one which does not require any specialized finite element code, is based on a mapping of the field determined concrete deterioration on the ensuing finite element mesh. The analysis, is then calibrated with some of the field measurements. Thus, a separate analysis will be conducted for each year of recorded mechanical properties.

2.1.1.1 AAR Modeling

One would start with testing cores (E, f_c and f_t, but not necessarily all three of them all the times) recovered from the dam at time t_i. Then, one would, semi-arbitrarily but certainly approximately, assign a representative region to each one of the cores. Within that region, elements of the mesh will be assigned the same mechanical properties.

Separately, at time t_i one would estimate the AAR expansion $\varepsilon^{\infty}(t_i)$, and its spatial distribution $\varepsilon^{AAR}(t_i, x, y)$.

Finally, combining those two, a finite element analysis is performed. However, this is very likely to yield good correlation with recorded field displacements. Hence, correction are made with *some* of the recorded data, and verification is made with the others. This is repeated until adequate comparison at time t_i is achieved. Adjustments are for a given time t_i and are very unlikely to be the same for time t_j.

The outcome of such a calibration (for $E|f_t|f_c$) is a spatial and temporal partitioning shown below, Fig. 2.3

$$
\begin{aligned}
[E|f_t|f_c](h,t) \quad = \quad & \begin{cases}
a_1 f_1(h) \times f_2(t) & yr_1 \le t \le yr_2 \quad \& \quad h \ge h_1 \quad ① \\
a_2 f_2(t) & yr_1 \le t \le yr_2 \quad \& \quad h < h_1 \quad ② \\
a_3 f_1(h) & t < yr_1 \quad \& \quad h \ge h_1 \quad ③ \\
a_4 f_1(h) & t > yr_2 \quad \& \quad h \ge h_1 \quad ④ \\
a_5 & t < yr_1 \quad \& \quad h < h_1 \quad ⑤ \\
a_6 & t > yr_2 \quad \& \quad h < h_1 \quad ⑥
\end{cases} \\
f_1(h) \quad = \quad & b_1 + b_2 h + b_3 h^2 \\
f_2(t) \quad = \quad & c_1 + c_2 t + c_3 t^2
\end{aligned}
\tag{2.1}
$$

The major (but not only) concern with this method, is that typically one would have not only very limited measurements but those are also widely spaced in times. This is further exacerbated by the seldom performance of tensile strength. This handicap is best illustrated by Fig. 2.4. One can readily note the very gross approximation one has to resort to in such an analysis[1].

Typically, only few cores are drilled and tested during the life of the dam. Hence, mapping deterioration over the dam is at best approximate. Furthermore, the idiosyncrasies of the AAR (**saouma2014AARBook**) are not captured.

This approach has been primarily used by consulting engineers.

[1]Though an idealization, these curves are based on an actual study espousing this method.

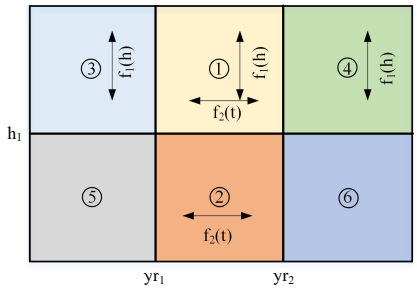

Figure 2.3: Spatial and temporal partitioning

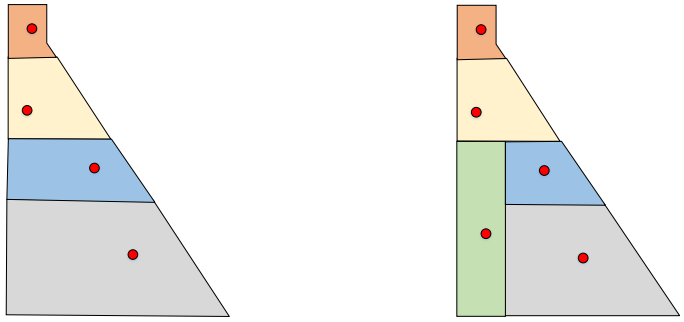

(a) Time t_1 (b) Time t_2

Figure 2.4: Mapping of recovered core test results (E, f_c, f_t) measurement into finite element mesh

2.1.1.2 Failure Criterion

Typically, the failure criterion is a post-processing of an otherwise linear elastic analysis (with possible exception for the contact elements). Those would include:

1. Uniaxial compression failure criterion
2. Uniaxial tension failure criterion
3. Triaxial failure criterion

Also, a final '*concrete cracking analysis* may be performed using the so-called *smeared crack model*. This will inherently allow for internal stress redistribution and a corresponding increase in compressive stresses.

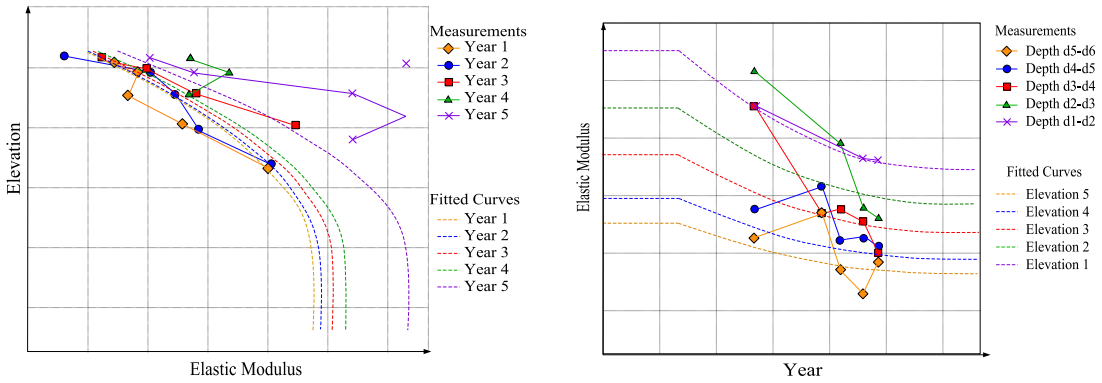

(a) Elastic modulus

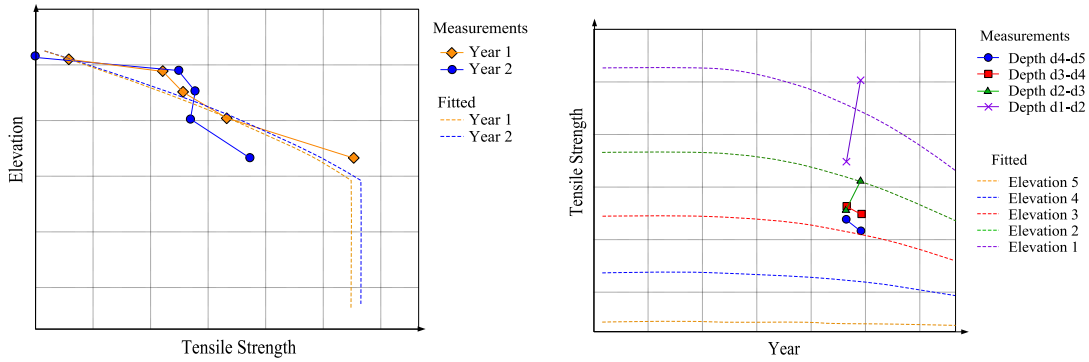

(b) Tensile strength

Figure 2.5: Spatial and temporal fitting for concrete mechanical properties based on limited cores and observations (courtesy Y. Gakuhari)

2.1.2 State of the Art

In this second approach, one that is rooted in the State of the Art, one would take into account apparent (or not so apparent) synergy between investigative tools, Fig. 2.6(a).

It should be noted that the approach about to be presented has been used by some researchers already, (**saouma-aar-2**) (**Comi09**) (**sellier2009**) (**huangspencer16**) to name a few. The most recent, and comprehensive, study was recently presented by **joshi2021timeempty citation**.

This approach consists of three major stages, each one will be described separately in the next section.

2.1.2.1 AAR Modeling

It should be emphasized that, in htis approach, any quantitative assessment will have to rely on a mathematical model for the concrete expansion. The model usually adopted is based on the one of **ulm00empty citation** which is nearly universally accepted.

2.2 AAR model

This section describes the AAR model used in the thesis and is adapted from (**saouma-aar-1**) and (**saouma-aar-book**).

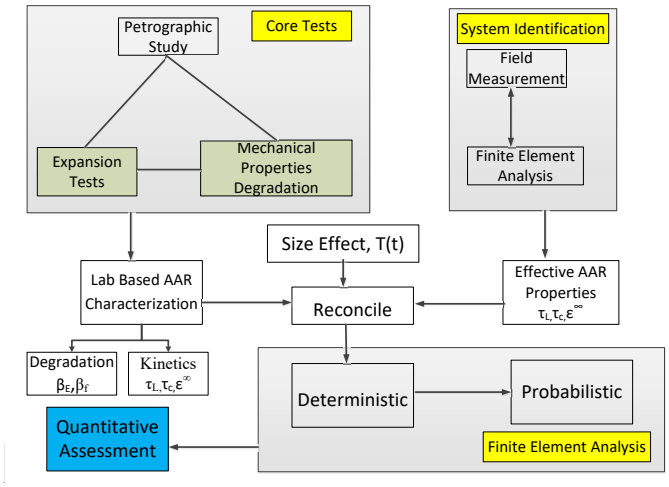

(a) Proposed

Figure 2.6: Assessment paradigms for AAR affected structures

2.2.1 Premises

Two different aspects of mathematical modeling of AAR in concrete may be distinguished: 1) the kinetics of the chemical reactions and diffusion processes involved and 2) the mechanics of fracture that affects volume expansion and causes loss of strength, with possible disintegration of the material (**bazant00a**). The proposed model (**saouma-aar-1**) (**saouma-aar-book**) is driven by the following considerations:

1. AAR is a volumetric expansion, and as such can not be addressed individually along a principal direction without due regard to what may occur along the other two orthogonal ones.
2. The kinetics component is taken from the work of (**larive98**) and (**ulm00**).
3. AAR is sufficiently influenced by temperature to account for its temporal variation in an analysis.
4. AAR expansion is constrained by compression and is redirected in other less constrained principal directions. This will be accomplished by assigning "weights" to each of the three principal directions.
5. Relatively high compressive or tensile stresses inhibit AAR expansion due to the formation of micro or macro cracks which absorb the expanding gel.
6. High compressive hydrostatic stresses slow down the reaction.
7. Triaxial compressive state of stress reduces but does not eliminate expansion.
8. Accompanying AAR expansion is a reduction in tensile strength and elastic modulus.

2.2.2 Kinetics

One of the most extensive and rigorous AAR investigations has been conducted by **larive98empty citation**, who tested more than 600 specimens, Figure 2.7(a), with various mixes, ambient and mechanical conditions, and proposed a numerical model that governs concrete expansion. This thermodynamically-based, semi-analytical model was then calibrated using laboratory results in order to determine two key parameters: the latency time and characteristic times shown in Figure 2.7(b) for the normalized expansion.

$$\xi(t,T) = \frac{1 - e^{-\frac{t}{\tau_c(T)}}}{1 + e^{-\frac{(t-\tau_l(T))}{\tau_c(T)}}} \tag{2.2}$$

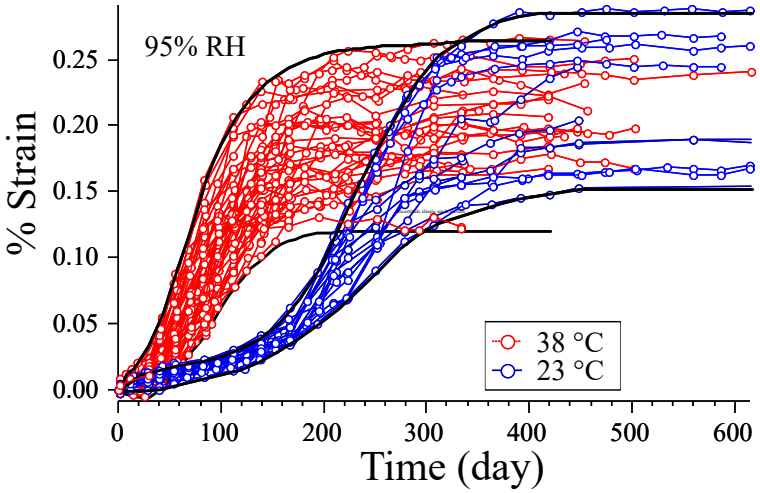

(a) Bracket of experimentally measured expansion at two different temperatures (**larive98**) (Courtesy of S. Multon)

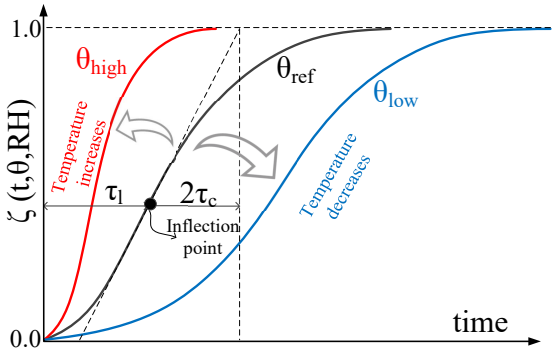

(b) Normalized Expansion Curve ($\xi(t) = \epsilon^{AAR}_{F,Vol}(t)/\epsilon(\infty)$)

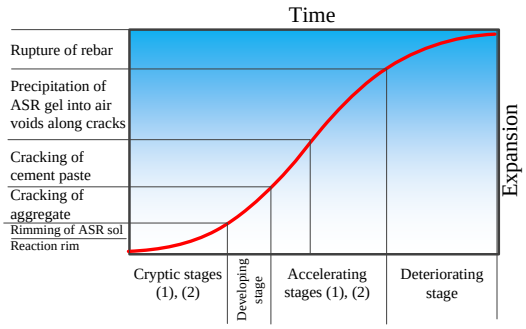

(c) Physical deterioration associated with AAR (**saouma2017riskinformed**)

Figure 2.7: ASR expansion curve

or in rate form

$$\dot{\xi}(t,T) = \frac{e^{t/\tau_c}\left(e^{\frac{\tau_l}{\tau_c}}+1\right)}{\tau_c\left(e^{t/\tau_c}+e^{\frac{\tau_l}{\tau_c}}\right)^2} \tag{2.3}$$

where $Tisthetemperature$ τ_l and τ_c are the latency and characteristic times, calibrated at T_0. The first corresponds to the inflection point while the second is defined relative to the intersection of the tangent at τ_L with the asymptotic unit value of ξ. Like all chemical reactions, AAR is subject to Arrhenius Law (**arrhenius89**), which relates the dependence of the rate constant, k, of a chemical reaction on absolute temperature (T expressed in Kelvin, $TK = 273 + T^oC$) and activation energy, E_a.

$$k = Ae^{-\frac{E_a}{RT}} \tag{2.4}$$

Table 2.2: Variation of $\epsilon(\infty)$, τ_c and τ_l for 4 specimens, (**larive98**)

specimen		501	475	287	19	Mean	NSD (%)
$\epsilon(\infty)$	%	0.198	0.195	0.168	0.230	0.198	12.8
τ_c	days	19.9	35.3	25.8	22.0	25.7	26.5
τ_l	days	102.1	83.9	94.8	64.8	86.4	18.8
τ_l/τ_c	-	5.1	2.4	3.7	2.9	3.4	0.7

Substituting k with τ_L and τ_C, **ulm00empty citation** has shown that these values at temperature T can be expressed in terms of the corresponding values at temperature T_0 through:

$$\begin{aligned} \tau_l(T) &= \tau_l(T_0)\exp\left[U_l\left(\tfrac{1}{T}-\tfrac{1}{T_0}\right)\right] \\ \tau_c(T) &= \tau_c(T_0)\exp\left[U_c\left(\tfrac{1}{T}-\tfrac{1}{T_0}\right)\right] \end{aligned} \tag{2.5}$$

where U_l and U_c are the activation energies required to trigger the reaction for latency and characteristic times, respectively. Activation energies can be easily determined by rewriting Eq. 2.5 in its non-exponential form:

$$\ln k = \ln\left(Ae^{-\frac{E_a}{RT}}\right) = \ln A - \frac{E_a}{RT} \tag{2.6}$$

which is the equation of a straight line with slope $-E_a/RT$ We can thus determine the activation energy from values of k observed at different temperatures by simply plotting k as a function of $1/T$.Activation energies for Eq. 2.5 were determined to be:

$$\begin{aligned} U_l &= 9,400 \pm 500K \\ U_c &= 5,400 \pm 500K \end{aligned} \tag{2.7}$$

To the best of the authors' knowledge, the only other tests for these values were performed by **benhaha06empty citation**, who obtained values within 20% of Larive's, while dependency on the types of aggregates and alkali content of the cement has not been investigated. In the absence of other tests, these values can thus be reasonably considered as representative.

It should be emphasized that not only are the latency and characteristic times temperature-dependent, but considerable variability can also be present for the same concrete specimen chosen from among others. This point is illustrated in Table 2.2 for four specimens (ϕ13H24 kept at 38^oC) tested by **larive98empty citation**.

Role of temperature on expansion is shown in Figure 2.8(b).

Parameters affecting the kinetics of the ASR can be obtained by accelerated expansion tests. **saouma-tc259empty citati** has a compilation of numerous such tests, along with other investigative tools for a thorough diagnosis o ASR.

2.2.3 Volumetric Expansion

The general (uncoupled) equation for the incremental free volumetric AAR strain is given by

$$\dot{\boldsymbol{\varepsilon}}_V^{AAR}(t) = \Gamma_t(f_t'|w_c,\sigma_I|COD_{max})\Gamma_c(\overline{\sigma},f_c')g(h)\dot{\xi}(t,\theta)\,\boldsymbol{\varepsilon}^{\infty}|_{\theta=\theta_0} \tag{2.8}$$

where COD is the crack opening displacement, $\xi(t,\theta)$ is a sigmoid curve expressing the volumetric expansion in time as a function of temperature and is given by Eq. 2.2, and ε^{∞} is the laboratory determined (or predicted) maximum free volumetric expansion at the reference temperature θ_0, Figure 2.7(b).

The retardation effect of the hydrostatic compressive stress manifests itself through τ_l. Hence, Eq. 2.5 is expanded as follows

$$\tau_l(\theta,\theta_0,I_\sigma,f'_c) = f(I_\sigma,f'_c)\tau_l(\theta_0)\exp\left[U_l\left(\frac{1}{\theta}-\frac{1}{\theta_0}\right)\right] \tag{2.9}$$

where

$$f(I_\sigma,f'_c) = \begin{cases} 1 & \text{if } I_\sigma \geq 0 \\ 1+\alpha\frac{I_\sigma}{3f'_c} & \text{if } I_\sigma < 0 \end{cases} \tag{2.10}$$

I_σ is the first invariant of the stress tensor and f'_c the compressive strength. Based on a careful analysis of (**multon03**), it was determined that $\alpha = 4/3$.

The stress dependency (through I_σ) of the kinetic parameter τ_l makes the model a truly coupled one between the chemical and mechanical phases.

Coupling with the thermal component is a loose one (hence a thermal analysis can be separately run); $0 < g(h) \leq 1$ is a reduction function to account for humidity given by

$$g(h) = h^m \tag{2.11}$$

where h is the relative humidity **capra98**. However, one can reasonably assume that (contrary to bridges) inside a dam, $g(h) = 1$ for all temperatures. Figure 2.8(a) highlights the role of RH.

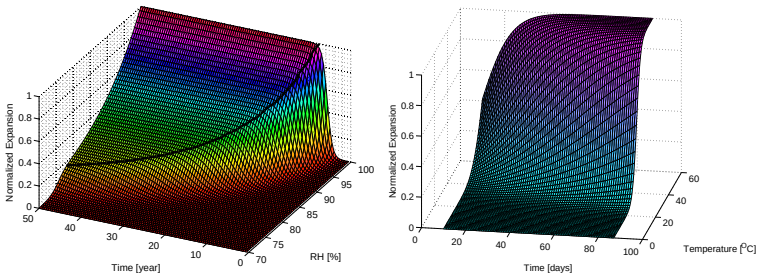

(a) Role of RH (b) Role of Temperature

Figure 2.8: Environmental factors affecting AAR expansion

$\Gamma_t(f'_t|w_c,\sigma_I|COD_{max})$ accounts for AAR reduction due to tensile cracking (in which case gel is absorbed by macro-cracks), Figure 2.9.

A hyperbolic decay with a non-zero residual value is adopted, Figure 2.10:

$$\text{Smeared Crack}\begin{cases} \text{No} \quad \Gamma_t = \begin{cases} 1 & \text{if} \quad \sigma_I \leq \gamma_t f'_t \\ \Gamma_r + (1-\Gamma_r)\gamma_t\frac{f'_t}{\sigma_I} & \text{if} \quad \gamma_t f'_t < \sigma_I \end{cases} \\ \text{Yes} \quad \Gamma_t = \begin{cases} 1 & \text{if} \quad \text{COD}_{max} \leq \gamma_t w_c \\ \Gamma_r + (1-\Gamma_r)\gamma_t\frac{w_c}{\text{COD}_{max}} & \text{if} \quad \gamma_t w_c < \text{COD}_{max} \end{cases} \end{cases} \tag{2.12}$$

γ_t is the fraction of the tensile strength beyond which gel is absorbed by the crack; Γ_r is a residual AAR retention factor for AAR under tension. If an elastic model is used, then f'_t is the the tensile strength and σ_I the maximum principal tensile stress. If a smeared crack model is adopted, then COD_{max} is the maximum

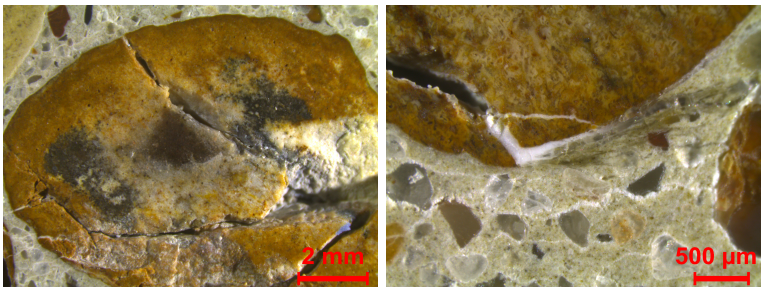

(a) Chert in CA causing AAR (b) Chert with gel close to crack

Figure 2.9: Stress induced cracks with potential gel absorption

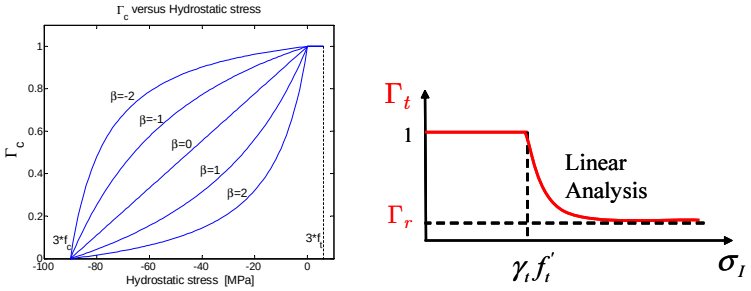

Figure 2.10: Graphical representation of Γ_c and Γ_t

crack opening displacement at the current Gauss point, and w_c the maximum crack opening displacement in the tensile softening curve **wittmann88**.

Concrete pores being seldom interconnected and the gel viscosity relatively high, gel absorption by the pores is not explicitly accounted for. Furthermore, gel absorption by the pores is accounted for by the kinetic equation through the latency time which depends on concrete porosity. The higher the porosity, the larger the latency time.

Γ_c in turn accounts for the reduction in AAR volumetric expansion under compressive stresses (in which case gel is absorbed by diffused micro-cracks) **multon03**:

$$\Gamma_c = \begin{cases} 1 & \text{if} \quad \overline{\sigma} \leq 0. \quad \text{Tension} \\ 1 - \frac{e^{\beta}\overline{\sigma}}{1+(e^{\beta}-1.)\overline{\sigma}} & \text{if} \quad \overline{\sigma} > 0. \quad \text{Compression} \end{cases} \tag{2.13}$$

$$\overline{\sigma} = \frac{\sigma_I + \sigma_{II} + \sigma_{III}}{3f'_c} \tag{2.14}$$

This expression will also reduce expansion under uniaxial or biaxial confinement, Figure 2.10; these conditions are more directly accounted for below through the assignment of weights.

2.2.4 AAR Strain Redistribution

The third major premise of the model is that the volumetric AAR strain must be redistributed to the three principal directions according to their relative propensity for expansion on the basis of a weight which is a function of the respective stresses.

The determination of the weight is relatively straightforward for triaxial AAR expansion under uniaxial

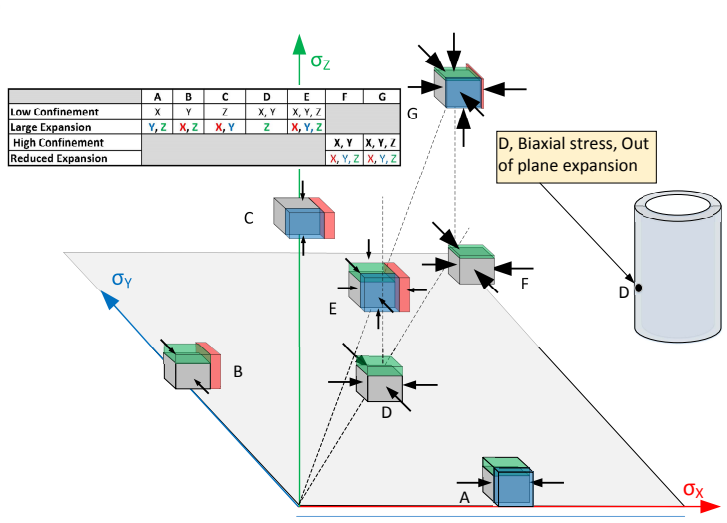

Figure 2.11: Effect of confinement on AAR strain redistribution

confinement (for which some experimental data is available), but it is more problematic for biaxially or triaxially confined concrete. Given a principal stress vector defined by $\sigma_k, \sigma_l, \sigma_m$, we need to assign a weight to each of those three principal directions. These weights will control the AAR volumetric expansion distribution. For instance, with reference to Figure E.1, we consider three scenarios.

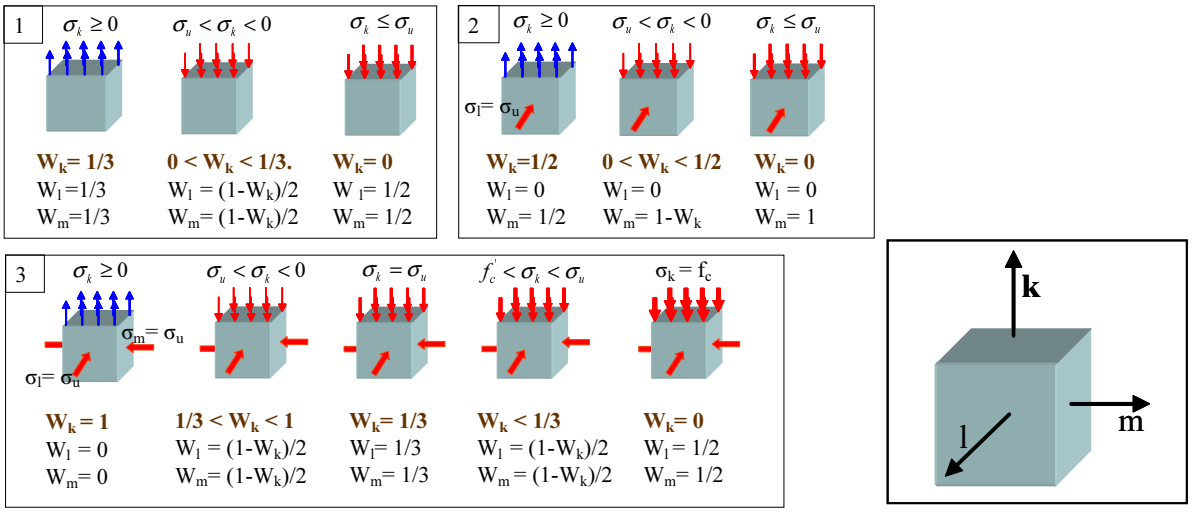

Figure 2.12: Weight of volumetric aar redistribution in selected cases

Uniaxial state of stress, where we distinguish the following three cases:

1. In the first case, we have uniaxial tension, and hence, the volumetric AAR strain is equally redistributed in all three directions.
2. Under a compressive stress greater than the limiting one (σ_u), the weight in the corresponding (k) direction should be less than one third. The remaining AAR has to be equally redistributed in the other two directions.
3. If the compressive stress is lower than σ_u, than AAR expansion in the corresponding direction is

prevented (weight equal zero), and thus the other two weights must be equal to one half.

Biaxial state of stress in which we have a compressive stress equal to σ_u in one of the three principal directions. In this case, the corresponding weight will always be equal to zero. As to the possible three combinations:

1. Tension in one direction, equal weights of one half.
2. Compression greater than σ_u in one direction, then the corresponding weight must be less than one half, and the remaining weight is assigned to the third direction.
3. Compression less than σ_u, then the corresponding weight is again zero, and a unit weight is assigned to the third direction.

Triaxial state of stress in which we have σ_u acting on two of the three principle directions. We identify the following five cases:

1. Tension along direction k, then all the expansion is along k.
2. Compressive stress greater than σ_u, then we have a triaxial state of compressive stress, and the corresponding weight will be between one and one third. The remaining complement of the weight is equally distributed in the other two directions.
3. Compression equal to σ_u, hence we have a perfect triaxial state of compressive stress. In this case we have equal weights of one third. It should be noted that the overall expansion is reduced through Γ_c.
4. Compression less than σ_u but greater than the compressive strength. In this case, the weight along k should be less than one third, and the remaining equally distributed along the other two directions.
5. Compression equal to the compressive strength. In this case, the corresponding weight is reduced to zero, and the other two weights are equal to one half each.

Based on the preceding discussion, we generalize this weight allocation scheme along direction k as follows

1. Given σ_k, identify the quadrant encompassing σ_l and σ_m, Figure 2.13. Weight will be determined through a bilinear interpolation for those four neighboring nodes.

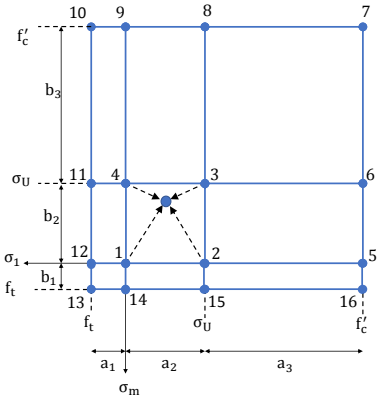

Figure 2.13: Weight regions

2. Determine the weights of the neighboring nodes from Table 2.3 through proper linear interpolation of σ_k.

Table 2.3: Triaxial weights

Node			Weights		
No.	σ_l	σ_m	$\sigma_k \geq 0$	$\sigma_k = \sigma_u$	$\sigma_k = f'_c$
1	0.	0.	1/3	0.	0.
2	σ_u	0.	1/2	0.	0.
3	σ_u	σ_u	1.	1/3	0.
4	0.	σ_u	1/2	0.	0.
5	f'_c	0.	1/2	0.	0.
6	f'_c	σ_u	1.	1/2	0.
7	f'_c	f'_c	1.	1.	1/3
8	σ_u	f'_c	1.	1/2	0.
9	0.	f'_c	1/2	0.	0.
10	f'_t	f'_c	1/2	0.	0.
11	f'_t	σ_u	1/2	0.	0.
12	f'_t	0.	1/3	0.	0.
13	f'_t	f'_t	1/3	0.	0.
14	0.	f'_t	1/3	0.	0.
15	σ_u	f'_t	1/2	0.	0.
16	f'_c	f'_t	1/2	0.	0.

3. Compute the weight from:

$$W_k(\sigma_k, \sigma_l, \sigma_m) = \sum_{i=1}^{4} N_i(\sigma_l, \sigma_m) W_i(\sigma_k) \tag{2.15}$$

where N_i is the usual two bilinear shape function used in finite element and is given by

$$\mathbf{N}(\sigma_l, \sigma_m) = \frac{1}{ab} \lfloor\ (a-\sigma_l)(b-\sigma_m) \quad \sigma_l(b-\sigma_m) \quad \sigma_l\sigma_m \quad (a-\sigma_l)\sigma_m\ \rfloor \tag{2.16}$$

$$\mathbf{W}(k) = \lfloor\ W_1(\sigma_k) \quad W_2(\sigma_k) \quad W_3(\sigma_k) \quad W_4(\sigma_k)\ \rfloor^t \tag{2.17}$$

$$a = (a_1|a_2|a_3) \qquad b = (b_1|b_2|b_3) \tag{2.18}$$

$$\sigma_l = (\sigma_l|f'_c - \sigma_l) \qquad \sigma_m = (\sigma_m|f'_c - \sigma_m) \tag{2.19}$$

The $i-j$ stress space is decomposed into nine distinct regions, Figure 2.13, where σ_u is the upper (signed) compressive stress below which no AAR expansion can occur along the corresponding direction (except in triaxially loaded cases). Hence, a and b are the dimensions of the quadrant inside which σ_i and σ_j reside.

Weights of the individual nodes are in turn interpolated according to the principal stress component in the third direction σ_k, Table 2.3. Those weights are for the most part based on the work of (**larive98**) and (**multon03**), but in some cases due to lack of sufficient experimental data, based on simple "engineering common sense."

A simple example for weight determination is shown here. Assuming that the principal stresses are given by $\lfloor\ \sigma_l \quad \sigma_m \quad \sigma_k\ \rfloor = \lfloor\ -5.0 \quad -8.0 \quad -5.0\ \rfloor$ MPa, and that f_c, f'_t, and σ_u are equal to -30.0, 2.0, and -10.0 MPa respectively, we seek to determine W_k. The stress tensor places us inside the quadrant defined by nodes 1-2-3-4 whose respective weights are equal to: $W_1 = \frac{1}{2}\left(\frac{1}{3}\right) = \frac{1}{6}$, $W_2 = \frac{1}{2}\left(\frac{1}{2}\right) = \frac{1}{4}$, $W_3 = \frac{1}{3} + \frac{1}{2}\left(1.0 - \frac{1}{3}\right) = \frac{2}{3}$, and $W_4 = \frac{1}{2}\left(\frac{1}{2}\right) = \frac{1}{4}$. Also, a and b are both equal to -10 MPa, and the "shape factors" will be $N_1 = \frac{1}{100}\left[(-10+5)(-10+8)\right] = \frac{1}{10}$, $N_2 = \frac{1}{100}\left[-5(-10+8)\right] = \frac{1}{10}$, $N_3 = \frac{1}{100}\left[(-5)(-8)\right] = \frac{4}{10}$, $N_4 = \frac{1}{100}\left[-8(-10+5)\right] = \frac{4}{10}$, and finally $W_k = \frac{1}{10} \times \frac{1}{6} + \frac{1}{10} \times \frac{1}{4} + \frac{4}{10} \times \frac{2}{3} + \frac{4}{10} \times \frac{1}{4} = 0.40833$.

Based on the earlier work of (**struble81**) in which it was reported that no gel expansion can occur at pressures above 11 MPa, σ_u is taken as -10 MPa. This value was also confirmed by (**larive98**). f'_t and f'_c are the concrete tensile and compressive strengths respectively.

Individual strain is given by

$$\dot{\varepsilon}_i^{AAR} = W_i \dot{\varepsilon}_V^{AAR} \tag{2.20}$$

The proposed model will indeed result in an anisotropic AAR expansion. While not explicitly expressed in tensorial form, the anisotropy stems from the different weights assigned to each of the three principal directions.

2.2.5 Degradation

Deterioration being time dependent, the following time dependent non-linear model is considered, Figure 2.14.

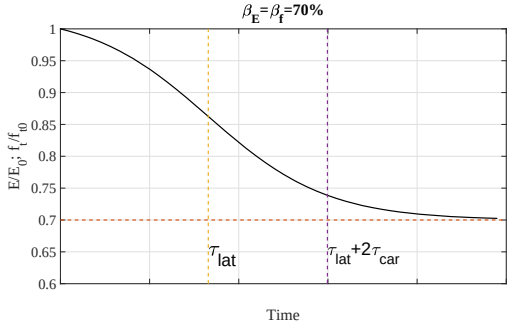

Figure 2.14: Degradation of E and f'_t

$$E(t,\theta) = E_0 \left[1 - (1 - \beta_E)\, \xi(t,\theta)\right] \tag{2.21}$$

$$f'_t(t,\theta) = f'_{t,0} \left[1 - (1 - \beta_f)\, \xi(t,\theta)\right] \tag{2.22}$$

where E_0 and $f'_{t,0}$ are the original elastic modulus and tensile strength; β_E and β_f are the corresponding residual fractional values when ε_{AAR} tends to $\varepsilon^{\infty}_{AAR}$.

Chapter 3

Methodology for Thermal Analysis with Solar Radiation

Abstract

This chapter discusses the fundamentals and formulations of solar radiation. More specifically, this chapter contains the methodology on how to calculate the amount of solar radiation on a surface of interest and consequently the amount of temperature increase due to it.

3.1 Preliminaries

3.1.1 Units

Proper attention must be given to the units. In this context, we distinguish between thermal and stress analyses.

For thermal analyses, units are shown in Table 3.1. The time unit is the so-called Analysis tTime Unit(ATU) which is equivalent to one month. In such an analysis, there are no applied forces

For stress analysis, the units are defined in Table 3.2. Note that in the incremental stress analysis, each increment will be one ATU.

3.1.2 Conversions for selected quantities

One has to be particularly attentive to the conversion facotrs for the variables, especially in the thermal analysis. Here are some key conversions.

Thermal Conductivity; SI Converting to month:

$$\begin{aligned}[\mathrm{J\,m^{-1}\,K^{-1}\,mo^{-1}}] &= \frac{\mathrm{J}}{\mathrm{sW}} 3,600 \frac{\mathrm{s}}{\mathrm{h}} 24 \frac{\mathrm{h}}{\mathrm{d}} 30.438 \frac{\mathrm{d}}{\mathrm{mo}} [\mathrm{W\,m^{-1}\,K^{-1}}] \\ &= (2,629,843)[\mathrm{W\,m^{-1}\,K^{-1}}] \end{aligned} \tag{3.1}$$

Thermal Conductivity; Imperial from Engineering Toolbox: $[\mathrm{J\,m^{-1}\,K^{-1}\,h^{-1}}]$=6,230 $[\mathrm{BTU\,ft^{-1}\,h^{-1}\,^{\circ}F^{-1}}]$

Table 3.1: Thermal Analysis

Quantity	Dimensions		Units	
	Technical	Base Units	Definition	Used in this report
Length	L	L	m	
Time	t	t	s	
Mass	M	M	Kg	
Temperature	T	T	K	
Mass Density (ρ)	$M.L^{-3}$	$M.L^{-3}$		$Kg.m^{-3}$
Force (F)	F	$M.L.t^{-2}$	N	$Kg.m.s^{-2}$
Heat (Q)	F.L	$M.L^2.t^{-2}$	J	$Kg.m^2.ATU^{-2}$
Power	$J.t^{-1}$	$M.L^2.t^{-3}$	W	$Kg.m^2.ATU^{-3}$
Specific heat (c_p)	$J.T^{-1}.M^{-1}$	$L^2.t^{-2}.T^{-1}$	$J.M^{-1}.T^{-1}$	$J.Kg^{-1}.K^{-1}$
Thermal Conductivity (k)	$W.L^{-1}.T^{-1}$	$M.L.t^{-3}.T^{-1}$	$J.t^{-1}.L^{-1}.T^{-1}$	$J.ATU^{-1}.m^{-1}.\ K^{-1}$
Thermal diffusivity (μ)	$M^2.T^{-1}$	$L^2.t^{-1}$	$L^2.t^{-1}$	

Table 3.2: Stress Analysis

Quantity	Dimensions		Units
	Technical	Base Units	Used in this report
Length	L	L	m
Time	t	t	s
Mass	M	M	Kg
Temperature	T	t	K
Force (F)	F	$M.L.t^{-2}$	MN
Pressure (p)	$F.L^{-2}$	$M.L^{-3}.t^{-2}$	MPa

$$[\mathrm{J\,m^{-1}\,K^{-1}\,mo^{-1}}] = 6,230[\mathrm{BTU\,ft^{-1}\,h^{-1}\,{}^\circ F^{-1}}]24\frac{\mathrm{h}}{\mathrm{d}}30.438\frac{\mathrm{d}}{\mathrm{mo}}$$
$$= 4,551,090[\mathrm{BTU\,ft^{-1}\,h^{-1}\,{}^\circ F^{-1}}] \tag{3.2}$$

Specific Heat; Imperial From this table:

$$[\mathrm{BTU\,lb^{-1}\,{}^\circ F^{-1}}] = 2.3885^{-4}[\mathrm{J\,kg^{-1}\,K^{-1}}] \tag{3.3}$$

Film Coefficient; SI Converting to month

$$[\mathrm{W\,m^{-2}\,K^{-1}}] = \frac{\mathrm{sW}}{\mathrm{J}}\frac{\mathrm{h}}{3600\mathrm{s}}\frac{\mathrm{d}}{24\mathrm{h}}\frac{\mathrm{mo}}{30.438\mathrm{d}}[\mathrm{J\,m^{-2}\,K^{-1}\,mo^{-1}}]$$
$$= (3.8025e-7)[\mathrm{J\,m^{-2}\,K^{-1}\,mo^{-1}}] \tag{3.4}$$

Film Coefficient; Imperial From here

$$
\begin{aligned}
[\mathrm{W\,m^{-2}\,K^{-1}}] &= 0.1761[\mathrm{BTU\,ft^{-2}\,h^{-1}\,{}^{\circ}F^{-1}}]24\frac{\mathrm{h}}{\mathrm{d}}30.438\frac{\mathrm{d}}{\mathrm{mo}} \\
&= 128.6432[\mathrm{BTU\,ft^{-2}\,mo^{-1}\,{}^{\circ}F^{-1}}] \qquad (3.5)
\end{aligned}
$$

From Equation 3.4 and 3.5 :

$$
\begin{aligned}
[\mathrm{J\,m^{-2}\,K^{-1}\,mo^{-1}}] &= \frac{128.6432}{3.8025e-7}[\mathrm{BTU\,ft^{-2}\,mo^{-1}\,{}^{\circ}F^{-1}}] \\
&= (3.3831e+08)[\mathrm{BTU\,ft^{-2}\,mo^{-1}\,{}^{\circ}F^{-1}}] \qquad (3.6)
\end{aligned}
$$

3.1.3 Concrete Thermal Properties

Concrete thermal properties are taken from (**hatch**)
Mass density $\rho = 155.3$ [lb/ft^3]

$$
\begin{aligned}
\rho &= 155.3\mathrm{lb/ft^3} \\
&= (155.3)(16.02) \\
&= 2487\mathrm{kg/m^3} \qquad (3.7)
\end{aligned}
$$

Specific heat $c_p = 0.2$ [BTU lb^{-1} °F^{-1}]
Using equation 3.3 c_p is converted to [J kg^{-1} K^{-1}] units:

$$
\begin{aligned}
c_p &= 0.2\mathrm{BTU/lb/^{\circ}F} \\
&= \frac{(0.2)}{(2.3885e-4)} \\
&= 837\mathrm{J/kg/K} \qquad (3.8)
\end{aligned}
$$

Thermal Conductivity $k = 1.99$ [BTU ft^{-1} h^{-1} °F^{-1}]
From Equation 3.2.

$$
\begin{aligned}
k &= 1.99\mathrm{BTU/ft/h/^{\circ}F} \\
&= (1.99)(4,551,090) \\
&= 9,056,669\mathrm{J/m/K/mo} \qquad (3.9)
\end{aligned}
$$

Also, from Equation 3.1 we can compute:

$$
\begin{aligned}
k &= 9,056,669\mathrm{J/m/K/mo} \\
&= \frac{(9,056,669)}{(2,629,843)} \\
&= 3.44\mathrm{W/m/K} \qquad (3.10)
\end{aligned}
$$

For the purpose of validating the material properties of the concrete used in this study the values are compared to those taken from (**malm2017proceedings**) which are as follows and they have the same order of magnitude with those used herein.

Table 3.3: Concrete thermal properties;
* From (**hatch**)
** From (**malm2017proceedings**)

Quantity	Symbol	Hatch*	Icold**	units
Mass Density	ρ	2,487	2,300	$\mathrm{kg\,m^{-3}}$
Specific Heat	c_p	837	900	$\mathrm{J\,kg^{-1}\,K^{-1}}$
Conductivity	k	3.44 9,057,000	2	$\mathrm{W\,m^{-1}\,K^{-1}}$ $\mathrm{J\,m^{-1}\,K^{-1}\,mo^{-1}}$
Thermal Diffusivity	μ	0.143 4.35	?? $\mathrm{m^2\,mo^{-1}}$	$\mathrm{m^2\,d^{-1}}$

3.2 Solar Radiation

Solar Radiation refers to the power (J/m^2) received by the sun in the form of electromagnetic radiation. It is a function of the orientation of the surface with respect to the sun. An exact mathematical model for solar radiation is quite complex, and an approximation by **kreiderempty citation** offered the following linear simplification

$$q_s = \alpha\, I(s,t) \tag{3.11}$$

where I is total solar radiation or global radiation on a surface s at time t and α is the absorptivity of the surface which is defined by the fraction of I absorbed by the surface structure. For concrete, $\alpha = 0.65$.

The global radiation ,I_{glo}, is the sum of the diffuse radiation, I_{diff} (i.e. solar radiation received its direction has been changed by scattering by the atmosphere), and direct radiation, I_{dir} (solar radiation intercepted by a surface with negligible direction change and scattering in the atmosphere). Those radiations are naturally site specifics and can be downloaded from various Typical Meteorological Years (TMY) sites such as (**energyplus**).

3.2.1 Preliminary Definitions

3.2.1.1 Solar Time

t_{sol} is the time based on apparent angular motion of the sun across the sky with solar noon being the time the sun crosses the meridian of the observer. It is given by

$$t_{sol} = t_{std} + \frac{L_{std} - L_{loc}}{15} + \frac{ET}{60} \tag{3.12}$$

where

L_{std} = longitude of the standard time zone (*degrees*). For example, in the United States, the longitudes of the standard time zones are 75^oW for Eastern, 90^oW for Central, 105^oW for Mountain, and 120^oW for Pacific.

L_{loc} = site longitude (*degrees*) Whereas exact, this equation does not account for the eccentricity of the Earth's orbit and the Earth's axial tilt. Hence, the equation is adjusted by an approximation empirical term

ET defined by the following:

$$ET = 9.87 \sin 2\left(360^o \times \frac{n-81}{364}\right) - 7.53 \cos\left(360^o \times \frac{n-81}{364}\right) - 1.5 \sin\left(360^o \times \frac{n-81}{364}\right) \tag{3.13}$$

and n is day of the year (i.e. $n = 1$ for Jan 1).

3.2.1.2 Solar Angles

δ is the angular position of the sun at solar noon (when the sun is in the local meridian) with respect to the plane of the equator, north positive, and $-23.45° \leq \delta \leq 23.45°$, Figure 3.1. It can be expressed by

$$\sin \delta = -\sin 23.45^o \cos \frac{360^o \times (n+10)}{365.25} \tag{3.14}$$

where n is defined as mentioned before.

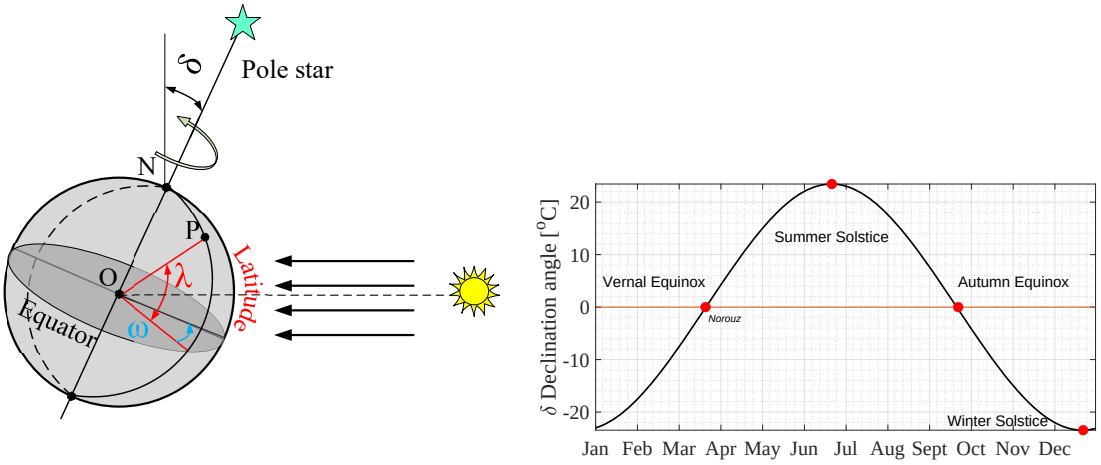

(a) Declination angle

(b) Seasonal variation of δ

Figure 3.1: Solar declination

Note that the heat flux, q_s, can only be applied during the hours between sunrise and sunset. The sunrise (t_{sr}) and sunset times (t_{ss}) can be determined from the following:

$$t_{sr} = 12 - \frac{1}{15} \cos^{-1}(-\tan\lambda \tan\delta) \tag{3.15}$$

$$t_{ss} = 12 + \frac{1}{15} \cos^{-1}(-\tan\lambda \tan\delta) \tag{3.16}$$

in which λ is latitude of the location and δ is solar declination.

Zenith Angle

θ_s is the angle between the zenith and the centre of the Sun's disc. as shown in Figure 3.2 is given by

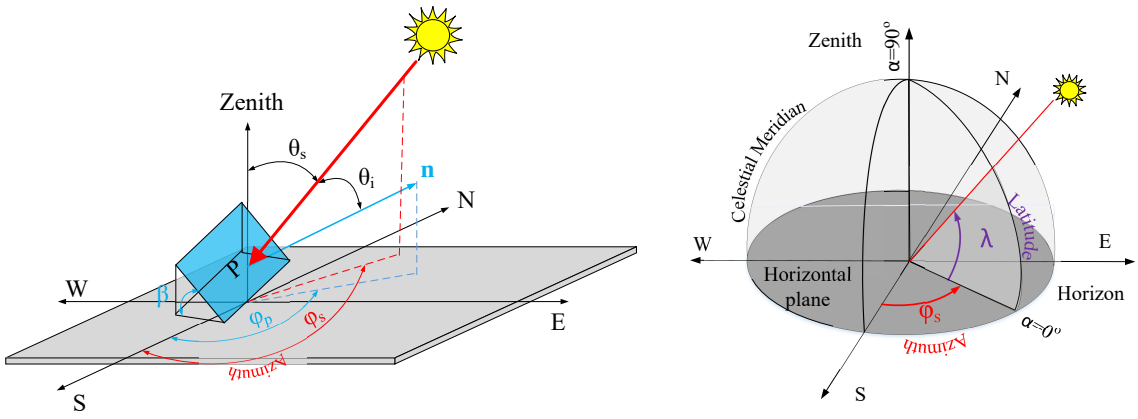

Figure 3.2: Solar characteristic angles

$$\cos\theta_s = \cos\lambda\cos\delta\cos\omega + \sin\lambda\sin\delta \tag{3.17}$$

where λ is the latitude of the location (north is positive), δ the solar declination, and ω is the angular displacement of the sun east or west of the local meridian due to rotation of the earth on its axis at 14° per hour; morning negative, afternoon positive; it is given by

$$\omega = \frac{t_{sol} - 12}{24} \times 360^o \tag{3.18}$$

where t_{sol} is the solar time in *hours*.

Incidence Angle

θ_i is the angle between the normal of the surface at point P and the line from point P to the sun, Figure 3.2 given by

$$\cos\theta_i = \cos\theta_s\cos\beta + \sin\theta_s\sin\beta\cos(\phi_s - \phi_p) \tag{3.19}$$

In this equation β is the angle between the surface and horizontal direction.

Plane azimuth angle

ϕ_p is the angle, measured on the surface, between the south and the projection of the plane normal **n**, Figure 3.2.

Sun azimuth angle

ϕ_s is the angle of the Sun's position. This horizontal coordinate defines the Sun's relative direction along the local horizon whereas the solar zenith angle (or its complementary angle solar elevation) defines the Sun's apparent altitude, Figure 3.2. It is defined by

$$\sin\phi_s = \frac{\cos\delta\sin\omega}{\sin\theta_s} \tag{3.20}$$

Table 3.4: Reflectivity of selected surfaces (**kreider**)

Surface	Reflectivity ρ_g
Soils	0.75
Water	0.07
Concrete, new	0.35
Concrete, old	0.25
Earth roads	0.04
Grass, dry	0.20
Grass, green	0.26

3.2.2 Solar Flux

3.2.2.1 Horizontal Surfaces

The total radiation on the horizontal surface or, in other words, global horizontal radiation is given by

$$I_{glo,hor} = I_{dir} \cos\theta_s + I_{diff} \tag{3.21}$$

where θ_s is the zenith angle of the sun.

3.2.2.2 Inclined Surfaces

Calculation of the total radiation on an inclined surface is far more complex, and is given by

$$I_{global} = I_{dir} \cos\theta_i + I_{diff} \frac{(1 + cos\beta)}{2} + I_{glo,hor} \rho_g \frac{(1 - cos\beta)}{2} \tag{3.22}$$

where θ_i is the incidence angle, Figure 3.2.

ρ_g = Reflectivity of the ground. The values of the reflectivity of some selected surfaces can be tabulated in Table 3.4

3.2.3 Discussion

3.2.3.1 Incidence angle

The role of the incidence angle in attenuating I_{dir} is further clarified by Figure 3.3 which shows the results of average monthly solar radiation calculations of a plane facing various directions in the space ($0^o < \phi_p < 270^o$). Eq. 3.22 suggests that the solar radiation intensity depends on cosine of the incidence angle ($cos(\theta_i)$) and therefore depends on the direction of the sun and also the surface. Figure 3.3(a) is an illustration of the physical meaning of this equation. Based on the assumption behind the equation, the surfaces facing South, West, North, and East would have $\phi_p = 0^o$, 90^o 180^o and 270^o respectively.

Figure 3.3(b) shows that in February the azimuth angle of the sun (ϕ_s) is about -2^o.

On the other hand, Figure 3.3(c) shows that $\cos(\theta_i)$ is maximum and therefore the direct solar radiation is also maximum facing South and minimum facing East. For other directions, the direct flux would be zero. This is consistent with Figure 3.3(a).

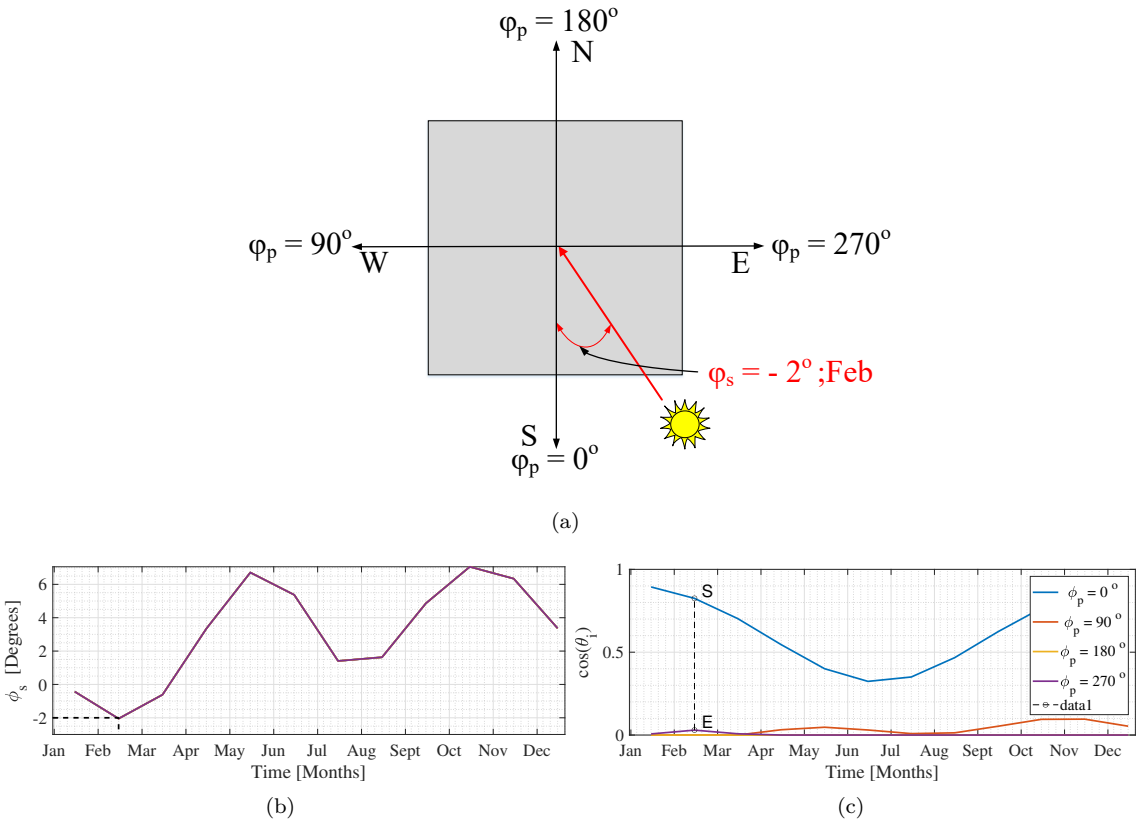

Figure 3.3: Seasonal impact on incidence angle for different plane orientations ϕ_p

3.2.3.2 Roles of various solar radiation forms

Finally, the preceding equations are best understood through Figure 3.4 associated with location latitude =42.1558°, longitude=-106.908° (site of a dam suffering from AAR), concrete reflectivity ρ_g =0.25, reflectivity α =0.65 in terms of ϕ_p and time. Solar flux are obtained from (**energyplus**).

These plots call for the following observations:

1. Direct flux is predominant, Figure 3.4(a), it is minimum at $\phi_p = 270$ (East) and maximum at $\phi_p = 0$ (South) where we have full southern exposure. The cutting (green) plane shows that in February the amount of direct radiation is dominant for southern exposure and diffuse radiation has the greatest participation in global radiation for other directions.
2. Diffuse and global horizontal intensities are both very small compared to the direct (except for $\phi_p \sim 0$).
3. Flux is very sensitive to ϕ_p.
4. Global solar radiation in February is shown for different exposures in Figure 3.4(b); as expected it is maximum for $\phi_p = 0$.
5. Yearly variation of I_{glo} is shown in Figure 3.4(c). As the azimuth angle of the sun (ϕ_s) varies from $\sim -2^o$ to $\sim 7^o$ (measured from South Figure 3.3(b)), it is expected that surfaces facing South experience higher direct solar radiation; in addition, based on our comments regarding Figure 3.4(a), direct radiation has higher participation in the total solar radiation amount and thus, it is expected that the lower incidence angle θ_i (higher direct radiation) results in generally higher global solar radiation intake. Figure 3.4(c) also shows higher global solar radiation values for South facing plane throughout the year compared to other directions.
6. Throughout the year, solar zenith angle is out of phase (90°) with the incidence angle, Figure 3.4(d). Furthermore, the incidence angle (θ_i) is clearly smallest for South facing plane which explains why solar radiation is largest for southern exposure for the specified location.

It is worth mentioning that the amount of direct solar radiation ($I_{dir}cos(\theta_i)$) received by a surface of interest depends on various factors including the time of the year, the declination and orientation of the surface and the direction of the sun radiation. To illustrate, figure 3.5(a) shows the variation of the three important declination, zenith and incidence angles for a vertical surface facing south. As seen, the zenith angle(θ_s) trend is the reverse of the declination angle (δ) and reaches its minimum value in June. On the other hand, as the surface is vertical, the incidence angle(θ_i) is the complementary angle of the zenith angle and becomes maximum in July. In other words, The sun radiates nearly parallel to the vertical surface in July which is expected to result in receiving less amount of solar radiation in July. However, another important factor is the amount of available direct solar radiation(I_{dir}) itself obtained for the horizontal surface which is then multiplied by $cos(\theta_i)$ to account for the surface declination. Figure 3.5(b) shows the amount of I_{dir} and $I_{dir}cos(\theta_i)$ on the left axis versus the amount of θ_i and $cos(\theta_i)$ on the right axis. It is shown that although the θ_i is maximum in June, the final calculated direct solar radiation $I_{dir}cos(\theta_i)$, is maximum in August since I_{dir} is greater at this time.

3.2.4 Algorithms

3.2.4.1 Solar Flux

The algorithm to determine the solar flux on a surfce is shown in Figure 3.6. The following quantities are site specific, and are assumed to be known: I_{diff}, I_{dir}, ρ_g, λ, ϕ_p, n, t_{loc}, and t_{std}.

1. Determine the equation of time (ET) using Eq. 3.13 and the solar declination angle (δ) from eq. 3.14

2. Using Eq. 3.12 calculate the solar time (t_{sol}) and solar hour angle (ω) from Eq. 3.18
3. Having the latitude of the location(λ) and using (δ) and (ω) from the previous steps, zenith angle of the sun (θ_s) is then determined using eq. 3.17
4. The azimuth angle of the sun (ϕ_s) can then be determined using Eq. 3.20
5. Using values for ϕ_p, ϕ_s and θ_s from steps above, the incidence angle (θ_i) can then be calculated using equation Eq. 3.19 which can take values between 0 and 90 degrees.
6. Finally Eq. 3.22 determines the solar radiation

3.2.4.2 Finite element determination of ϕ_p

In the thermal (finite element) analysis of a dam, one needs to determine ϕ_p for each element in order to determine the solar flux, Figure 3.7. It is assumed that the element is planar, and node numbering is counterclockwise looking from the outside. The procedure is as follows, Figure 3.8.

1. Define two (non colinear) vectors along first and last edge: $\mathbf{V}_{12}$ and $\mathbf{V}_{14}$, Figure 3.7
2. Take the cross product of those two vectors to define the normal

$$\mathbf{n}' = \mathbf{V}_{12} \times \mathbf{V}_{14} \tag{3.23}$$

3. Determine the projection of $\mathbf{n}'$ into $\mathbf{n}$ on the horizontal plane ($\mathbf{n}'(x, y, z) \rightarrow \mathbf{n}(x, y)$.
4. Determine ϕ_p

$$\phi_p = \cos^{-1} \frac{\mathbf{S} \cdot \mathbf{n}}{||\mathbf{n}||\ ||\mathbf{S}||} \tag{3.24}$$

where $\mathbf{S}$ is a normalized vector along the south direction.

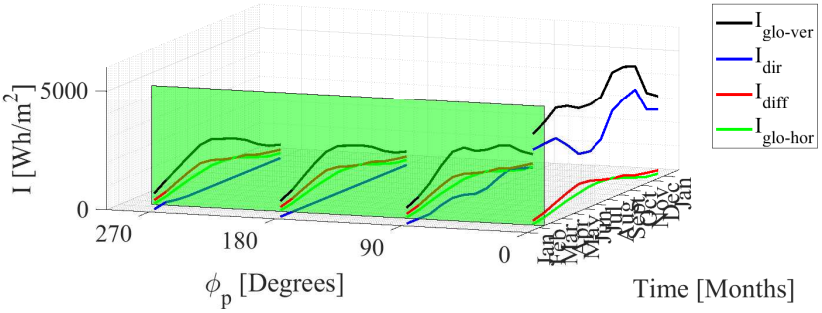

(a) Individual radiation in terms of month and ϕ_p

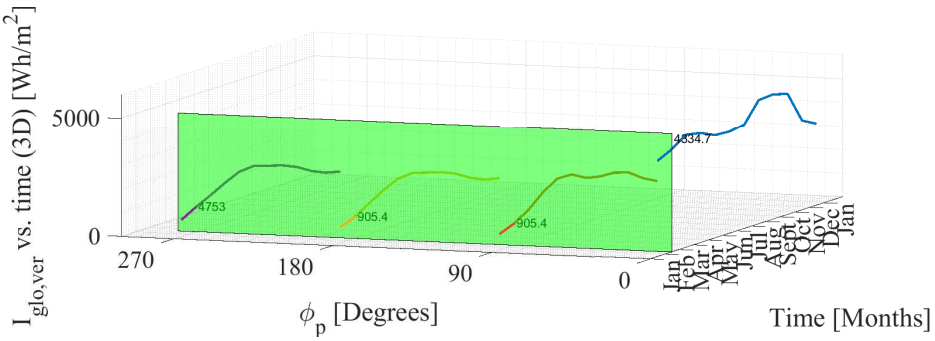

(b) Global solar radiation in February

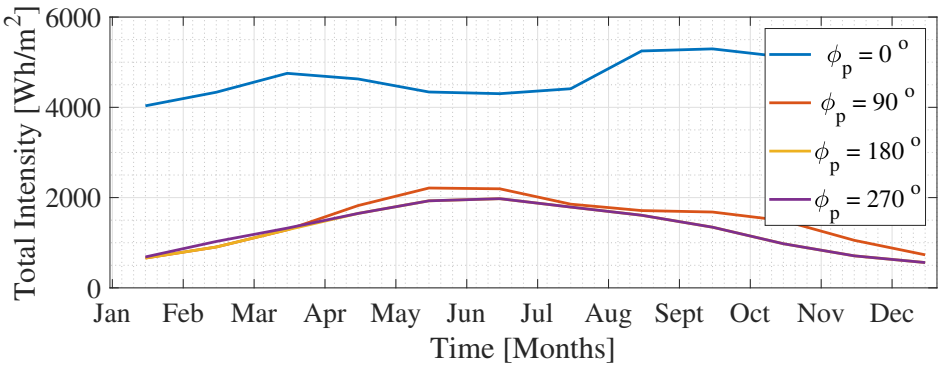

(c) Monthly total intensity

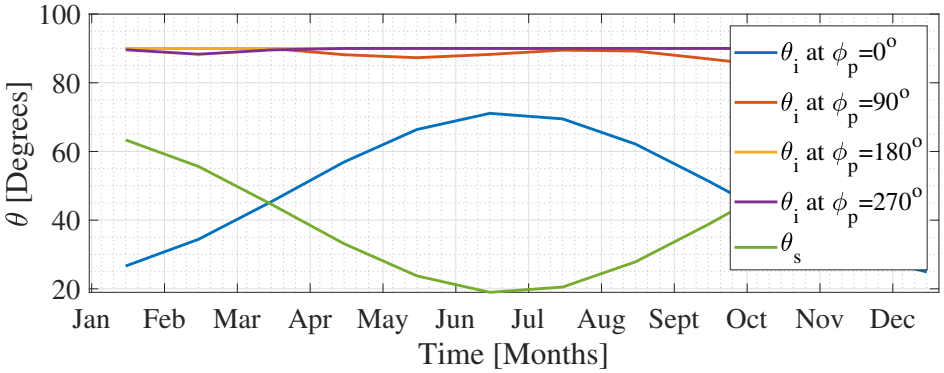

(d) Incidence and surface azimuth angles

Figure 3.4: Solar fluxes at latitude 42.1558° and longitude -106.908°

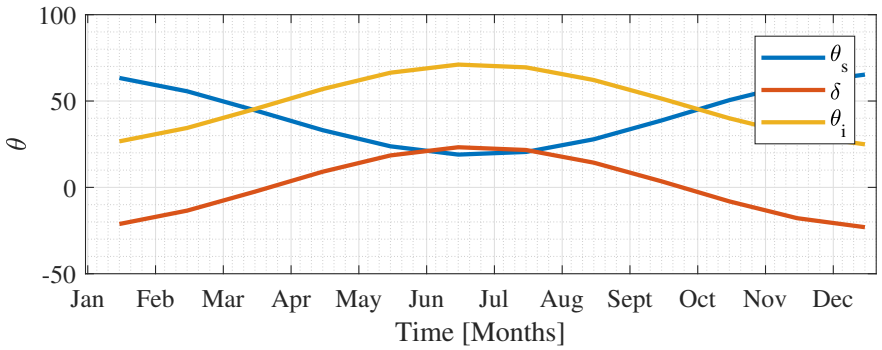

(a) Variation of zenith, declination and incidence angles throughout a year for a vertical surface

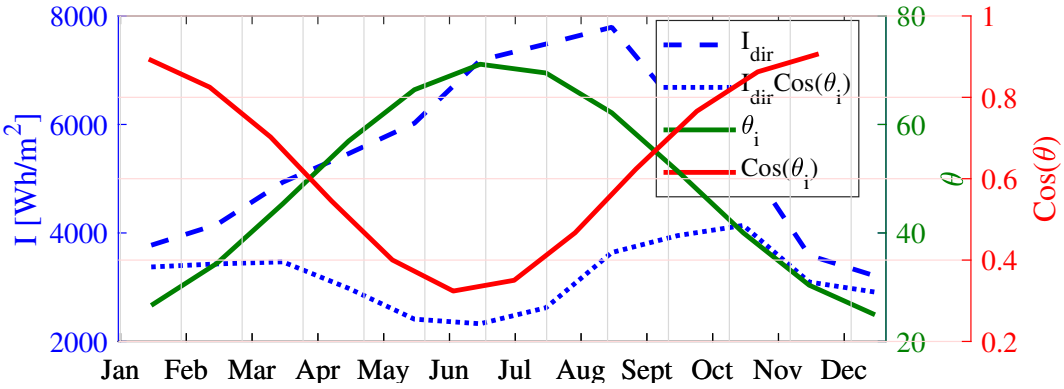

(b) Amount of solar radiation versus incidence angle throughtout a year for a vertical surface

Figure 3.5: Solar radiation and solar angles for a vertical surface at at latitude 42.1558° and longitude -106.908°

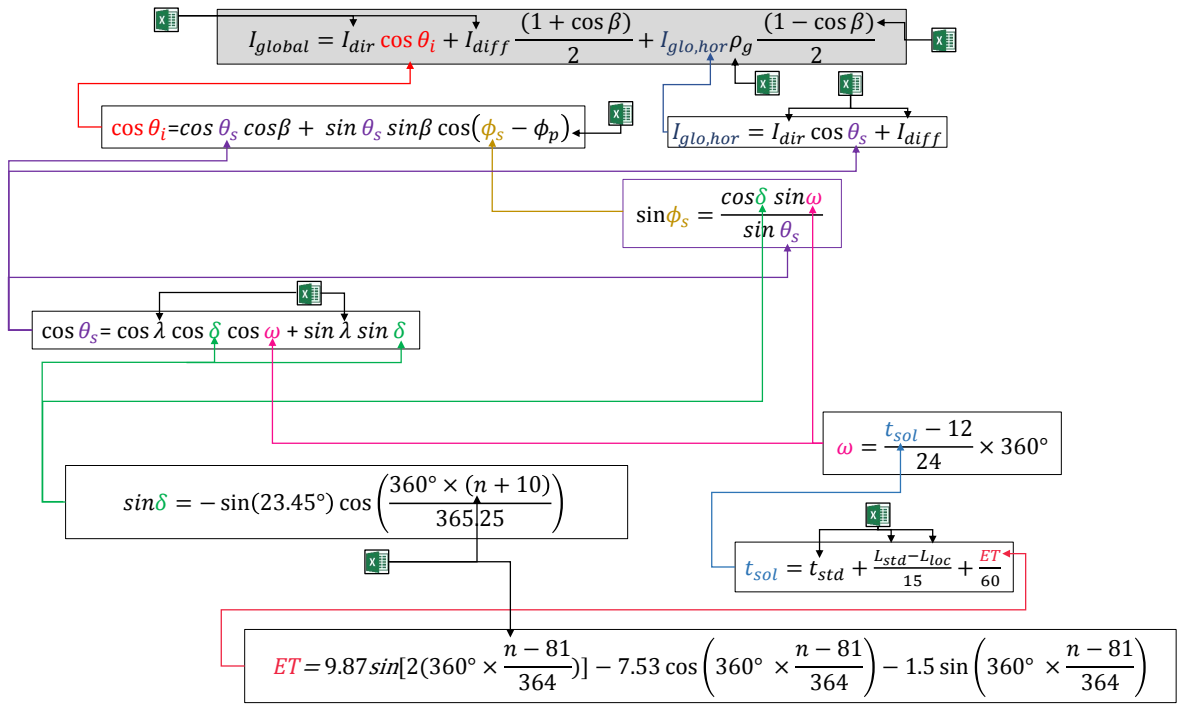

Figure 3.6: Algorithm to determine the solar radiation intensity

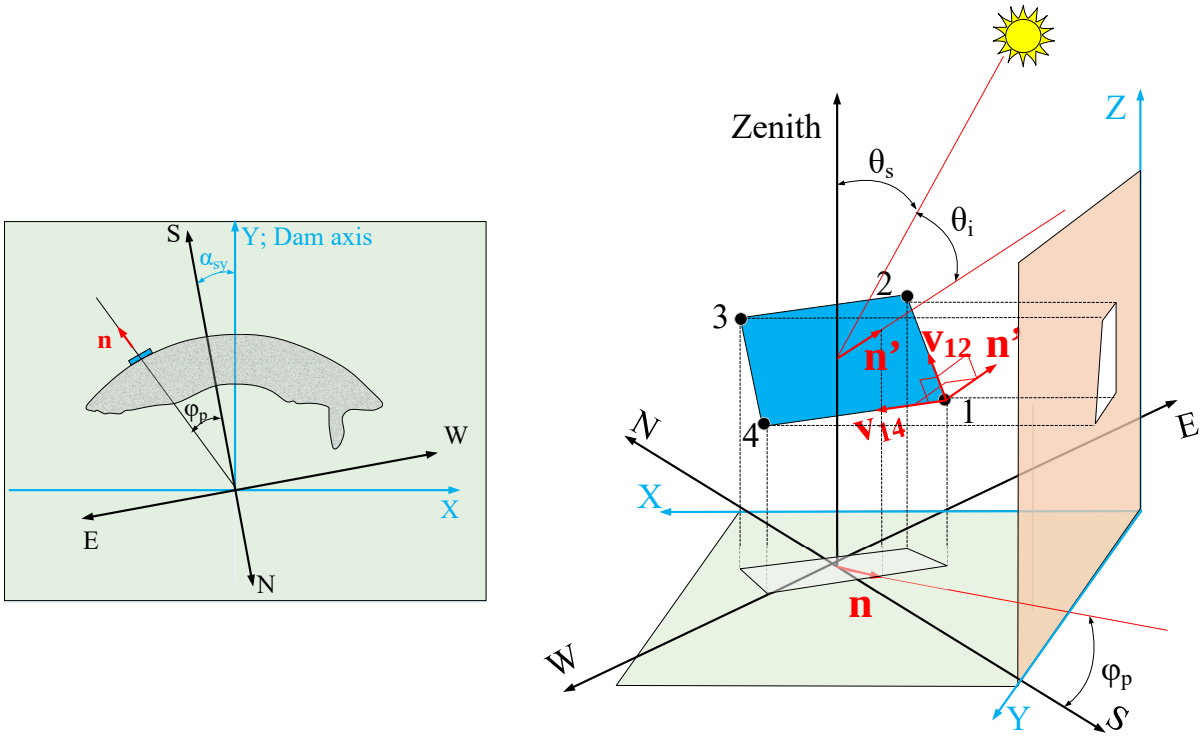

Figure 3.7: Solar radiation on a concrete dam surface

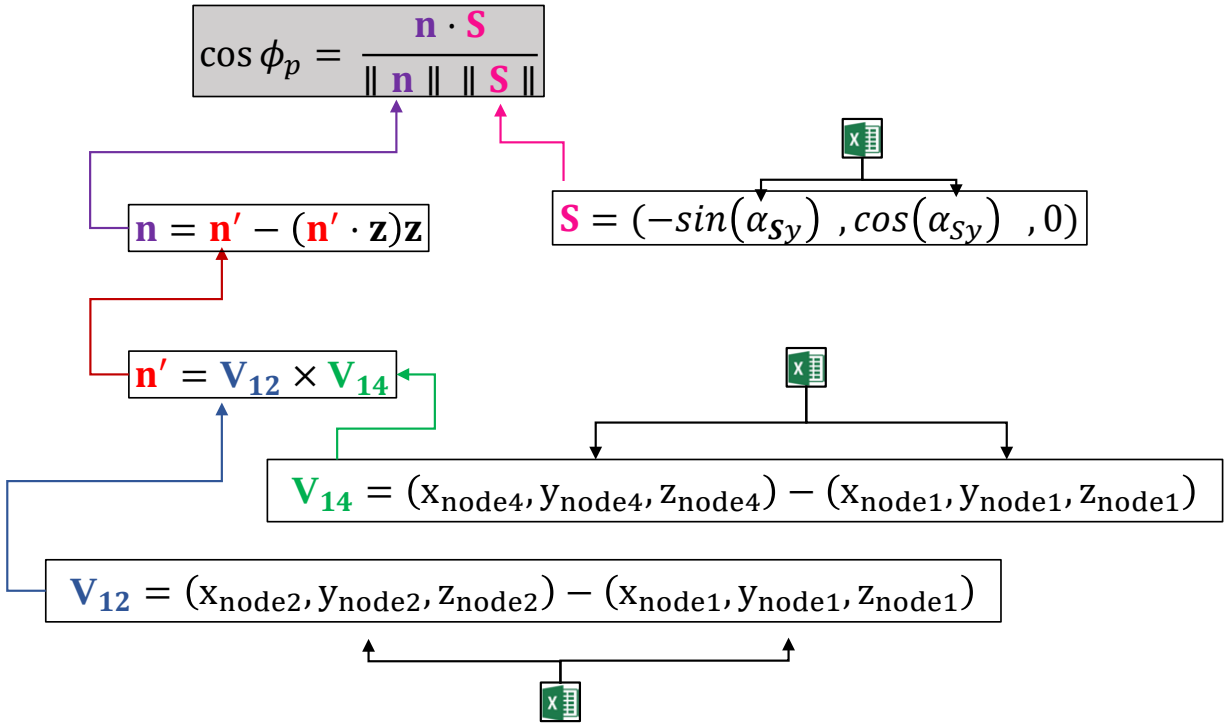

Figure 3.8: Algorithm to determine ϕ_p for a mesh element

3.2.4.3 Temperature Variation Due to Solar Radiation

After the solar flux is calculated using the above-mentioned equations, the next step is to determine the amount of temperature increase caused by the solar radiation using equation 3.25. In this equation q is the solar flux and h is the film coefficient which herein is taken equal to 20 [$\mathrm{W\,m^{-2}\,K^{-1}}$] for air-concrete interface and was obtained from **hatchempty citation**.

$$\Delta T = \frac{q}{h} \tag{3.25}$$

em34empty citation report provides the temperature increase due to solar radiation at several locations. The reported data are the mean annual temperature variation for tilted surfaces with different inclination and orientations.Figure 3.9 shows the data for latitudes between 40^o to 45^o. In this study, in order to validate the adopted solar radiation solution, the temperature variation at latitude of 42^o is calculated and compared to figure 3.9. Figure 3.10 shows temperature increase resulted from our solution and **em34empty citation**. As seen, they both follow the same trend as the solar radiation is maximum while the surface angle to the vertical direction increases and the surface faces south (the angle between surface normal and North direction approaches 180); On the other side, the minimum value occurs while the surface is facing the North direction and tilted downward (the angle between the surface and vertical direction is negative). Although the trend is the same for both figures, the two figures are not showing identical minimum temperature values which is due to the fact that there are a set of assumptions made for the calculations which might be different from those from **em34empty citation**.

em34empty citation report also provides the average monthly temperature increase due to solar radiation in figure 3.11 for the upstream face of Seminoe. In figure 3.12 the temperature values from figure 3.11 are re-plotted in centigrade degrees and compared to the results from equation 3.25. The major observations from this figure are that computed temperatures fall within the observed range and the slopes are nearly identical and the dispersion of the numerical case is less than the other one.

3.3 Conclusion

To summarize, this chapter presented a set of preliminary yet highly important studies to ensure the accuracy of the subsequent complex analysis. In the first section the units and unit conversions are clarified to make all the units consistent within the analysis. In the second part the solar radiation concept is defined and the formulations are discussed; in addition, the procedure of solar radiation calculation was shown in two explaining flowcharts.

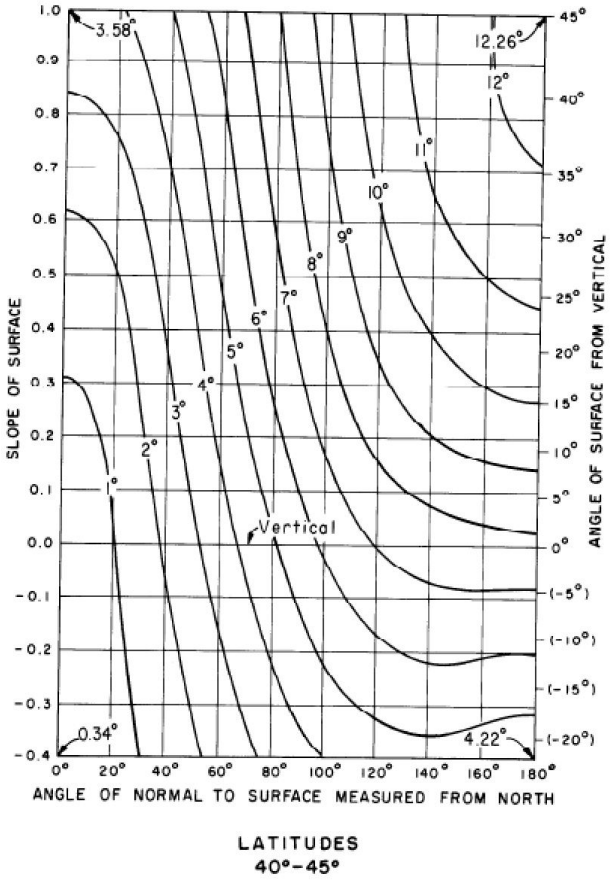

Figure 3.9: Mean annual temperature variation due to solar radiation for surfaces with various orientations and inclinations adopted from **em34empty citation**

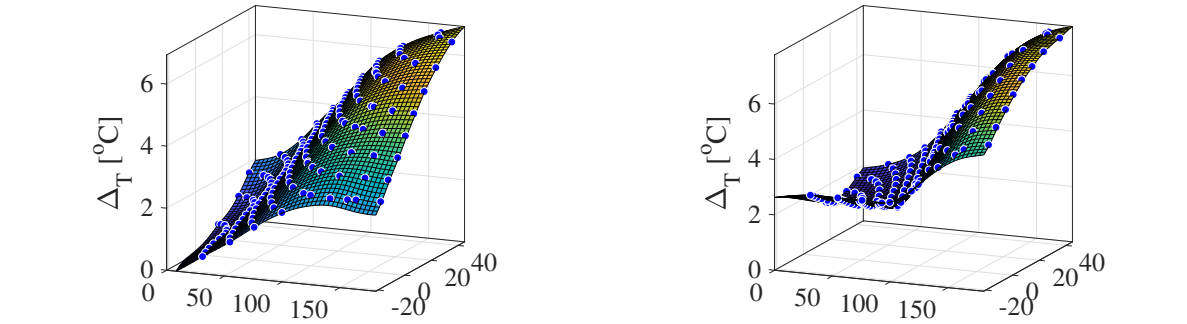

(a) from **em34empty citation**

(b) from equation 3.25

Figure 3.10: Comparison of temperature variation due to solar radiation at latitude 42.1558° and longitude -106.908°

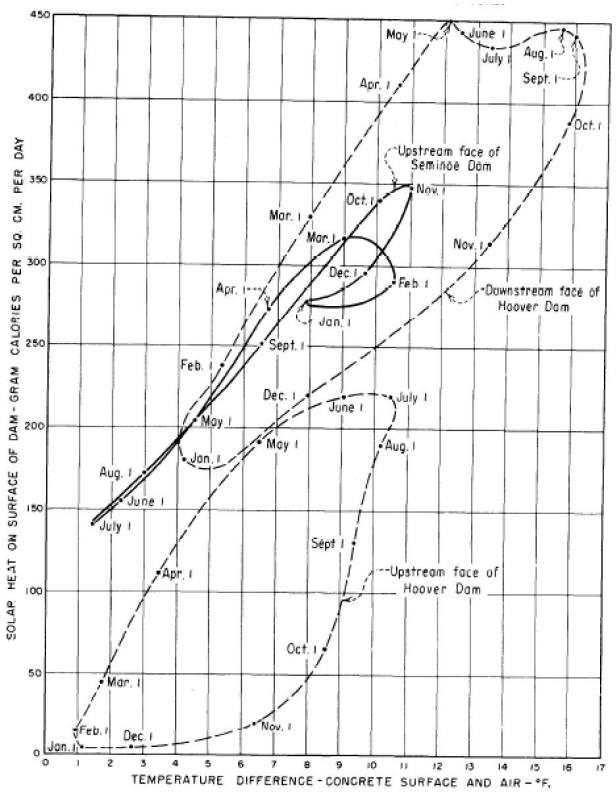

Figure 3.11: Average monthly temperature increase due to solar radiation for upstream face of Seminoe from **em34empty citation**

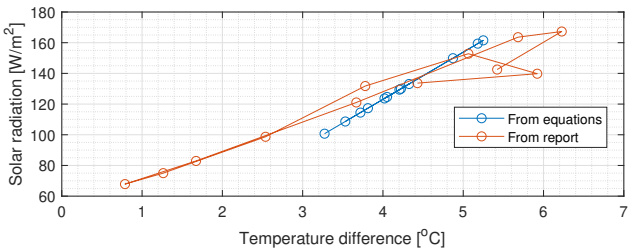

Figure 3.12: Comparison of solar radiation and the resulting temperature increase from **em34empty citation** and equation 3.25

Part II

APPLICATION; Seminoe Dam

Chapter 4

Physical Properties

Abstract

The complexity of the analysis involving a 3D nonlinear analysis of an arch-gravity dam subjected to AAR commands great care in proper preparation of all relevant input parameters.

This will be covered in this chapter extracting key and relevant parameters that have been summarized in Appendix A.

4.1 Properties

4.1.1 Thermal Analysis

The input data for the thermal analysis of the Seminoe including concrete material properties and film coefficients are described in this section. Based on the discussions in previous chapters, the input data for air and water temperatures are derived and presented herein.

4.1.1.1 Concrete Material Properties

The material properties of the dam concrete used during the thermal analysis is presented in table 4.1. It is worth mentioning that the units provided in this table are exactly adopted in the thermal analysis.

Table 4.1: Concrete material Properties used in thermal analysis
* From (**hatch**)

Quantity	Symbol	Value*	units
Mass Density	ρ	2,487	$\mathrm{kg\,m^{-3}}$
Specific Heat	c_p	837	$\mathrm{J\,kg^{-1}\,K^{-1}}$
Conductivity	k	9,057,000	$\mathrm{J\,m^{-1}\,K^{-1}\,mo^{-1}}$
Thermal Diffusivity	μ	4.35	$\mathrm{m^2\,mo^{-1}}$

Table 4.2: Air and water film coefficients

	Film Coefficient	units
Air	20	$W\,m^{-2}\,K^{-1}$
	$5.26 * 10^7$	$J\,m^{-2}\,K^{-1}\,mo^{-1}$
Water	60	$W\,m^{-2}\,K^{-1}$
	$1.6 * 10^8$	$J\,m^{-2}\,K^{-1}\,mo^{-1}$

4.1.1.2 Film Coefficient

In thermal analysis the surrounding fluid temperature are applied through a film to the structure. For this purpose the film coefficient of water and air are used as shown in table 4.2 which are adopted from **hatchempty citation**. It is important to note that the film coefficient units should be converted to be consistent with the analysis time step unit.

4.1.1.3 Air Temperature

Seminoe dam is exposed to the air at its downstream, crest and a part of upstream above the water level. The air temperature data is available from USBR. For the purpose of conducting a thermal analysis, a sine curve is fitted to the available data to represent the temperature variation throughout the year figure 4.1. The resulting sinusoidal equation used for the application of air temperature is presented below. In this equation t denotes the analysis time in days.

$$T(t)_{DS,Air} = 12.7 + 13.4sin(0.0175t - 1.95) \tag{4.1}$$

$$T(t)_{US,Air} = 12.8 + 12.98sin(0.0175t - 1.96) \tag{4.2}$$

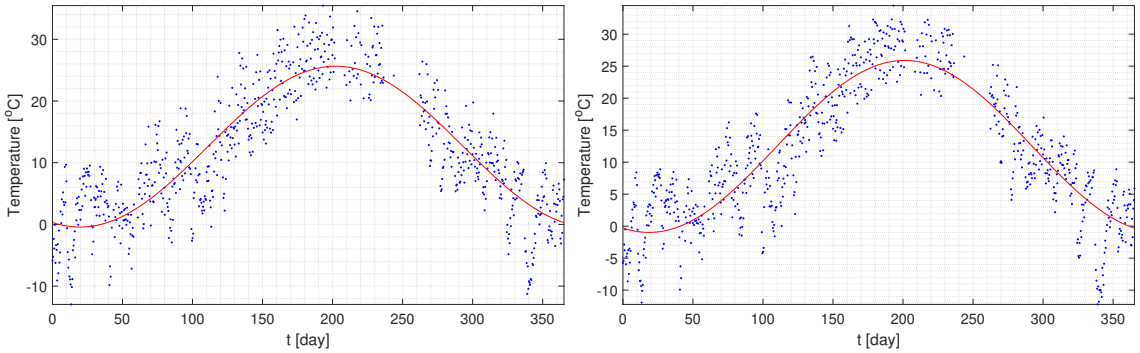

(a) Upstream (b) Downstream

Figure 4.1: Seminoe air temperature

4.1.1.4 Solar Radiation

In addition to the surrounding air, the surface temperature of Seminoe is affected by the amount of solar energy radiating during the daylight hours which should be taken into account during the thermal analysis.

Because Seminoe upstream is facing the south direction with an angle of about $3^o3'30"$, and as a matter of fact, the solar direct radiation is maximum at the south direction, the seminoe upstream which is facing south receives the maximum amount of solar radiation while the downstream is facing back to the sun. Therefore, the effect of solar radiation is applied at the exposed part of the upstream face of the Seminoe. It is worth mentioning that the temperature increase due to solar radiation for Seminoe crest is computed using the solar flux for horizontal surfaces obtained from (**energyplus**).

4.1.1.5 Water Temperature

Approximation of the monthly variation of the water temperature at different depths is an important task in the lack of sufficient field data during thermal analysis. For Seminoe, the water temperature during various months at 10 different depths from surface down to 100 ft is available. However, the equations suggested for the water temperature approximation in dams, require that at least some data from the bottom of the reservoir be available. In this case the available reservoir temperatures are used to fit a sin curve to represent the surface temperature and a constant temperature equal to 4^oC is taken as the bottom temperature based on the statement in **tatin2018statisticalempty citation** that the water temperature cannot become less than this value. the Maier **ardito2008diagnosticempty citation** equation B.5 parameter ϕ is then obtained by fitting the data to equation B.5 using those two defined top and bottom temperatures. The ϕ value was determined to be equal to -0.02 for Seminoe.

$$T_w(y_w,t) = T_{bot}(t).\frac{1-e^{-\phi y_w}}{1-e^{-\phi H}} + T_{top}(t).\frac{e^{-\phi y_w}-e^{-\phi H}}{1-e^{-\phi H}} \tag{4.3}$$

where T_{bot} is the time sequence of temperature measurements at $y_w = H$ (reservoir bottom); T_{top} is the time sequence of temperature measurements at $y_w = 0$ (reservoir top), and most importantly ϕ is an empirical parameter that must be properly determined for the specific dam. The resulted equation is presented below. It should be noted that the R-squared goodness of fit is about 0.6.

$$\begin{aligned} T_{Bottom} &= 4 \\ T_{Top} &= 10.3 - 5.3sin(\frac{2\pi}{12}t - 0.11) \\ T(t,y_w,H)_{Reservoir} &= (T_{Bottom}).\frac{1-e^{-(-0.02)y_w}}{1-e^{-(-0.02)H}} + (T_{Top}).\frac{e^{-(-0.02)y_w}-e^{-(-0.02)H}}{1-e^{-(-0.02)H}} \end{aligned} \tag{4.4}$$

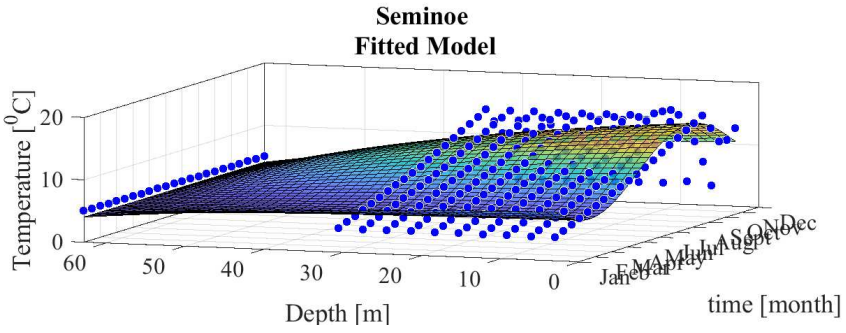

Figure 4.2: Seminoe reservoir temperature

4.1.1.6 Water Elevation

As discussed previously, the water elevation does not maintain the similar values for a particular day within several years. Yet as shown in figure 4.3 here the mean value of the whole available data of about 63$[m]$ and a variation of 2.2$[m]$ is considered for the water level elevation variation.

$$T(t, y_w, H)_{Reservoir} = 63 + 2.2sin(0.0172t + 220/63) \tag{4.5}$$

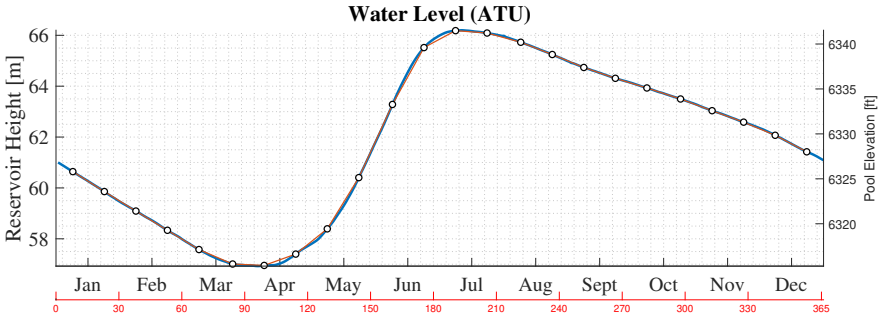

Figure 4.3: Pool Elevations

4.1.2 AAR Analysis

4.1.2.1 Concrete and AAR Properties

The concrete, and (initial, as some values will be determined later from the parameter identification process, Chapter 7) AAR properties used for the AAR analysis are summarized in tables 4.3 and 4.4. It should be noted that the module of elasticity is considered variable through the height of the dam considering lower values at the top portion of the dam. Since the AAR model automatically accounts for the reduction of the concrete elastic modulus and tensile strength as expansion occurs, the initial values for the elastic modulus was considered according to the reported values at 1980 which is the starting year of the AAR analysis and based on the later test results no more than 20% reduction is assumed for that. As for the concrete tensile strength, based on the available core test results in 2009 and 2013, the initial value in 1980 is considered to be equal to 1.5 MPa with a reduction factor of 0.33.

Also, the rock properties are briefly tabulated in 4.5.

4.1.2.2 Joint Properties

The Properties of the modeled contraction and peripheral joints used in the finite element analysis is shown in table 4.6. It should be noted that the concrete rock joint specified in this table only refers to the dam-abutment interface and a full concrete-rock bound is considered below the dam.

Table 4.3: Concrete Material Properties

Concrete					
No.	**Description**	**Symbol**	**Unit (SI)**	**Mean**	
1	Thickness	t	m	1	
2	Mass density	ρ	Gg/m^3	0.00225	
3	Thermal expansion coefficient	α	$1/°C$	9.90E-06	
4	Poisson's ratio	ν		0.2	
No.	**Description**	**Symbol**	**Unit (SI)**	**Mean elevation(m)**	**Mean**
5	Modulus of elasticity	E1	Mpa	1929.5	16217.3
		E2	Mpa	1,912.6	24,515.3
		E3	Mpa	1,897.4	30,083.2
		E4	Mpa	1,882.2	30,083.2
		E5	Mpa	1,870.7	30,083.2

4.2 Analysis Procedures

4.2.1 Procedure for Thermal Analysis

Since AAR is a temperature dependent reaction, a thermal analysis is a prerequisite for conducting an AAR analysis. The detailed procedure for the input data preparation required for thermal analysis is summarized in the flowchart of figure 4.4.

As described in this figure, the first step is on the mesh preparation, as well as extraction and classification of elements to which the thermal loads are being applied. In other words, one needs to determine the nodes and elements at the upstream and downstream sides at which the water and air temperature will be applied; in addition the nodes at which the adiabatic boundary conditions are defined has to be separately specified.

The second step for performing a thermal transient analysis is to gather the data corresponding to the thermal loads:

- Air Temperature: The recordings of air temperature at the location of the dam can help to have a good estimate of the temporal variation of the air temperature for the considered analysis time step.
- Solar radiation: The temperature increase due to the effect of solar radiation has to be determined based on the location of the dam and the orientation and inclination of different parts of the dam with respect to the sun. This temperature increase will be added to the air temperature.
- Water temperature: In the absence of sufficient recordings of water temperatures through the whole depth of the reservoir, one can utilize the empirical relations available in the literature to estimate the reservoir temperature.
- Water elevation

Furthermore, the concrete material properties needs to be determined along with air and water film coefficients. Finally, having all the above mentioned information in hand, the thermal loads can be applied to the finite element model, and a thermal transient analysis can be performed.

Table 4.4: Initial AAR Properties

Initial AAR Properties (Concrete)				
No.	**Description**	**Symbol**	**Unit (SI)**	**Mean**
1	material group ID	MatID #		1
	Expansion characteristics			
	1 ATU			
2	Maximum volumetric strain at temperature T0test	ε^{∞}		5.50E-01
3	Characteristic time at temperature $\theta_0^{test} = 273 + T_0^{test}$	τ_c	ATU	20,026.00
4	Latency time at temperature $\theta_0^{test} = 273 + T_0^{test}$	τ_l	ATU	271.20
	Thermodynamic properties			
5	Activation energy associated with τ_c	U_c	$\circ K$	5,400
6	Activation energy associated with τ_l	U_l	$\circ K$	9,400
12	Reference temperature (oC) of tests for τ_l and τ_c	T_0	$\circ C$	18
	Strength			
10	Tensile strength	$f_t^{'}$	MPa	1.5
9	Compressive strength (must be negative)	$f_c^{'}$	MPa	-30.0
	Γ_t			
7	Residual reduction factor for Γ_t	Γ_r		0.1
8	Fraction of ft prior to reduction of AAR expansion due to macro cracking	γ_t		0.5
13	Upper compressive stress beyond which there is no more AAR expansion; must be negative	σ_U	MPa	-10
	Γ_c			
11	Shape parameter (0. for straight line)	β		0.5
	Degradation Body			
14	Reduction fraction for Young's Modulus when AAR reaction ends	β_E		0.8
15	Reduction faction for tensile strength when AAR reaction ends	β_f		0.33

Table 4.5: Rock Material Properties

Rock	Weight Density	0.00247	Gg/m^3
	Elastic Modulus	20,684.3	MPa
	Thermal expansion coefficient	0.00	$1/^{\circ}C$

Table 4.6: Joint Properties

Seminoe				
Joint Properties		**Joint location**		**Units**
		7: Conc-Conc	**8:Conc-Rock**	
Thickness	h	1.00	1.00	m
Mass density	ρ	0.00	0.00	Gg/m3
Coefficient of thermal expansion	α	0.00	0.00	
Static Young's modulus	E_s	3.2610E+01	3.26E+01	MPa
Tangential stiffness	K_{ts}	3.2610E+03	3.26E+03	MPa
Normal stiffness	K_{ns}	3.2610E+03	3.26E+03	MPa
Tensile strength	f_{ts}	1.00	1.00	MPa
Cohesion	C_s	0.74	0.74	MPa
Friction angle	F_{fs}	35.00	35.00	degree
Dilatancy angle	F_{Ds}	10.00	10.00	degree
Fracture energy Mode I	$GIFs$	8.00E-05	8.00E-05	MN/m
Fracture energy Mode II	$GIIFs$	8.00E-04	8.00E-04	MN/m
Relative value of irreversible deformation	γ_s	0.30	0.30	
Maximal displacement for dilatancy	u_{Dmaxs}	0.01	0.01	m
Tensile stress at the break-point	s_{1s}	0.00	0.00	MPa
Crack opening displacement at the break- point	sw_{1s}	0.00	0.00	m
Cohesion at the break-point	c_{1s}	0.00	0.00	MPa
Crack sliding displacement at the break-point	cw_{1s}	0.00	0.00	m

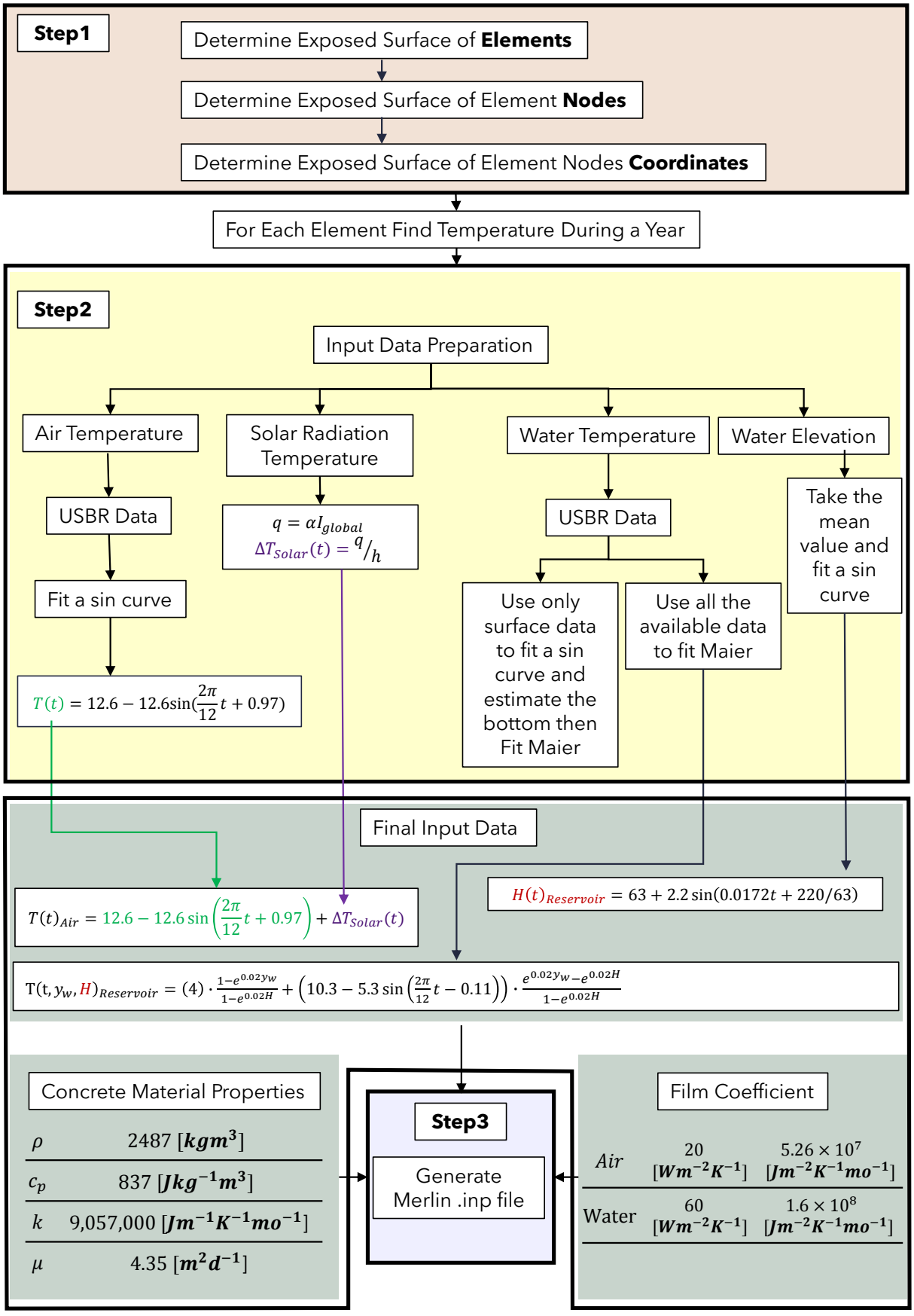

Figure 4.4: Flowchart describing the thermal analysis input data preparation procedure

4.2.2 Procedure for Uncertainty Quantification and Stress Analysis

The AAR analysis requires calibration of the AAR model parameters such that the resulting displacements match the recorded ones. To this purpose, a system identification procedure can be used to determine the parameters associated with the AAR model. When determined, those values will be used as the mean of those random variables for the uncertainty quantification of the stress analysis. As shown in figure 8.10 the procedure of performing the uncertainty quantification(UQ) is consisted of 2 main parts:

- Thermal Analysis
- Stress Analysis

In a uncertainty quantification procedure there are uncertaintites associated with the air and water temperature which in turn translates into the concrete internal temperature. As such, each stress analysis has to be paired with a thermal analysis which determines the concrete internal temperatures.

As seen in the flowchart of figure 8.10 the very first step for every uncertainty quantification is to determine the sources of uncertainty in the analysis and define them as the random variables. Then, the next step would be to determine a distribution which can best describe each random variable as well as the correlations between them. Next is to utilize a sampling technique such as the Latin Hypercube Sampling (LHS) to extract samples from the random variables. Combining these variables, finite element models can be generated and analyzed.

Starting from the thermal analysis, a number of models has to be created and analyzed. As seen in the flowchart, the concrete temperatures obtained from thermal analysis are then gathered and used as the inputs of the AAR analysis in the next stage.

The same sampling procedure as discussed above has to be repeated for the AAR analysis to incorporate the uncertainty associated with the AAR and other concrete properties. Last but not least is to gather and interpret the results from all analyses.

It should be noted that in order to interpret the results, one has to decide about what has to be the outcome of the analysis and what are the useful information which need to be recorded prior to launching the UQ procedure.

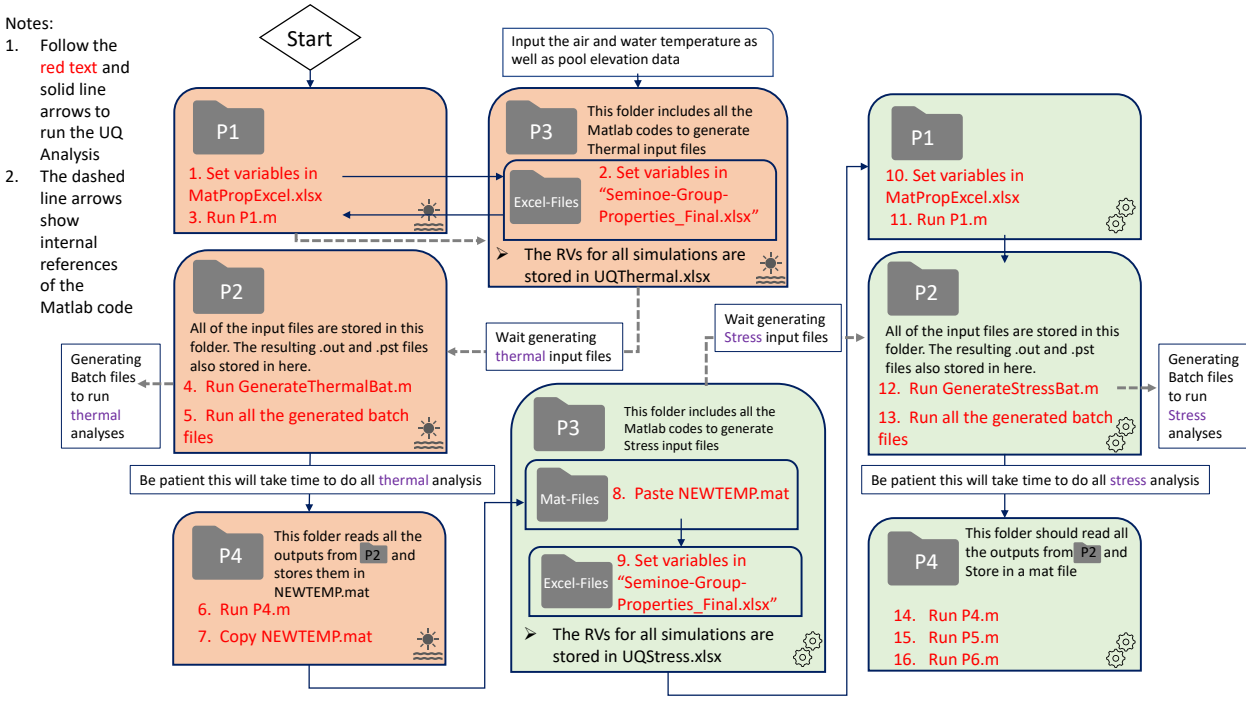

Figure 4.5: Flowchart of UQ Procedure

Chapter 5

Physical Modeling

Abstract

Whereas the preceding chapter has focused on the physical parameters associated with the analysis, this one will address modeling issues.

It will first address the "crafting" of a reasonable and representative finite element mesh obtained from the mathematical model of Seminoe dam using the description given in Appendix A.

It will be followed by the modeling of stage construction and will highlight its importance.

Then, recognizing that the application of the full hydrostatic load in one load increment may cause convergence errors, it will be shown that that adoping three increments will suffice to avoide this error.

Finally, it will be shown that computational time can be substantially cut if a reduced (yet accurate) foundation model is adopted.

5.1 Finite Element Mesh

The geometry model of Seminoe dam is prepared based on maps provided by USBR. The geometry model includes the joints (not used in thermal analysis), and multiple regions (blocks) which facilitate implementation of variable temperature. Table A.1 shows the Seminoe dam dimensions and elevations which are going to be used in the future analysis.

The geometry of the Seminoe as well as its orientation with respect to the north direction can be obtained from Fig. 5.1.For the purpose of the mathematical modeling of seminoe, the geometry of different parts are plotted precisely as shown in Fig. 5.2 and the model is generated through a matlab code which is illustrated as Fig. 5.3.

From Fig. 5.1, geometry of the mesh was first "dissected" to determine coordinates of key points, Fig. 5.4.

For the purpose of the mathematical modeling of Seminoe, the geometry of different parts are plotted precisely as shown in Fig. 5.2 and the model is generated through a matlab code which is illustrated as Fig.

A Matlab® model is then built as shown in Fig. 5.5.

The Matlab® model enabled us to define a "boundary file" of the mesh, which in turn was processed by T3D **rypl** to generate meshes.

Three meshes were generated:

Thermal: where no joints were inserted between the monoliths or under the concrete dams.

Full: mesh with joints inserted between all the monoliths, and another set "wrapped around" the dam to model the concrete rock-interface. The foundation was extended below the dam. To adequately simulate stage construction and various distribution of AAR expansion, the dam body was subdivided into 39 groups, Fig. 5.6.

Reduced: Identical to the previous one, however rock was modeled by a single layer of elements to reduce computational time while maintaining fidelity.

It should be noted that the lift joints were not modeled as (**Dolen99**) reported very good bonds in the 1998 investigation.

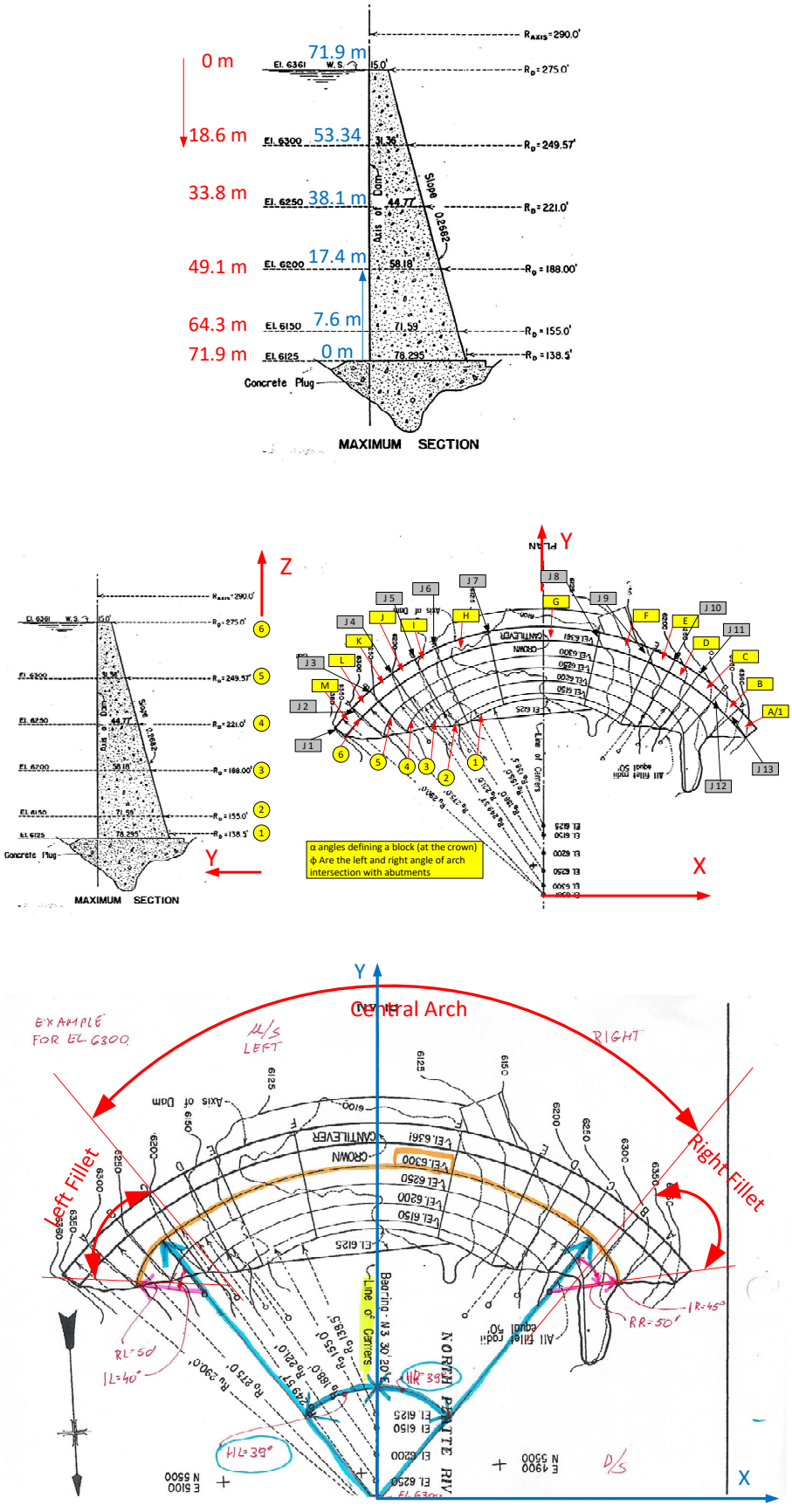

Figure 5.1: Geometry of Seminoe Dam

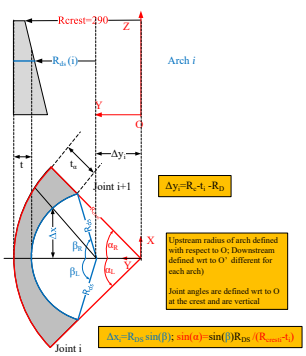

(a) Intrados and Extrados Radii

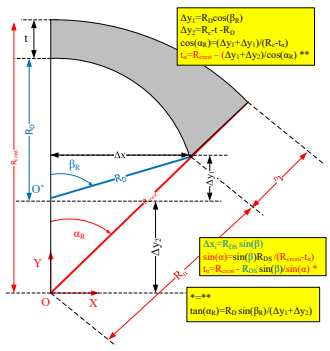

(b) Right fillet

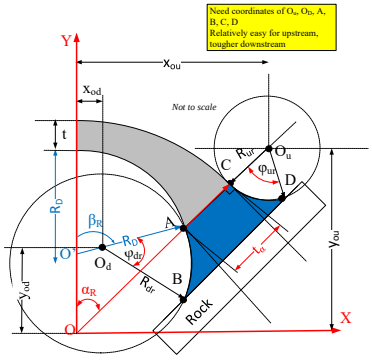

(c) Left and right fillet downstream

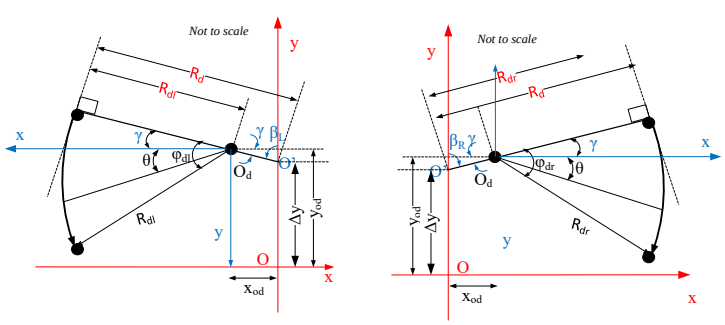

(d) Right fillet upstream

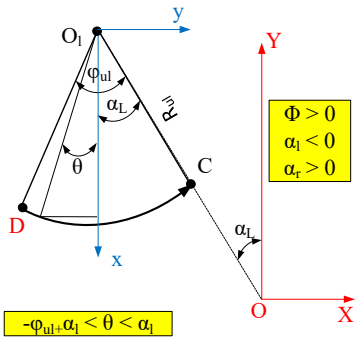

(e) Final model

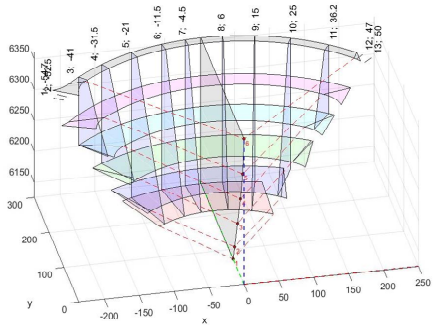

Figure 5.2: Mathematical Modeling of Seminoe Dam

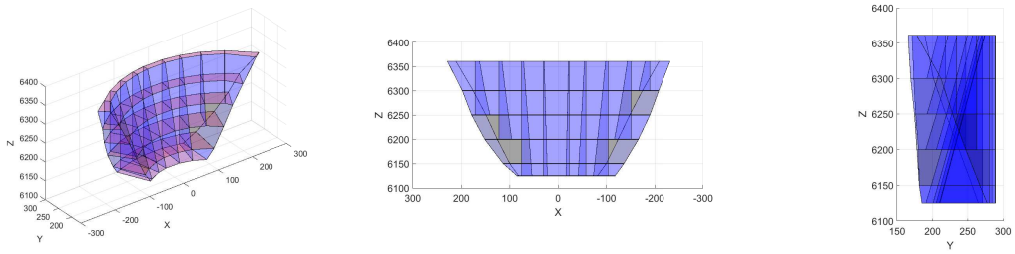

(a) 3D model (b) X-Z view (c) Y-Z view

Figure 5.3: Completed Matlab model

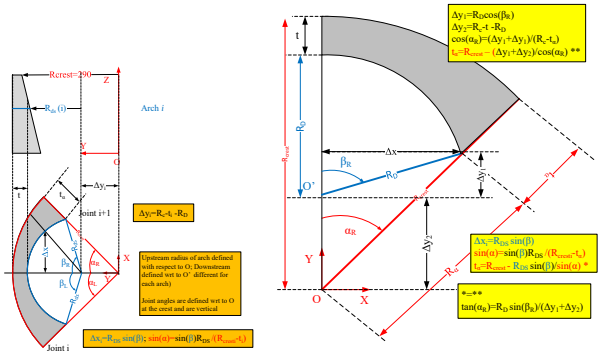

(a) Intrados and Extrados Radii

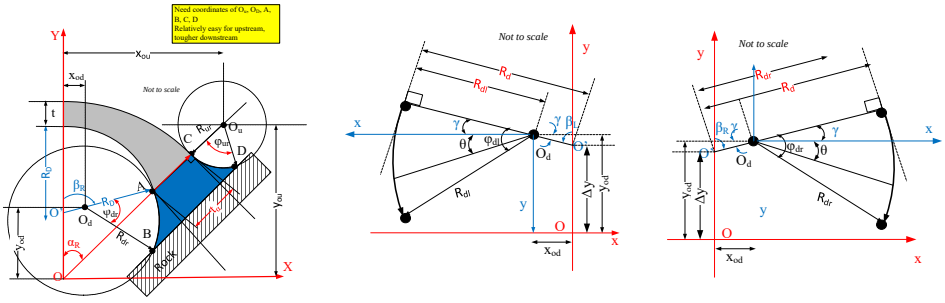

(b) Right fillet (c) Left and right fillet downstream

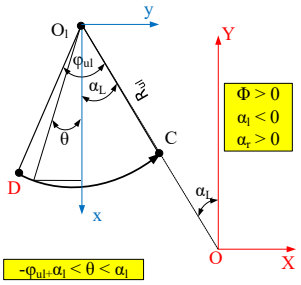

(d) Right fillet upstream

Figure 5.4: Coordinates of controlling points in the mesh

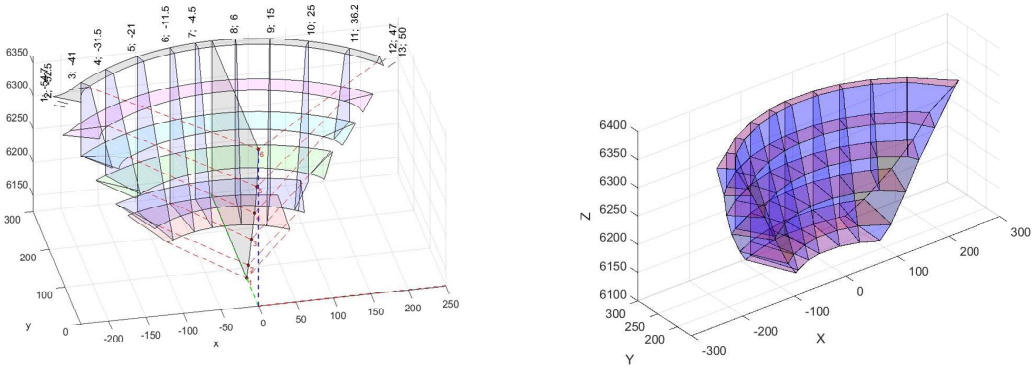

(a) Final model (b) 3D model

Figure 5.5: Mathematical Modeling of Seminoe Dam

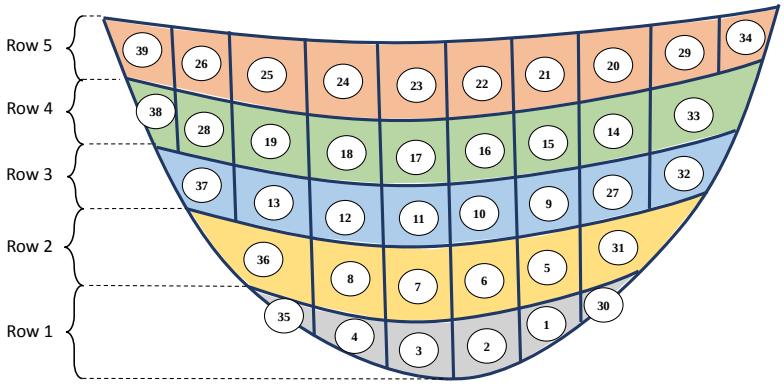

Figure 5.6: Staged construction modeling plan Seminoe upstream

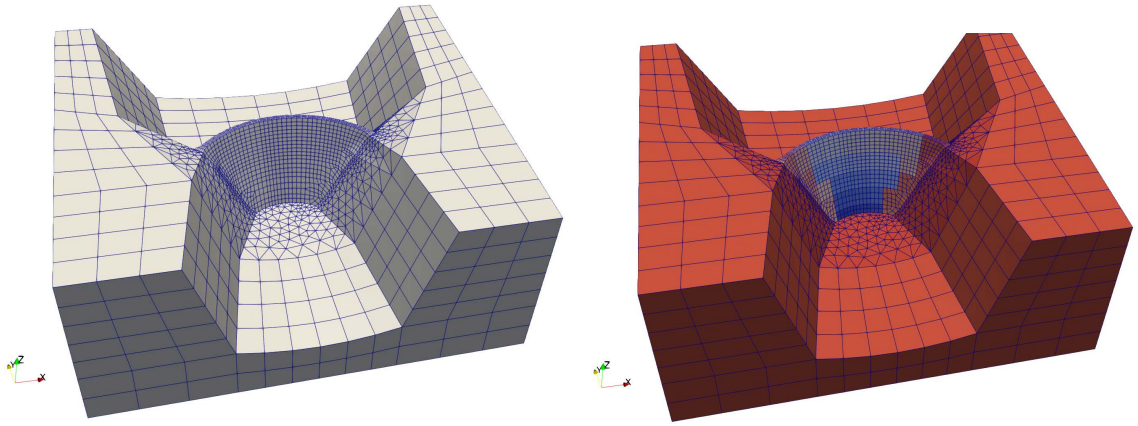

(a) Full mesh

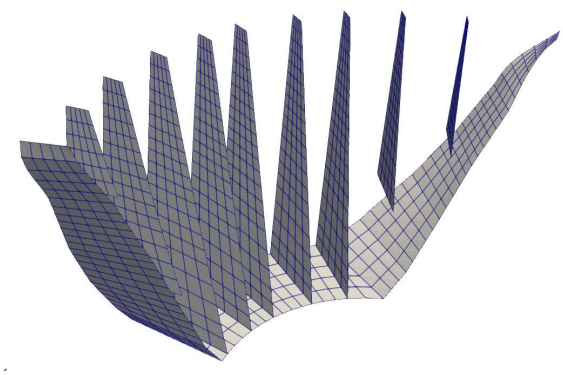

(b) Joints in stress analysis meshes

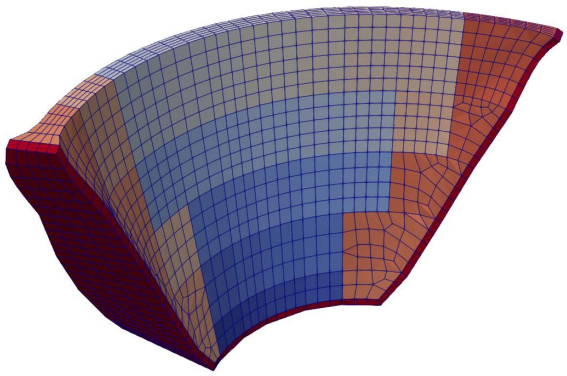

(c) Material groups

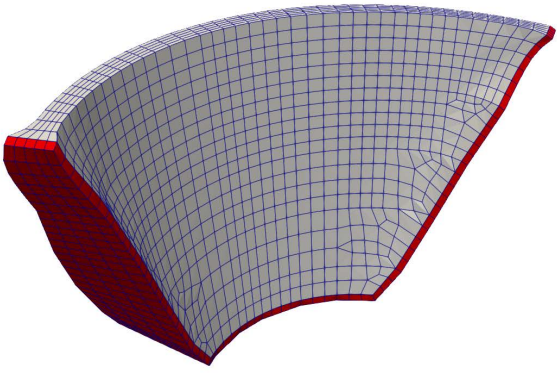

(d) Reduced foundation; Foundation shown in red

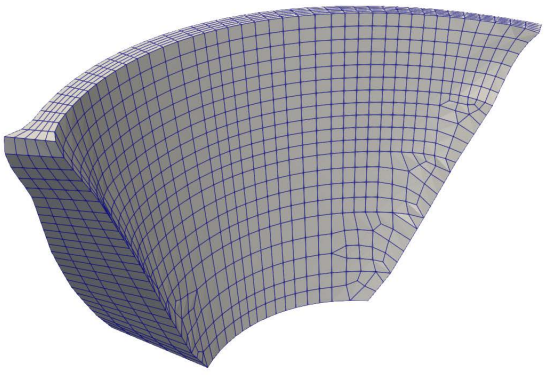

(e) Thermal analysis

Figure 5.7: Finite element mesh

5.2 Stage Construction

In the stress analysis of an arch dam, it is important to properly simulate the self weight of the structure and the resulting stresses during the construction. In most cases the construction stages is simulated through activating the elements in a sequential manner such that it can represent the construction procedure and capture the induced appropriate stresses by the self-weight of the structure. As a matter of fact, the sequence of activating elements depends on the real construction procedure and therefore it might consist of several stages. It has been widely accepted that applying the self weight of an arch dam with the assumption of being a single monolith results in inaccurately estimating the stresses in the structure. As presented in **malm2017proceedingsempty citation** the self weight of the structure is applied sequentially as a part of the static and seismic analysis of an arch dam. This procedure was followed in other studies as well, such as **hariri2013seismicempty citation** and **alembagheri2019studyempty citation**.

5.2.1 Proposed methodology

Ideally, a computer program should be able to handle so-called "ghost elements" that can be activated or deactivated to model staged construction or excavation respectively.

When this is not possible in a finite element code, one which allws modification of the elastic properties within a load increment (as is the case with Merlin), then an alternative approach is possible.

With reference to Fig. 5.8 A necessary condition is for the used finite element code be capable of modifying material properties (specific weight in particular) within a load increment. This feature may not be present in some programs. the approach is as follows:

1. Break the dam in groups (n=5 in the Fig.)
2. Apply gravity load only to the first layer
3. Tag the next group to have its properties altered (this is necessary in Merlin, but not necessarily in other codes)
4. Apply gravity to that layer
5. Repeat the process for all layers
6. Set the displacements to zero

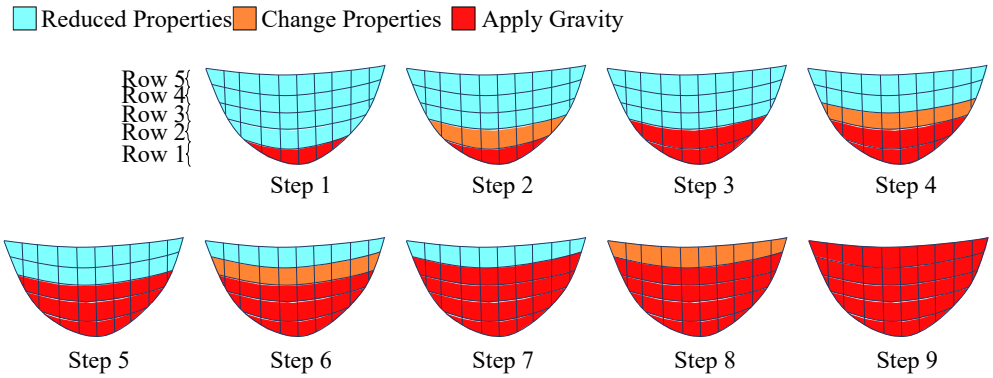

Figure 5.8: Modeling of stage construction

5.2.2 Verification Study

In order to investigate the effect of modeling staged construction in Seminoe dam, the finite element model is analyzed assuming 2 different cases. In the first case, the body force is applied directly to the whole structure at once and in the second attempt the body force is applied gradually through 5 stages to the whole dam body; as shown in Fig. 5.6 each construction stages are differentiated through various colors. In other words, it is assumed that the dam was constructed such that at first the blocks at the first level in gray are built, then the second level was put on top of that and so on. Therefore, we have activated the body forces assuming this sequence in our finite element analysis to account for the effect of the staged construction. The results of the 2 above mentioned cases are shown and compared in Fig.s 5.11 through 5.10 for upstream, downstream and a vertical cut at the middle of the dam. It is shown in Fig. 5.9 that in stage one only a portion of the bottom of the dam is experiencing stresses due to the body force which is shown in light red color. In the second stage the light red color climbs up and the stress at the bottom of the dam increases accordingly. As seen this trend continues until the 5th stage in which again the stress distribution is an indicative of the gradual application of the body force to the body of the dam.

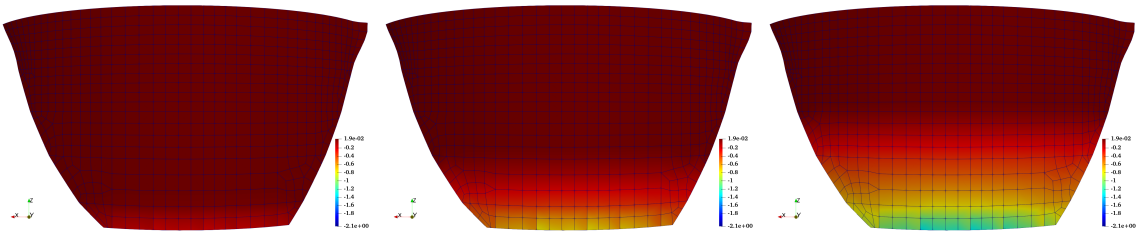

(a) σ_{zz}, Stage 1 (b) σ_{zz}, Stage 2 (c) σ_{zz}, Stage 3

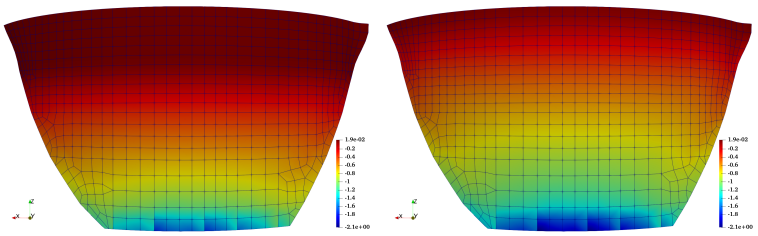

(d) σ_{zz}, Stage 4 (e) σ_{zz}, Stage 5

Figure 5.9: Effect of modeling staged construction Seminoe Upstream; different stages

5.2.3 Verification

In order to better compare the results of staged construction a segment of the dam is isolated, as shown in Fig. 5.15, and the vertical stresses integrated at 0, 25, 50 and 75% of the height and the resultant force is compared with the weight of the concrete "column" above the section using the simple formula:

$$W = \rho g V \tag{5.1}$$

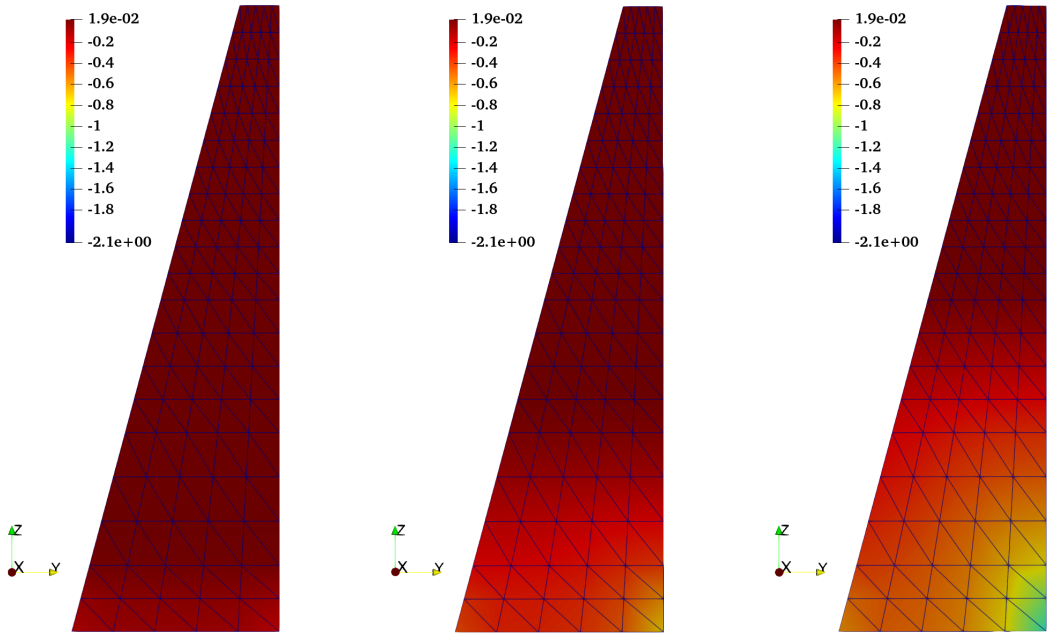

(a) σ_{zz}, Stage 1 (b) σ_{zz}, Stage 2 (c) σ_{zz}, Stage 3

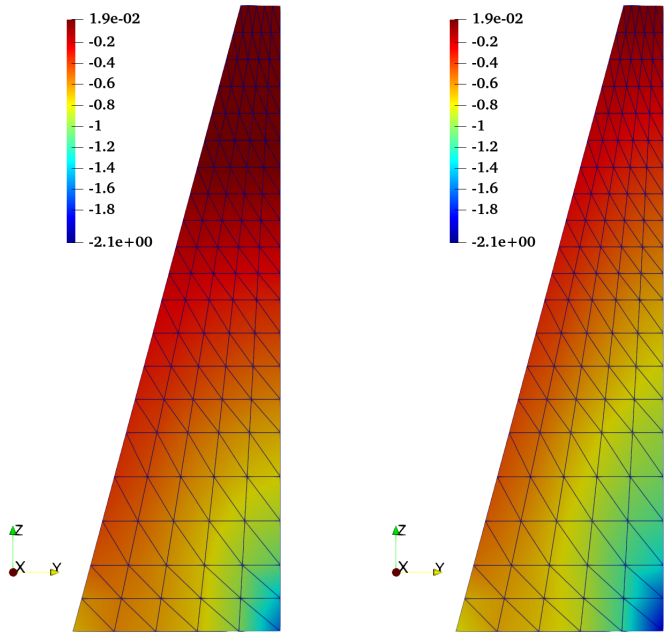

(d) σ_{zz}, Stage 4 (e) σ_{zz}, Stage 5

Figure 5.10: Effect of modeling staged construction vertical cut from middle of Seminoe; different stages

where W is the total weight (kN), V is the concrete volume (m^3), ρ the mass density of concrete ($2,500Kg/m3$), g the acceleration of gravity ($9.81m/s2$). Then the error is computed using staged construction and without using staged construction. At all four elevations, the error is much smaller using staged construction

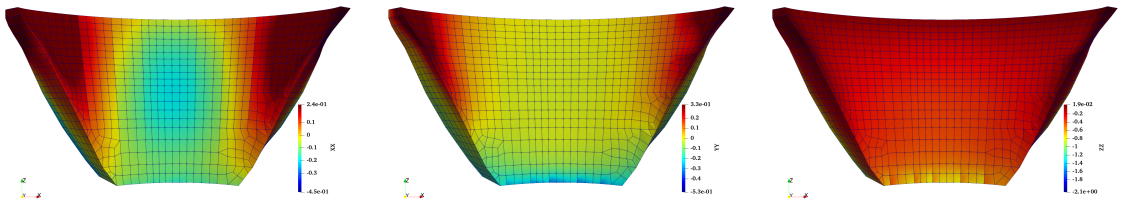

(a) σ_{xx}, without staged construction (b) σ_{yy}, without staged construction (c) σ_{zz}, without staged construction

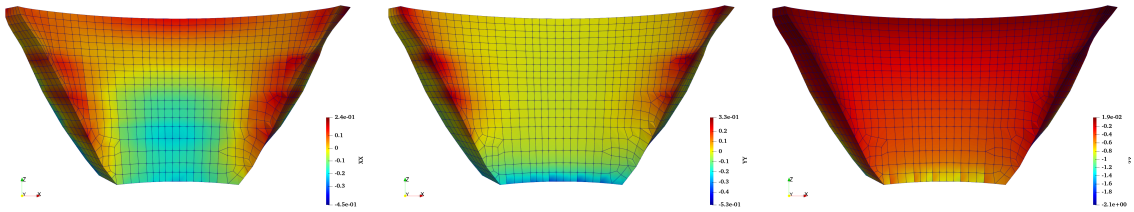

(d) σ_{xx}, staged construction (e) σ_{yy}, staged construction (f) σ_{zz}, staged construction

Figure 5.11: Effect of modeling staged construction Seminoe Downstream

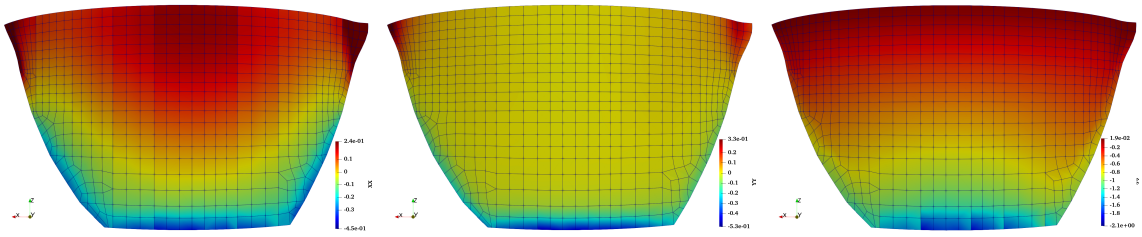

(a) σ_{xx}, without staged construction (b) σ_{yy}, without staged construction (c) σ_{zz}, without staged construction

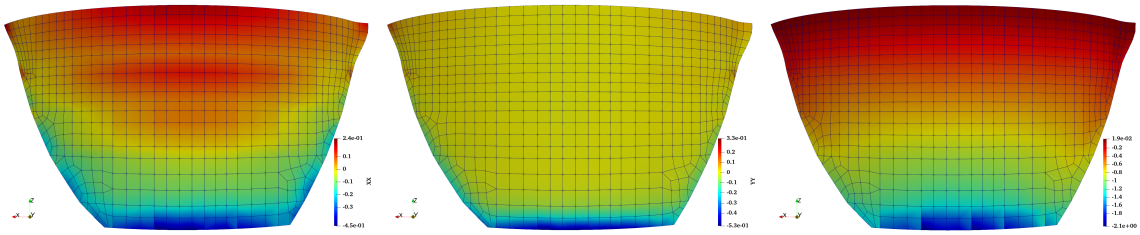

(d) σ_{xx}, staged construction (e) σ_{yy}, staged construction (f) σ_{zz}, staged construction

Figure 5.12: Stress distribution; with vs. without Staged construction

as shown in Fig. 5.16. Interestingly, the error with staged construction (well within 5% at all elevations) increases with height. This may be reflective of local stress redistribution/bridging occurring with height.

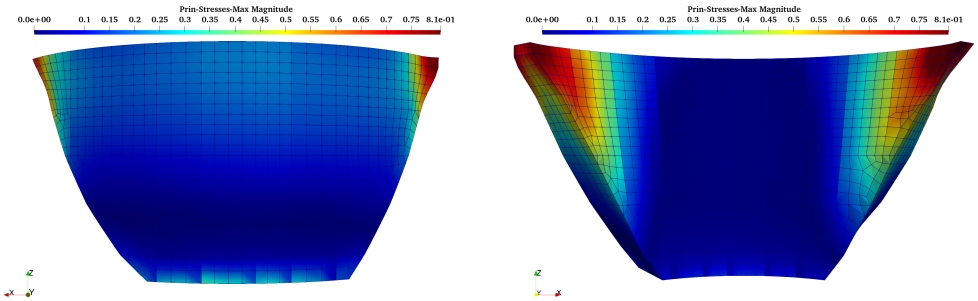

(a) σ_1, without staged construction

(b) σ_1, without staged construction

(c) σ_1, staged construction

(d) σ_1, staged construction

Figure 5.13: Principal Stresses; With vs. without Staged construction

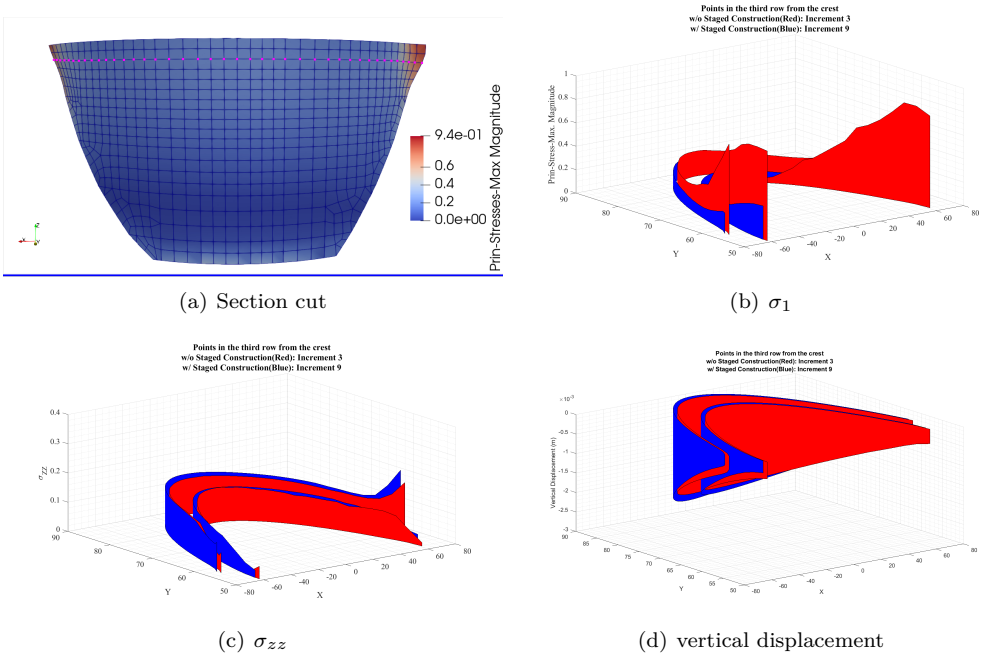

(a) Section cut

(b) σ_1

(c) σ_{zz}

(d) vertical displacement

Figure 5.14: Stresse and displacements near Crest; With vs. without Staged construction

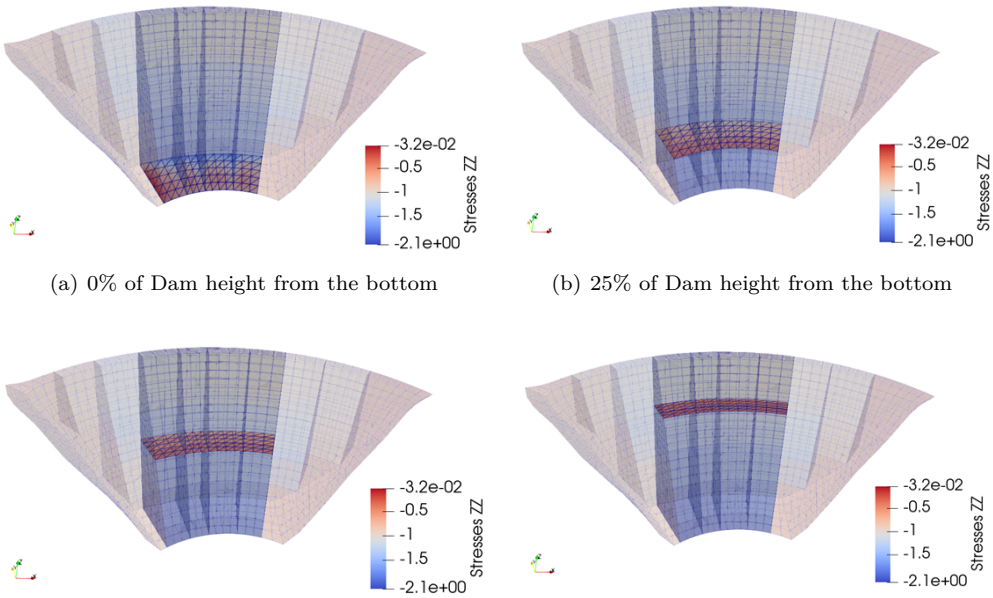

(a) 0% of Dam height from the bottom

(b) 25% of Dam height from the bottom

(c) 50% of Dam height from the bottom

(d) 70% of Dam height from the bottom

Figure 5.15: Four sections considered for stress integration and comparison with the self-weight

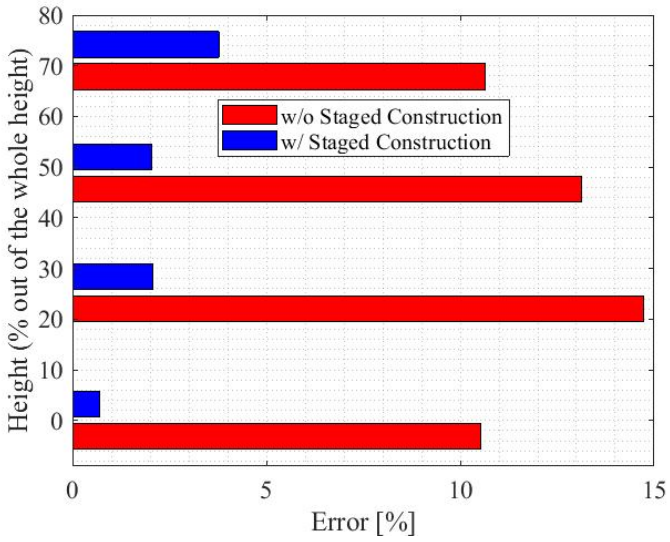

Figure 5.16: Error comparison between the two self-weight analyses

5.3 Hydrostatic Load

The next step to the stress analysis, is to apply the hydrostatic load behind the dam. In order to ensure the convergence rather than applying the total amount of water at once, the loading was started from a very low depth and increased in 3 steps. 5.17 shows the increment steps of hydrostatic load application. It can be seen through the Fig. that the principal stresses are increasing as the reservoir level elevates.

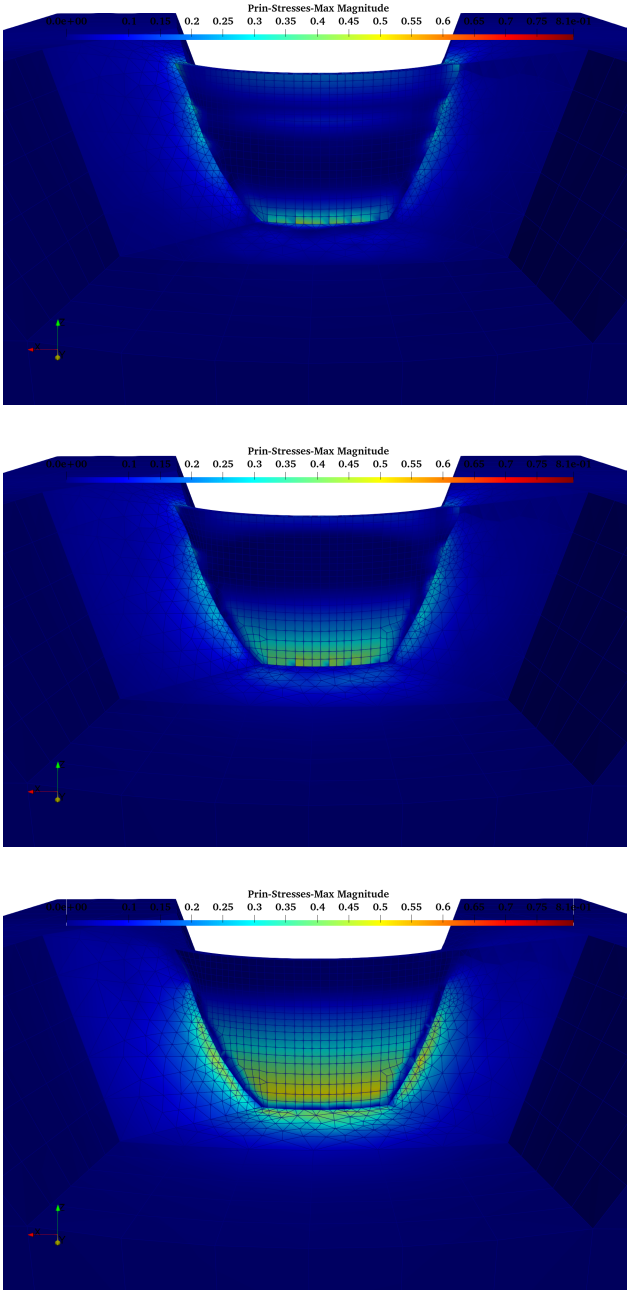

Figure 5.17: Gradual application of hydrostatic load in 3 steps

5.4 Foundation Modeling

The AAR Analysis was conducted based on the calibration of the data on the recorded crest displacements to the AAR model described in chapter 1. The contour plots of the crest displacement in z direction are shown in Fig. 5.18 after 20 and 40 years of AAR analysis.For clarity, we show only the dam without the foundations.The contour plots for the maximum principal stress is also shown in Fig. 5.19 which also features the joint openings and the deformed shape of the dm after 40 years of AAR analysis. Since each analysis

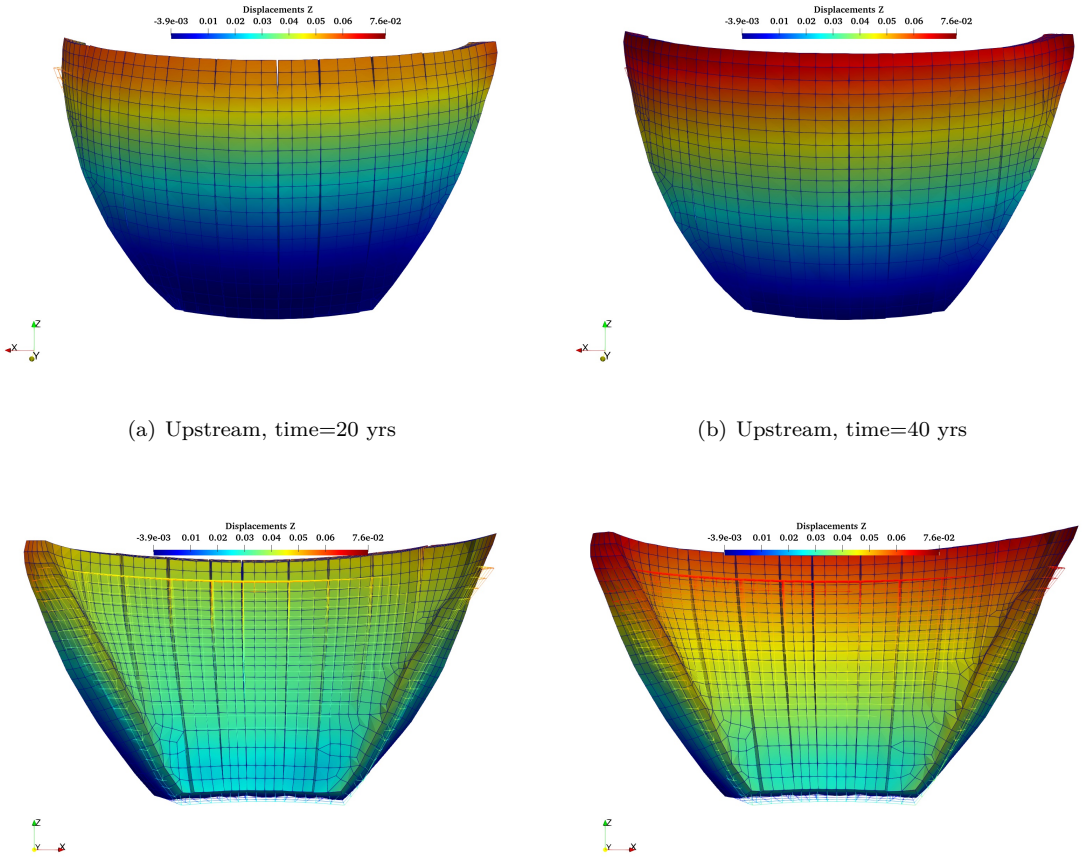

(a) Upstream, time=20 yrs

(b) Upstream, time=40 yrs

(c) Downstream, time=20 yrs

(d) Downstream, time=40 yrs

Figure 5.18: Z direction Displacement contour plots

takes about 7 hours to complete, and both the system identification procedure, and specially the probabilistic analysis will require multiple executions (100), we have modified the mesh by reducing the rock foundation to its simplest form (wrapped around the dam)(Fig. 5.20). Execution time was cut by about one third.

Table 5.1: Add caption

	Number of Nodes	Execution time [hours:mins:seconds]
Full Foundation	12461	7:44:32
Reduced Foundation	8682	01:16.1

To assess the reliability of the new mesh, identical analyses were performed with the mesh with full foundation and the one with reduced, following is a comparison of the results. Fig. 5.22 shows the difference of the displacements from the 2 meshes.

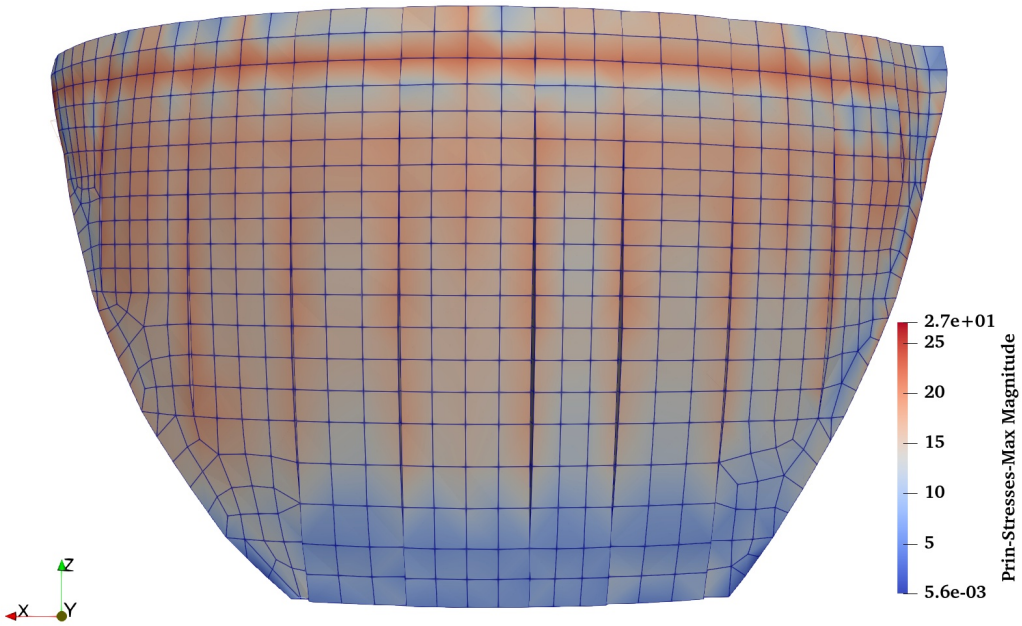

(a) Upstream

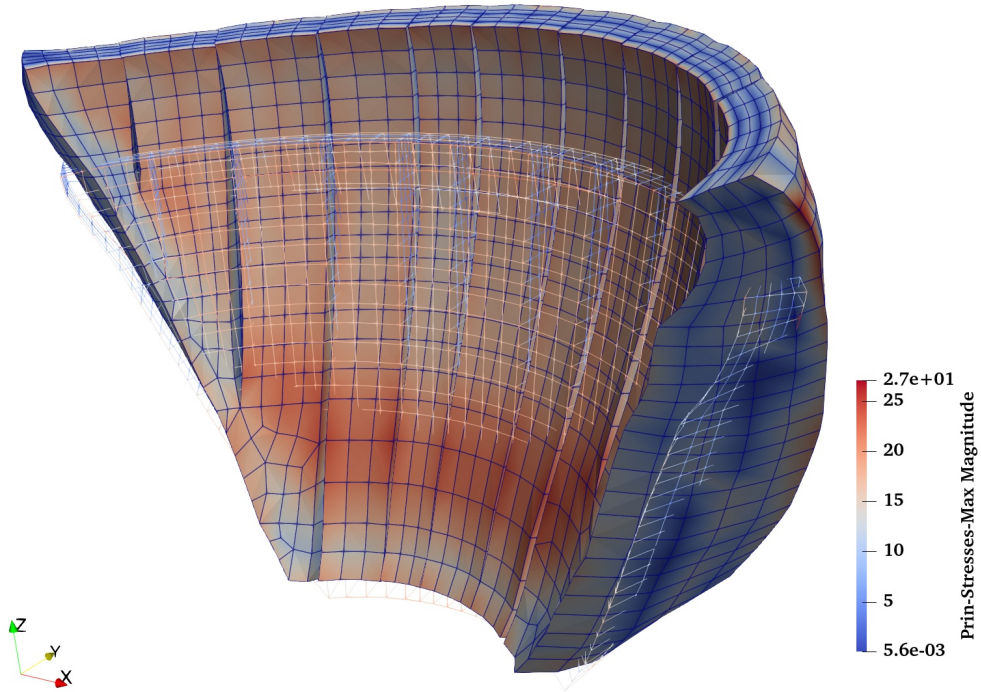

(b) Downstream

Figure 5.19: Maximum principal stresses after 40 years

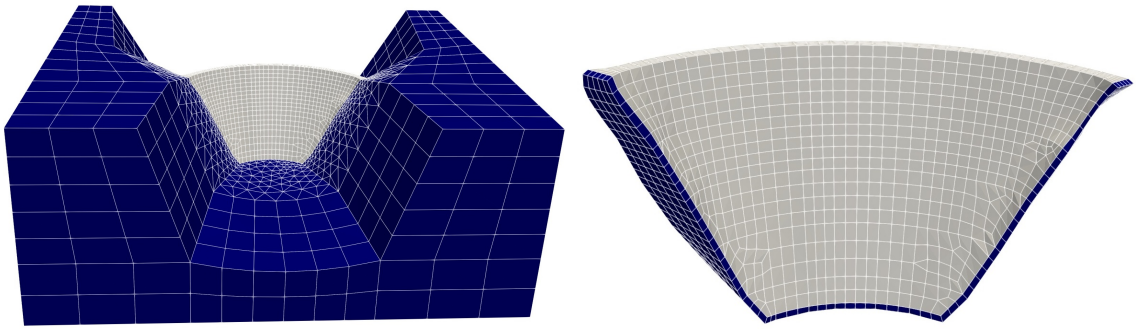

(a) Old Mesh, 12461 nodes (b) New Mesh, 8682 nodes

Figure 5.20: The old versus New mesh where the foundation is shown in blue

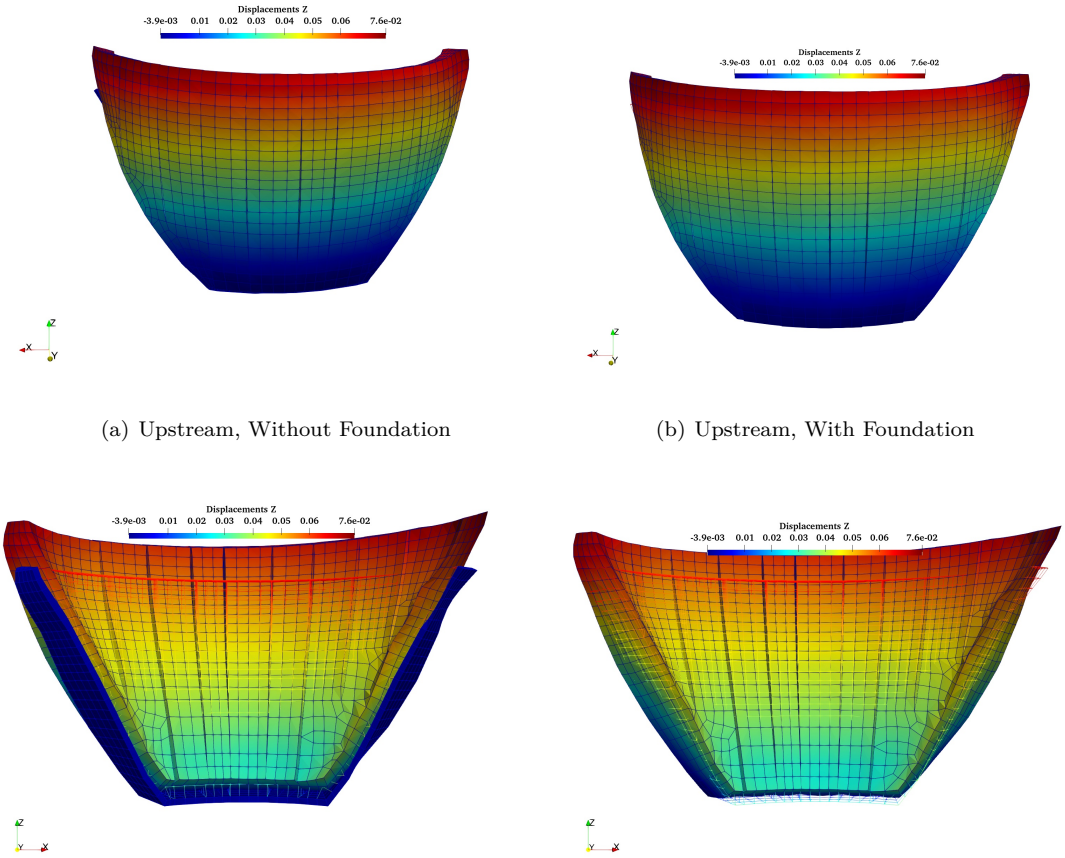

(a) Upstream, Without Foundation (b) Upstream, With Foundation

(c) Downstream, Without Foundation (d) Downstream, With Foundation

Figure 5.21: Z direction Displacement contour plots, comparison of models with full and reduced foundation

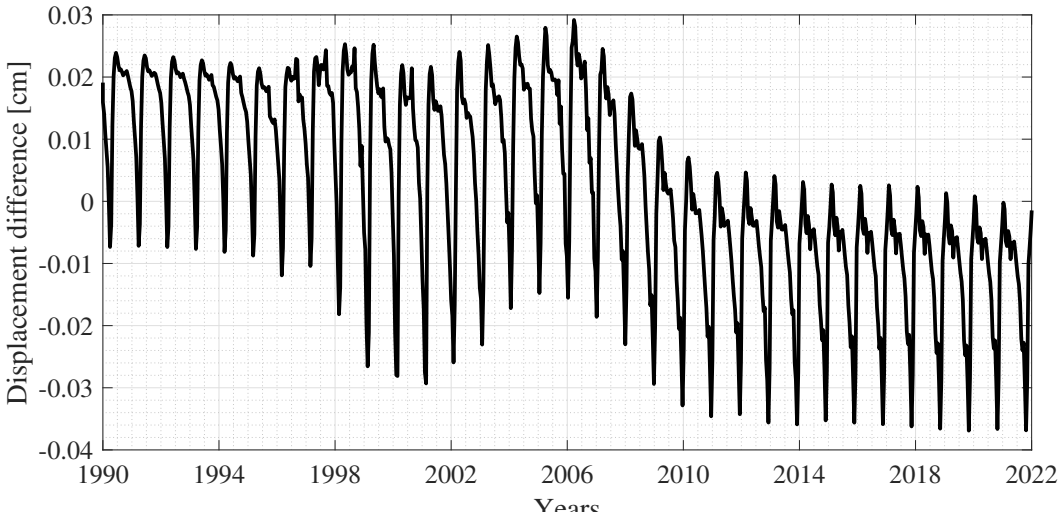

Figure 5.22: Difference of the crest displacement for the 2 meshes with full and reduced foundation

Chapter 6

Deterministic Thermal Analysis

Abstract

This chapter will detail the deterministic thermal analysis. First, results will be compared both with those obtained by Hatch, and the recorded field measurements. Impacts of time steps, solar radiations, and comparison between convection and conduction studies will be reported.

Finally, the spatial and temporal temperature distribution will be shown.

6.1 Analysis Procedure

The input temperature and elevation data have been presented in chapter 4 and will be now used to conduct the thermal analysis assuming the analysis time step equal to 15 days per each increment. Air temperature is applied at the downstream and crest as well as a portion of the upstream face which is exposed to air. Furthermore, the temperature increase due to solar radiation is applied at the upstream and crest elements. The reservoir temperature is applied to the elements beneath the water level taking into account the water level variation in different months.

6.2 Comparison with hatchempty citation

Using film coefficients for air and water the temperatures are applied at the surface elements and the thermal analysis results for 3 nodes inside the concrete are compared with the measurements from DH03-01 instruments recorded at 3 different elevations of 6360 [ft], 6351 [ft] and 6288 [ft]. It should be noted that the nodes were chosen to be closest to the location of DH03-01 instruments The results specially, for the 2 upper nodes, show a good match between the measured and computed temperatures besides showing stability within the first few years which vouches for the accuracy of the analysis (figure 6.1). Also, in this figure the results from **hatch** are presented for each of the measured elevations. Based on the figures, our results show closer match with the measured data.

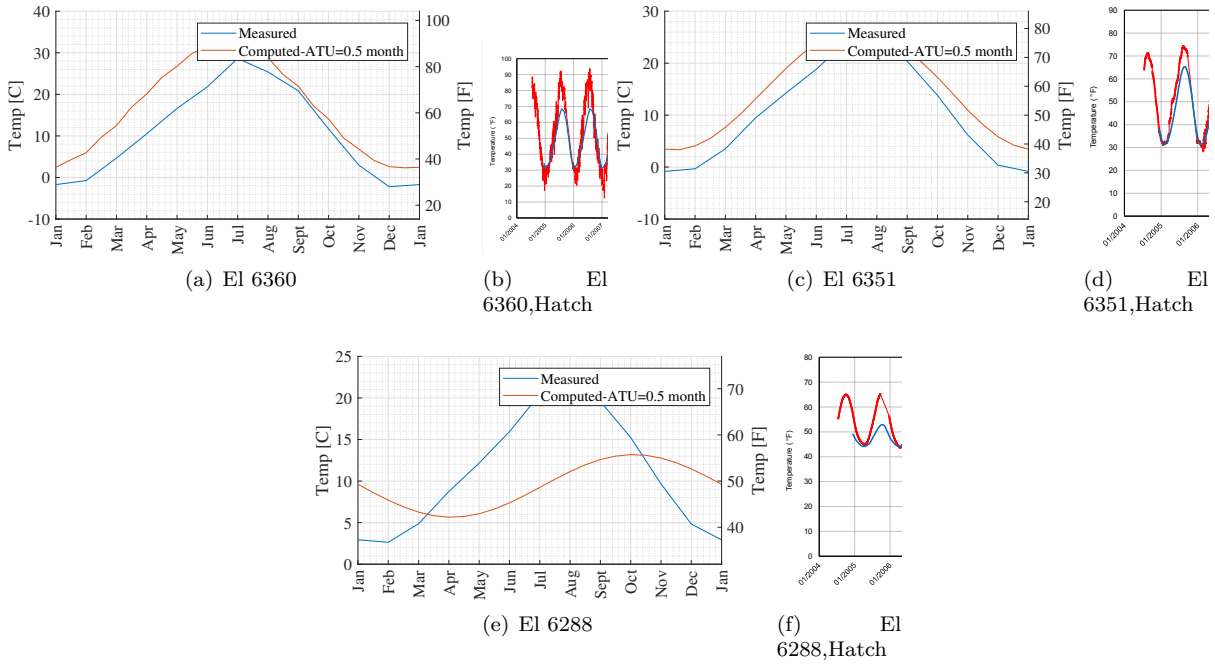

(a) El 6360 (b) El 6360,Hatch (c) El 6351 (d) El 6351,Hatch

(e) El 6288 (f) El 6288,Hatch

Figure 6.1: Comparison of thermal analysis results with measured values

6.3 Impact of Time Step

Figure 6.2 compares the thermal analysis results for 3 different time steps of approximately 7.5 days, 15 days and 30 days. Accordingly, the 15 days time step provides the closest values for temperatures to the measured data. In addition, decreasing time step to half, 7.5 days, does not have significant effect on the results and therefore is not worth adding the computational effort.

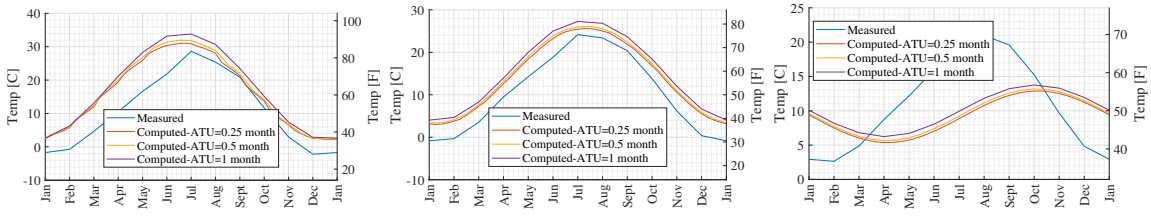

(a) Eleveation 6360 (b) Eleveation 6351 (c) Eleveation 6288

Figure 6.2: Comparison of thermal analysis results with measured values assuming 3 different time steps

6.4 Impact of Solar Radiation

Figure 6.3 is to show the importance of applying temperature difference due to solar radiation. It is shown that the solar radiation results in higher internal temperatures which would affect the further analysis results by increasing the stresses caused by higher temperatures.

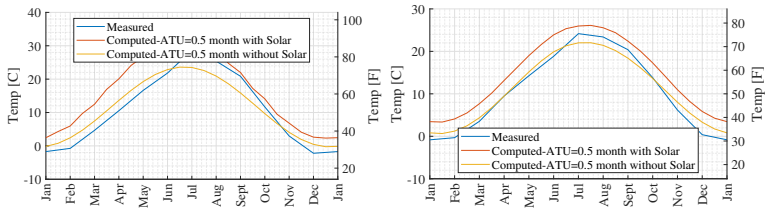

(a) Eleveation 6360 (b) Eleveation 6351

Figure 6.3: Comparison of thermal analysis results with measured values with and without solar radiation

6.5 Comparison of Convection and Conduction

The results presented so far, were obtained through modeling of convection. In other words the heat transfer was assumed to take place through the movement of the surrounding liquid. However, for the sake of comparison the thermal analysis is repeated for conduction in which the heat transfer occurs through direct contact . Figure 6.4 illustrates the difference of the above mentioned cases . As expected, the heat transfer through conduction results in higher internal temperatures compared to convection which gives closer results to the real measured data.

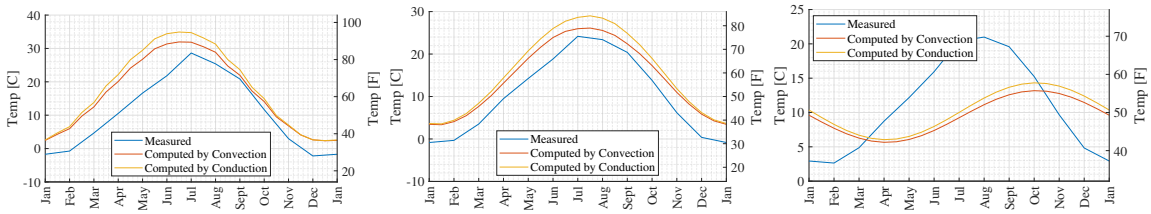

(a) Eleveation 6360 (b) Eleveation 6351 (c) Eleveation 6288

Figure 6.4: Comparison of thermal analysis results with measured values assuming high values for film coefficients

6.6 Internal Temperatures

The concrete internal temperatures obtained from thermal analysis are shown at 3 different cuts throughout the dam. First a cantilever cut through the height of the dam located at the middle of the arch dam (figure 6.5). Second, a horizontal section showing a complete arch of the dam cut from below the water level (Elevation 6243 [ft]) figure 6.6. Third, is the same as second cut except that the section is at an elevation above the water level (Elevation 6348 [ft]) in order to show the temperatures for the portion of the dam which is exposed to the air 6.7. Furthermore, the upstream face of the dam is shown in figure 6.8 in which the water level can be distinguished through the sudden temperature change observed at the top of the dam which is due to the exposure of the area to the solar radiation as well as air temperature. Finally figure 6.9 shows the temperature contour plots throughout one year at the downstream face. From the figures above it is observed that starting January the concrete internal temperature starts gradually decreasing until may, then with the rise of temperature in May through September the concrete internal temperature also increases and the heat propagates to the whole dam structure. The contour plot in november shows that there is just a corner at the bottom of the dam at the upstream side that almost always maintains its low temperature. As

shown, the effect of temperature increase inside the dam starts vanishing as approaching the colder months of the year and the procedure is followed by the first month of the following year. Furthermore, it is shown that the temperatures are highest during June through August. Also, The highest temperatures occur at the crest and on upstream face above the water level. These observations can be verified with the other cuts in the following figures. Due to the fact that figure 6.6 is a section from mid height of the dam. The upstream side is showing the water temperature which is lower than the air temperature observed at the downstream side. Similar to the observations from previous figures, these figures also show the temperature increase starts in May and continues through September and subsequently starts disappearing in October through December followed by the first 3 months of the next year. In figure 6.7, similar to 6.6, the section is horizontal but at a high elevation close to the crest. This figure is provided to show the internal temperatures above the water level. This figure also supports our previous observations throught out the year. Another, key observation drawn from this figure is that the temperature increase is almost uniform throughout the whole arch from East side to the west.

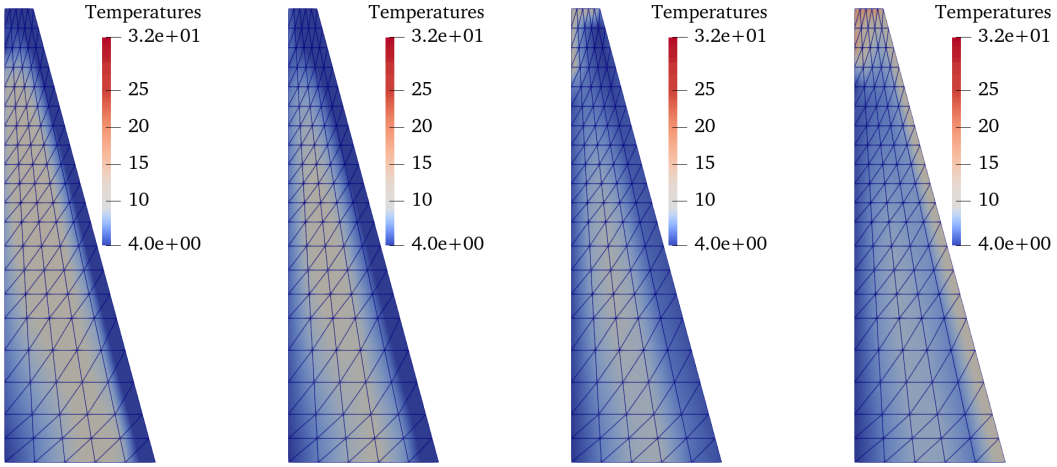

(a) January (b) February (c) March (d) April

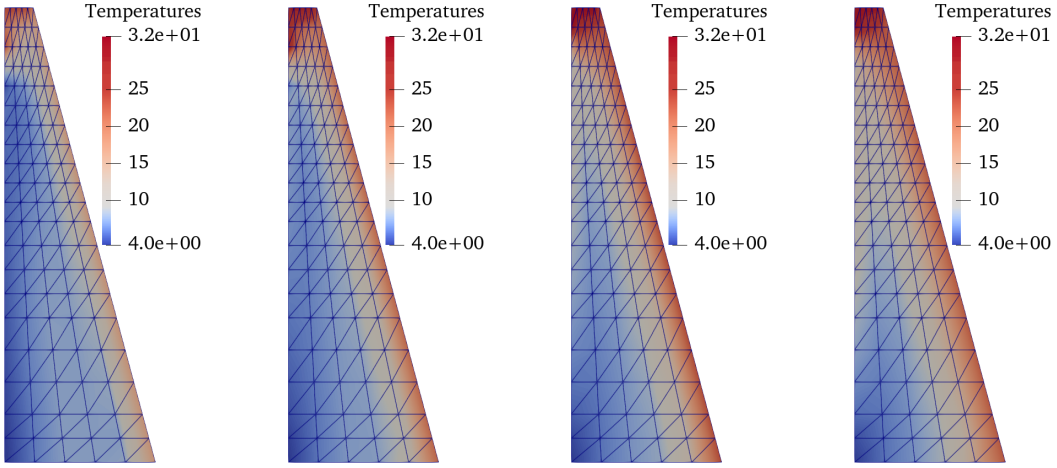

(e) May (f) June (g) July (h) August

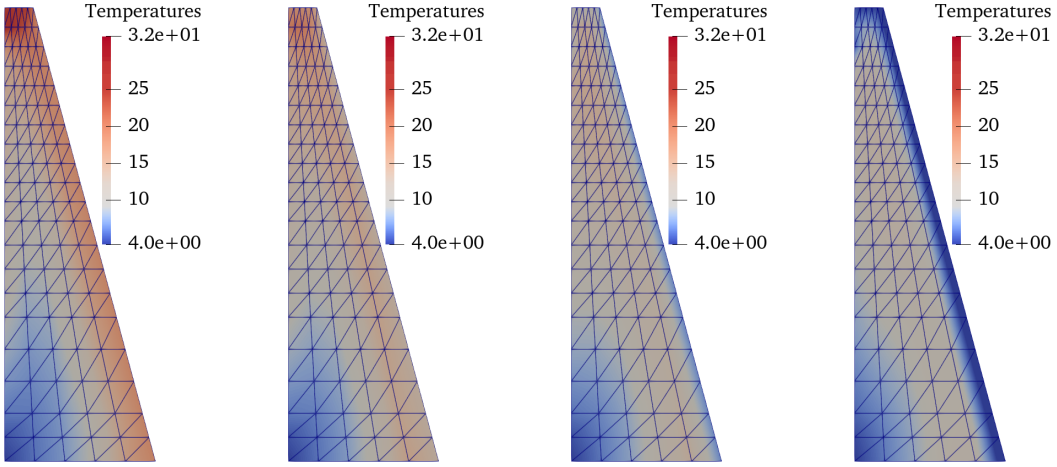

(i) September (j) October (k) November (l) December

Figure 6.5: Temperature contour plots of various months throughout one year at a vertical section cut from the middle of the arch dam

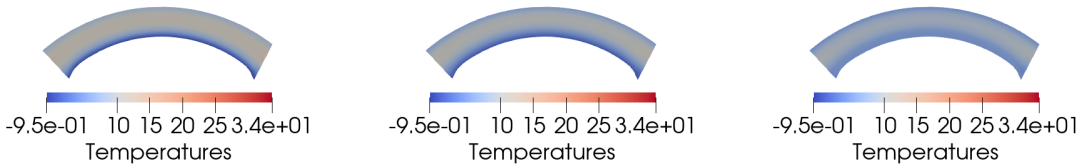

(a) January (b) February (c) March

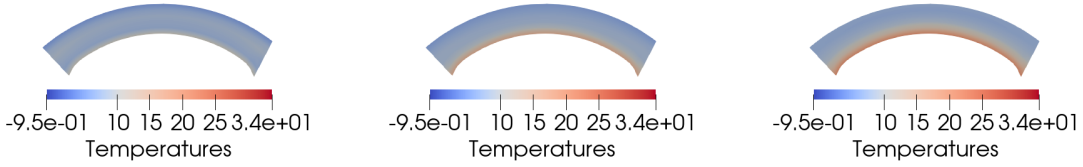

(d) April (e) May (f) June

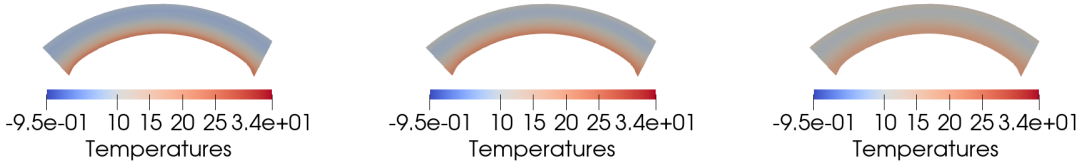

(g) July (h) August (i) September

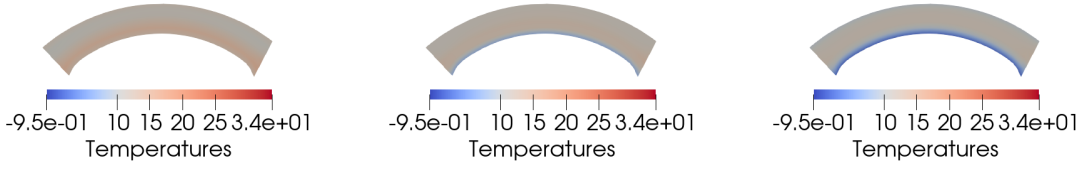

(j) October (k) November (l) December

Figure 6.6: Temperature contour plots of various months throughout one year at a horizontal section cut from below the water level (Elevation 6243 [ft])

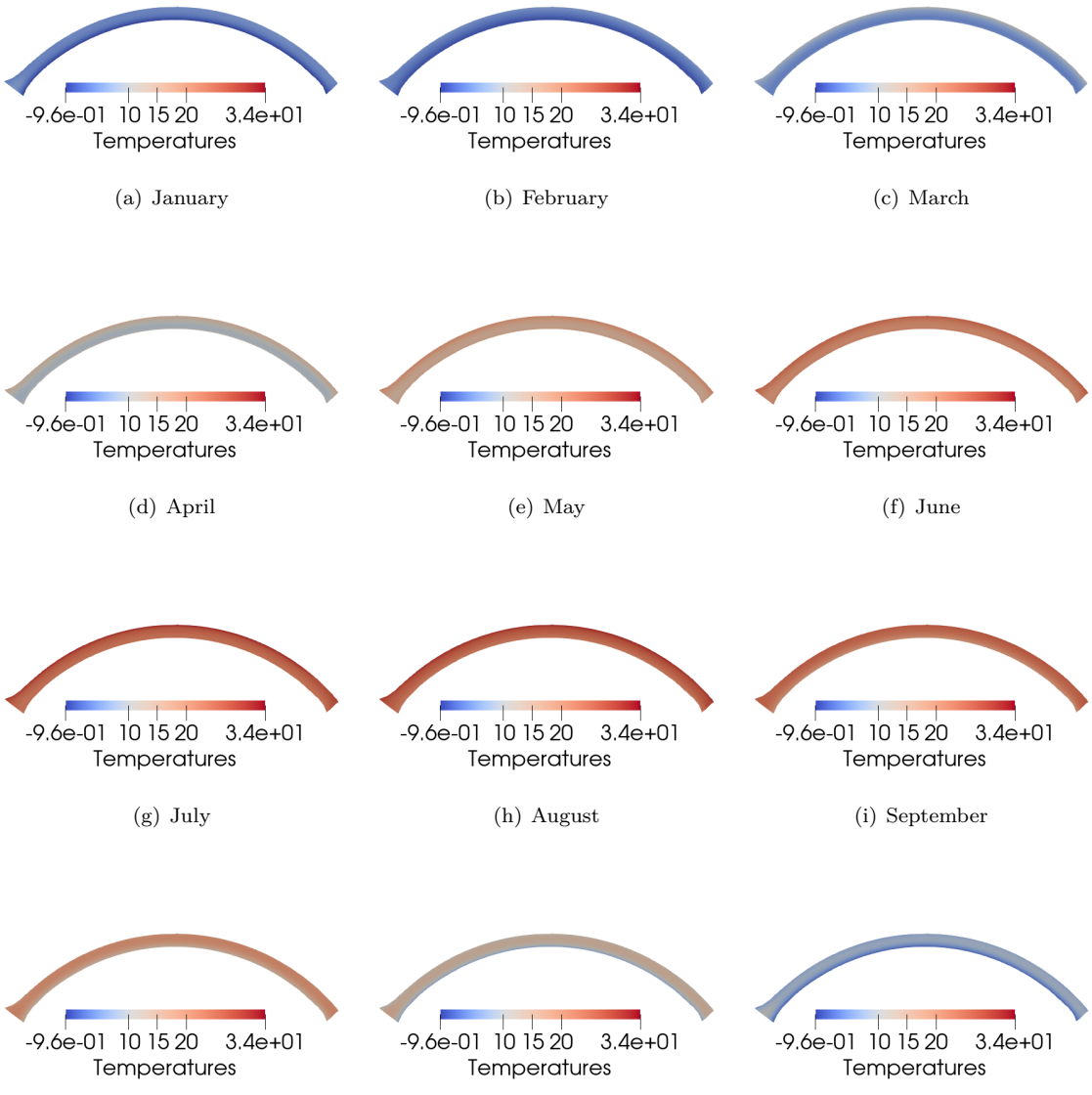

(a) January (b) February (c) March

(d) April (e) May (f) June

(g) July (h) August (i) September

(j) October (k) November (l) December

Figure 6.7: Temperature contour plots of various months throughout one year at a horizontal section cut from above the water level (Elevation 6348 [ft])

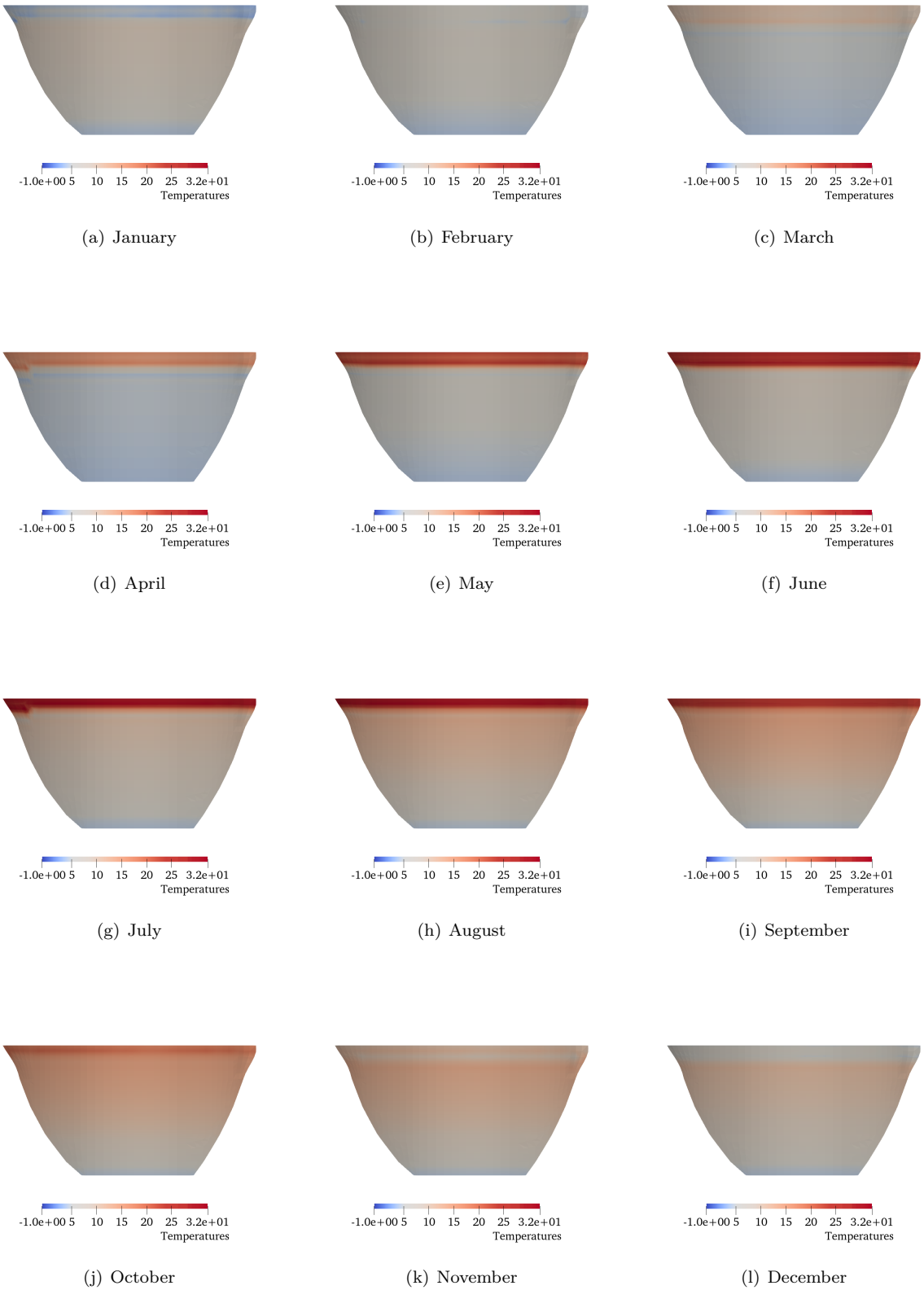

(a) January (b) February (c) March

(d) April (e) May (f) June

(g) July (h) August (i) September

(j) October (k) November (l) December

Figure 6.8: Temperature contour plots of various months throughout one year at the upstream face of Seminoe

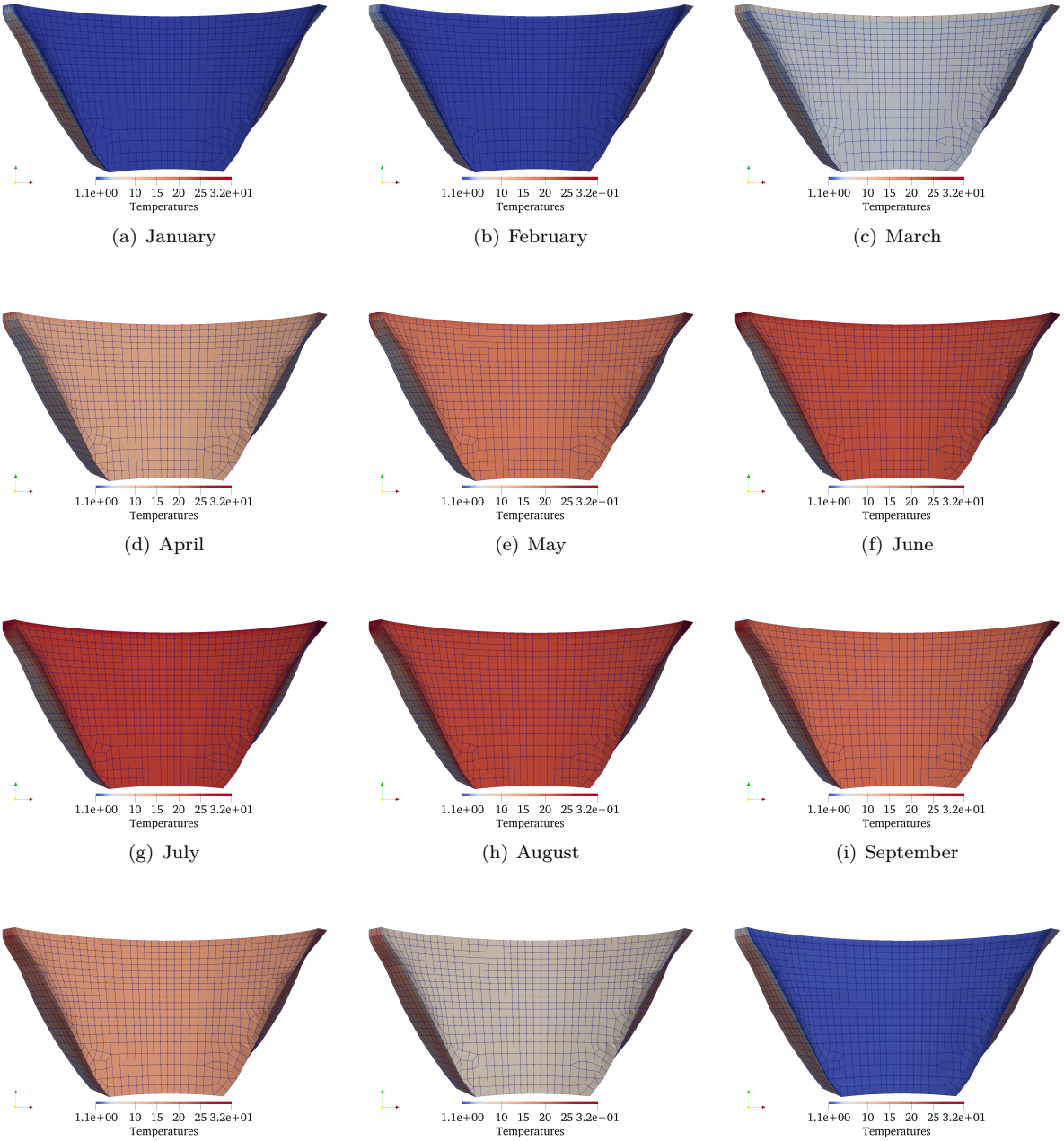

(a) January (b) February (c) March

(d) April (e) May (f) June

(g) July (h) August (i) September

(j) October (k) November (l) December

Figure 6.9: Temperature contour plots of various months throughout one year at the downstream face of Seminoe

Chapter 7

Deterministic Stress Analyses Results

Abstract

In this chapter, the parameter identification procedure is first described and then will be used to identify the equivalent set of AAR parameters (ε^{∞}, τ_L and τ_C) that would yield the "best" numerical (displacement) prediction in comparison to the recorded ones. Note that in this study set, only the nonlinearity of the joint is modeled (so as to maintain reasonable computational time). Subsequently, the same set of parameters will be used for a full nonlinear analysis of the dam (including not only joints, but also concrete).

7.1 Parameter Identification Procedure

A major challenge in the numerical simulation of the temporal concrete expansion (and deterioration) is the ability to use reliable kinetics coefficients, ε^{∞}, τ_l and τ_c introduced in §2.2.2. Whereas those can be obtained through carefully carried laboratory tests (**saouma-tc259**), an alternative approach is through system identification.

Mathematically speaking, the problem can be simply formulated as follows. The field-recorded displacements (e.g. crest displacement on a dam) are denoted by $\mathbf{u}(t)$, the target parameters by $\mathbf{x}$ (in our case $x(1) = \tau_c$, $x(2) = \tau_l$ and $(x(3) = \varepsilon(\infty))$, the finite element "operator" by $f(.)$, and computed results by $\mathbf{u}'(t)$. We thus have:

$$f(\mathbf{x}) = \mathbf{u}'(t) \neq \mathbf{u}(t) \tag{7.1}$$

and are seeking to minimize $(\mathbf{u}(t) - \mathbf{u}'(t))^2$, see Fig. 7.1.

Such an approach has been often used for dam analysis (**ardito2008diagnostic**) (**oliveira2012damage**), and is conceptually similar to system identification in nonlinear dynamic systems (**ghanem1995structural**).

7.2 Parameter Identification for Linear Concrete Model

Prior to undertaking the process of parameter identification, the user should first identify the control parameters, and then identify the field measurements which are to be captured through the parameter identification process.

[h!t]

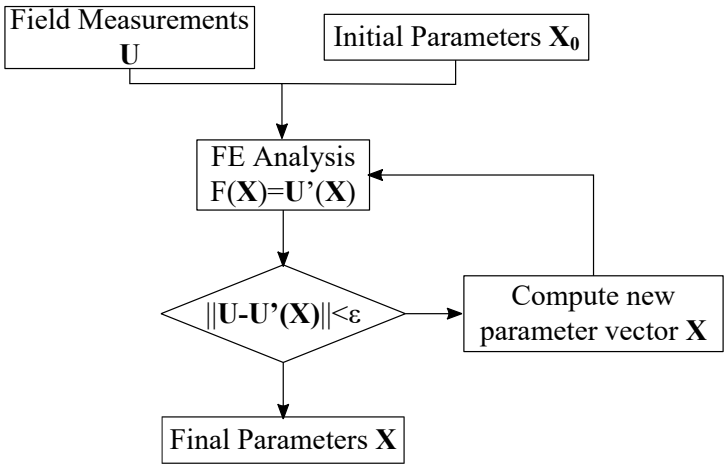

Figure 7.1: Principle of the system identification approach

7.2.1 Control Parameters

Control parameters corresponding to the AAR model of **saouma-aar-1empty citation** must first be defined.

This is done through an excel file, Table 7.1, that includes: lower and upper bound values for each of the active parameters (identified by 1), the initial starting point, and a `typical` value which provides the algorithm with an order of magnitude of the variable.

Table 7.1: Data preparation for parameter identification

			Actual Values					
		Active	**UB**	**LB**	**Default**	**Typical**	**factor**	**Finite Dif**
1	ε^{∞}	1	0.20	0.00	0.060	1.00	0.0010	0.05
2	τ_C	1	50,000	500	20,000	1.00	1,000	0.10
3	τ_L	1	100,000	500	40,000	1.00	1,000	0.10
4	U_C	0						
5	U_L	0						
6	γ_c	0						
7	γ_t	0						
8	ε_c	0						
9	ε_t	0						
10	W	0						
11	Ref Temp	0						
12	σ_2	0						
13	β_E	0						
14	β_f	0						

7.2.2 Measured displacements

In the case of Seminoe dam, measurements were taken at two locations shown in Fig. 7.2.

Table 7.2: Displacement instrumentation coordinates

Device	Coordinates [m]			Closest Node	Coordinates [m]		
	X	Y	Z	ID	X	Y	Z
T3A	-34.8	77.8	71.9	3651	-34.3	78.4	71.9
T3B	8.8	84.7	71.9	1394	8.8	84.3	71.9

As we will need to correlate measured displacements with computed ones, the corresponding nodal coordinates, Fig. 7.2, are given in Table 7.2.

[!ht]

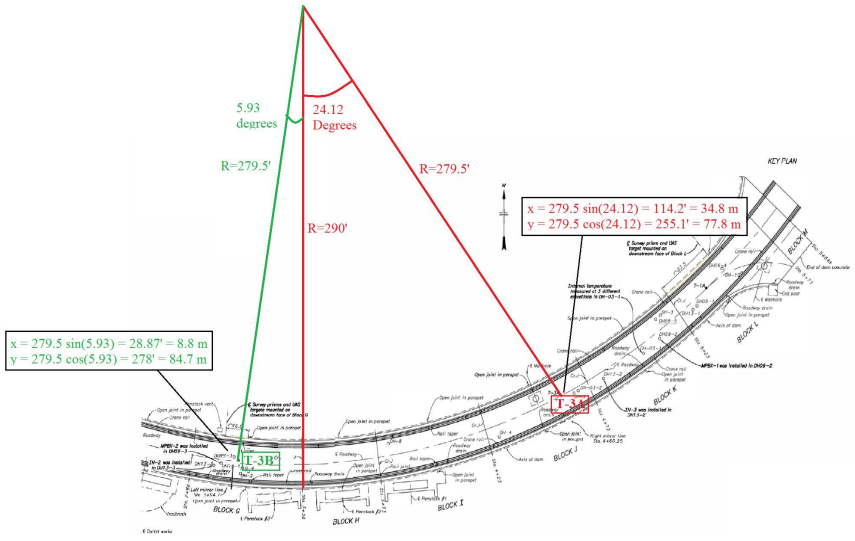

Figure 7.2: Instrumentation locations

The measured displacements **U** are shown in Table G.2. Prior to their use in the parameter identification process, a four step pre-processing is needed:

1. The raw data are first plotted, Fig. 7.3(a) and 7.4(a). We note that when the horizontal displacements were first recorded, the initial reading was not zero. Furhermore, it was not until 10 years later that the vertical displacements were recorded.
2. In the next step, Fig. 7.3(b) and 7.4(b) we "zero" the crest displacements. The horizontal one is shifted down to zero, and the vertical one is shifted up by an *arbitrary* amount to reflect that with respect to the first horizontal recording, a vertical one did occur. Yet, we do not know its magnitude, at best this can be numerically estimated later.
3. Focusing on the horizontal displacement, it is evident that there is certain "ruggedness" which may be caused either by measurement errors, or variable temperature/pool elevation at the time of measurement. Hence it would be reasonable to "smooth" the data using the Matlab® function `smoothdata` with the option `loess` (*Local regression using weighted linear least squares and a 2nd degree polynomial model.*), Fig. 7.3(c)-7.3(d) and 7.4(c)-7.4(d) for vertical-horizontal readings, T3B and T3A respectively.
4. The smoothed curve has now as many data points as were recorded. However, we would need to have `Nincrement` data points (corresponding to the number of increments in the finite element analysis). Hence the Matlab® `interpolate` function is used to determine those points. Fig. 7.3(e)-7.3(f) and 7.4(e)-7.4(f) for vertical-horizontal dat, T3B and T3A respectively. Recorded values are shown as black

Table 7.3: T_3B Measurements (**Seminoe-Crest-Displ**)

Date	Deflection	Settlement	Date	Deflection	Settlement
Date	(cm)	(cm)	Date	(cm)	(cm)
3/17/2020	21.8	-7.5	9/10/2002	14.0	-4.0
9/19/2019	22.3	-7.6	4/12/2002	11.6	-3.4
4/24/2019	23.2	-7.9	10/6/2001	12.2	-3.7
9/27/2018	22.9	-7.6	4/17/2001	12.2	-3.7
3/20/2018	22.6	-7.6	4/4/2000	10.4	-3.0
10/4/2017	23.2	-7.0	9/23/1999	-	-3.7
4/5/2017	20.4	-	4/16/1999	10.4	-2.7
3/13/2017	-	-7.3	9/9/1998	11.3	-3.4
9/21/2016	22.3	-7.6	4/29/1998	10.1	-3.0
9/24/2015	22.9	-	9/15/1997	11.6	-3.0
9/23/2015	-	-7.3	4/25/1997	10.4	-2.7
3/27/2015	21.0	-7.0	9/27/1996	11.0	-2.7
9/15/2014	21.0	-7.0	3/22/1996	9.1	-2.4
3/24/2014	20.6	-6.5	9/26/1995	10.1	-2.4
9/24/2013	20.1	-	4/4/1995	9.4	-1.8
9/17/2013	-	-6.4	9/9/1994	10.4	-2.1
3/27/2013	18.3	-6.1	4/1/1994	9.8	-1.5
9/21/2012	20.4	-6.4	10/5/1993	9.8	-1.5
3/29/2012	18.0	-5.8	4/2/1993	-	-0.6
9/13/2011	19.8	-6.4	9/22/1992	8.5	-1.2
4/1/2011	18.0	-5.5	3/26/1992	8.2	-0.6
9/28/2010	19.2	-5.8	9/19/1991	8.8	-0.9
3/15/2010	18.6	-5.8	4/23/1991	7.0	-0.3
10/2/2009	18.6	-5.8	9/11/1990	7.6	-0.3
5/4/2009	17.7	-	11/28/1989	-	-
4/14/2009	-	-5.2	10/19/1989	7.0	-
10/27/2008	18.9	-5.2	4/26/1989	5.8	-
4/23/2008	18.0	-4.9	9/19/1988	7.3	-
9/12/2007	18.3	-5.2	6/1/1988	5.5	-
4/9/2007	16.5	-4.9	9/21/1987	5.2	-
9/18/2006	-	-4.9	4/7/1987	3.7	-
4/3/2006	15.5	-4.3	10/30/1986	4.6	-
9/1/2005	16.2	-4.9	4/22/1986	3.7	-
4/1/2005	13.7	-4.3	4/11/1985	1.8	-
9/23/2004	15.5	-4.3	10/30/1984	3.4	-
3/23/2004	14.0	-4.0	4/16/1984	0.9	-
12/4/2003	14.3	-3.4	7/27/1982	0.3	-
4/2/2003	12.8	-4.0	3/26/1982	2.4	-
			7/2/1979	1.2	-

filled circles, and interpolated ones as red filled circles.

[!ht]

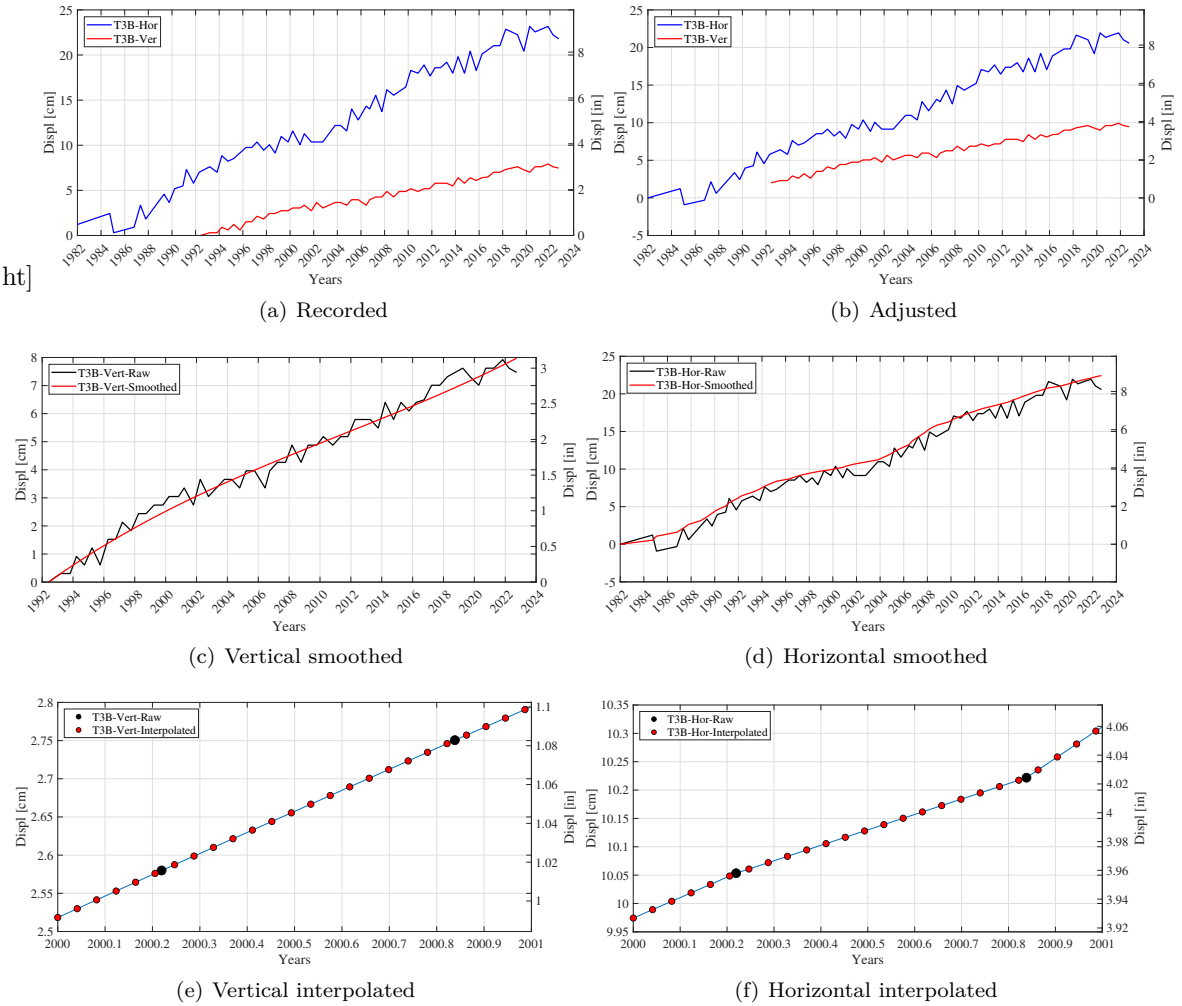

(a) Recorded

(b) Adjusted

(c) Vertical smoothed

(d) Horizontal smoothed

(e) Vertical interpolated

(f) Horizontal interpolated

Figure 7.3: T3B Measurements and adjustments

We note that readings (and thus interpolated values) did not start exactly on January 1 at year zero for the vertical reading (1992), and at nearly January 1 for the horizontal reading (1982). Nevertheless, we shall use these smoothed data for parameter identification. We also note that the seasonal temperature is nearly obliterated by the smoothing process. This should not be an issue in the context of parameter identification as we attempt globally to approach the target curve without the distraction of small oscillations.

[!ht]

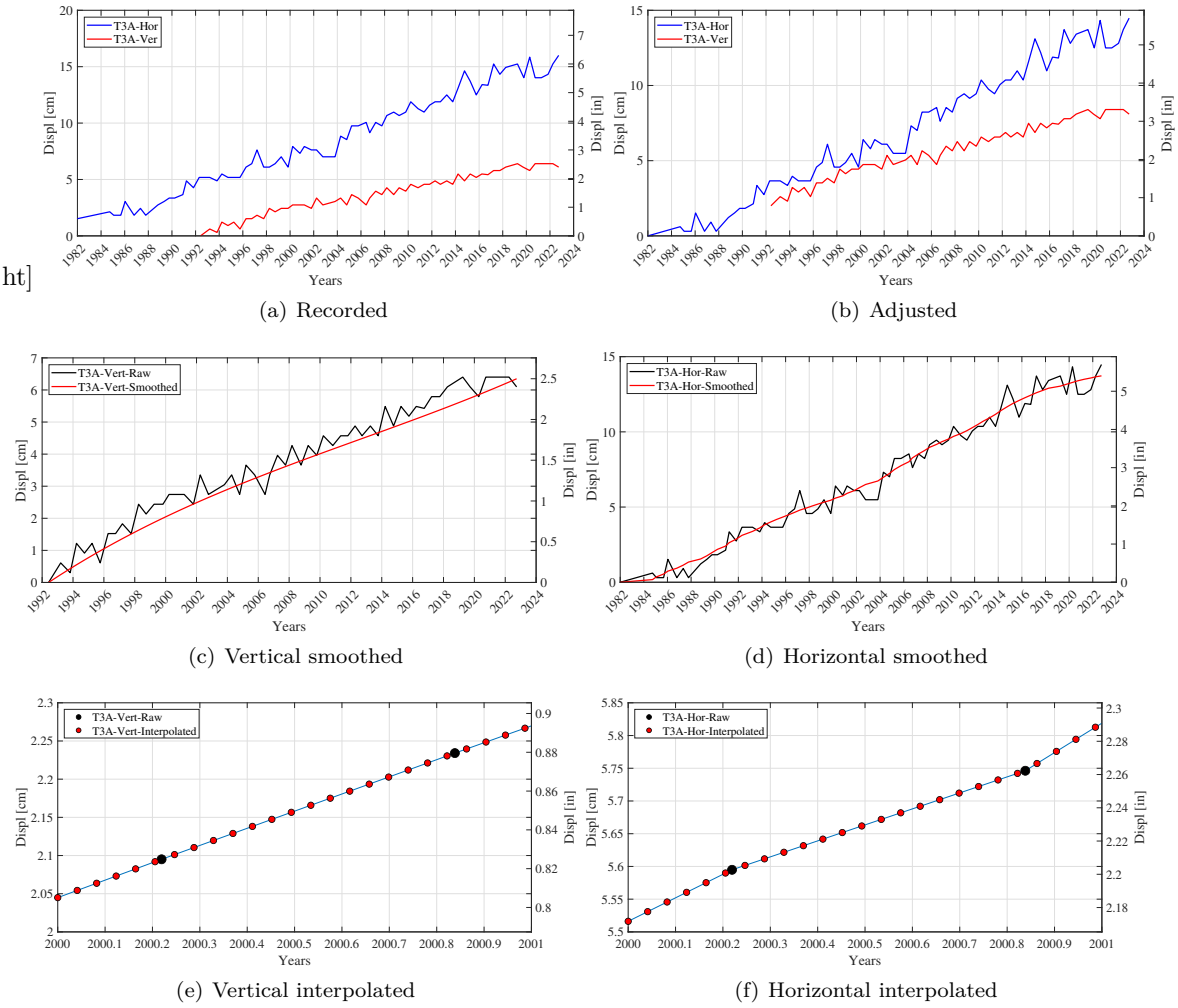

(a) Recorded

(b) Adjusted

(c) Vertical smoothed

(d) Horizontal smoothed

(e) Vertical interpolated

(f) Horizontal interpolated

Figure 7.4: T3A Measurements and adjustments

7.2.3 Results

Fig. 7.5 is a plot of the system identification user interface which shows the iterative procedure in which the variables are altered one at a time until the termination condition is satisfied; in other words the computed displacement curve becomes as close as possible to the recorded data.

In Fig. 7.6 and 7.7 the displacements obtained from the optimal analysis suggested by the system identification process is plotted with the recorded data. Since the horizontal displacement of the T3B instrument is the most reliable measurement, the system identification objective function was set to optimize the corresponding displacement and as seen in Fig. 7.6 the resulting curve matches well with the recorded data for the displacement of interest.

As such, the parameters suggested by the system identification will be used as the mean values for the uncertainty quantification of the stress analysis.

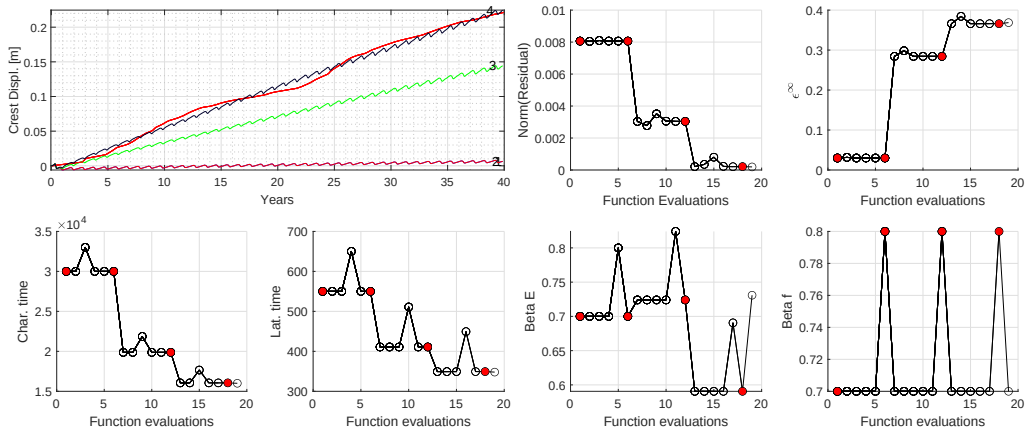

Figure 7.5: System Identification user interface

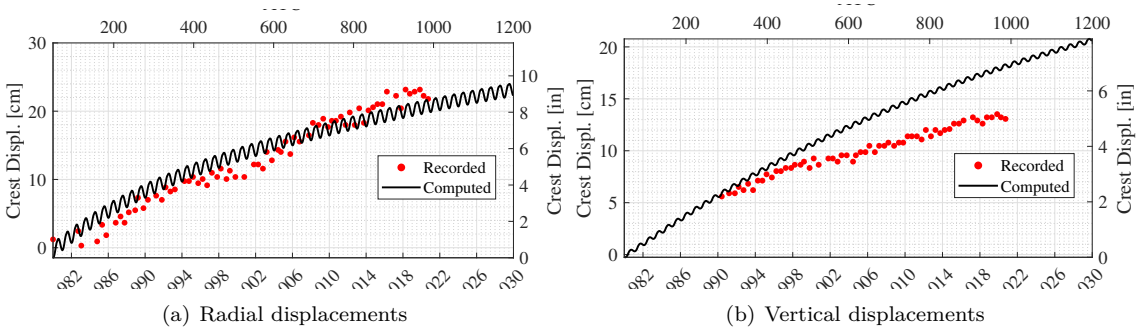

(a) Radial displacements (b) Vertical displacements

Figure 7.6: Displacement comparison following system identification for T3B

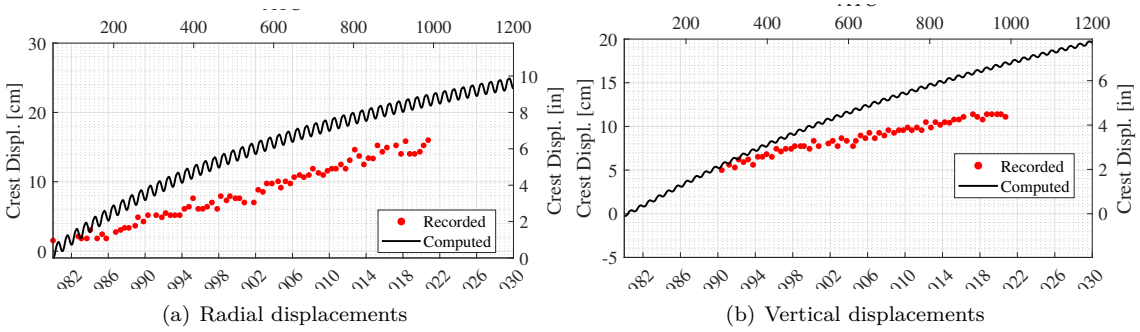

(a) Radial displacements (b) Vertical displacements

Figure 7.7: Displacement comparison following system identification for T3A

7.3 Deterministic Analysis with Nonlinear Concrete Model

In this section the results of the AAR analysis of the dam considering nonlinear material properties is demonstrated and discussed. The concrete model is the one of the computer program ATENA, and described in (**cervenka08**). It should be noted that this can be a particularly challenging problem, as there are two sources of nonlinearities, concrete material, and joints.

7.3.1 Displacements

The resulting displacements of the nonlinear analysis at the locations corresponding to T3B and T3A instruments are plotted and compared to that of the linear analysis (Fig. 7.8 and 7.9). As seen, the nonlinear analysis suggests linearly increasing displacement while the displacements obtained from the linear analysis is gradually reaching a plateau; however, both analyses demonstrate good match with the measured displacements of interest. Fig. 7.10 shows the dam displacements in the 3 directions after 50 years of nonlinear

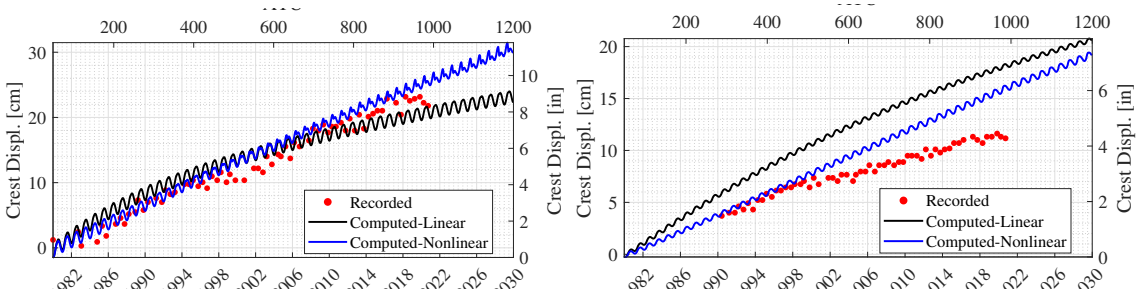

(a) Radial displacements (b) Vertical displacements

Figure 7.8: Displacement comparison from linear and nonlinear analysis for T3B

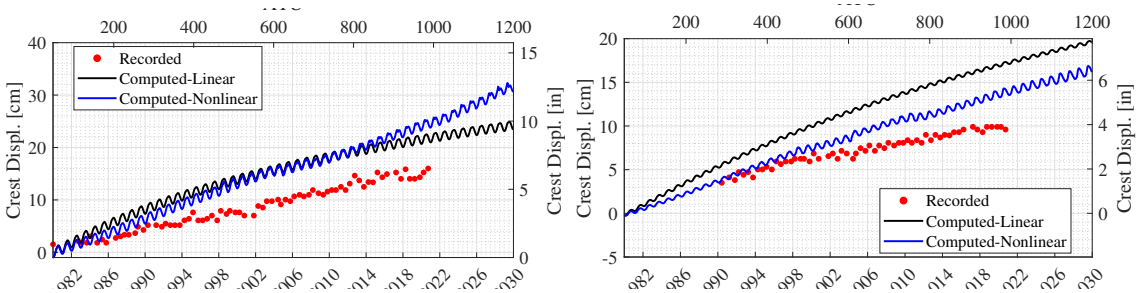

(a) Radial displacements (b) Vertical displacements

Figure 7.9: Displacement comparison from linear and nonlinear analysis for T3A

analysis.

Finally, the deformed shape is shown in Fig. 7.11.

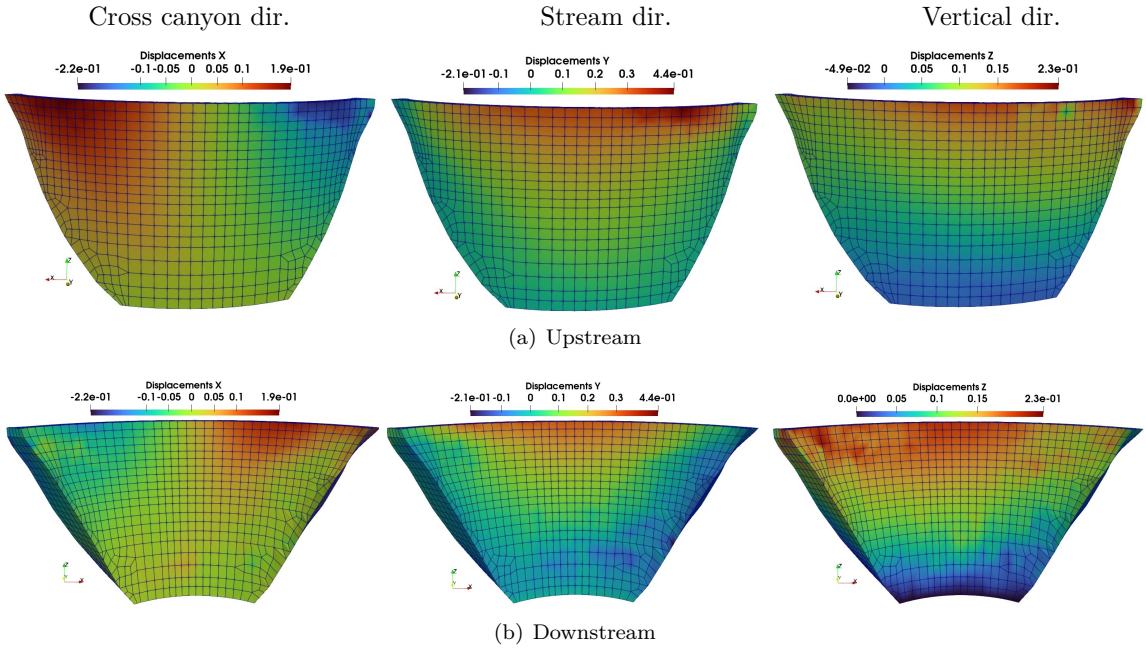

Figure 7.10: Displacement plots after 50 years of Nonlinear analysis

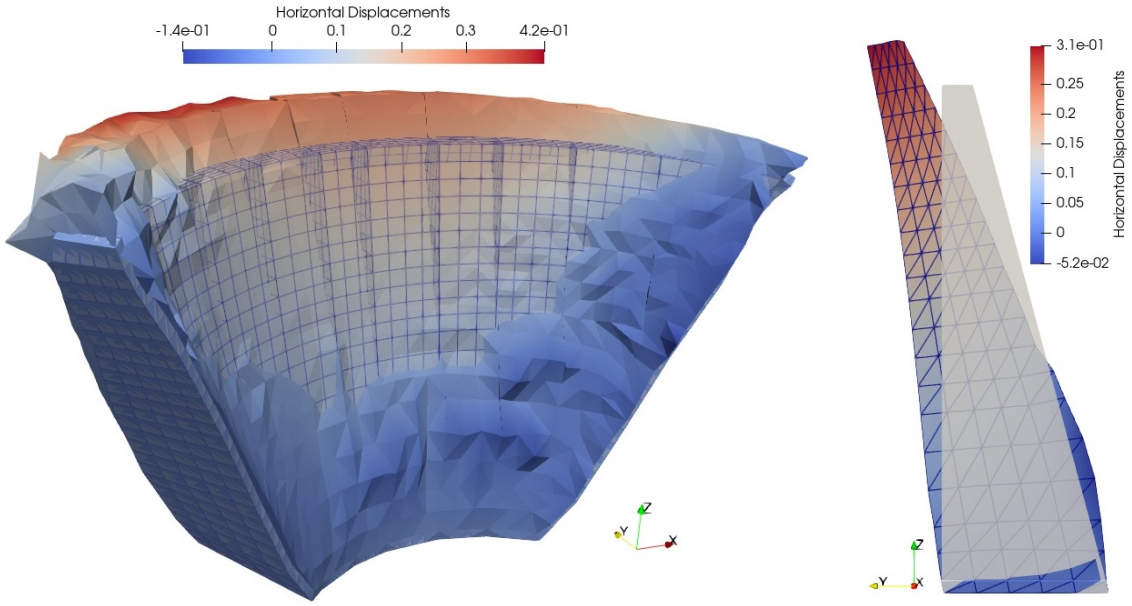

Figure 7.11: Dam deformed shape after 50 years of analysis; Nonlinear analysis

7.3.2 Stress Distribution

7.3.2.1 Stress and Strains

Although the dam does not have a complete symmetrical geometry, the results of the displacements as well as the stress and strain distributions seen in Fig. 7.12 are almost symmetric.

Therefore it can be concluded that the material and other properties have been assigned symmetrically.

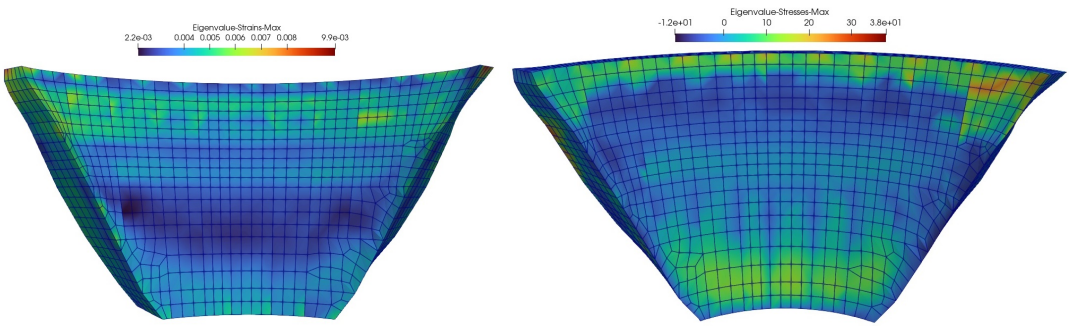

(a) Strain (b) Stress

Figure 7.12: Principal Stress and strain distributions after 50 years of Linear analysis

7.3.2.2 Crack Pattern

7.3.2.2.1 After 50 years

The cracking pattern shown in Fig. 7.13 is demonstrating an asymmetric formation of the cracks mostly on one side. It is noted that even the smallest asymmetry in the geometry of the dam can result in significant differences between the crack development on the 2 sides of the dam. Thus formation a weak point on a side results in the cracks initiation and propagation from there.

As seen, the cracks are mostly developed at the bottom and inside the dam which can be due to the fact that the higher confinement prevents the concrete from expanding in the vertical direction and thus the expansion is occurred mostly in the 2 horizontal directions as the orientation of the disks also suggest. The detailed explanation of the AAR strain redistribution is also discussed in Chapter 2 and demonstrated in Fig. E.1.

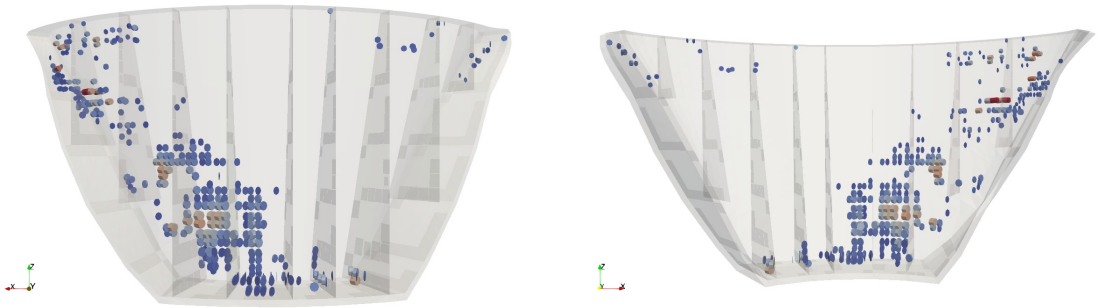

(a) Upstream (b) Downstream

Figure 7.13: Smeared crack profile after 50 years of analysis

7.3.2.2.2 Crack Patters and Principal Stresses

In Fig. 7.14 the development of the cracks over the time is shown along with the corresponding maximum principal stresses.

The results show that the cracking initiated in 1998 after 18 years of analysis and they are mostly inside

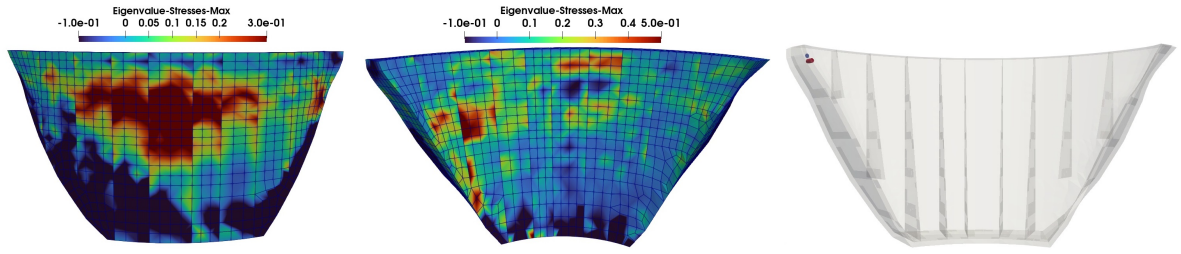

(a) 1998

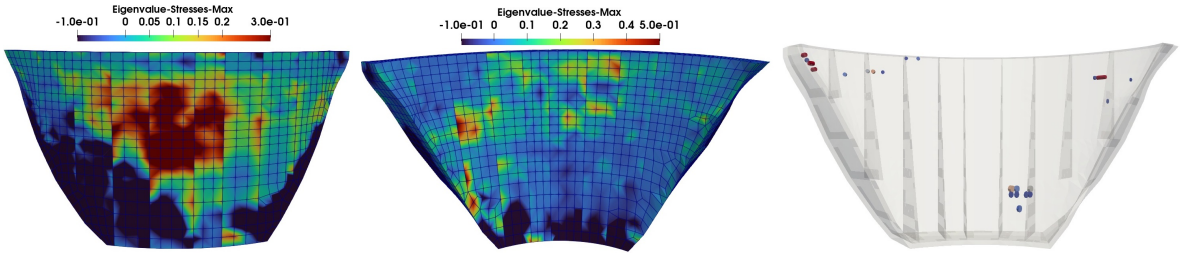

(b) 2005

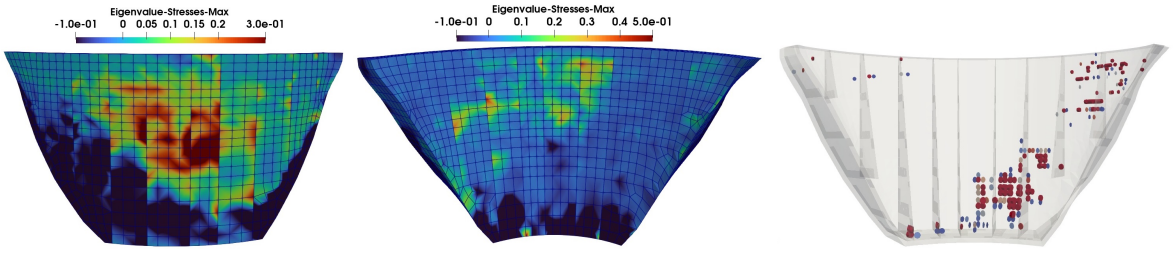

(c) 2020

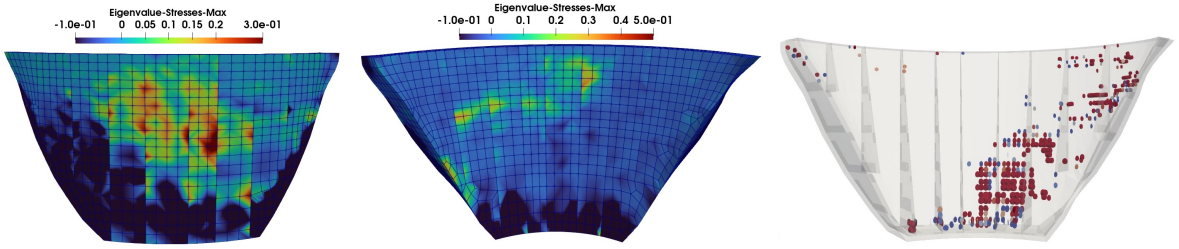

(d) 2030

Figure 7.14: Smeared crack profile over the time compared to the maximum principal stresses

the dam.

7.3.2.2.3 Sectional Cuts of Principal Stresses Over Time In order to better visualize the results a vertical section cut is selected and the maximum principal stress and strain distributions are plotted in Fig. 7.15.

As seen the majority of the lower portion of the dam and upstream is in compression while the top of the dam and mostly on the downstream side is in tension which can be indicative of possible cracking in that portion.

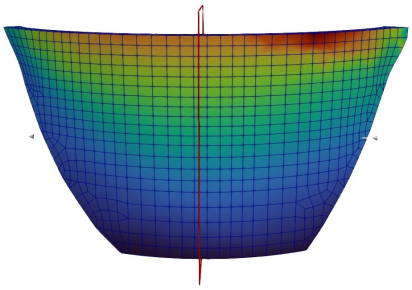

(a) Section cut location

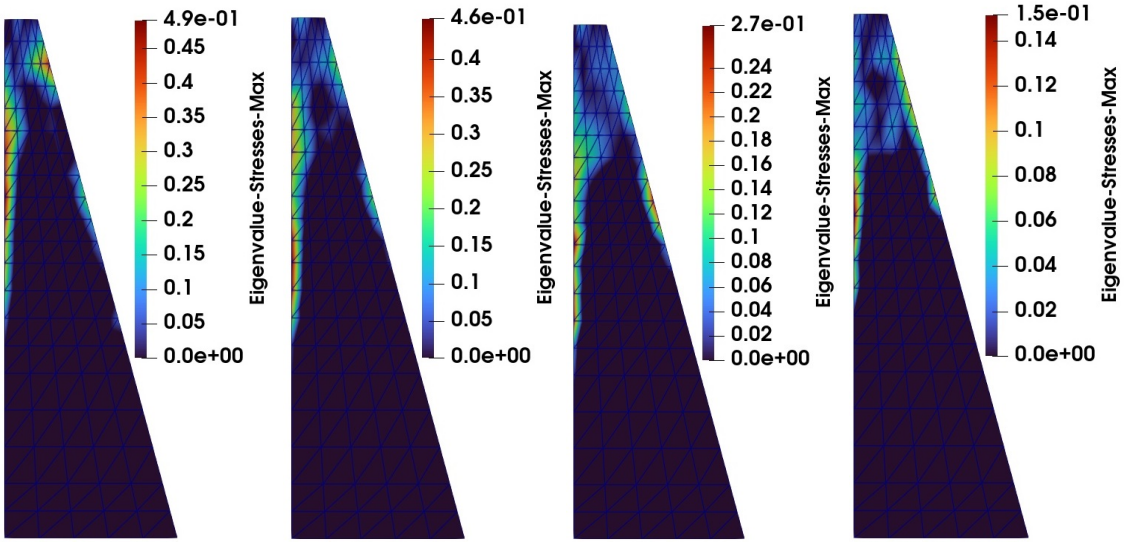

(b) 1998 (c) 2005 (d) 2020 (e) 2030

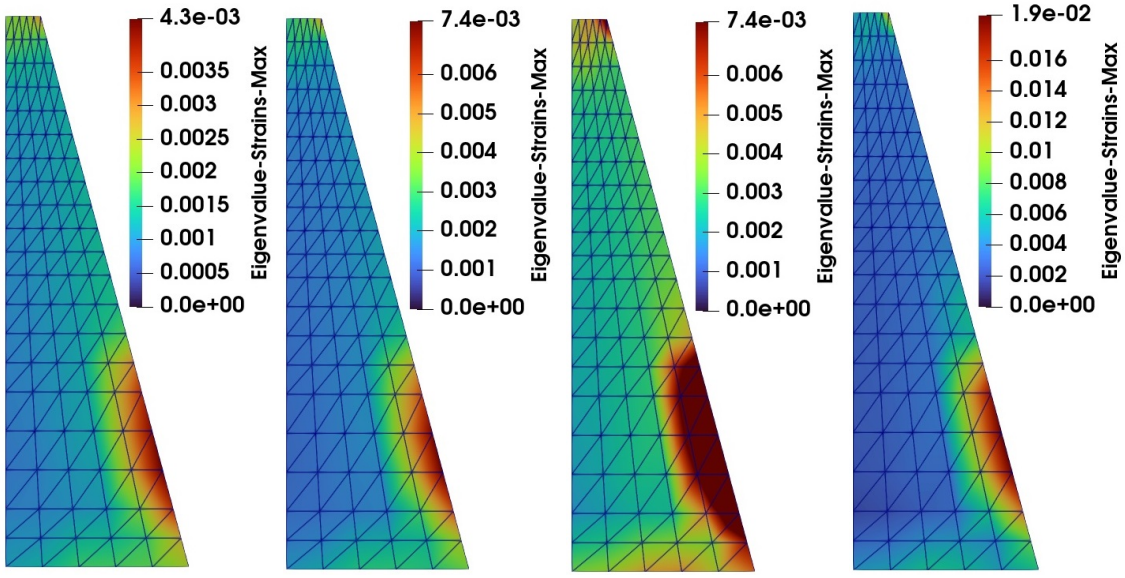

(f) 1998 (g) 2005 (h) 2020 (i) 2030

Figure 7.15: Maximum principal stresses at a section cut over time

7.3.2.2.4 Winter Summer Principal Stresses Over Time

The maximum principal stresses over time for both summer and winter are shown in Fig. 7.16.

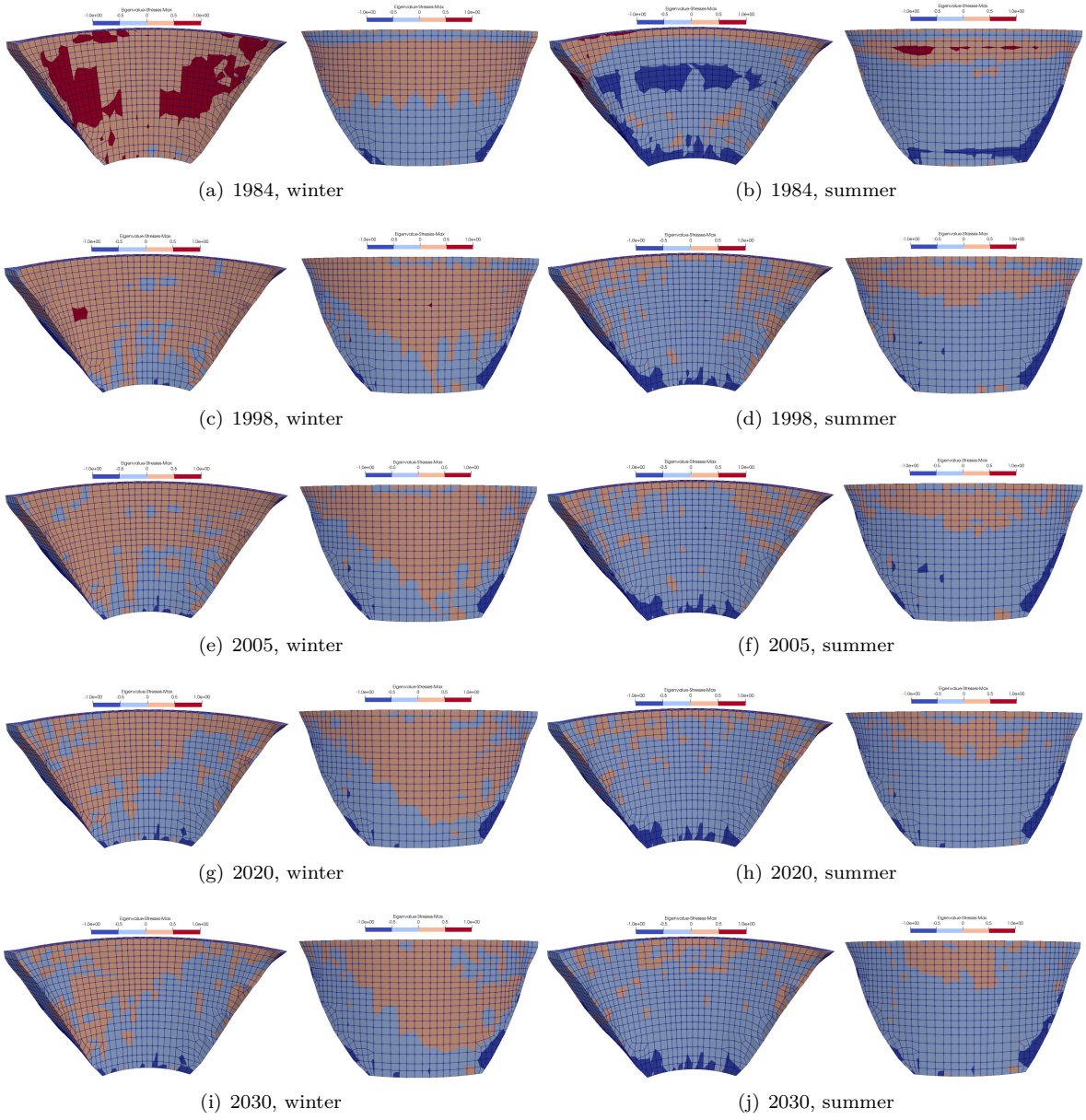

(a) 1984, winter (b) 1984, summer

(c) 1998, winter (d) 1998, summer

(e) 2005, winter (f) 2005, summer

(g) 2020, winter (h) 2020, summer

(i) 2030, winter (j) 2030, summer

Figure 7.16: Maximum principal stresses over summer and winter

Whereas Fig. 7.17 shows the maximum principal stresses at different vertical sections in 2020.

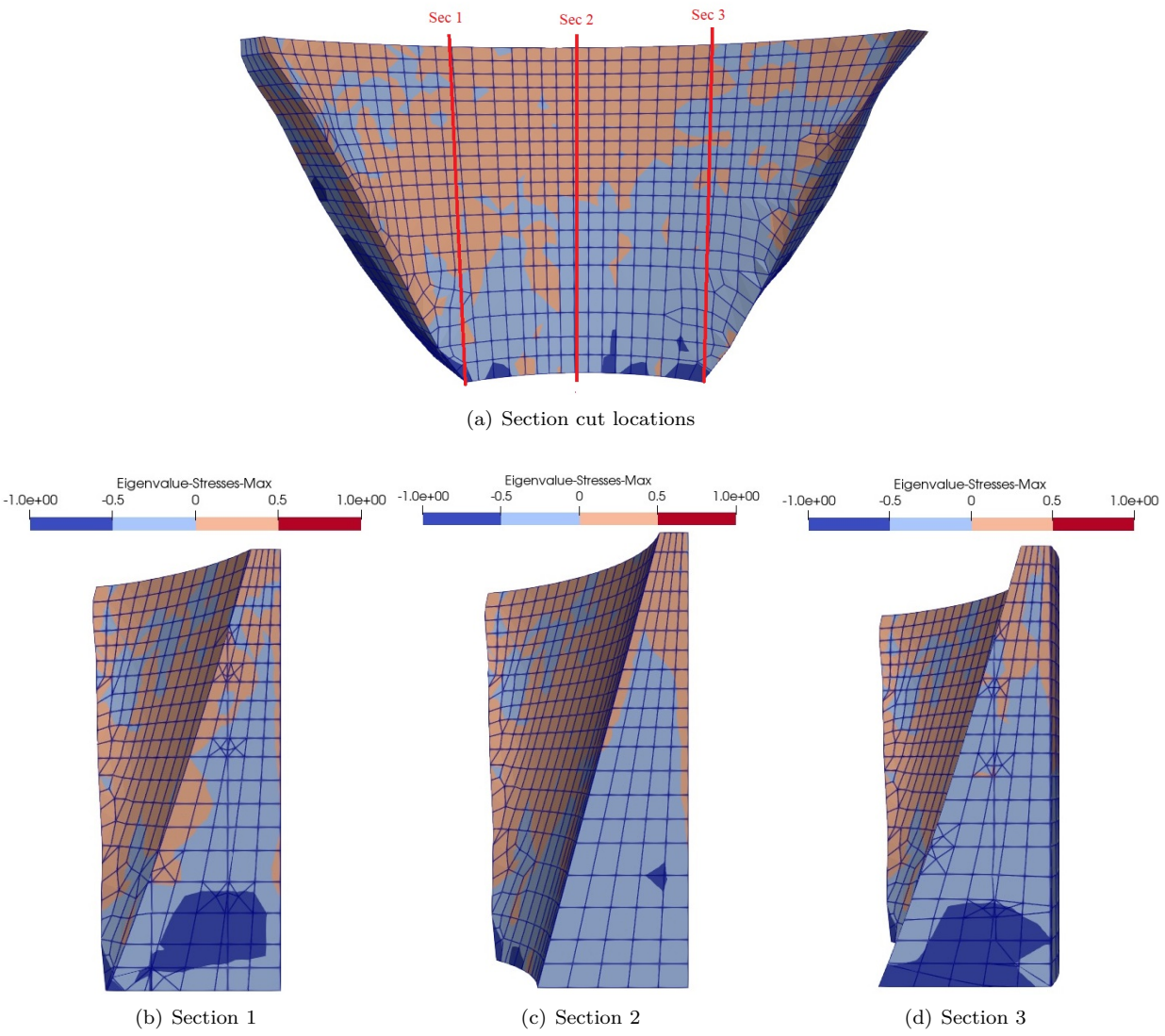

(a) Section cut locations

(b) Section 1

(c) Section 2

(d) Section 3

Figure 7.17: Maximum principal stresses at different vertical sections in 2020

7.3.2.2.5 Evolution of Principal AAR Strains over Time

To show the development of AAR, the maximum principal AAR strain profiles are presented in Fig. 7.18. It is seen that there is higher AAR at the crest on the upstream side and on the mid to lower height on the downstream side of the dam.

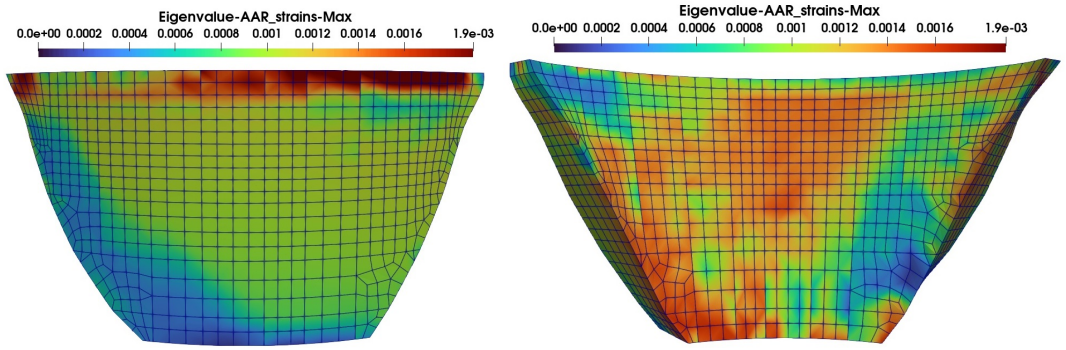

(a) 1998

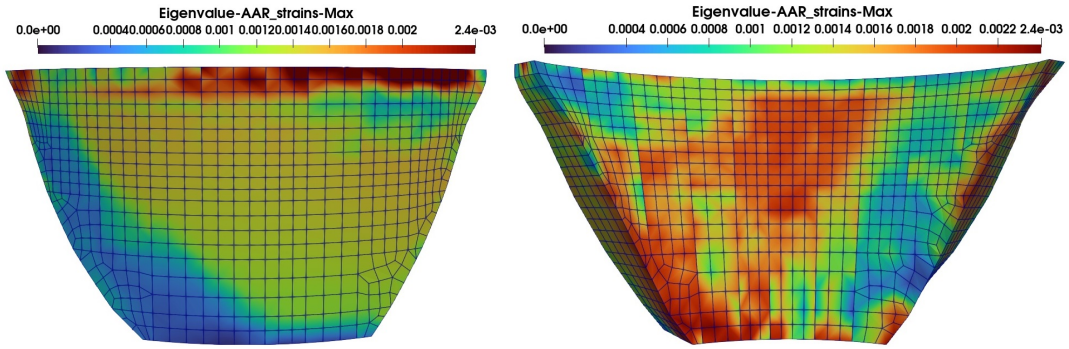

(b) 2005

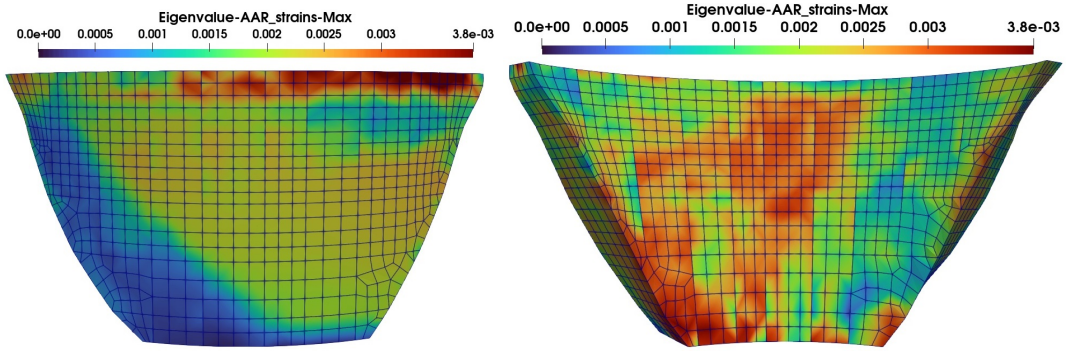

(c) 2020

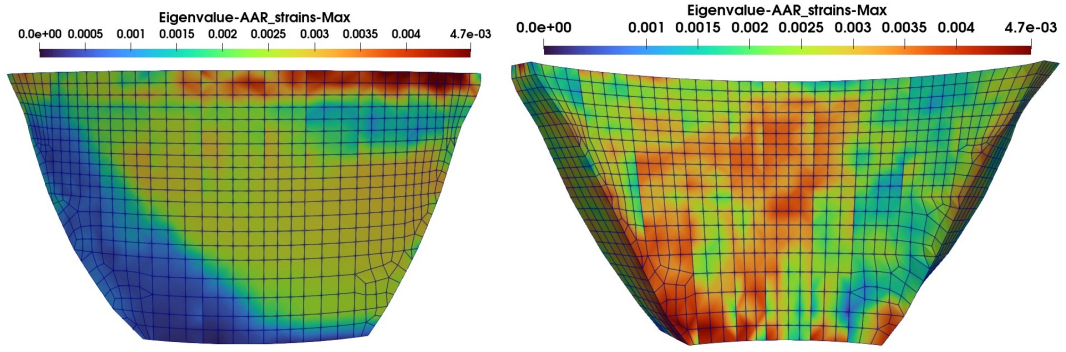

(d) 2030

Figure 7.18: AAR development over the time

7.3.2.2.6 80 Years Analysis

In order to further investigate the development of cracks the analysis was extended for 30 more years and yet no cracks on the upper portion of the downstream side were detected even after 80 years of AAR. Fig. 7.19 shows the maximum principal stress along with the vertical stress distributions for the end of the 80-year analysis.

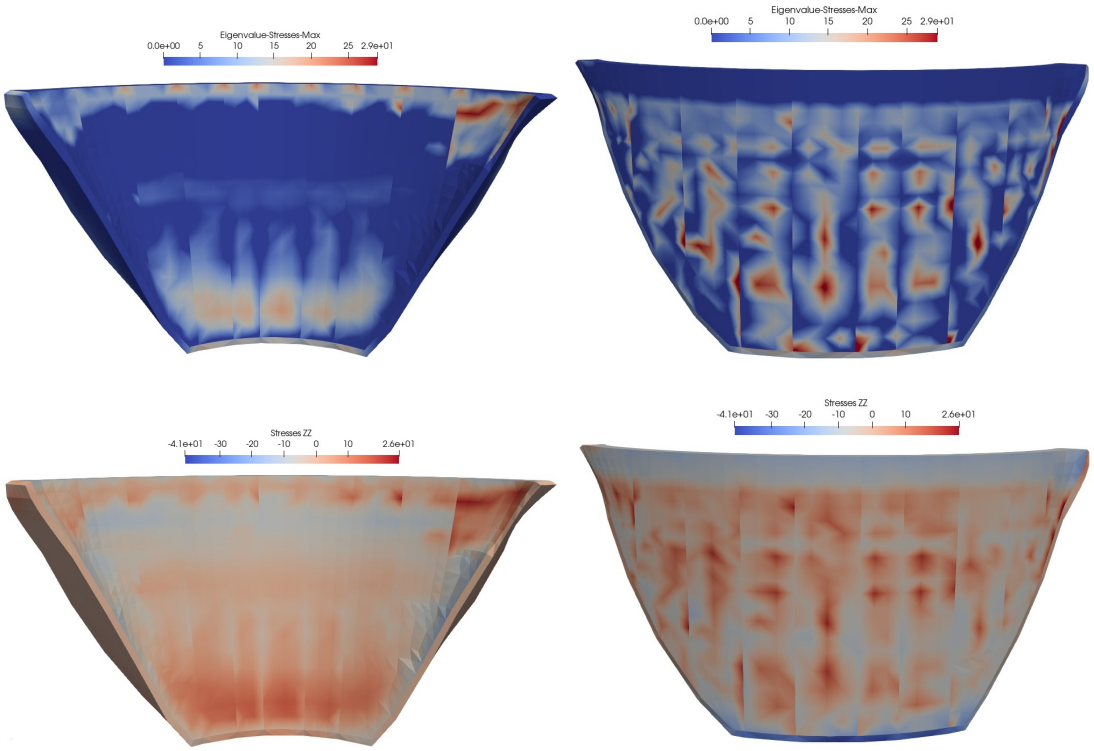

Figure 7.19: Maximum principal stress and vertical stress distribution after 80 years of analysis; Nonlinear analysis

However, it is note worthy that the analysis time started in 1980 and the considered material properties were those corresponding to the same time. which means that the assumed concrete properties at the initial time of the analysis had already experienced some amount of AAR and probably cracking by then.

Chapter 8

Uncertainty Quantification

Abstract

In so far, all analyses were deterministic. In this final chapter, we will perform an uncertainty quantification (a.k.a. "Monte Carlo" simulation) study for both thermal and stress analysis.

In the stress analysis the only source of non-linearity will be the presence of the joints (this is justified by Fig. 7.8).

Probabilities of exceedance of critical threshold values will be analytically developed, along with the importance of the sample sizes (three were used: 50, 100 and 200).

8.1 Thermal Analysis

Since thermal analysis is a prerequisite to the stress analysis, the uncertainty quantification of thermal parameters is also required prior to conducting any uncertainty assessment of stress analysis. Therefore, this section is to discuss the effect of parameter uncertainties used in thermal analysis of Seminoe on the resulting concrete internal temperatures. To this purpose, among all (figure 8.1), the thermal parameters which were believed to have some extent of uncertainty were taken as random variables. These parameters are as follows:

- Specific heat
- Conductivity
- Air temperature amplitude
- Water surface temperature amplitude
- Water bottom temperature amplitude

The particular point of interest (POI) for nodal temperature has the recorded values shown in Fig. 8.2.

It should be noted that other thermal parameters, such as film coefficients were assumed to be deterministic variables as there are certain values available for them in the literature and there is no need to treat them as uncertain variables. Also, the mass density of the concrete is believed to be determined. Assuming a lognormal distribution for the aforementioned variables and a coefficient of variation(COV) equal to 15%, 1000 number of simulations were generated using the Latin hypercube sampling (LHS) method assuming that these parameters have zero correlation with each other. The 1,000 thermal models were generated based

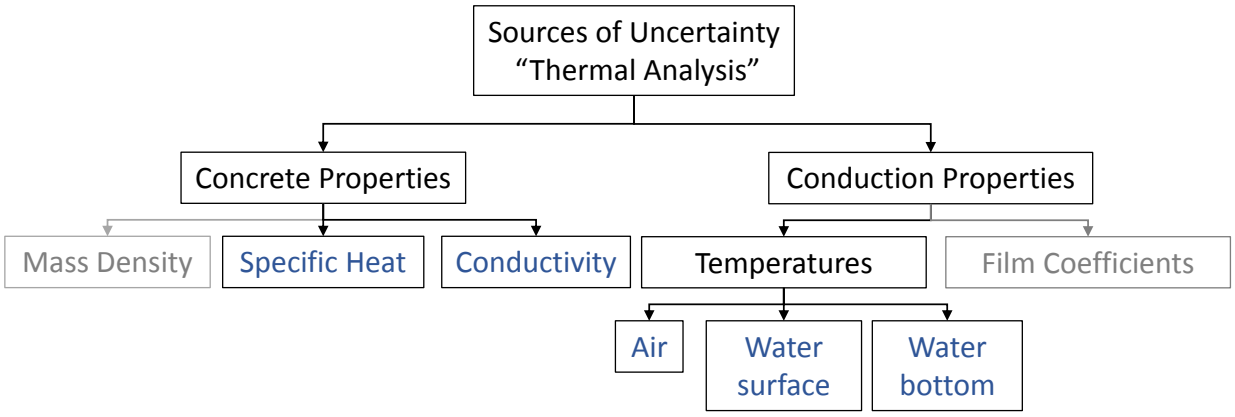

Figure 8.1: Sources of uncertainty in thermal analysis

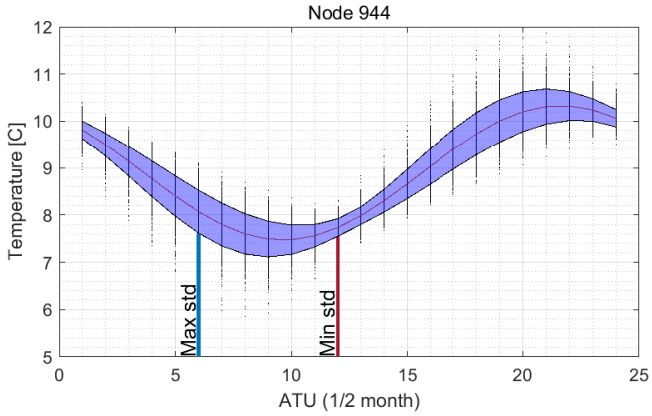

Figure 8.2: Monthly temperatures at PoI (Node 944), with mean and standard deviation

on those simulations for which the temperature of 6 node inside the dam body for 2 months is shown in figure 8.3.

As seen in the plot, the maximum inside dam temperature is occurring around mid October which stems from the thermal inertia phenomenon which is a description for the delay in the inside dam body temperature to feel the temperature increase of the surrounding fluid. This fact can also be interpreted from the seasonal water temperatures demonstrated in table G.16 taken from the (**hatch**) report. As seen in this table, around depth 7.7 [m], which corresponds to the depth of our point of interest, the maximum temperature of the whole year is measured in October.

8.1.1 Procedure

The procedure itself is algorithmically implemented through a sequence of MATLAB®files, Fig. 8.4. Note that this procedure is tied to the computer program used (Merlin).

Selection of random variables and application of the Latin Hypercube Sampling method are shown in Fig. 8.5.

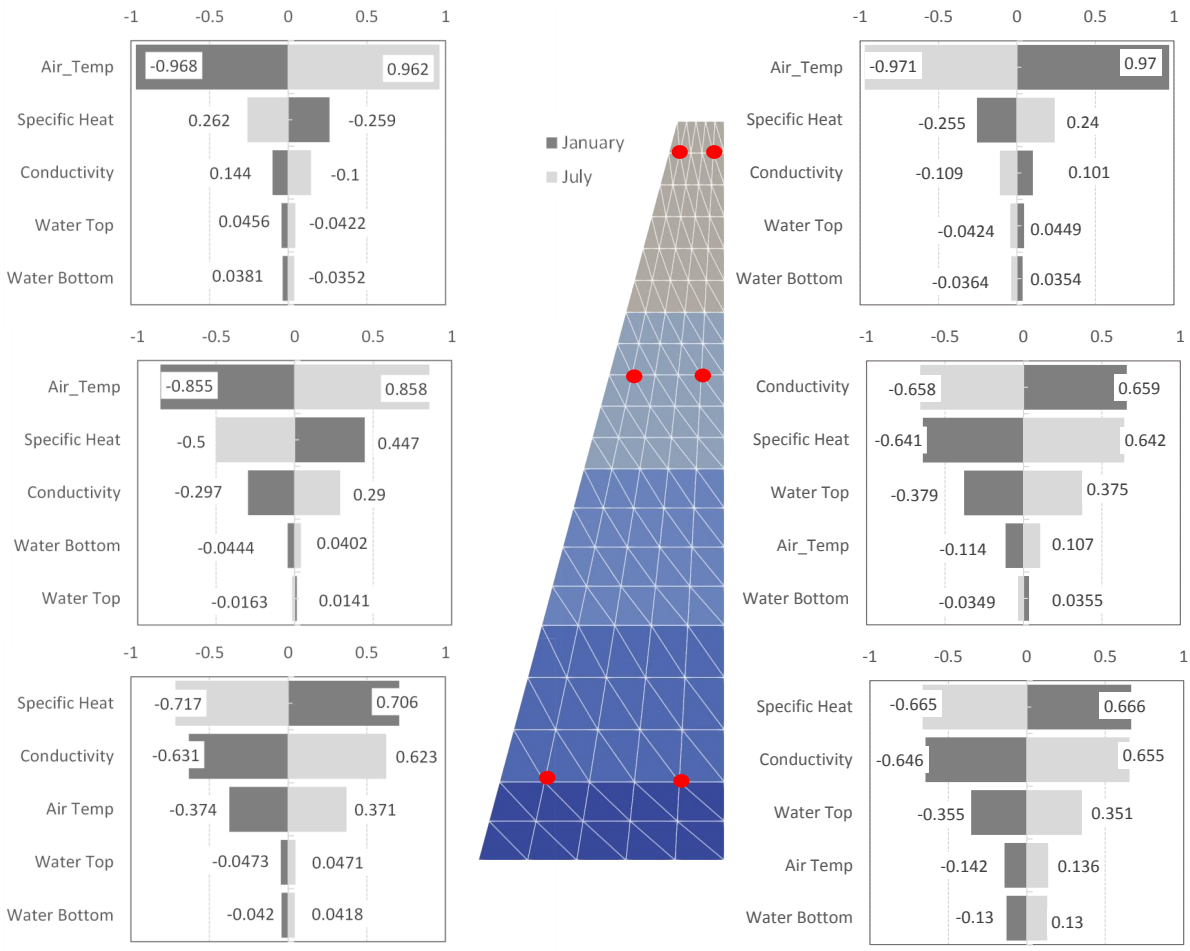

Figure 8.3: Correlation of nodal temperatures and variables at 6 different nodes in January and July

8.1.2 Observations

From figure 8.3 we can draw the following main conclusions from this thermal uncertainty quantification:

- First of all this is showing that the results of the sensitivity analysis for the dam cannot be generalized to the whole dam body and throughout the year. In other words, there is a temporal and spacial variation in the results of thermal analysis.
- While at the top of the dam, which is exposed to the air, the air temperature is the most effective variable at the bottom of the dam close to the upstream face the temperature is more sensitive to the specific heat value.
- Even at the bottom of the dam the temperature is more sensitive to the top water temperature rather than bottom water temperature which is due to the higher variation of top temperature compared to bottom.
- The temperatures of the nodes below water level are more sensitive to the conductivity at the upstream face and to air temperature at the downstream side.

Figure 8.6 is showing the monthly temperature variation and the resullting temperature mean and standard deviation at the 6 nodes. as seen, the maximum temperature moves as the node goes into the depth.

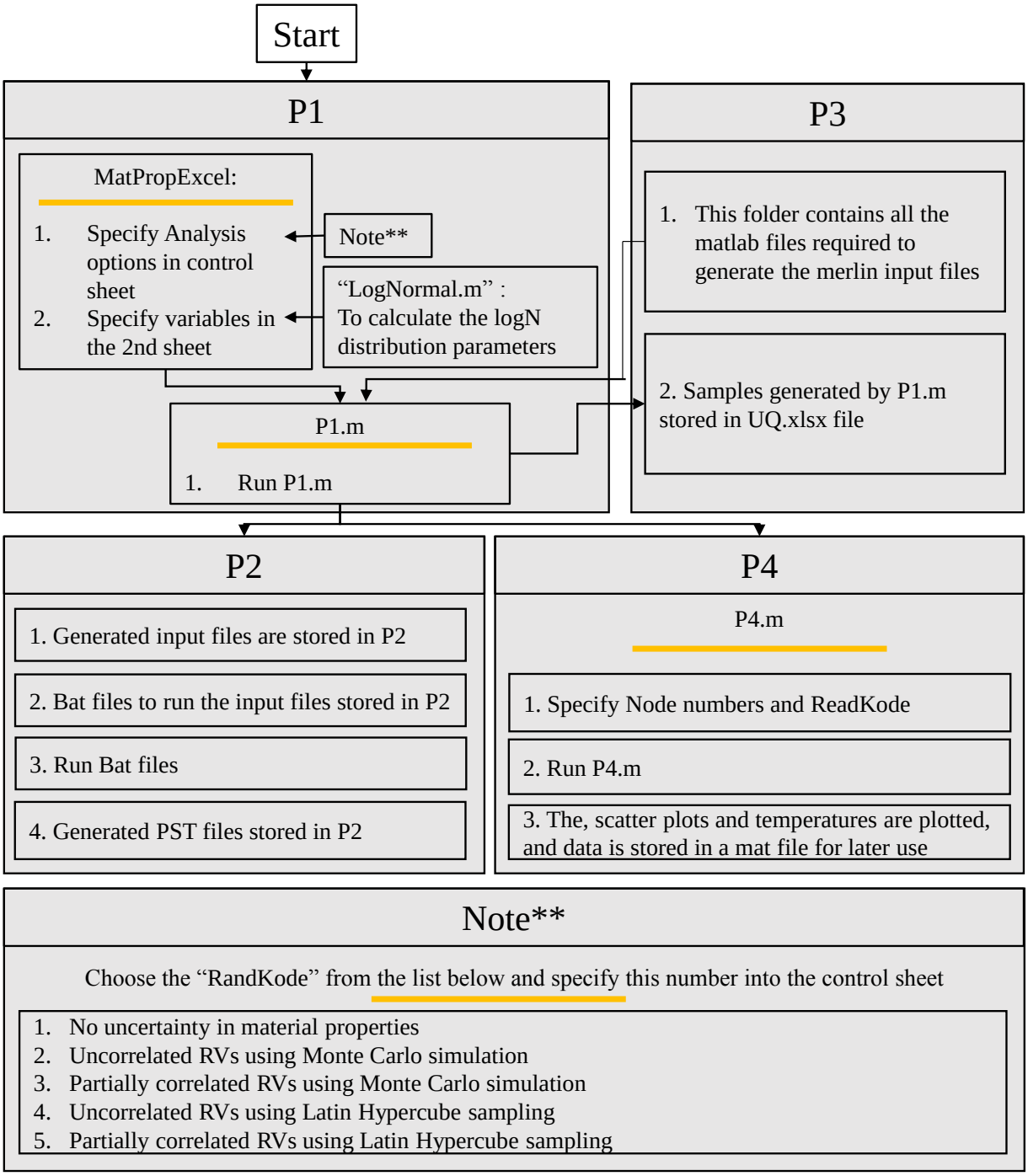

Figure 8.4: Uncertainty Quantification Flowchart

Taking another point inside dam body as a point of interest, the scatter plots of each variable versus the nodal temperature can be presented for every month of the year. Figure F.1 through F.4 show the correlation plots of each variable versus the resulted nodal temperature at the point of interest. There are correlations associated with the thermal parameters and thermal results. As expected the conductivity has negative correlation with the temperature through almost the whole year.

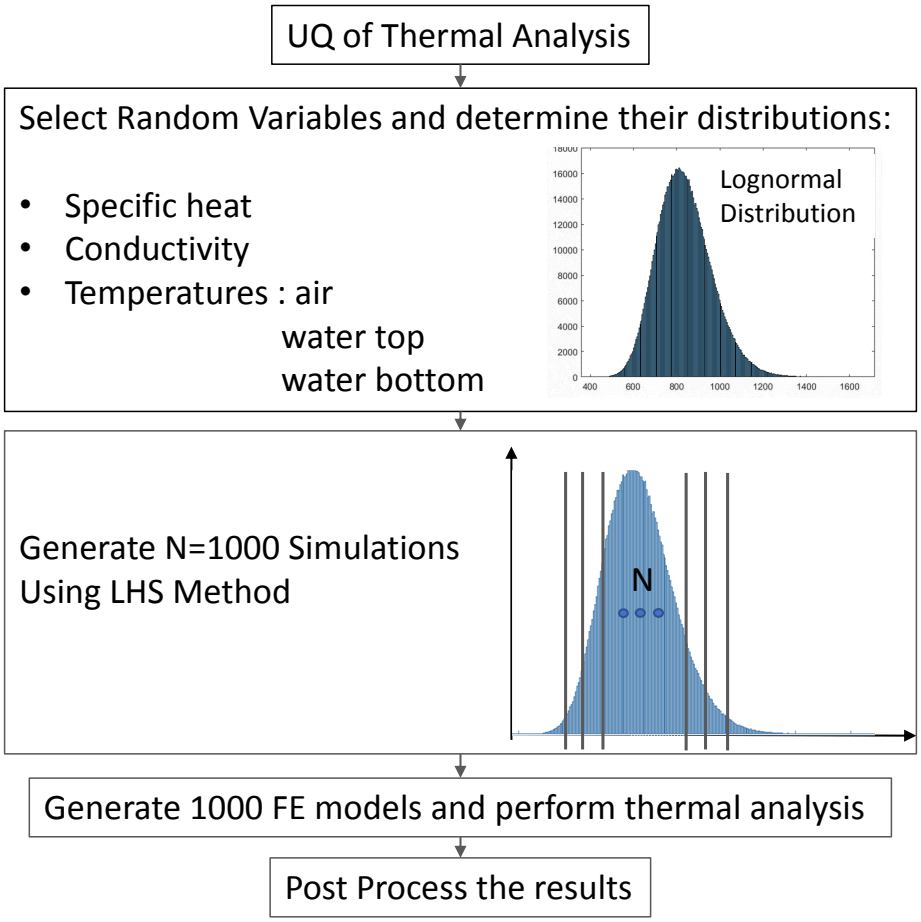

Figure 8.5: Procedure for thermal uncertainty analysis

As seen in figure 8.7 the correlation between the air temperature amplitide and the concrete internal temperature is positive during the colder months of the year and is negative during the warmer months. Figure F.3 and F.4, show almost zero correlation between the nodal temperature at the point of interest and water temperature variation. While air temperature has noticeable correlation with the internal node temperature. This shows that the point of interest is more under the influence of the air temperature rather than water. Since, our data on the reservoir temperature was limited, this observation underlines the fact that the lack of data is not affecting the results significantly as the point of interest is selected to be an internal node below the water level.

The nodal temperature distribution, figure 8.8, resulted from thermal UQ analysis will be eventually incorporated into the stress UQ analysis.

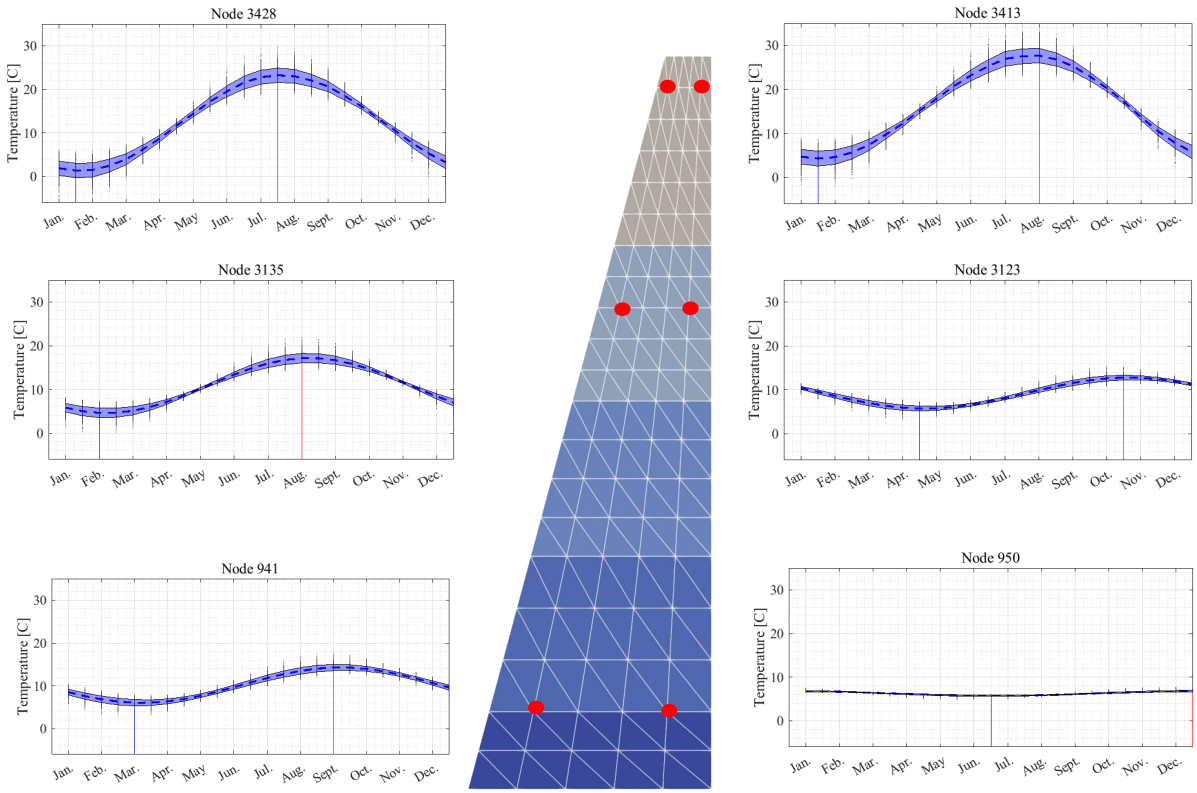

Figure 8.6: Monthly variation of temperature at 6 nodes throughout a year

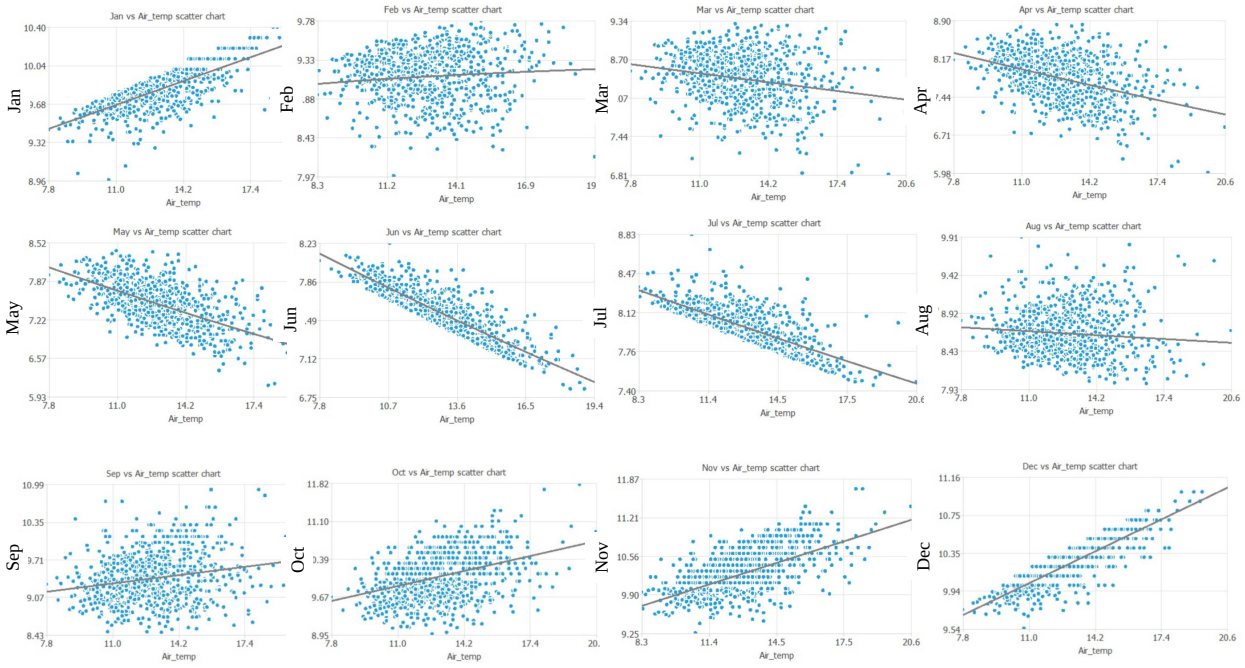

Figure 8.7: Monthly air temperature correlation coefficients at node 944 (PoI)

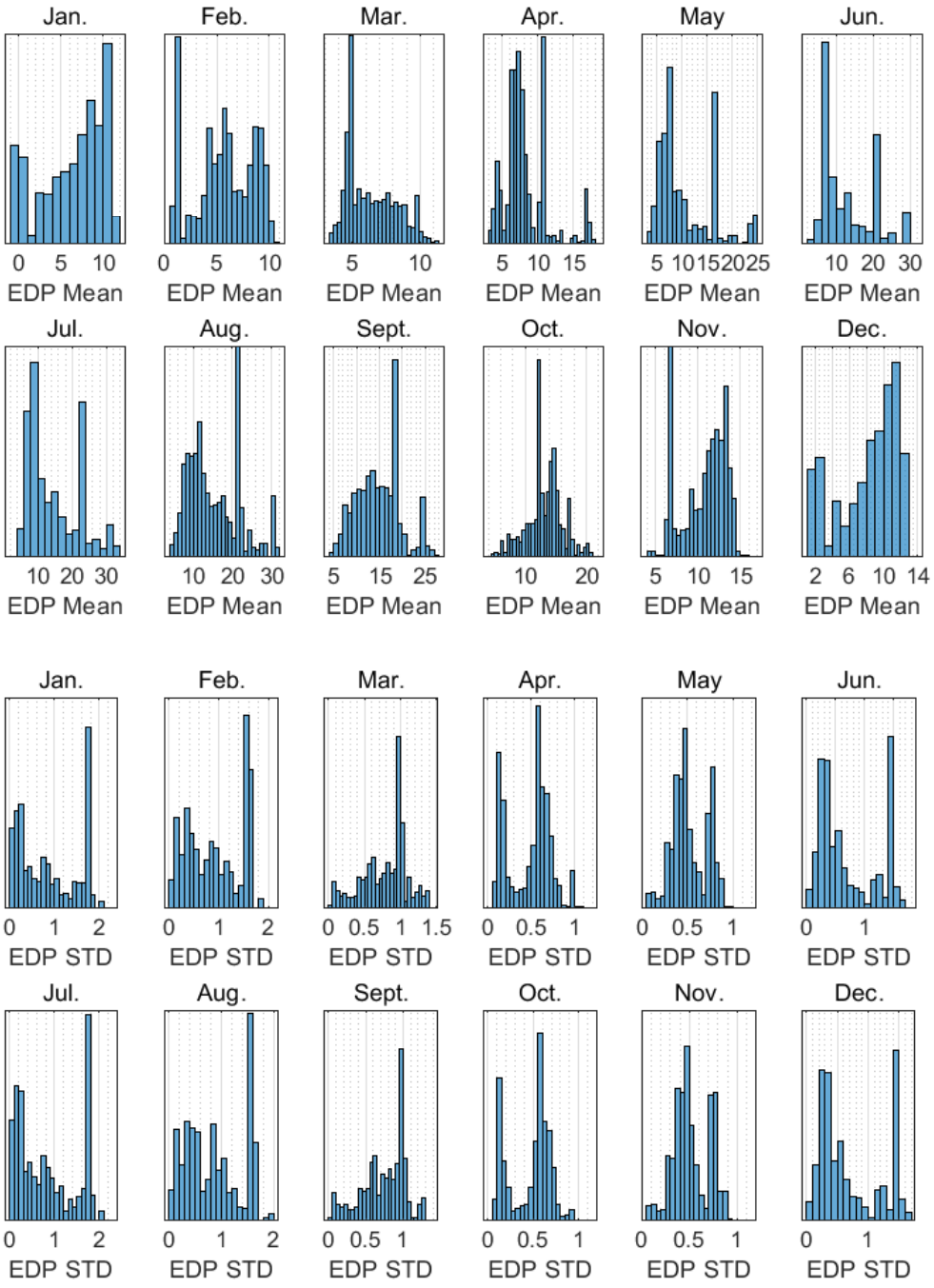

Figure 8.8: Monthly mean and standard deviations histograms for temperatures inside entire mesh

8.2 Stress Analysis

The uncertainty quantification of the dam stress analysis is a function of temperature variability and depends on the uncertainties associated with the uncertainty in the dam internal temperatures. Therefore, the uncertainty quantification of the stress analysis requires performing a number of thermal analysis as well. As such, 13 variables have been selected as the input random variables which are as follows:

1. Specific heat
2. Conductivity
3. Air temperature amplitude
4. Reservoir top temperature amplitude
5. Reservoir bottom temperature amplitude
6. Elastic modulus of Concrete (Top)
7. Elastic modulus of Concrete (middle)
8. Elastic modulus of Concrete (bottom)
9. AAR maximum volumetric strain
10. Characteristic time (τ_c)
11. Latency time (τ_l)
12. Activation energy associated with τ_c (U_c)
13. Activation energy associated with τ_l (U_l)

As seen, the random variables can be categorized as concrete material properties, Air and water temperature inputs and the AAR model properties. It should be noted that the module of elasticity of concrete is considered to be variable through the height of the dam and thus, 3 different values have been considered for that. Figure 8.9 shows a matrix plot for the 13 random variables and their correlations. As seen the random variables each have a log-normal distribution with almost zero correlations.

In order to investigate the effect of sample size on the results, 3 samples with 50, 100 and 200 models are selected, analyzed, and the results are compared. Each model is analyzed for 50 years starting from 1980 when the first AAR effects was observed.

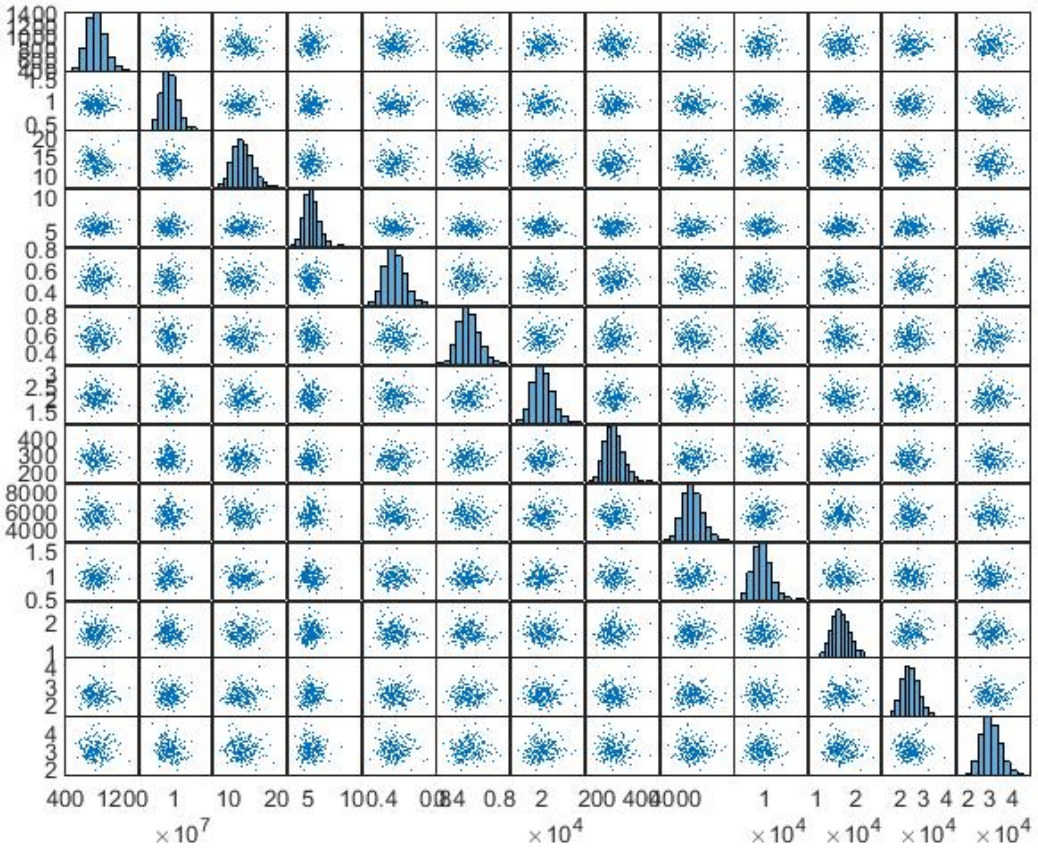

Figure 8.9: Matrix plot of the 13 input variables

Uncertainty Quantification of Stress Analysis

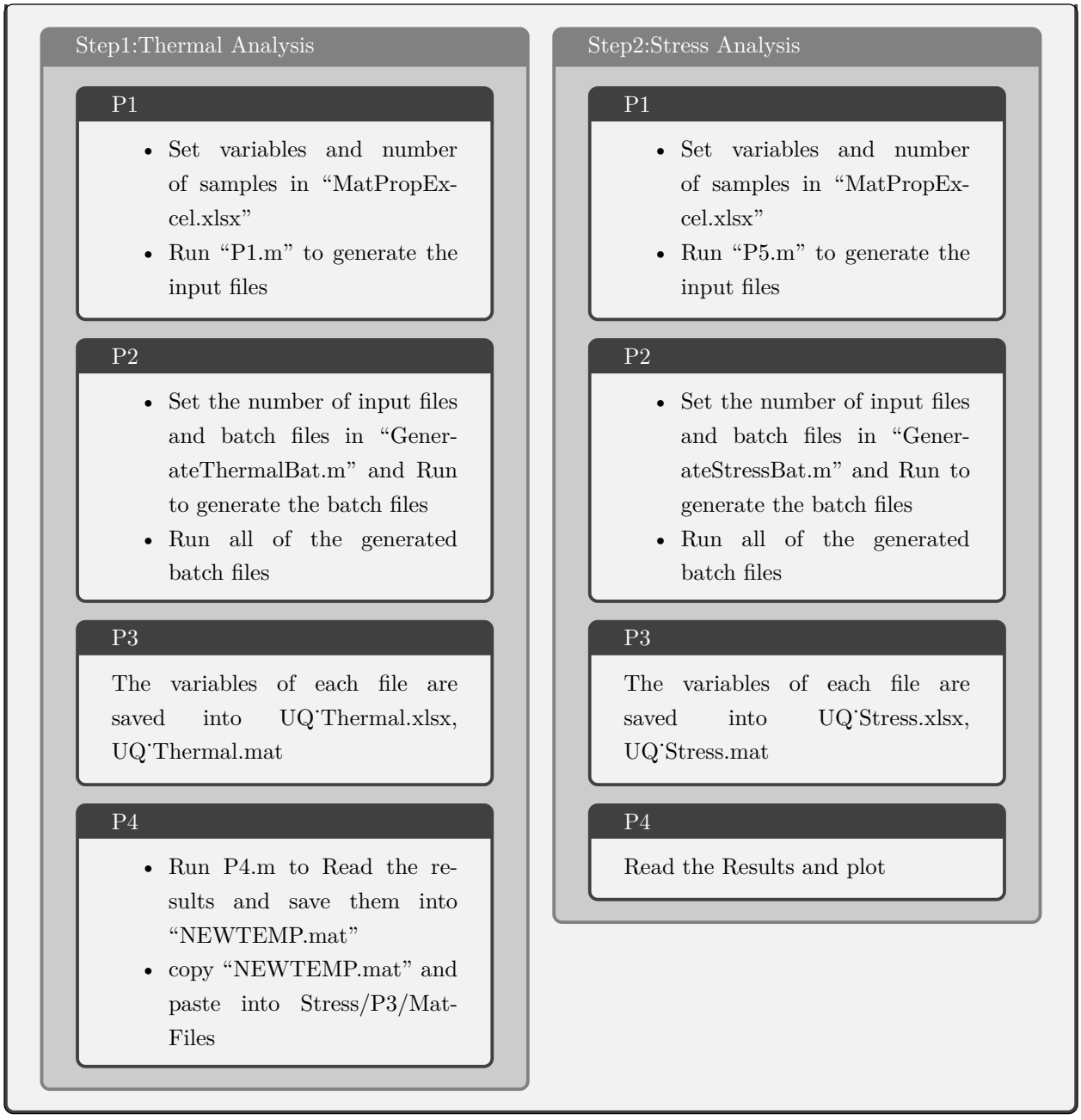
Step1:Thermal Analysis
P1
Set variables and number of samples in "MatPropExcel.xlsx"
Run "P1.m" to generate the input files
P2
Set the number of input files and batch files in "GenerateThermalBat.m" and Run to generate the batch files
Run all of the generated batch files
P3
The variables of each file are saved into UQ˙Thermal.xlsx, UQ˙Thermal.mat
P4
Run P4.m to Read the results and save them into "NEWTEMP.mat"
copy "NEWTEMP.mat" and paste into Stress/P3/MatFiles
Step2:Stress Analysis
P1
Set variables and number of samples in "MatPropExcel.xlsx"
Run "P5.m" to generate the input files
P2
Set the number of input files and batch files in "GenerateStressBat.m" and Run to generate the batch files
Run all of the generated batch files
P3
The variables of each file are saved into UQ˙Stress.xlsx, UQ˙Stress.mat
P4
Read the Results and plot

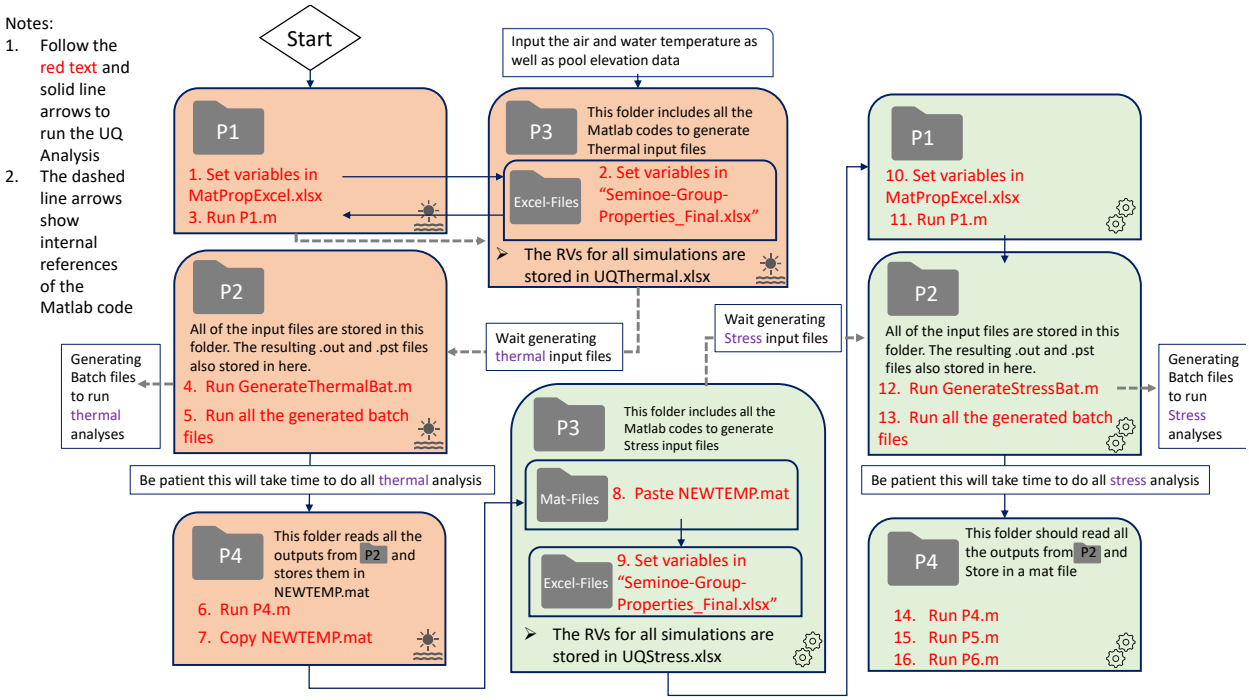

Figure 8.10: Flowchart of UQ Procedure

In order to present the displacements results 18 points at the rock-concrete interface and 2 points at the Crest are selected and to record the stresses in the body of the dam, in total 14 nodes have been chosen on the upstream and downstream sides which are shown in figure 8.11.

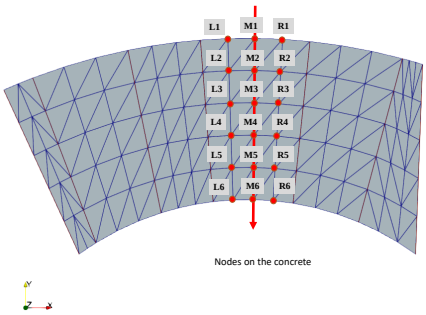

(a) COD

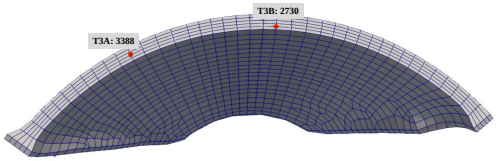

(b) Crest Displacement

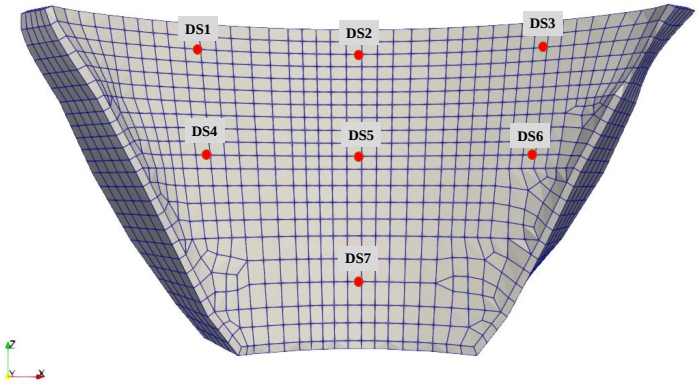

(c) Downstream,Stresses

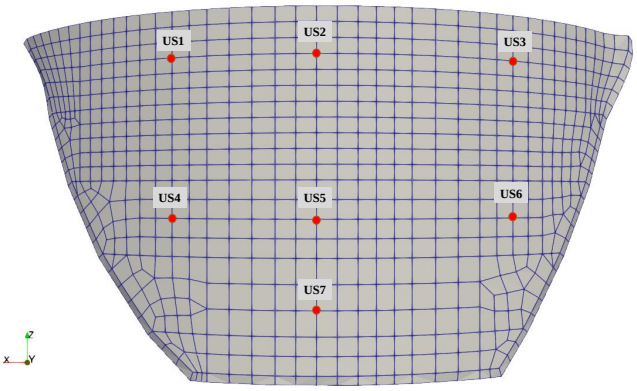

(d) Upstream, Stresses

Figure 8.11: Location of recorded nodes

8.2.1 Results

In this section the results of the uncertainty quantification, using 200 analysis sample, are demonstrated in terms of crest displacements and maximum principal stresses.

8.2.1.1 Displacements

Figure 8.12 shows the variation of the response of the nodes corresponding to the location of the T3A and T3B instruments in terms of the 2 horizontal and 1 vertical displcements as well as the mean and mean ± 1 standard deviation. As seen, the mean value of the most reliable recording (T3B in radial direction) is about 25 cm at the end of the analysis time which is in the December of 2030.

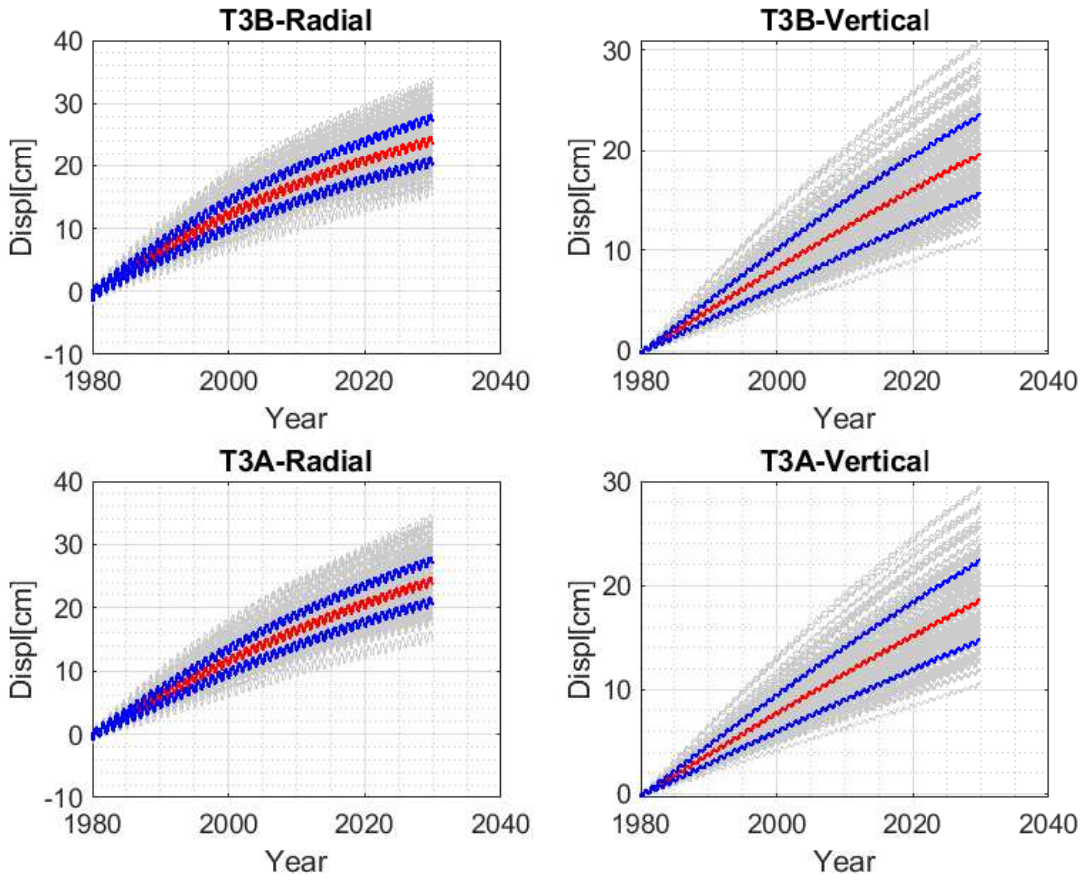

Figure 8.12: Crest Displacements (stream and vertical directions); (+ve is toward the upstream and upward)

8.2.1.2 Stresses

The maximum principal stresses for the 7 points on each side are shown separately in figure 8.13 and 8.14. The results suggest an overall higher stresses on the downstream side compared to the upstream.

It should be noted that the positive stress values indicates tension and thus at the points with higher stresses cracking can be expected. However, for the more detailed assessment of cracking a full nonlinear analysis is required.

To have a more clear interpretation of the results, the normalized maximum principal stresses with respect to the tensile strength of the concrete is plotted in figures 8.15 and 8.16. The higher ratios on the downstream side and the top nodes indicates that the concrete in that section will experience the cracking and as seen this is happening at earlier times for the top of the downstream side.

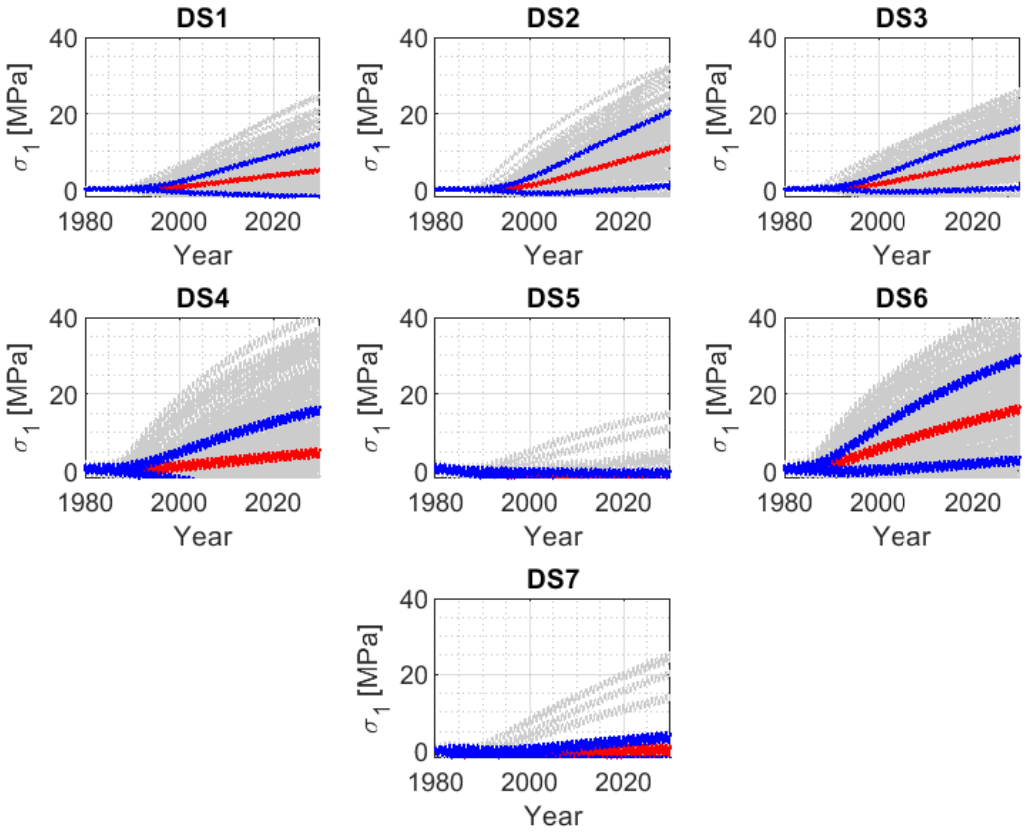

Figure 8.13: Maximum Principal Stress (+ve indicates tension); Downstream

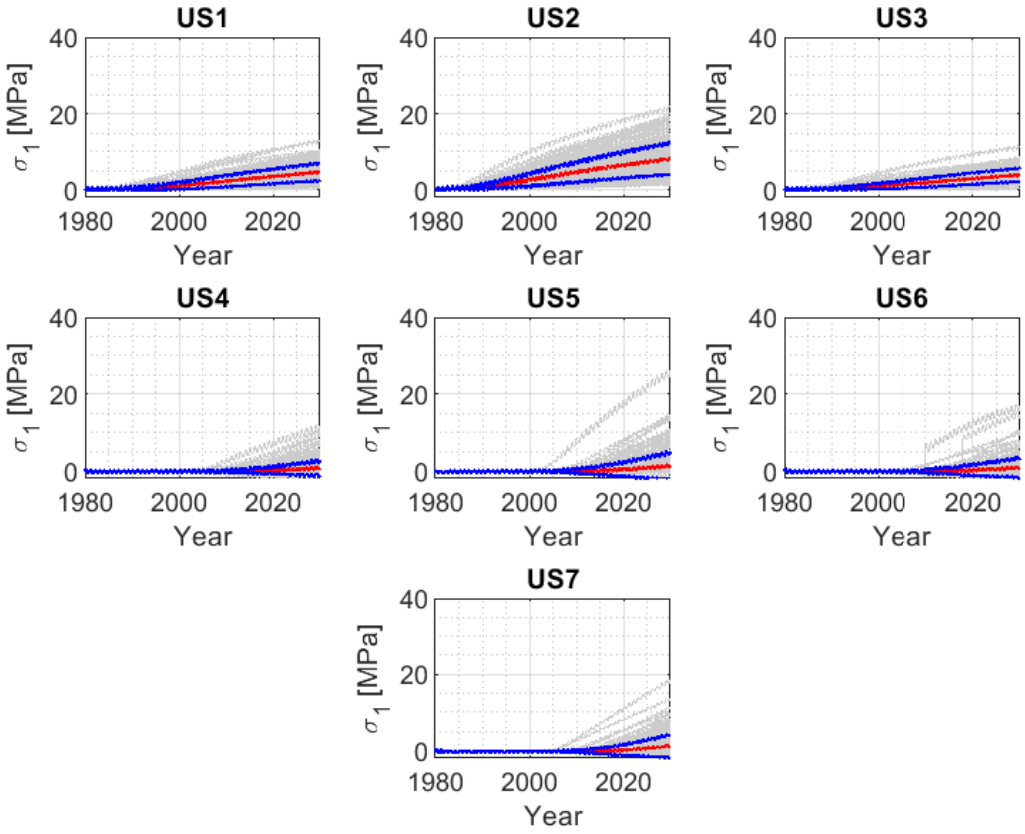

Figure 8.14: Maximum Principal Stres (+ve indicates tension)s; Upstream

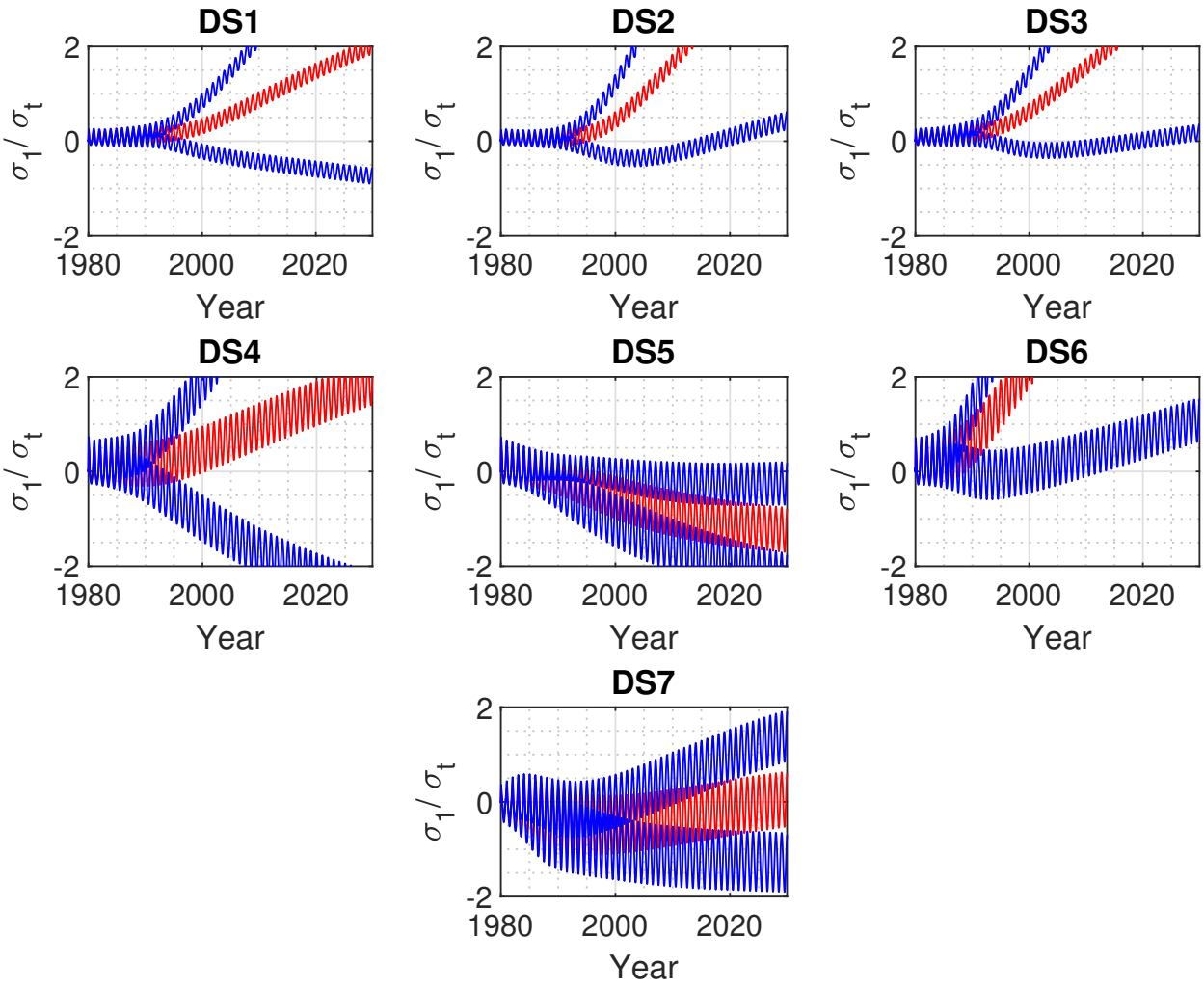

Figure 8.15: Normalized Maximum Principal Stress with respect to Tensile Strength(+ve indicates tension); Downstream

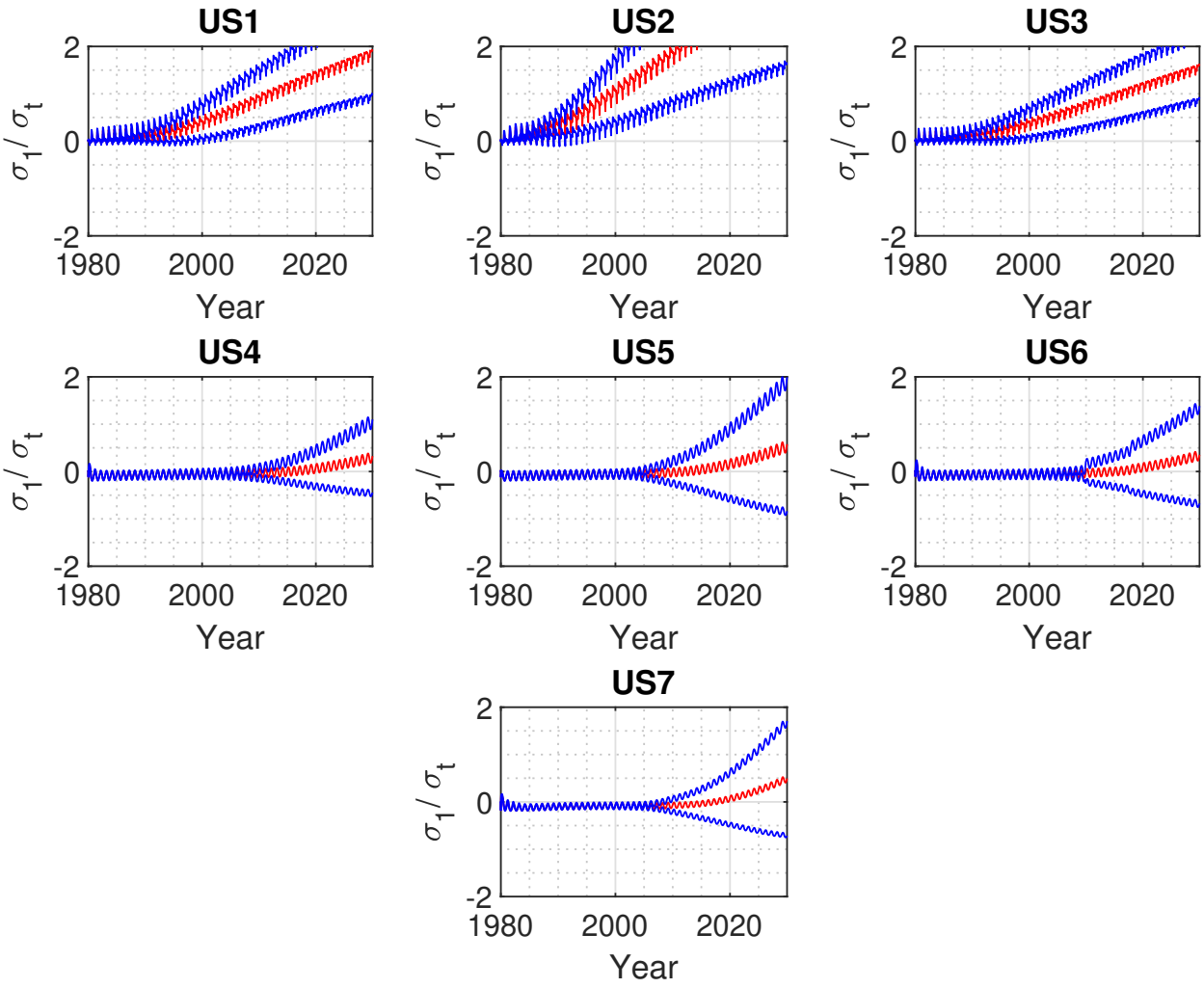

Figure 8.16: Normalized Maximum Principal Stress with respect to Tensile Strength (+ve indicates tension); Upstream

8.2.1.3 Probability of Exceedance

In order to determine the probability of exceedance from a certain limit state, the 2 methods have been selected to determine the fitting function using(**baker2015efficient**):

- Maximum likelihood Estimation: In this method the parameters are determined such that a certain distribution is most likely to produce the observed data. In the current study, the maximum likelihood estimation is used to fit a log-normal cumulative distribution function to the stress ratios in time (figure 8.17). In other words, the objective is to find the probability of the principal stresses exceeding the tensile strength at different time steps. For each specific point on the dam, at each time step t_j, a number of analysis out of total (200 analyses in this study) would result in the stress to exceed the threshold(tensile strength). Assuming 2 possible event: 1. exceed the threshold and 2. Not to exceed the threshold, the probability of observing z_j exceedance out of n_j analyses at each x_j can be determined by the binomial distribution:

$$P(z_j\text{exceedance in } n_j \text{ analyses}) \equiv \begin{pmatrix} n_j \\ z_j \end{pmatrix} p_j^{z_j} (1-p_j)^{n_j - z_j} \tag{8.1}$$

  where p_j is the probability that an analysis at time t_j will exceed the threshold. In order to find the likelihood of the whole data, the probabilities at all time steps are multiplied:

$$\text{Likelihood} \equiv \prod_{j=1}^{m} \begin{pmatrix} n_j \\ z_j \end{pmatrix} p_j^{z_j} (1-p_j)^{n_j - z_j} \tag{8.2}$$

  where m is the number of time steps. substituting the equation for log-normal CDF into the equation above We then have:

$$\text{Likelihood} \equiv \prod_{j=1}^{m} \begin{pmatrix} n_j \\ z_j \end{pmatrix} \Phi\left(\frac{\ln(x_j/\theta)}{\beta}\right)^{z_j} \left[1 - \Phi\left(\frac{\ln(x_j/\theta)}{\beta}\right)\right]^{n_j - z_j} \tag{8.3}$$

  As mentioned above the goal is to find the parameters so that the the distribution has the highest likelihood of representing the data. Thus the next step is to find the parameters that maximize the logarithm of the likelihood funtion, since it is easier, therefore we have:

$$\begin{aligned} \left\{\hat{\theta}, \hat{\beta}\right\} \quad \equiv \quad & \underset{\theta,\beta}{\text{argmax}} \sum_{j=1}^{m} \left\{ \ln \begin{pmatrix} n_i \\ z_j \end{pmatrix} + z_j \ln \Phi\left(\frac{\ln(x_j/\theta)}{\beta}\right) \right. \\ & \left. + (n_j - z_j) \ln \left[1 - \Phi\left(\frac{\ln(x_j/\theta)}{\beta}\right)\right] \right\} \end{aligned} \tag{8.4}$$

  All these procedure is followed using the code by (**baker2015efficient**).
- Sum of squared errors: This method is based on minimizing the sum of squared errors (SSE) between the observed data and predicted ones.

$$\left\{\hat{\theta}, \hat{\beta}\right\} \equiv \underset{\theta,\beta}{\text{argmin}} \sum_{j=1}^{m} \left[\frac{z_j}{n_j} - \Phi\left(\frac{\ln(x_j/\theta)}{\beta}\right)\right]^2 \tag{8.5}$$

In the current study the probability of exceedance of maximum principal stresses from the tensile strength is shown in figures 8.18 and 8.19.

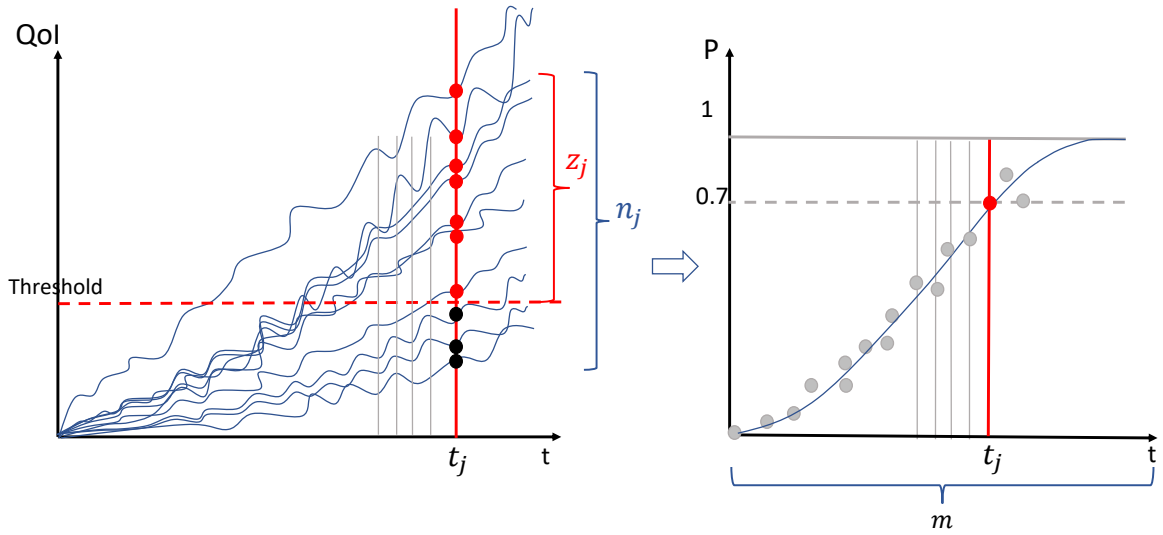

Figure 8.17: Schematic curve fitting procedure

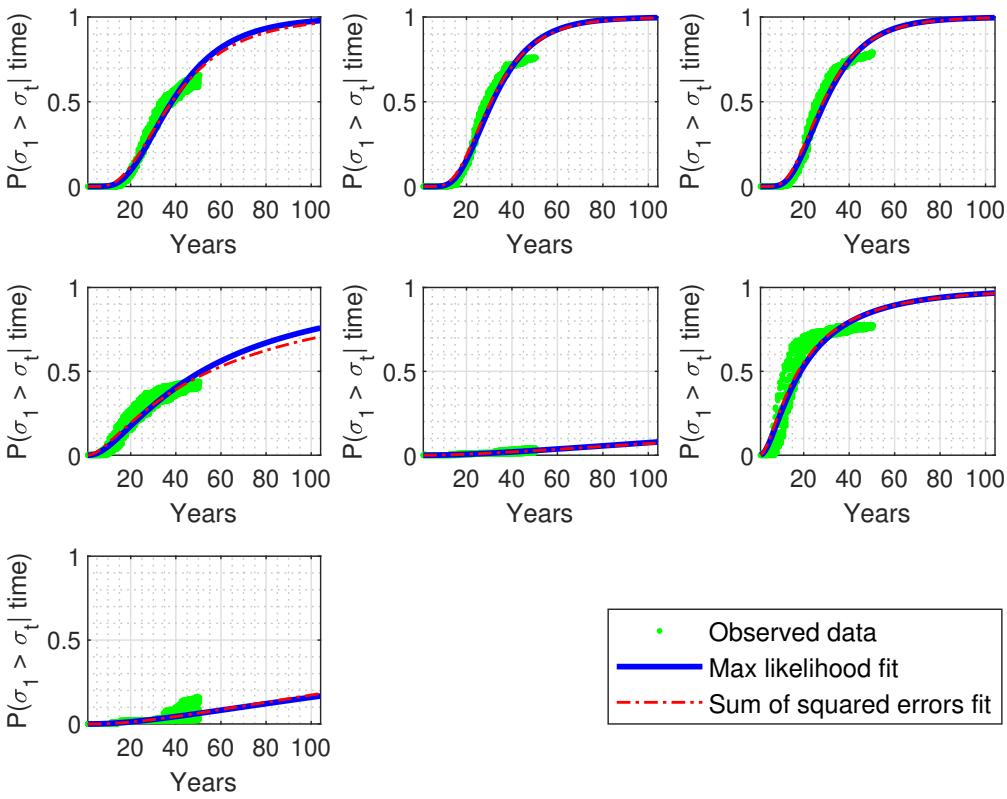

Figure 8.18: Probability of Exceedance; Downstream

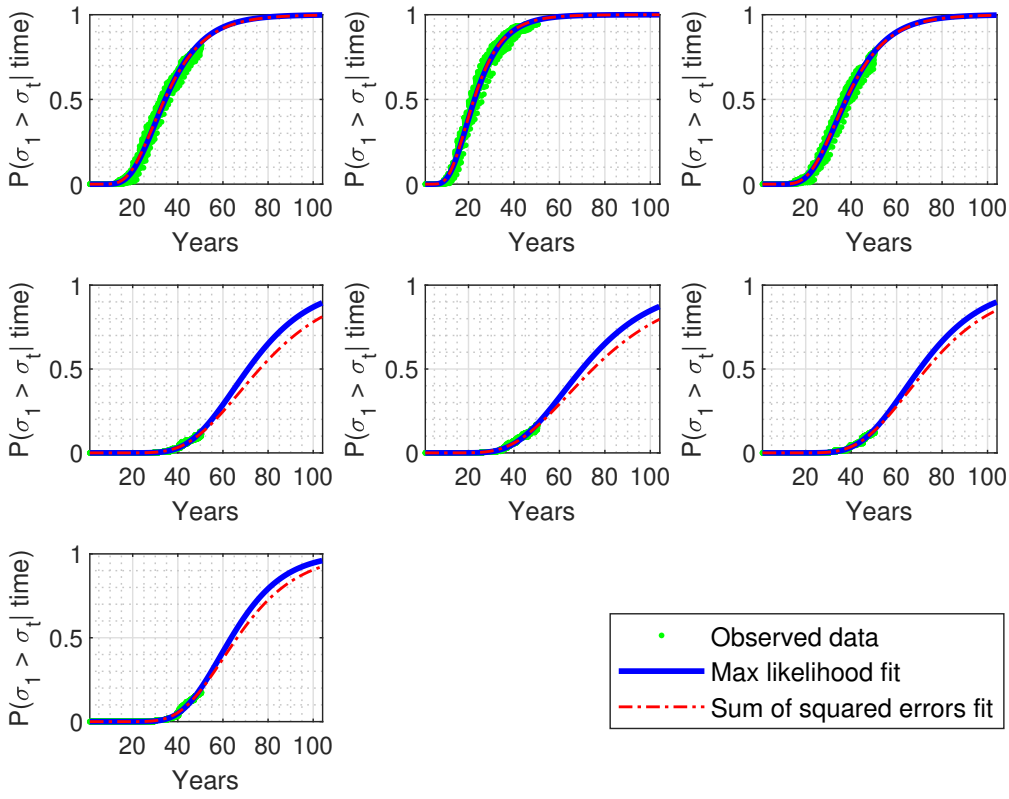

Figure 8.19: Probability of Exceedance; Upstream

8.2.1.4 Comparison of 3 sample sizes

As stated in the previous sections the uncertainty quantification was performed for 3 different samples with 50, 100 and 200 models. The standard error in terms of crest displacement and nodal stresses is calculated and plotted as a function of time. The standard error is a measure of how close the mean of each sample is likely to be to the true data mean. When the standard error increases, it is more likely that the sample mean is not a correct representation of the true data mean which can be determined using the following equation (**james2013introduction**):

$$SE = \frac{\sigma}{\sqrt{n}} \tag{8.6}$$

Where n is the sample size and σ is the standard deviation.

looking at the standard errors, shown in figure 8.20 of crest displacements and stresses, one can conclude that the 100 analysis is providing a far better estimation of the real model compared to the 50 analysis while the 200 analysis is less effective in improving the results of 100 analysis. Furthermore, the analyses indicate that, as expected, the 3 samplings result in similar mean value curve while their standard deviations are different.

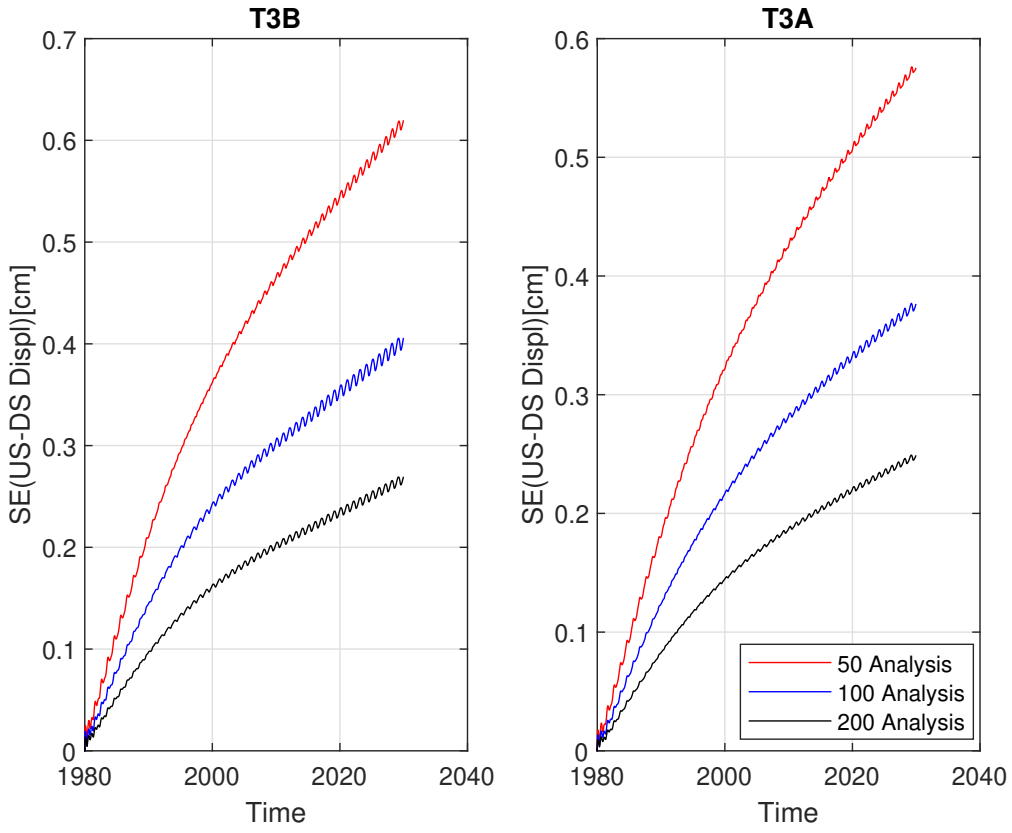

(a) Standard error

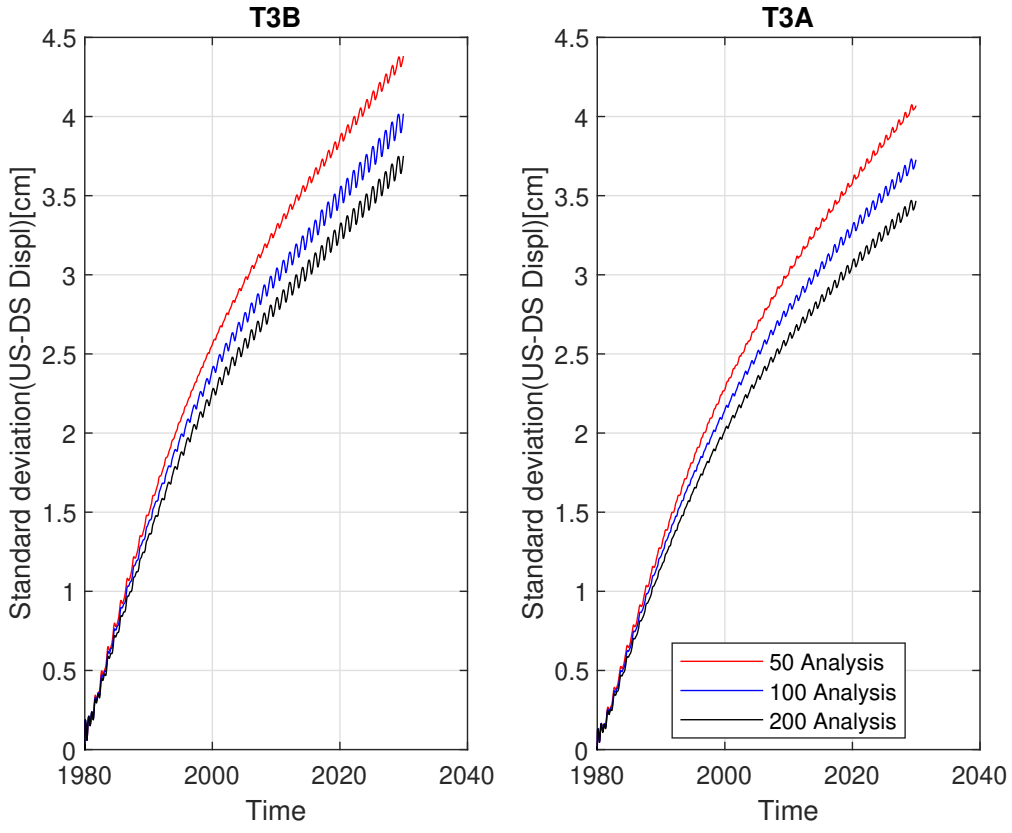

(b) Mean

Figure 8.20: Standard Error and Standard deviation curves of T3A and T3B US-DS displacements

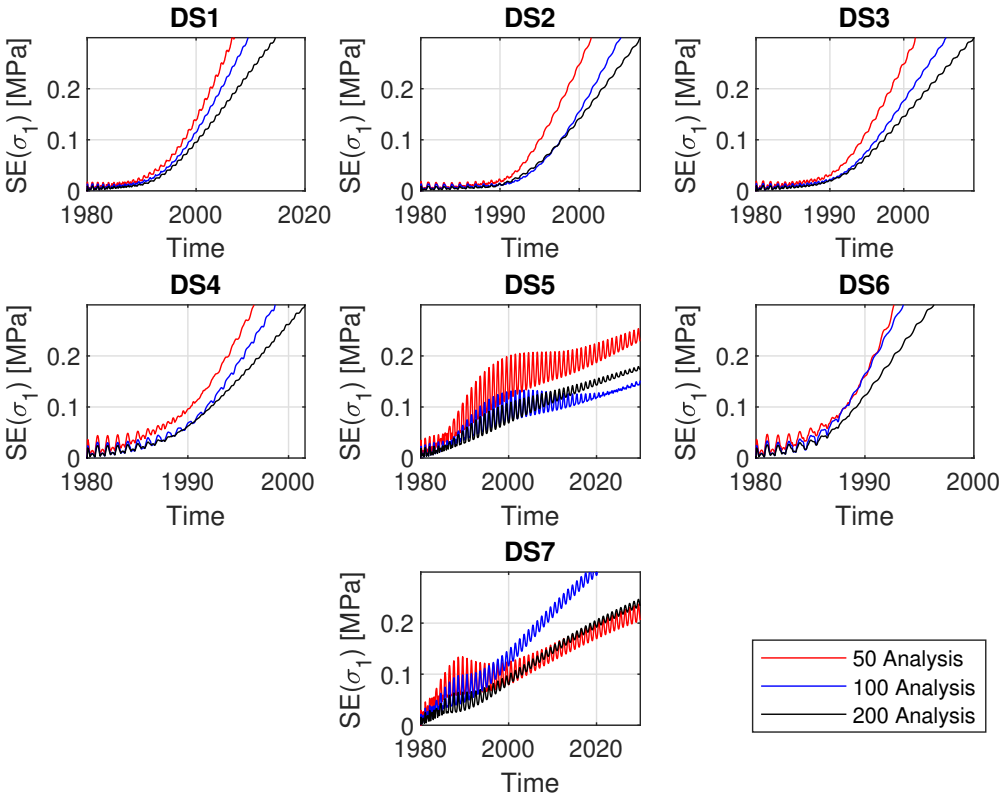

Figure 8.21: Standard Deviation; Downstream

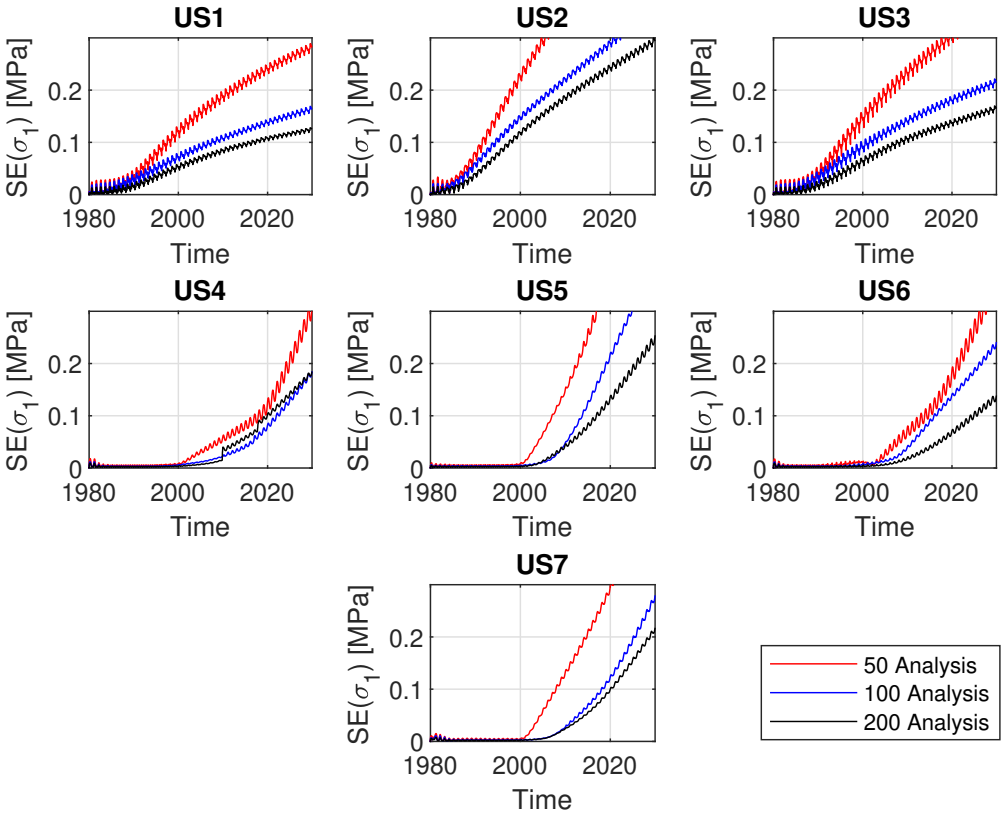

Figure 8.22: Standard Deviation; Upstream

Chapter 9

Conclusion and Recommendation for Future Work

Abstract

This final chapter will, very succinctly, summarize the findings of this research and make few recommendations for future work.

9.1 Conclusion

As discussed in the previous chapters from a deterministic nonlinear AAR analysis it can be concluded that:

- The cracking is mostly occurred on the lower portion and inside the dam.
- In general there is more AAR at the downstream side of the dam compared to the upstream.
- Downstream side of the dam is more in tension which can be an indicative of potential cracking.

The findings of the uncertainty quantification can be summarized as follows:

- Stresses : Mean values of the normalized stresses with respect to the tensile strength on the downstream and upstream sides indicate that there is a possibility of cracking occur:
  - at the top center and right side of the downstream starting about year 2005
  - at the top left side of the downstream starting about year 2015
  - at the mid height right side of the downstream starting about year 2020
  - at the mid height left side of the downstream starting about year 2020
    while it wouldn't be a concern at other heights of the center of the dam on the downstream.
  - at the top right side of the upstream starting about year 2020
  - at the top left side of the upstream starting about year 2015
  - at the top center of the upstream starting about year 2000
    while the stresses are lower than our concerning limit in the mid-height and bottom of the upstream.
- Probability of Exceedance
  - The probability of exceednace of the maximum principal stress (σ_1) from the concrete tensile

strength can be interpreted as a possibility of cracking at a certain point. As seen the 50% probability of exceedance at the top mid portion of the dam happens after about 30 years of analysis (year 2010) on the downstream and after 20 years of analysis (year 2000) on the upstream. Overall, the stress values have higher probability of exceeding the threshold on the upstream compared to downstream at the top of the dam. However, the mid-height of the dam is showing a higher probability of exceedance on the downstream side while on the upstream side the 50 % probability of exceednace is likely to occur around 70 years of analysis(year 2050)

- Effect of Sample size
  - The number of analysis chosen for the uncertainty quantification has to be determined to be a good representative of the true data. To this aim, the uncertainty quantification has been repeated with 3 different sample sizes of 50, 100 and 150 analyses. The comparison of the results from the 3 samples indicate that the 100 analyses sample can provide a relatively better estimation compared to the 50 analyses sample however this improvement is not as significant when it comes to the comparison of the 200 and 100 analyses samples. As seen in figure 8.20 the T3B and T3A horizontal displacement have standard error of about 2.5 mm at the end of the analysis time which can be even more reduced by increasing the number of analyses.
  - Comparing standard errors for stress (figures 8.21 and 8.22) shows that the 200 analyses sample is slighlty better than the 100 and thus increasing the number of analysis will not probably improve the accuracy of the model.

9.2 Recommendation for Future work

- Horizontal joints
- Laboratory Data for AAR compatible with finite element analysis
- Reliable field measurement of water temperature from top to bottom
- Field measurements of *in-situ* stresses
- Seismic analysis (Soil structure interaction, free field)
- Seismic fragility curve
- Complete detailed risk assessment, Fig. 9.1
- Uncertainty quantification with nonlinear analysis (though this may require extensive computational support).
- Add downstream tensile stresses to the list of parameters that have to be reconciled between analysis and field observations.

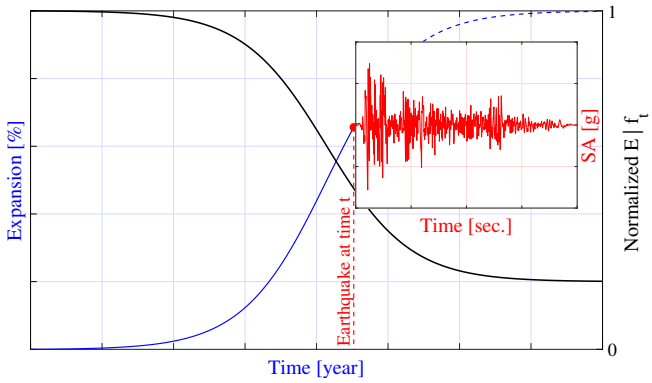

Figure 9.1: Earthquake occurring after substantial AAR expansion

Appendix A

Case Study Description

Abstract

This Appendix provides general information on the Seminoe Dam itself, and the recorded data by USBR. In the first section the geometry and location of the dam as well as the physical model is described. Second part is to provide the survey data from tilt measurements, joint meter data and geophysical investigations. Moreover, the test results of concrete material properties are illustrated in this chapter. The measured temperatures as well as pool elevation variation data is provided herein.

A.1 Dam Description

Seminoe Dam, Fig. A.1, is a concrete arch dam located on the North Platte River about 31 miles northeast of Rawlins, Wyoming. The dam was completed in 1939 with a structural height of 90 m (295 ft), a hydraulic height of 63 m (206 ft), a crest length of 161.5 m (530 ft) at el 1938m (6,361 ft), and a total concrete volume of 210,000 cu yd. The reservoir provides water storage for irrigation, hydroelectric power generation and recreation.

The arch dam has a crest width of 6.4m, a maximum base width of 26 m, a 88 m radius for the vertical upstream face, a variable radius for the sloping downstream face, and 1m high concrete parapet walls to el 1940.

The dam was constructed in one construction season. Construction started on January 19, 1938, and it was completed on November 28, 1938.

Seminoe Dam is experiencing concrete expansion, cracking and deterioration due to alkali-silica reaction (ASR) and freeze-thaw damage.

Key dimensions are given in Table A.1.

A.2 Instrumentation

In the following section, reference will be made to various locations inside the dam where measurements were taken. Coordinates of those points are given in Table A.2.

Table A.1: Seminoe Dam dimensions

Structural height (m)	89.9
Hydraulic height(m)	62.8
Crest elevation(m)	1938.8
Crest width(m)	5.2
Roadway width(m)	4.9
Top of parapet wall elev.(m)	1939.9
Crest length(m)	161.5
Volume(yrd^3)	52120.8
Base thickness(m)	25.9

Table A.2: Core recovery locations

Instrument	**Station**	**R** m	θ deg	**X** m	**Y** m
DH-1		87.24	33.4	48.0	72.8
DH-2		87.24	0.75	1.1	87.2
DH-98-1	1+42	87.24	33.4	48.0	72.8
DH-98-2	2+31	87.24	17.5	26.2	83.2
DH-98-2A	2+29	87.24	17.5	26.2	83.2
DH-98-2B	2+26	87.24	17.5	26.2	83.2
DH-98-3	3+07	86.09	0.75	1.1	86.1
DH-98-4	3+15	87.24	0.75	1.1	87.2
DH-98-5	5+13	84.94	-38.625	-53.0	66.4
DH03-01	4+97	87.24	-36.25	-51.6	70.4
DH03-02	4+68	86.09	34.125	48.3	71.3
DH03-03	3+00			0.0	0.0
DH03-04A	4+40			0.0	0.0
DH-09-1		86.09	-38.125	-53.2	67.7
DH-09-2		86.09	-36.25	-50.9	69.4
DH-09-3		86.09	0.75	1.1	86.1
DH-09-4		86.09	12.5	18.6	84.0
DH-09-5		86.09	41.6	57.2	64.4
DH-13-1	5+29	86.09	-38.125	-53.2	67.7
DH-13-2	4+80	86.09	-38.625	-53.7	67.3
DH-13-3	2+98	86.09	3.375	5.1	85.9
DH-13-4	2+98	86.09	12.5	18.6	84.0
DH-13-5	1+23	86.09	33.5	47.5	71.8
T-1A		86.09	-38.125	-53.2	67.7
T-1B		86.09	30.8	44.1	73.9
T-2		86.09	10	14.9	84.8
T-3A		86.09	-38.375	-53.4	67.5
T-3b		86.09	0.75	1.1	86.1

Figure A.1: Seminoe Dam

A.3 Geophysical Investigation

This part is from Hatch report

In order to determine the in situ properties of the concrete, a geophysical borehole investigation is performed at Seminoe in 2010. Table G.1 presents a summary of the obtained data using different tools.

These results will not be used in this report.

A.4 Irreversible Displacement Measurements

Of particular relevance to this study are the field measurements of irreversible displacements. Whereas those are the most undeniable signs of internal swelling (ASR in this case), but they would also constitute data sets for calibration and verification of the models.

Figure A.2 and A.3 show the location of the various measurement locations. It should be noted that T3A, T3B, and T2 are located on the crest, whereas BC L-3 is located on top of the trachrack of the middle penstock.

A.4.1 Crest Displacements

A top of dam survey survey is presented in the form of elevations measured at selected locations at the top of the dam in (**Pdf-Drawing**). It also show locations of survey tacks and previous investigation drill holes.

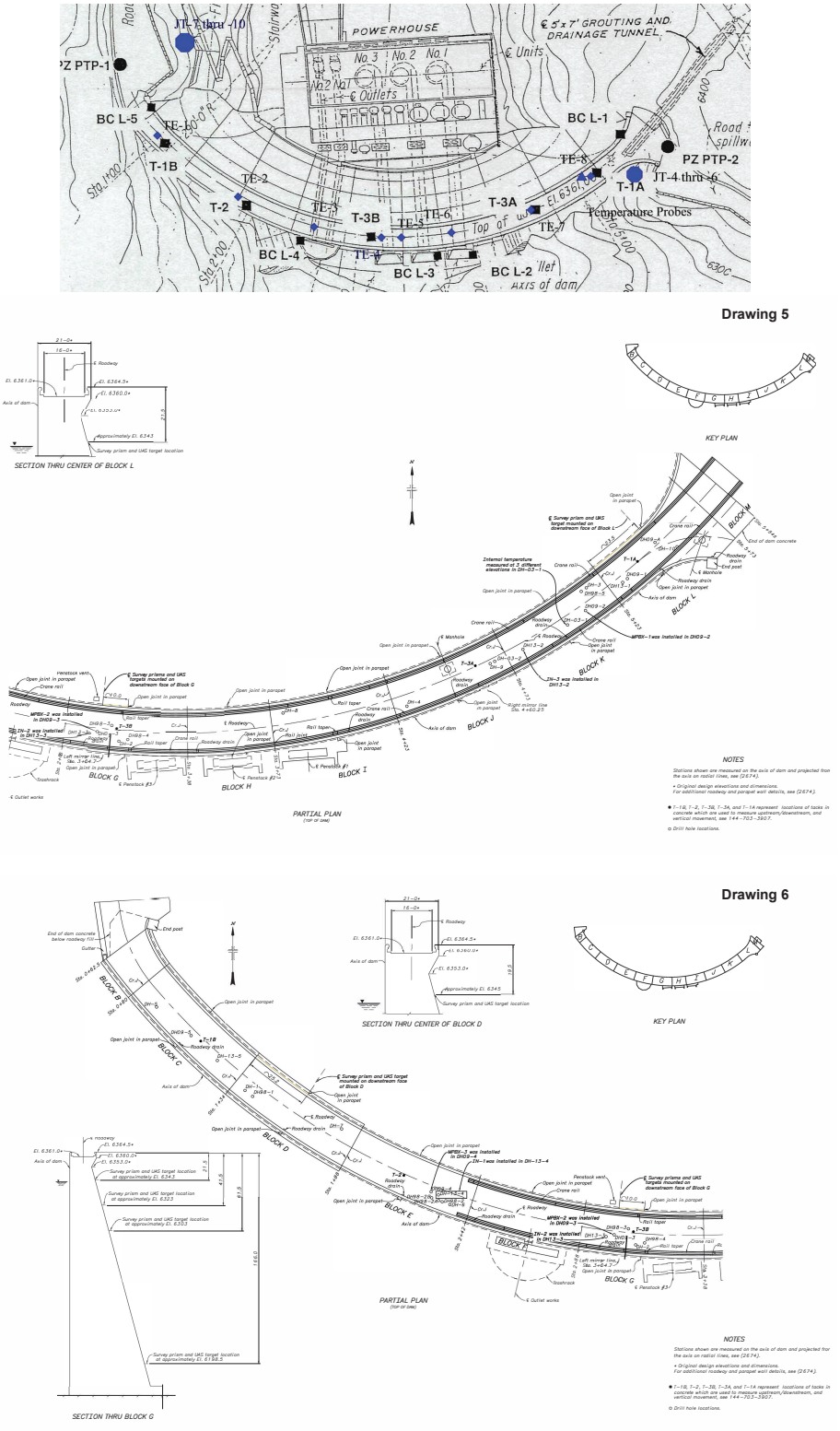

Figure A.2: Location of core extractions

Figure A.3: Pictures showing key instruments

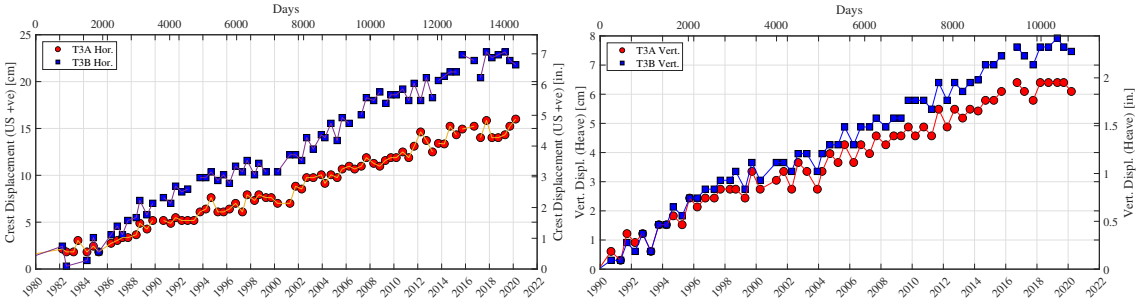

(a) Crest upstream

(b) Crest settlement

Figure A.4: Irreversible measurements

A.4.2 Tilt measurements of upstream face

in 2012 a survey, consisting of hanging a plumb bob on the upstream face of the dam and measuring the distance from plum to the face of the dam, was conducted (**lung2012**), Figure A.5. The verticality survey was completed at the same three locations as the 2002 one. The first location was dam station 4+60, the second at station 3+04, and the third at station 2+18. To make direct comparisons between the two surveys the measurement at the 0 point, at the parapet wall, was subtracted from all measurements below. The survey results are presented in Table G.3 and plotted for the three stations in figure A.6. However,

Figure A.5: Climb Team members measuring upstream dam face to plumb line (**lung2012**)

Reclamation informed us that those readings may not be as reliable as the measured crest displacements, and thus will not be used.

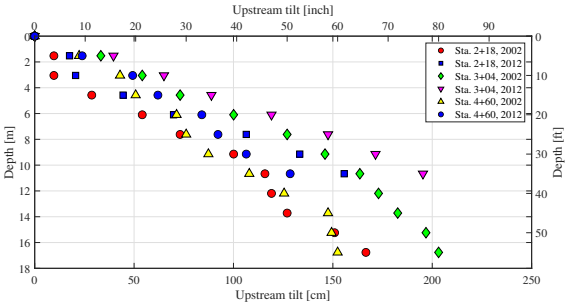

Figure A.6: Plumbline tilting Measurements

A.4.3 Tape Extensometers at Top of Dam

Analysis of measurements from tape extensometers at Top of Dam from 2004 to 2014 are shown in Table G.4. The annual growth rates from the four extensometers TE-3 to TE-6 are very close and consistent, however the tape extensometers are much more erratic than one would expect based on Reclamation experience from other projects. This may be due to issues with temperature correction of measurements. The tape extensometer measurements are providing reasonable overall estimates of rates of movement.

However, Reclamation informed us that those readings may not be as reliable as the measured crest displacements, and thus will not be used.

A.4.4 Abutment Joint Meter Data

Joint meters were installed at the crack on upper right abutments to monitor the crack movement, table G.5. However, this data was not used in our analysis.

A.5 Uplift/Piezometer Readings

Seminoe being an arch-gravity dam, uplift pressures may not be as relevant as if it was a gravity dam, yet more relevant than for regular arch one. In the absence of piezometer readings, one would assume uplift to be linearly distributed from the upstream headwater pressure to the downstream tailwater one (with some corrections if there was a functioning drain). On the other hand, The availability of piezometers allows for a correction of computed uplifts, as the two sets can be compared.

In Seminoe three lines were considered, Fig. A.7(a) **PrsnlJerzy-2-12-21**.

Line 1 lies below the foundation treatment gallery in blocks E and F (between stations 1+88 and 2+88), and consists of four vertical pipes from the gallery floor (A, B, C, and D).

Line 2 lies beneath block G (between stations 2+88 and 3+38), and consists of one vertical pipe from the gallery floor (B), two horizontal pipes from the gallery walls (A and C), and one vertical pipe from the downstream toe (D).

Line 3 lies beneath block I (between stations 3+73 and 4+23), and consists of four pipes having a similar configuration as for line 2. Foundation uplift pressure measurements are taken from pressure gauges.

However, there were two major impediments for the use of the piezometer readings in the context of this investigation:

1. The piezometer readings were taken at an elevation lower, Fig. A.7(b) than the one considered in the finite element discretization (6125').
2. The peizometer readings are too "coarse", Fig. A.7(c) to enable consideration of one representative year. In their present form, the readings are better suited to ensure their operation over time.

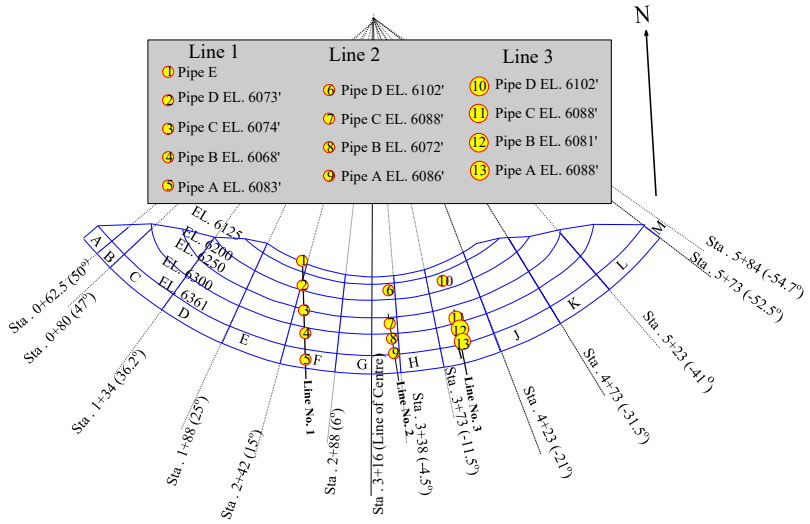

(a) Locations of piezometers adapted by Y. Gakuhari from 144-D-1932

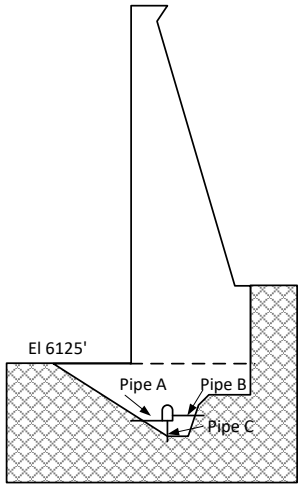

(b) Location of pipes

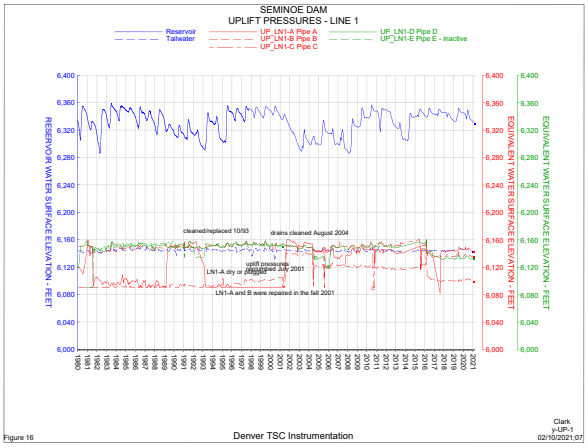

(c) Representative piezometer readings

Figure A.7: Piezometer readings

A.6 Concrete Testing Data

A.6.1 Petrography

A.6.1.1 1973 Study

Petrography analysis conducted in 1973 was on four rock outcrop hand specimens from Seminoe abutments. The location of the samples are from elevation 6370, 6365 and 6385. The analysis was conducted to determine the rock type and its physical condition.

A.6.1.2 2014 Study

The samples for the conducted petrographic study (**usbr-seminoe-petrography**) is shown in figure A.8. A plot of the 2013 compressive strength data compared to depth is presented in figure A.9, which shows that the compressive strength has a great amounts of scatter.

(a) The general condition of concrete core DH-13-2, at depths greater than 5.4 feet for comparison

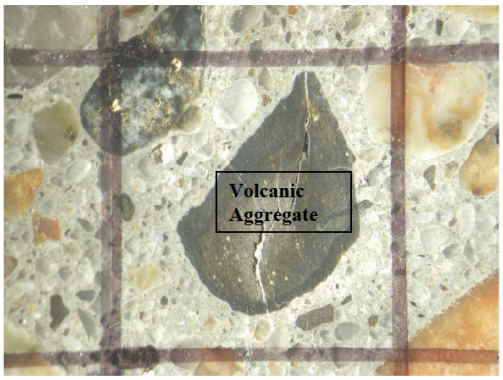

(b) Sample polished surface with 10x10 mm grid

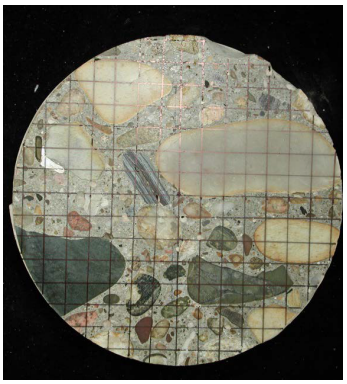

(c) Reactive volcanic aggregate with internal cracks filled with alkali-silica gel with the cracks penetrating paste

Figure A.8: Petrographic study (**usbr-seminoe-petrography**)

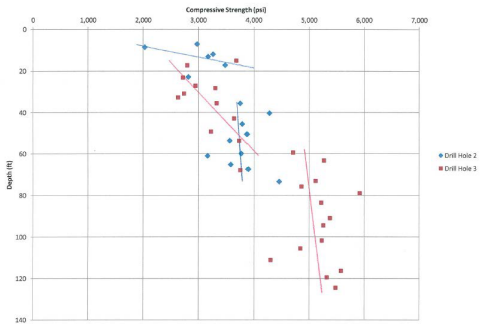

Figure A.9: 2013 Compressive strength data from petrographic study (**usbr-seminoe-petrography**)

A.6.2 Elastic Modulus and Compressive Strengths

Cores were extracted in 1975, 1999, 2003, 2009-2013, from locations shown in Fig. A.10. Coordinates of instrument location is tabulated in Table A.2.

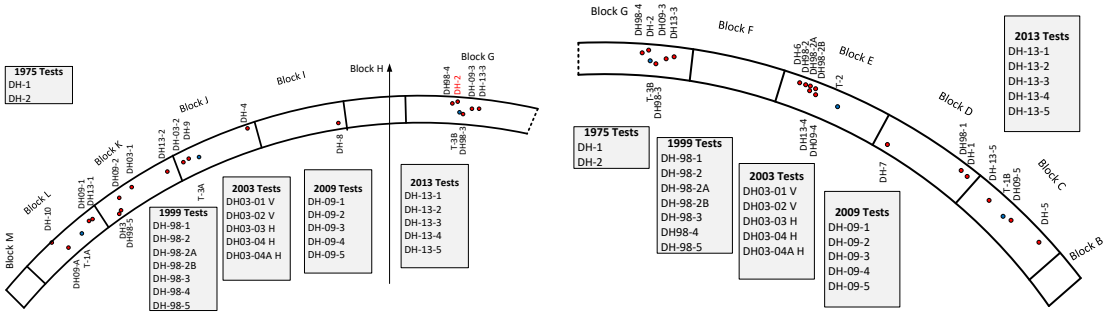

(a) Right (b) Left

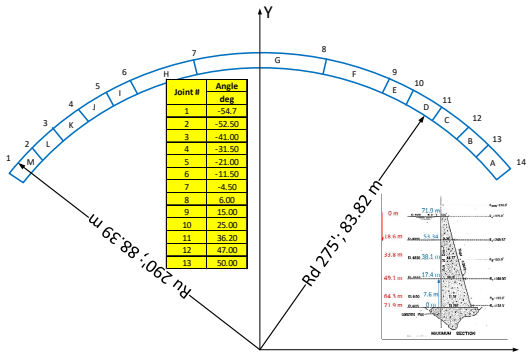

(c) Blocks

Figure A.10: Location of core extractions

DH-03-1 and DH-03-2 were drilled from the top of the dam, Fig. A.11, DH-03-01 is the closest arrow in the photograph (**Touseull03**).

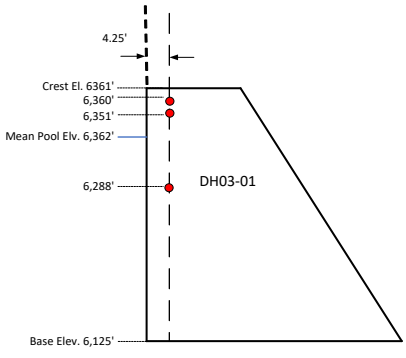

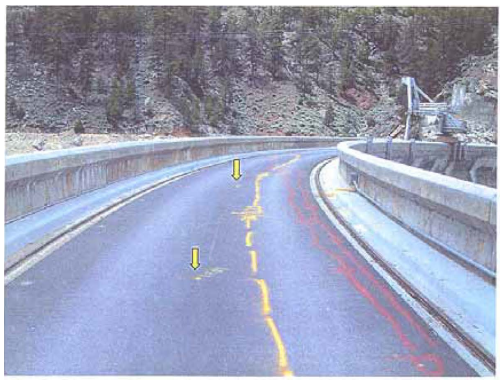

(b) (**Touseull03**)

Figure A.11: Location of DH03

A.6.2.1 Early Age

*Adapted from (***Dolen99***)*

Table A.3: Original mix design (**hubert42**)

Cement	376	lb/yd^3
Water	203	lb/yd^3
Sand	1062	lb/yd^3
Coarse Aggregate	2550	lb/yd^3
Entrapped Air	1%	

The concrete mixture proportions cited in the Final Report on Construction of Seminoe Dam and Power Plant (**hubert42**) are based on weight relationships of one part cement to 0.54 parts water to 9.61 parts aggregate. The coarse aggregate to sand ratio was 2.4 to 1 by weight. The mass concrete does not air-entrainment, and has a total air content of about 1 percent by volume.

Mass concretes from this era typically had about one barrel (376 lb) of cement per cubic yard of concrete. Mass concrete mixtures are also reported in the pre-construction report, Aggregate and Concrete investigations for Seminoe Dam - Kendrick Project, 1938. Based upon these reports and assumptions for the density of the cement and aggregates, the estimated mixture proportions are given by Table A.3.

According to (**hubert42**), "This mix gave a resulting 28-day (compressive) strength of 5,000 psi for all test cylinders broken". The test cylinders were likely six - by- twelve inch test specimens obtained by wet screening the plus 1-1/2 inch coarse aggregate from the mass mix.

A.6.2.2 1975 Tests

Tests were performed on 24 concrete core, 1-7/8-inch in diameter, 12 each from DH-1 (vertical) and DH-2 (15° from vertical). These holes were drilled from top of dam, elevation 6,361 feet, and elastic mulis were measured at 6.9 MPa (1,000 psi).

As reported

> *Selection of samples for tests involved avoiding large aggregate particles, and obtaining uniform occurrence of smaller rock pebbles to provide companion test specimens. The aggregate size visible on the surface of core specimens actually ranged from 0.3 to 1.8 inches. As table G.6 shows, values of E are in the low to medium range. These values may not be truly representative of the mass concrete in the dam because of the small specimen size in relation to MSA. On the other hand, the concentration of pebbles exposed on the surface adjacent to the strain gages appears to have an influence on modulus values. A visual inspection of the specimens indicated lower moculus values were measured as the concentration of pebbles increased.*
>
> *Compressive strength ranged from 33.8 to 51.0 MPa (4,900 to 7,400 lb/in^2) for about 80 percent of the specimens. The lower strengths for about 20 percent of the specimens were due to initial rock pebble breakout at low loads as indicated in table G.7. These pebbles were possibly affected by drilling or were shallowly embedded portions of aggregate particles.*

The test results for module of elasticity and the unconfined compressive strength are shown in table G.6 and G.7 respectively. It can be seen that the compressive strength varies mostly from 4,900 to 7,400 lb/in^2.

Those measurements are further illustrated by Fig. A.12.

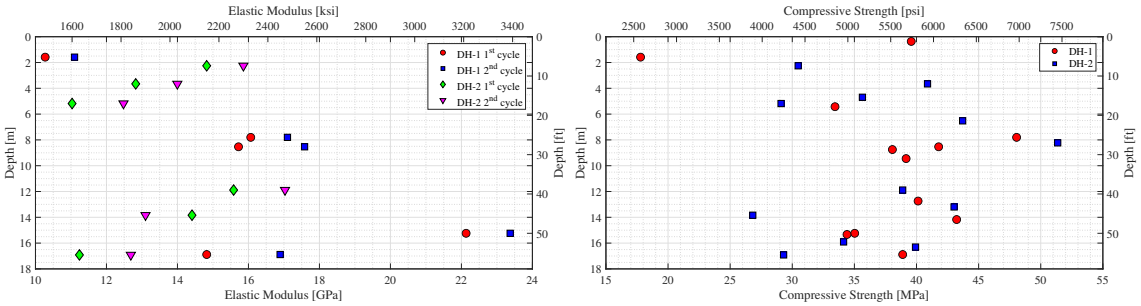

Figure A.12: 1975 Concrete test results

A.6.2.3 1999 Tests

Dolen99empty citation report a testing program that took place in 1998 consisting of coring and testing as it was already known that AAR and freeze-thaw damage has been taking place.

This is probably one of the best testing report for Seminoe dam. Its main conclusions were:

1. All drilled core exhibits signs of deterioration due to AAR and possibly freeze-thaw damage. Cores were severely micro fractured from the crest of the dam to its maximum depth of 15.2 m (50 feet). Approximately forty percent of the core from top 3.0m (10 feet) of the dam was recovered as rubble. Most of the intact core measured no longer than eighteen inches due to the frequency of rubble zones. Many aggregates are disbonded from the paste or fractured. White, gel-like extrusions, typical of AAR, have formed in cracks in the aggregate and at many of the paste-aggregate bonds. Although the deterioration appears most severe in the top 4.6 m (15 feet) of the structure, fractures and disbonded aggregate resulting from AAR are visible throughout the full length of the cores.
2. The average compressive strength of 34 specimens representing intact, testable concrete is 24.6 MPa (3,580 psi) with a coefficient of variation of 21%. This is about 58% of the expected strength and about 77% of the average strength of the 1980 test specimens. Furthermore, the 1998 averages include significantly more samples selected from the lower depths of the dam, where the concrete presumably is in better condition. About 40 % of the top 3.0 m (10 feet) of core and about 15% of the core below 3.0 m (10 feet) was comprised of deteriorated concrete that was of too poor quality to test. These deteriorated zones have little or no compressive strength and are not included in the average test results because they are not testable. If the deteriorated zones are included in the test results, the average compressive strength is about 19.4 MPa (2,820 psi).
3. The average modulus of elasticity of 32 specimens is 11.9 GPa (1.72×10^6 psi), with a coefficient of variation of 32%. This value is approximately the same as the average value of the 1980 test results. However, it is about one-third of the modulus of elasticity expected for the darn based on preconstruction test data. Reduction of modulus of elasticity is often an indication of ongoing AAR.
4. The strength of the intact, testable concrete increases with depth. The average compressive strength at various depth intervals from the crest is 20.9 MPa (3,030 psi) from zero to 3.0m (10 feet), 26.6 MPa (3,850 psi) from ten to 7.6 m (25 feet), and 25.9 MPa (3,760 psi) from 7.6 m to 215.2 m (25 to 50 feet). The average modulus of elasticity at these depth intervals is 9.7 GPa (1.41×10^6 psi) from zero to 3.0 m (10 feet), 11.9 GPa (1,730,000 psi) from 3.0 to 7.6 m (10 to 25 feet), and 13.6 GPa (1.97×10^6 psi) from 7.6 to 15.2 m (25 to 50 feet).
5. The rate of deterioration, based on material properties, appears to increase with depth. Since 1980, the compressive strength has decreased 18% in the top 3.0 m (10 feet), 23% from 3.0 to 7.62 m (10 to

25 feet), and 43% from 7.62 to 15.2 m (25 to 50 feet). The modulus of elasticity has dropped seven percent in the top 3.0 m (10 feet), 12 percent from 3.0 to 7.62 m (10 to 25 feet), and 39% from 7.62 to 15.2 m (25 to 50 feet) in this time.

6. The average direct tensile strength for six test specimens was 0.48 MPa (70 psi), with a coefficient of variation of 57%. This is about 1.8% percent of the average compressive strength, which is significantly lower than the expected range of four to six percent for this value. The low direct tensile strengths are likely due to the poor paste-aggregate bond, large rounded aggregates, and the micro fractures within the paste and the aggregate.
7. The concrete bond at the lift lines appears to be in good condition relative to the condition of the mass concrete. Breaks and disbands in the core reflect deterioration in the concrete, not weak zones at lift lines. The average direct tensile strengths at the lift lines and in the unjointed concrete are 0.38 MPa (55 psi) and 0.52 MPa (75 psi), respectively. Based on the variability of the test results, the difference among these averages is not significant.
8. The average splitting tensile strength of seven intact mass concrete specimens is 300 psi with a coefficient of variation of 15% percent. This is 8.4% of the average compressive strength of the concrete, which is within the expected range of eight to twelve percent for this value. Specimens often failed along the paste-aggregate bond near the intended plane of failure.
9. The average density of the 46 tested samples is 1.06 MPa (153.9 psi). Density measurements of intact core did not indicate spatial variation with respect to depth .
10. All test specimens were selected from the bonded, testable core. Results are biased to represent the "better" concrete core from the sample core population. The deteriorated concrete that contains little or no strength-bearing capacity is not included in the test results. Analyses of the dam should account for periodic zones of lower strength and modulus of elasticity at the rubble locations.

A.6.2.4 2003 Tests

This part is adapted from hatch report

Concrete cores from four holes, two vertical and two horizontal, were tested from in 2003. The location of drill holes were shown in figure A.10. Table G.8 shows the laboratory testing results. As shown in this table the averages of compressive strength and modulus of elasticity from vertical holes are smaller than those from horizontal holes.

Figure A.13 shows the comparison of the results of two vertical and horizontal specimens for both compressive strength and module of elasticity.

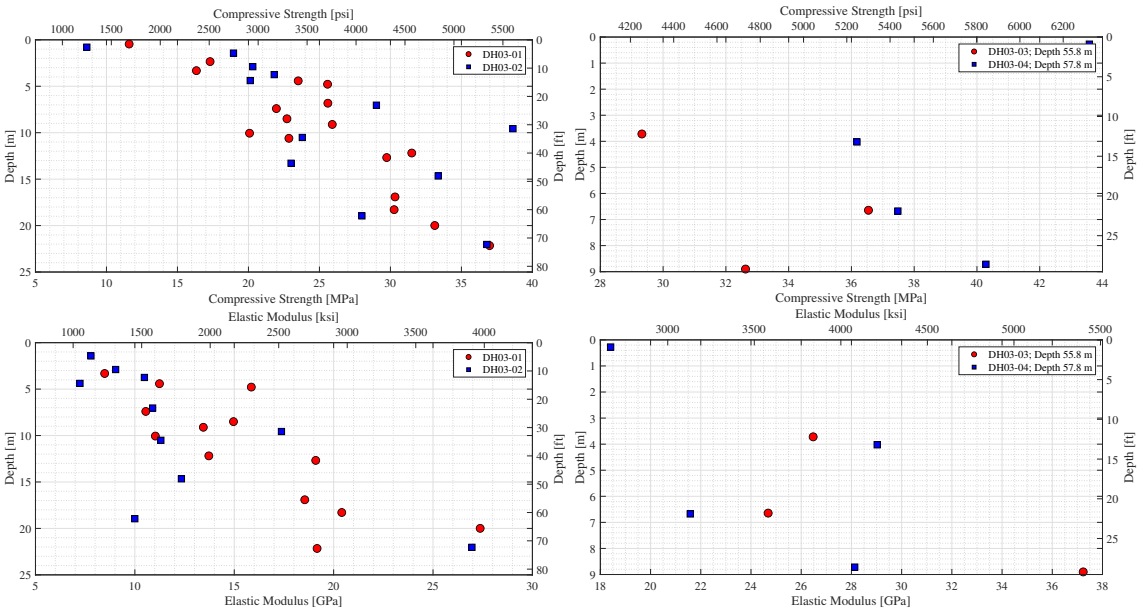

Figure A.13: 2003 Testing Results

A.6.2.5 2009-2013 Tests

Two campaigns of tests were conducted in 2009 and in 2013 using six-inch diameter concrete cores. Locations and results (average compressive strength, modulus of elasticity, Poisson's ratio, direct tension and splitting tension strength) are given in Table G.9 and G.10 for 2009 and 2013 tests respectively and shown in Fig. A.15.

From this figure, we note that concrete modulus, compressive and tensile strengths all vary with the height of the dam, with significant lower values at the top of the dam than those at the lower part of the dam. There is also substantial reduction in the module of elasticity and compression strength in 2013 compared to 2009.

The summary of the field test conducted at different elevation in several years is presented in table G.11 for the compressive strength and table G.12 for the module of elasticity of concrete.

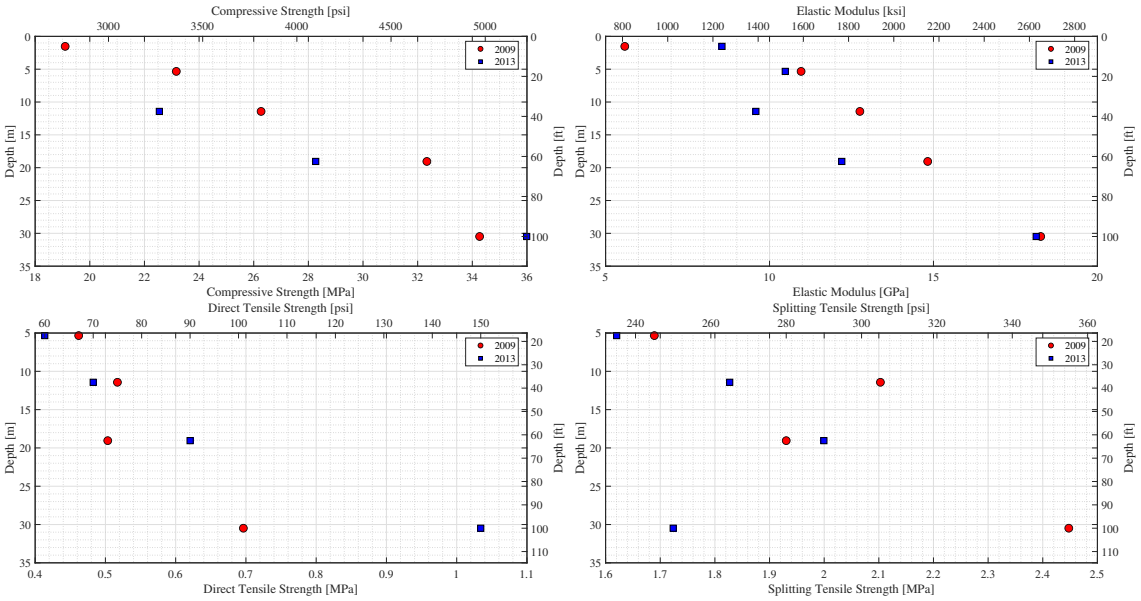

Figure A.14: 2009-2013 Testing Results

A.6.2.6 Summary of E and f'_c

In order to provide a better understanding of the variation of compressive strength and the module of elasticity throughout the years, figure A.15 is presented herein for various years of available test data.

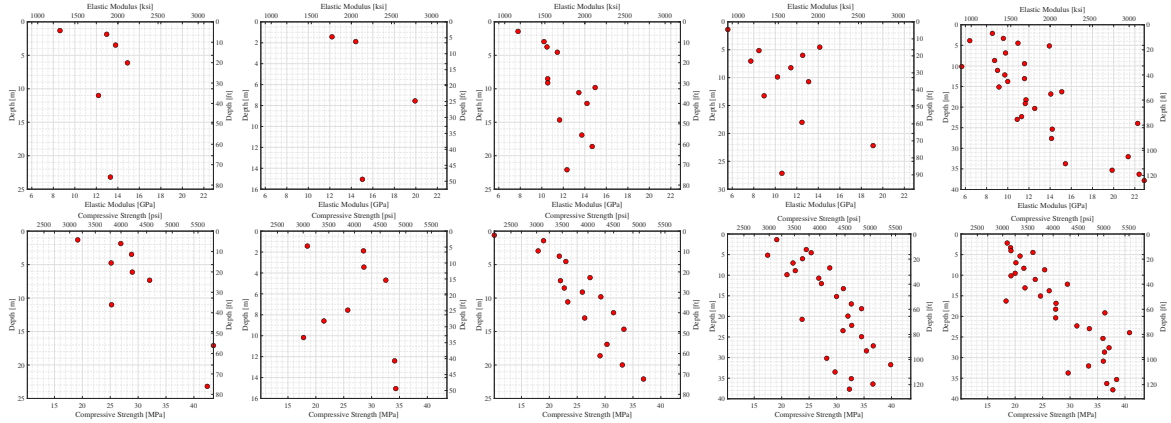

Figure A.15: Summary of Measured E and f'_c (**hatch**)

A.6.3 2003 Over Coring Tests

This part is adapted from Hatch report

Overcoring stress measurements were conducted with the purpose of determining the *in situ* stresses in dam. Table G.14 shows the overcoring location (along with the closest finite element node number) and results. Those are also illustrated in Fig. A.16.

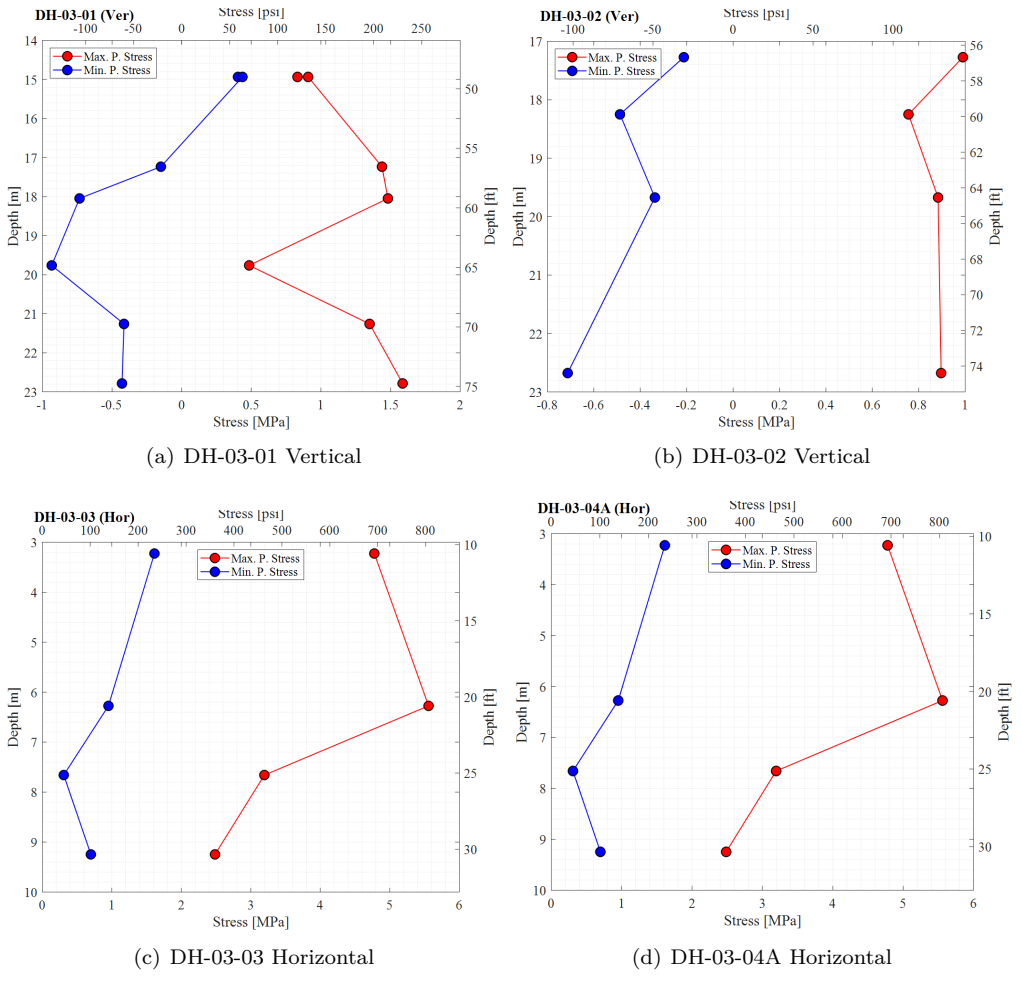

(a) DH-03-01 Vertical

(b) DH-03-02 Vertical

(c) DH-03-03 Horizontal

(d) DH-03-04A Horizontal

Figure A.16: Results of 2003 overcoring

A.6.4 Direct Shear Test Results

Direct shear test is conducted on a total of 18 specimens from 5 holes to represent parent concrete with high, medium, and low alkali-aggregate reaction. This testing program was performed to measure and report the shear strength under specified normal stresses, showing how the shear strength changed with displacement of the test surface. The combined intact shear data showed statistically very poor to good fit R-squared values as shown in table G.13.

Whereas these properties would be required for a model in which the nonlinearity of the concrete is modeled, they can not be used to model joints (concrete-concrete or concrete-rock) as needed in this analysis.

A.7 Temperatures

A.7.1 Concrete

The recorded concrete internal temperatures using the two types of DH03-1 and MPBX instruments are demonstrated in figures A.17 and A.18 respectively. The temperatures are shown at different elevations within several years.

As evidenced from figures A.17 and A.18 temperature recording with MPBX sensor are not much reliable and one should use only the DH03 values. This was confirmed by **dressel20empty citation**.

A.7.2 Closing Temperatures

It is of great importance to have a reliable data on the closure temperature of the dam since it will affect the results of the thermal analysis. The stable temperature to which the structure has reached after its construction would be the initial temperature that determines the amount of heat transfer through the surrounding fluid to the structure. The closure temperature of Seminoe is summarized in table A.4.

Table A.4: Closure temperature

Elevation Range (m)		**Average Closure T.** (°C)	**Time of Grouting**
0.00	1,866.90	12.8	May 1938
1,866.90	1,889.76	3.9	End of November 1938
1,889.76	1,905.00	2.2	April 18, 1939
1,905.00	1,920.24	4.4	May 8, 1939
1,920.24	1,938.83	6.7	May 12, 1939

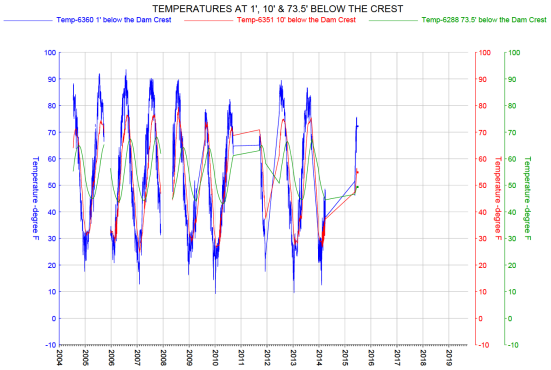

(a) DH03-1 readings

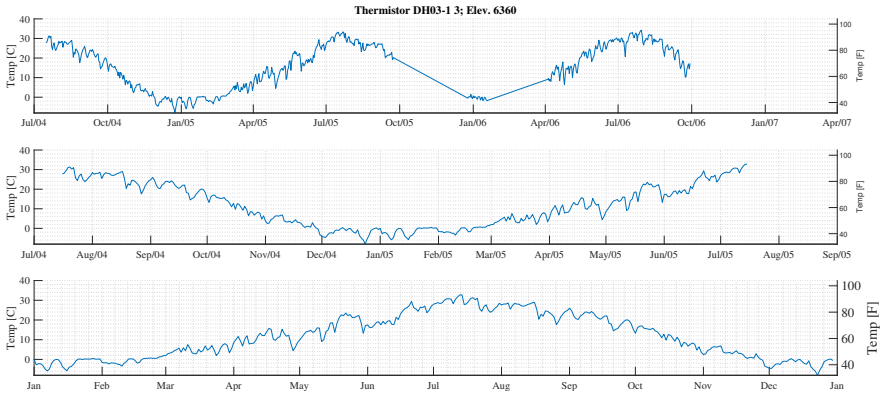

(b) Elevation 6288

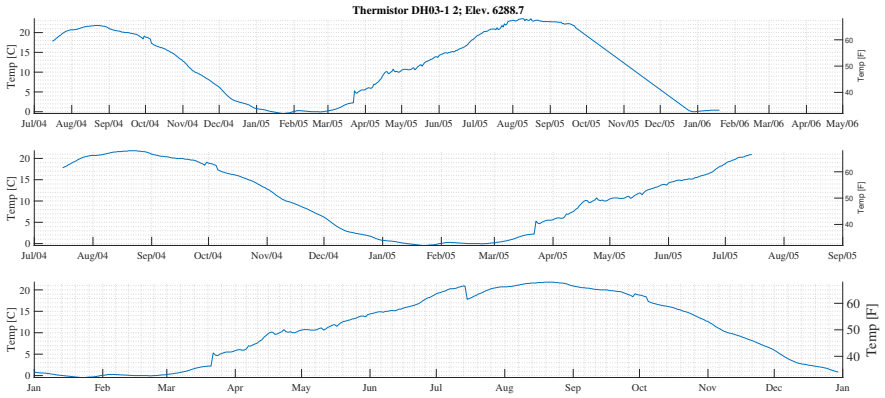

(c) Elevation 6351

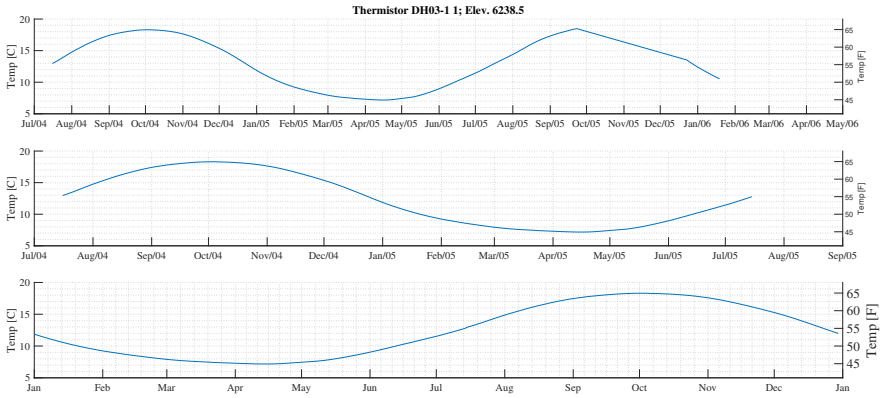

(d) Elevation 6360

Figure A.17: DH03-1-3 Based Concrete temperatures

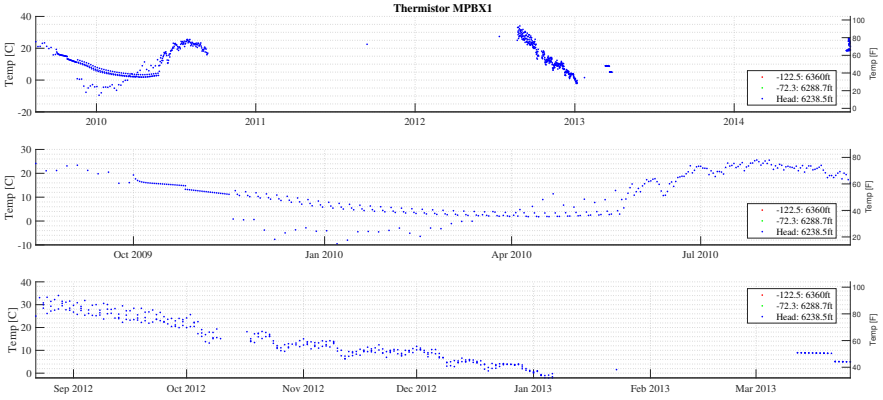

(a) MPBX 1

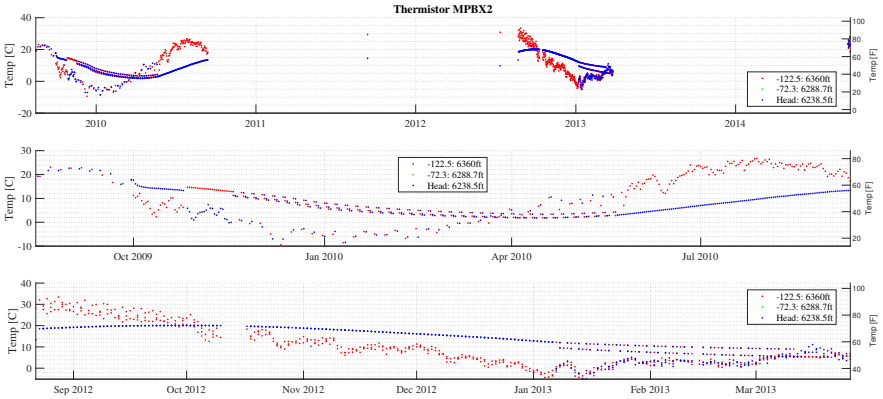

(b) MPBX 2

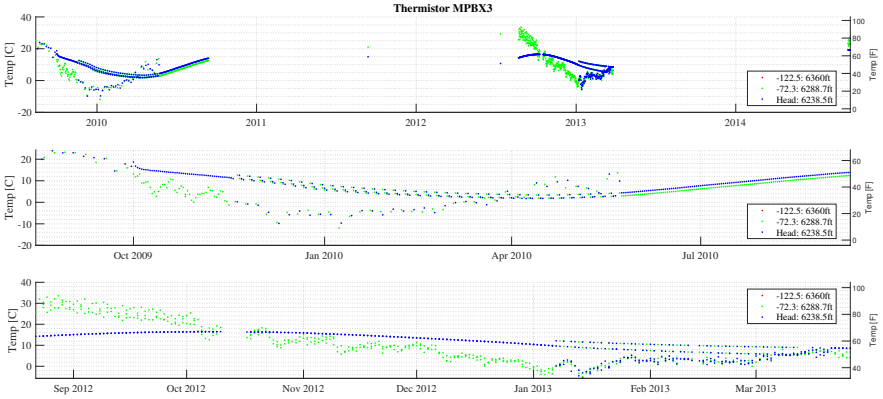

(c) MPBX 3

Figure A.18: MPBX Based Concrete temperatures

A.7.3 Air Temperature

A.7.3.1 From (hatch)

Table G.15 shows the air temperature that Hatch report has used for their thermal analysis purpose. Also, a constant temperature increase due to solar radiation is presented in the second row of the table for various months which is added to the air temperature in the analysis and shown in figure A.24.

Table A.5: Air temperature (**hatch**)

Month	**Jan**	**Feb**	**Mar**	**Apr**	**May**	**Jun**	**Jul**	**Aug**	**Sep**	**Oct**	**Nov**	**Dec**
T°C	-5.4	-5.0	-2.4	2.1	7.3	12.8	17.7	19.3	15.9	9.9	3.0	-2.9
$T^{\circ}_{Radiation}$C	-0.9	0.8	2.6	5.8	9.8	14.0	18.5	20.9	19.6	15.6	9.1	2.4

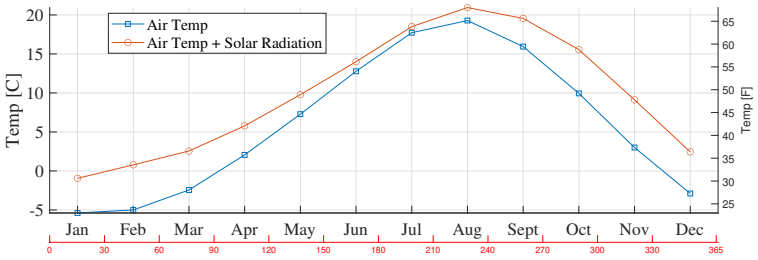

Figure A.19: Air Temperatures (**hatch**)

A.7.3.2 From Reclamation Files

USBR reported the "average" of air temperature at the downstream. This data set is derived from the average of 4 temperature readings measured using thermistors attached to joint meters mounted at approximately the same location on the downstream left abutment. Those joint meters are JT7, JT8, JT9, and JT10, Figure A.20(a).

(a) Downstream left abutment (b) Upstream right abutment

Figure A.20: Joint meters

Recorded upstream temperature is also obtained with a similar way to the one on downstream face. All data prior to 1999 is disregarded (as recommended by USBR). This data set is derived from the average of

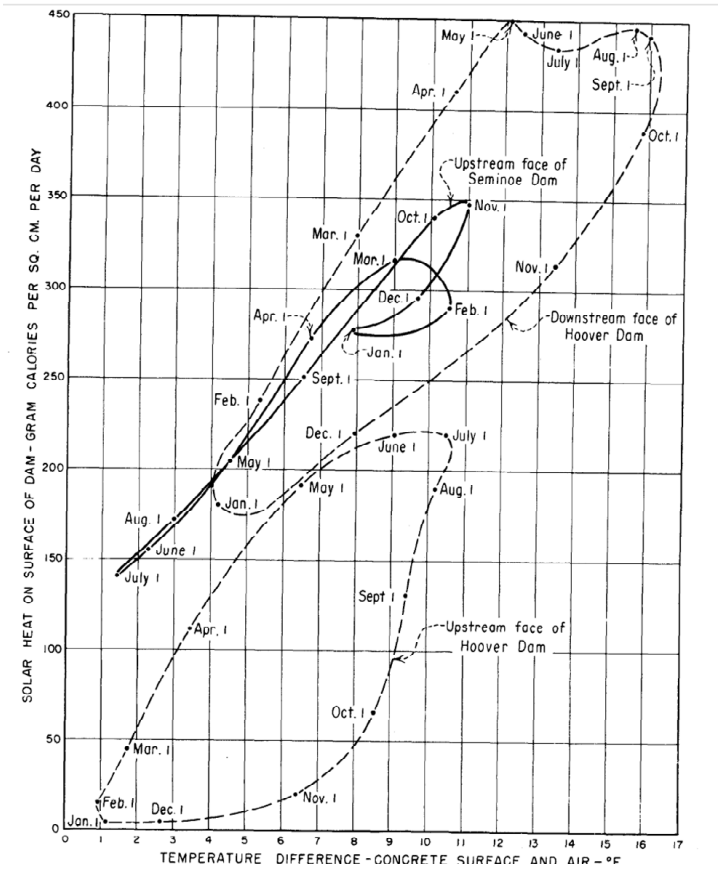

Figure A.21: Measured impact of radiation in various USBR dams (**em34**)

3 temperature readings measured using thermistors attached to joint meters mounted at approximately the same location on the upstream right abutment, i.e., JT4, JY5, and JT6, Figure A.20(b).

Temperature variation at those three locations are shown in Figure A.22 and A.23 for the upstream and downstream. As seen, there is a high correlation among the recordings.

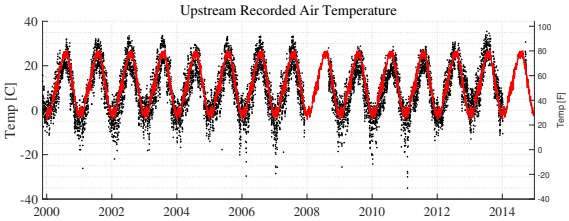

(a) Average yearly air temperatures

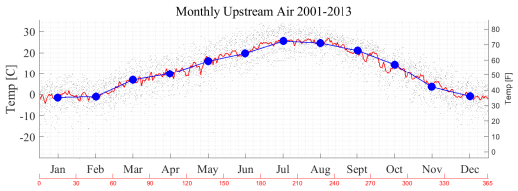

(b) Aggregate air temperatures

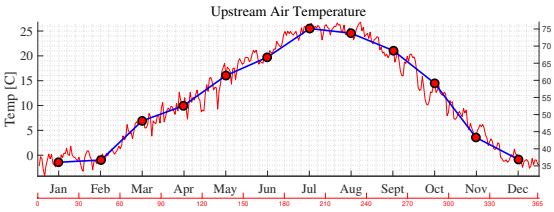

(c) Harmonic variation

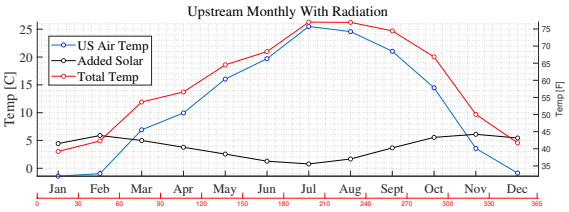

(d) Impact of radiation

Figure A.22: Recorded upstream air temperatures

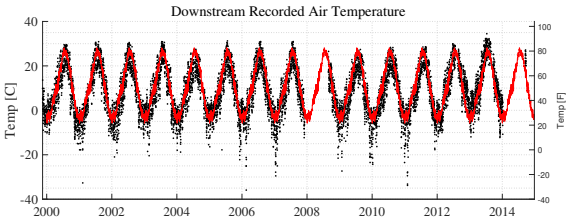

(a) Average yearly air temperatures

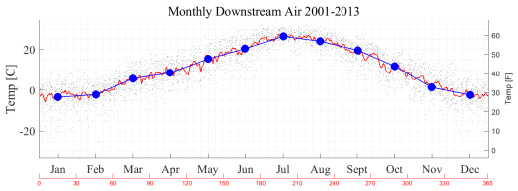

(b) Aggregate air temperatures

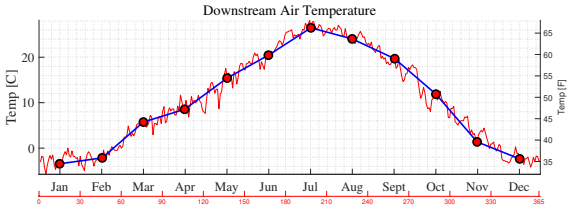

(c) Harmonic variation

Figure A.23: Recorded downstream air temperatures

A.7.4 Solar Radiation

It is critical to account for the impact of solar radiation in the thermal analysis of Seminoe dam. Hence, data are obtained from (**energyplus**) for The Seminoe location. The amount of direct normal solar radiation as well as diffuse solar radiation is demonstrate in table A.6 which are the raw data to be processed and applied to the Seminoe to account for the effect of solar radiation.

A.7.5 Water Temperature

A.7.5.1 From (hatch)

The available data on water temperature as reported by Hatch is presented in table G.16 and plotted in figure A.24. As seen the data is only available at specific depths down to 81 [m] and is missing in some

Table A.6: Solar radiation [Wh/m^2], Casper WY (**energyplus**)

	Jan	**Feb**	**Mar**	**Apr**	**May**	**Jun**	**Jul**	**Aug**	**Sep**	**Oct**	**Nov**	**Dec**
Direct normal	3774	4157	4936	5462	6023	7183	7483	7792	6334	5404	3588	3209
Diffuse Avg	807	1100	1551	1972	2312	2194	1858	1591	1449	1077	877	699
Global horizontal	2052	2843	4082	5304	6181	7032	6889	6506	4957	3514	2168	1690

months.

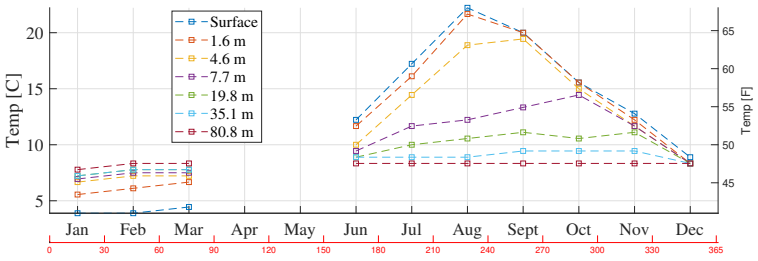

Figure A.24: Water Temperatures (**hatch**)

A.7.5.2 From Reclamation Files

The provided data by USBR covers only part of 2017 to 2019. The full data is only available for 2018. For this year, readings are provided at 10 depths (based on their elevations). Temperature is recorded using temperature probe (TP).

The temperature of the water is measured using a Solinst TLC meter Model 107-Mk3. This is a retractable temperature probe, essentially a thermistor attached to a tape. The measurements are taken at 10-ft intervals below the top of the parapet wall (i.e., 10 indicates El. 6351, 20 indicates El. 6341, etc.) for a total depth of 100 feet. USBR initially started taking the temperatures at the same time the inclinometers (installed in 2016 and measured quarterly) but are in the process of moving towards having the temperatures measured on a monthly basis. Care should be taken when evaluating this data as gaps in the data may indicate a "dry (reservoir lower than temperature probe) or frozen reservoir". Additionally, the reservoir elevation is different on each measurement date. Therefore, USBR recommends to plot the data for each individual date with the reservoir water surface elevation to delineate the actual water column temperature gradation.

Water temperature data at different elevations for 5 months is available for every 10 feet(total 100 ft) as shown in table G.17, where the elevations are measured from dam crest. It can be seen that the data for the top 2 measure points in Jun and Oct are missing, although, from the available pool elevation data it can be inferred that the pool elevation was higher than the measured elevation in these months at least for the second point in June. The pool temperature since may 2017 through July 2019 is demonstrated for the various depths in figure A.26.

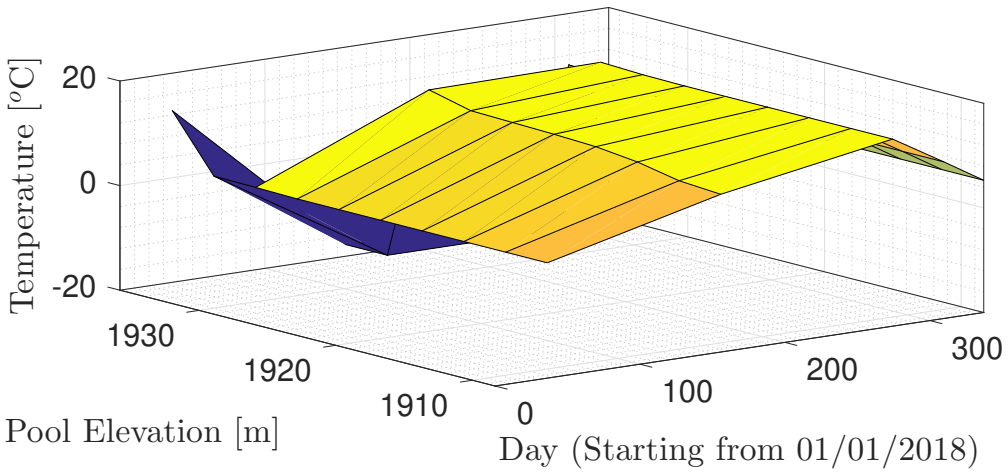

Figure A.25: Pool temperature at different depths and time of year for Seminoe Dam

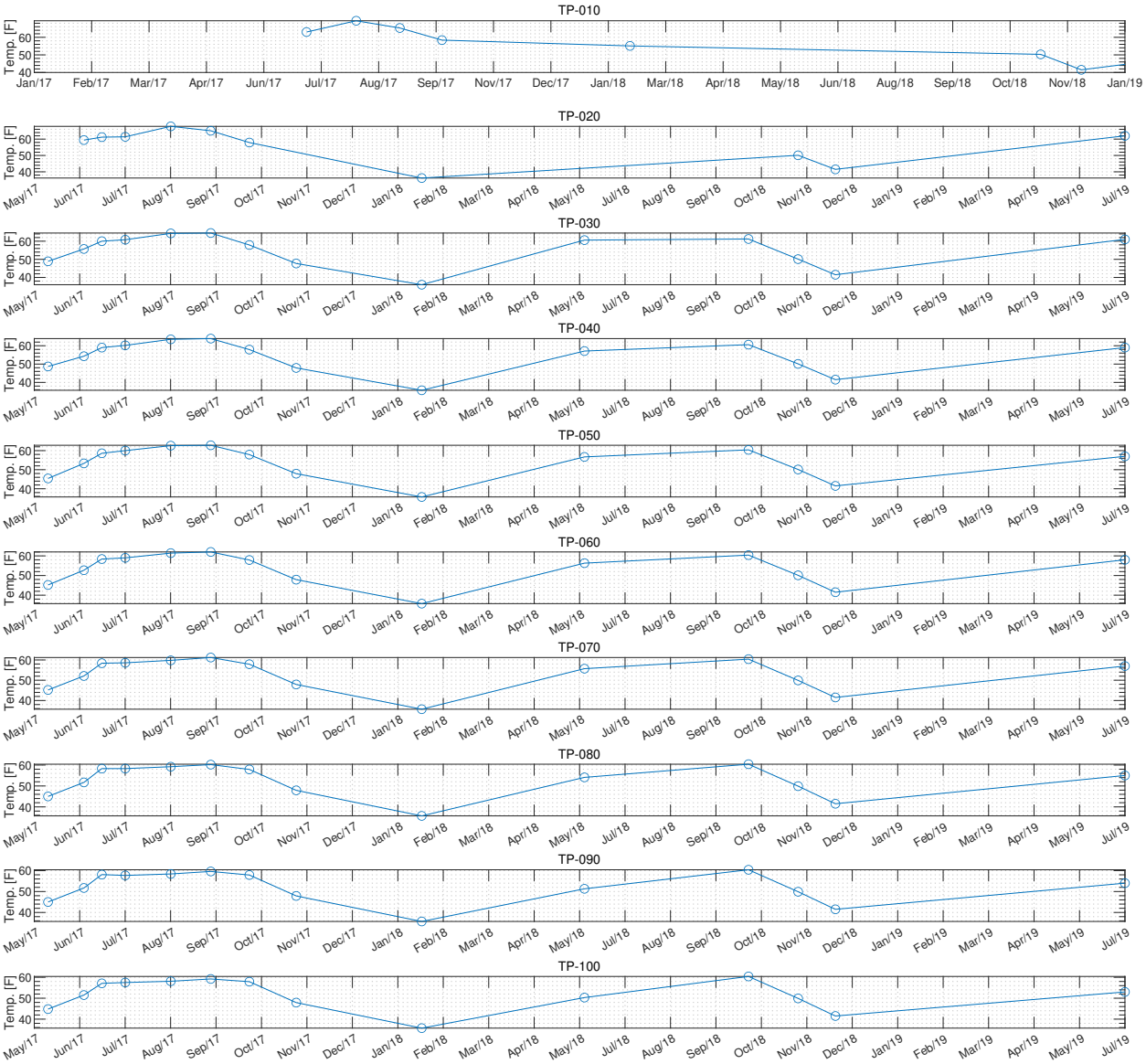

Figure A.26: Recorded pool water temperature

A.8 Pool Elevation

A summary of the recorded pool elevation data is illustrated in figure A.27. It is highly important to have a good measurement of the pool elevation during various months of the year since it determines the border between air and water which affects the amount of hydro-static pressure on the structure as well as the amount and source of heat transfer to the structure. As shown in figure A.27(a) there is a great dispersion in pool elevation from a year to another. In an effort to estimate a mean annual pool elevation a sine curve is fitted as the general mean value which is shown throughout the years in figure A.27(b) and for a single year in A.27(c)

A.9 Natural; Convection

For the convection over the planes, the convection coefficient is a function of the length of the surface in the direction of the flow, L, and the wind speed, v. It is given by (**kreider**)

1. if $vL < 15$ ft^2/s or 1.4 m$^2/s$

$$h_c = 0.35\left(\frac{v}{L}\right)^{1/2} \quad \text{[US unit]} \tag{A.1}$$

$$h_c = 2.0\left(\frac{v}{L}\right)^{1/2} \quad \text{[SI unit]} \tag{A.2}$$

2. if $vL > 15$ ft^2/s or 1.4 m^2/s

$$h_c = 0.54\left(\frac{v^4}{L}\right)^{1/5} \quad \text{[US unit]} \tag{A.3}$$

$$h_c = 6.2\left(\frac{v^4}{L}\right)^{1/5} \quad \text{[SI unit]} \tag{A.4}$$

A.10 Conclusion

In Summary, this chapter presented the basic data to be used in the futur analysis. The available survey data on the crest displacements, tilt measurements, the joint meter data as well as the results of the geophysiscal investigations were illustrated herein. Furthermore, the compressive strength and module of elasticity of the concrete from core testing through several years was presented. last but not least, the air and pool temperatures as well as the pool elevation recorded during several years was provided in this chapter.

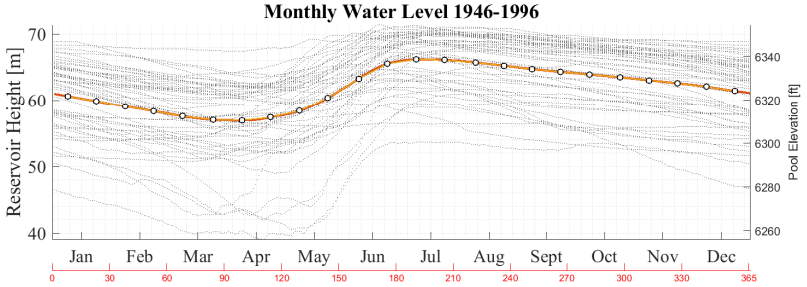

(a) Aggregate of readings

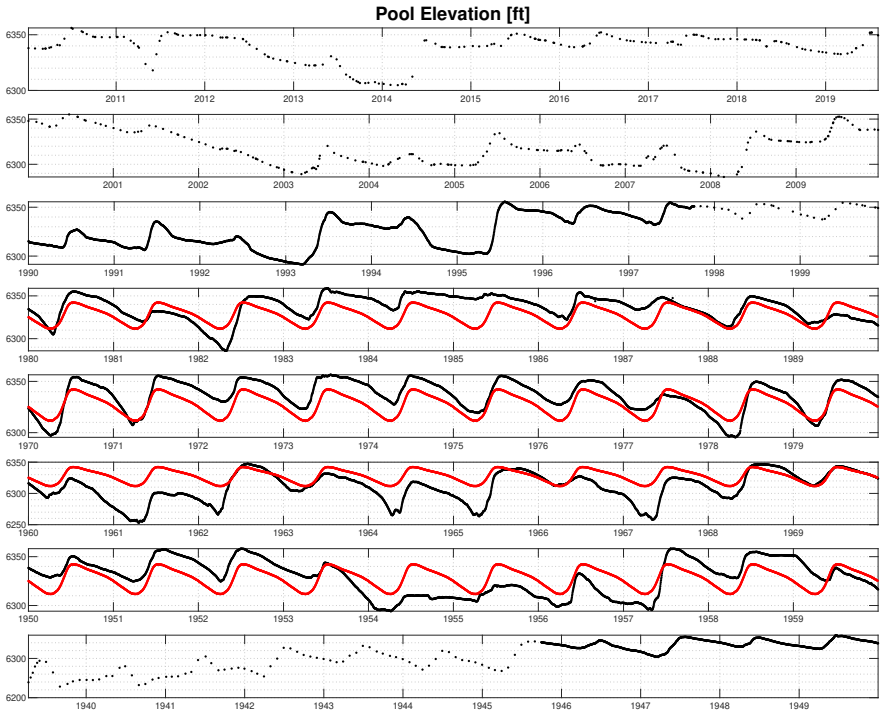

(b) Historical values

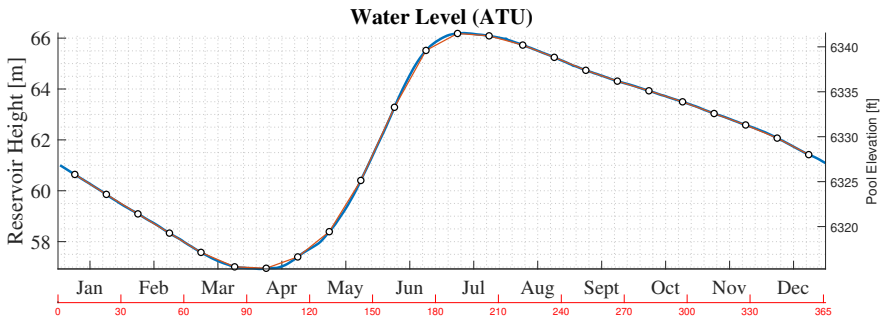

(c) Harmonic variaiton

Figure A.27: Recorded pool elevations

Appendix B

Thermal Load; Verification

Abstract

It is of great significance to validate the utilized method on a simple model prior to conducting any thermal analysis on a complicated mesh. This chapter includes three main parts in the first section a comprehensive study is conducted to determine and regenerate the pool temperature at different elevations for seven dams that their data was available from **em34** *report in order to evaluate the ability of the utilized formula for approximation of the pool temperature.*

In the second part, the thermal analysis is conducted on a single column and results are compared with the numerical solution, also the stability condition is discussed. last but not least, the calculations of solar radiation is validated on a cantilever and an arch.

B.1 Pool Temperature

ASR expansion being a thermodynamically reaction, expansion is very sensitive to water temperature in the dam reservoir. Whereas air temperature is usually well recorded, reservoir temperature is not. At best, we may have air and surface temperature. Hence, this section will make a best estimate determination of reservoir temperature at Seminoe based on recorded reservoir temperature in terms of depths at other dams. The governing equation for thermal diffusion is

$$\frac{\partial T}{\partial t} = \underbrace{\frac{k}{\rho c_p}}_{\mu} \frac{\partial^2 u}{\partial x^2} \tag{B.1}$$

where μ is the thermal diffusivity and describes the rate of temperature spread through a material.

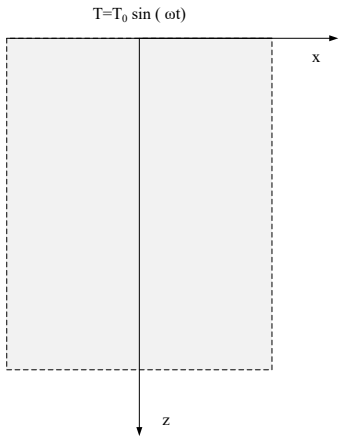

Figure B.1: Semi infinite plate subjected to surface harmonic temperature

B.1.1 Heat conduction in a semi-infinite plate

Considering a semi-infinite solid, Fig B.1, with its free surface is subjected to a periodic temperature variation $T(x,t)$

$$T(0,t) = T_m + T_0 \sin(\omega t) \tag{B.2}$$

Solution for $T(0,t) = T_M$ is well known, and is given by

$$T(x,t) = T_m \text{erfc}\left(\frac{x}{2\sqrt{\mu t}}\right) \tag{B.3}$$

Solution for $T(0,t) = T_0 \sin(\omega t)$ is given by (**selvadurai2013partial**), Fig. B.1. as

$$T(z,t) = T_0 \exp\left\{-\left(\frac{\omega}{2\mu}\right)^{\frac{1}{2}} z\right\} \sin\left[\omega t - \left(\frac{\omega}{2\mu}\right)^{\frac{1}{2}} z\right] \tag{B.4}$$

To visualize the temperature distribution in 1-D "column", we consider a top variation with amplitude ± 10, Fig. B.2(a); a bottom variation of ± 2.5, Fig. B.2(c); and the sum of the two Fig. B.2(e).

B.1.2 Pool water temperature distribution

B.1.2.1 Empirical Solution

An empirical equation for the temperature distribution was first given by **bofang1990thermalempty citation** in term of a mean top and bottom water temperatures and calibrated for a specific dam. The equation was later extended by **ardito2008diagnosticempty citation**.

$$T_w(y_w,t) = T_{bot}(t).\frac{1-e^{-\phi y_w}}{1-e^{-\phi H}} + T_{top}(t).\frac{e^{-\phi y_w} - e^{-\phi H}}{1-e^{-\phi H}} \tag{B.5}$$

where T_{bot} is the time sequence of temperature measurements at $y_w = H$ (reservoir bottom); T_{top} is the time sequence of temperature measurements at $y_w = 0$ (reservoir top), Figure B.3(a); and most importantly ϕ is

an empirical parameter that must be properly determined for the specific dam. For illustration, Figure B.3 shows the water temperature for a dam 100 m high, and $\phi = 0.04$.

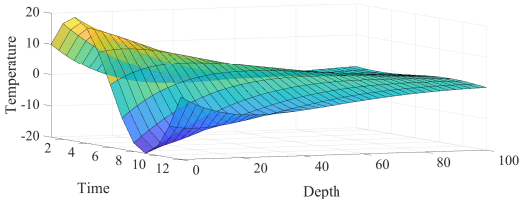

(a) Analytical; Top harmonic temperature ±10 (**selvadurai2013partial**)

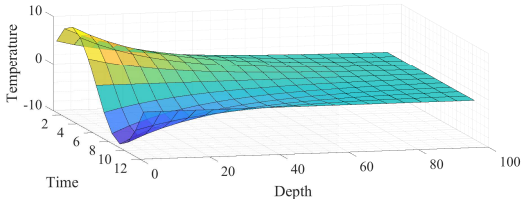

(b) Emperical; Top harmonic temperature ±10 (**ardito2008diagnostic**)

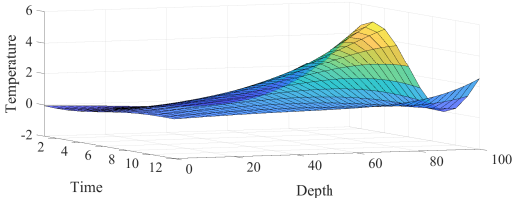

(c) Analtical; Bottom harmonic temperature ±2.5 (**selvadurai2013partial**)

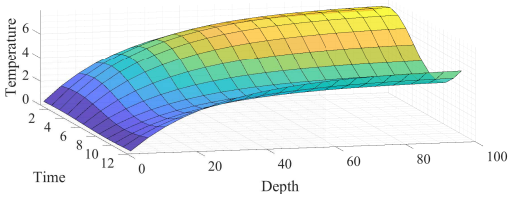

(d) Emperical; Bottom harmonic temperature ±2.5 (**ardito2008diagnostic**)

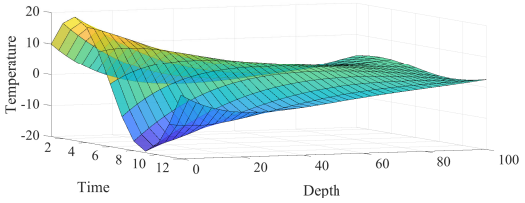

(e) Analytical; Net temperature distribution (**selvadurai2013partial**)

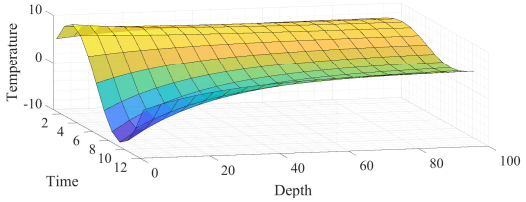

(f) Emperical; Net temperature distribution (**ardito2008diagnostic**)

Figure B.2: Analytical and emperical solution for water temperature distribution

B.1.2.2 Model comparisons

Figure B.2 qualitatively (and not quantitatively) compares the two previously described models for a 100 m high dam with a mean top and bottom temperatures of 20 and 6 °C, and a harmonic varioton with 10 and 2 °C respectively.

Whereas it is indeed expected that the analytical of solution (**selvadurai2013partial**) has equal impact for the top and bottom temperature diffusion (albeit with different weight due to difference in temperature), this is not the case in the empirical equation of **ardito2008diagnosticempty citation**.

This is most apparent in Figure B.2(d) where the bottom temperature has far greater impact on the top than the other way around. This can be simply explained by the fact that, contrarily to the analytical equation, there is inherent in this equation the notion of "bottom" and "top", and that heat simply moves upward.

Hence, the bottom reservoir temperature has a much greater impact that the top one, and should be recorded in as much as possible. In the absence of measurements, it can be argued that the temperature can not be lower than 4°C when the maximum water density is reached (except in particular conditions i.e.

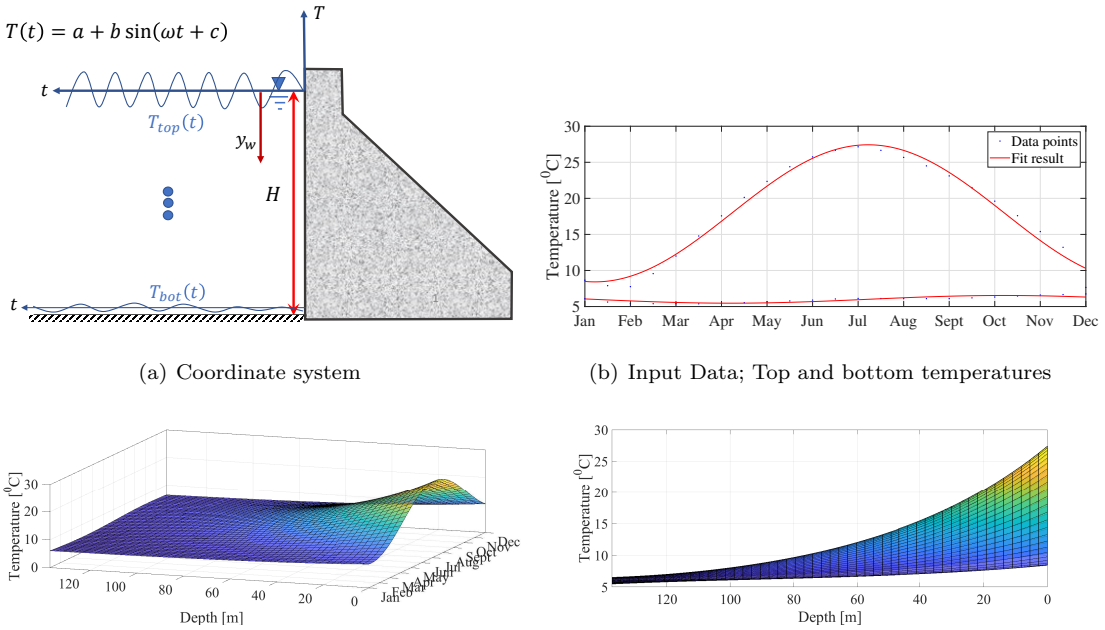

(a) Coordinate system

(b) Input Data; Top and bottom temperatures

(c) Fitted Model

Figure B.3: Fitted model of **ardito2008diagnosticempty citation**

when the reservoir is covered by ice, or near water intake structures) (**tatin2018statistical**).

B.1.2.3 Application

em34empty citation reports the temporal and spatial (in terms of depth) water temperature for seven dams including shown in Figure B.4.

Those plots have been digitized, and are shown in Figure B.5.

In the next step we seek to fit the data reported in Figure B.5 into Eq. B.5. First, all digitized data are fitted into harmonic equation

$$T(t, y) = A(y) + B(y)\sin(\omega t + C(y)) \tag{B.6}$$

Then two approaches are pursued

Model I Using T_{bot} and T_{top}, determine ϕ from all other curves.

Model II Use the entire set of curves to determine the coefficients for T_{bot}, T_{top}, and ϕ

Results for the fitted surfaces based on Model II are shown in Figure B.6 and table C.1.

The goodness of fit (based on R^2) is shown in the last two columns of this table for the two methods which is clearly better for model II which is the reason for demonstrating only the results of model II.

As for the Seminoe the same approach is followed herein using the available pool temperature data within the upper 100 ft and the results shown in figure B.7 indicate the lack of sufficient data to utilize this method to estimate the parameters of Eq. B.5. Also, the values based on model II are shown in table C.2. As seen in this table the goodness of fit is not in an acceptable range. Figure B.8 shows the location of each of those seven dams with respect to Seminoe and their ϕ values. This figure shows that while in all dams the water temperature can be estimated with a ϕ factor of 0.01 to 0.06, this value for Seminoe is about 0.24 which again underlines the fact that the insufficient data has led to inaccurate results.

B.2 Numerical Solution with Merlin; Concrete

B.2.1 Stability Condition

The Courant–Friedrichs–Lewy or CFL condition is a condition for the stability of unstable numerical methods that model convection or wave phenomena.

It states that the distance that any information travels during the time-step length within the mesh must be lower than the distance between mesh elements. In other words, information from a given cell or mesh element must propagate only to its immediate neighbors. This results in

$$\frac{\mu \Delta t}{h^2} \leq \frac{1}{2} \tag{B.7}$$

where μ is the diffusivity defined in Equation B.1.

B.2.2 Verification Problems

Before a comprehensive thermal study is undertaken, it is important to validate the ability of the finite element code (Merlin) to properly conduct linear transient thermal analysis of concrete subjected to: a) temperature, b) flux; and c) solar radiation. For this purpose a $1[m] \times 1[m] \times 100[m]$ concrete column is analyzed under various thermal load conditions in which the temperature is applied at one end of the column. The studied columns are shown in figure B.9. For this study, material properties of the concrete were taken from **hatchempty citation** presented in table 4.1 and the air-concrete film coefficient was taken to be equal

to 20[W m^{-2} K^{-1}] also obtained from **hatchempty citation** . The whole verification procedure presented in this section is summarized in figure B.10

B.2.2.1 Temperature

At first, the temperature is applied directly to the concrete column considering once a constant temperature which does not change with time and then a harmonic temperature that is defined using a sine function such that $T = -12.6\sin(\frac{2\pi}{12}t)$ which represents the harmonic term of the air temperature at Seminoe location. It is worth mentioning that the air temperature at Seminoe was estimated as $T = -12.6\sin(\frac{2\pi}{12}t) + 12.6$ based on the available data. Then, the results of the thermal analysis of this column from Merlin is compared to that of the analytical solution. The analytical solution for constant and harmonic temperatures are given by equation B.3 and B.4 respectively.

B.2.2.1.1 Constant The constant temperature of 12.6 [^oC] is applied directly at the end of the column the value considered for the temperature was obtained from the constant term of the equation representing the air temperature at Seminoe location. The results for both Merlin and analytical solutions are shown in figure B.11 and B.12. figure B.11 shows the temperature variation of the first 20[m] of the column within 4 years.

Figure B.12 shows that the 2 solutions are in good agreement and they have slight difference at the beginning of the thermal loading and gradually converging to a constant value in 4 years.

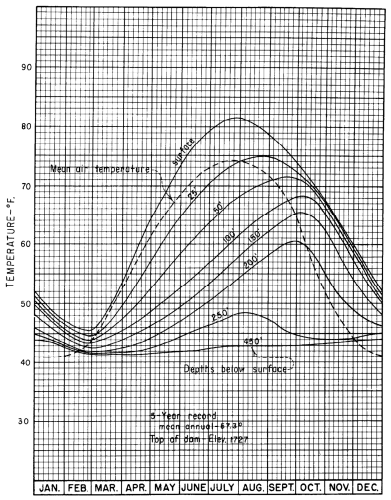

(a) Fontana

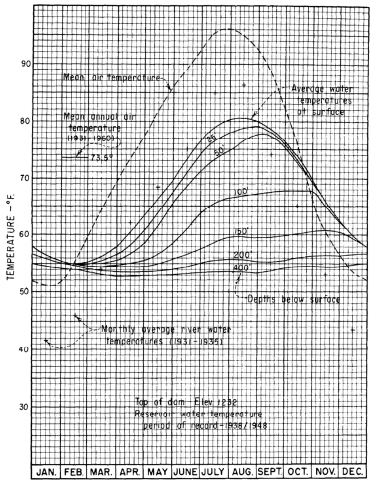

(b) Hoover

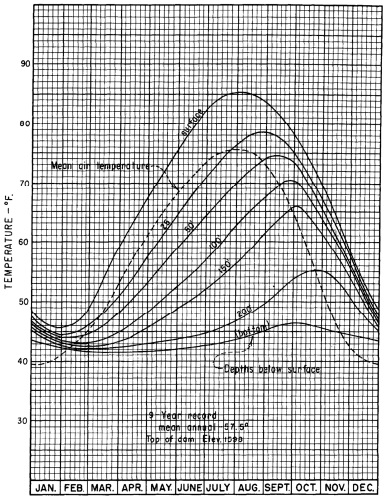

(c) Hiwassee

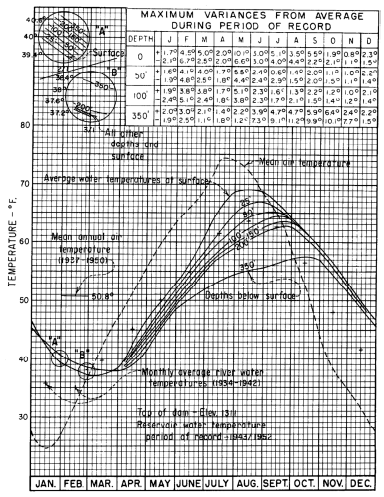

(d) Grand Coulee

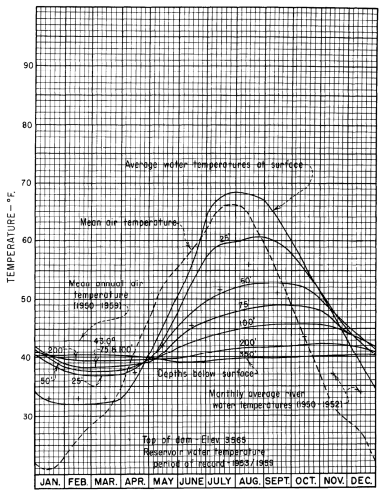

(e) Hungry Horse

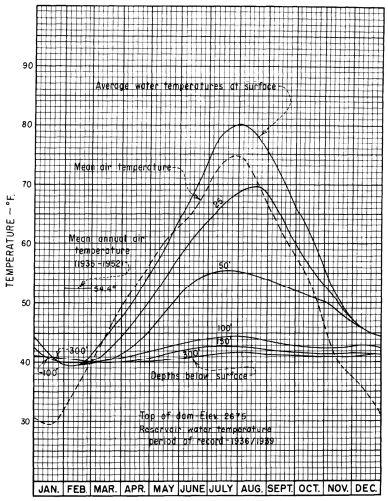

(f) Owyhee

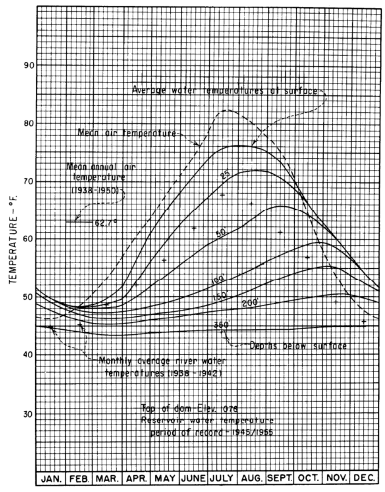

(g) Shasta

Figure B.4: Recorded pool temperatures (**em34**)

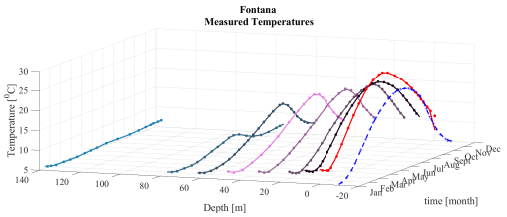

(a) Fontana

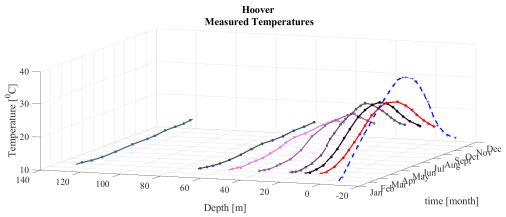

(b) Hoover

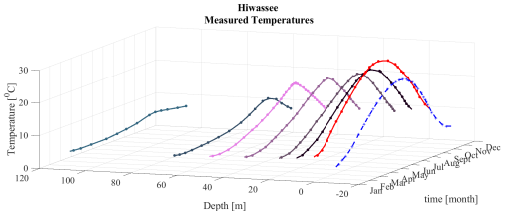

(c) Hiwassee

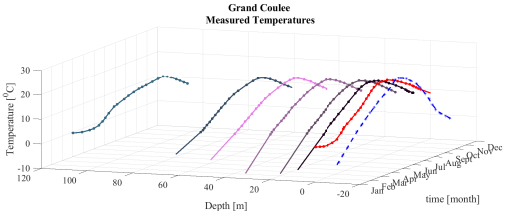

(d) Grand Coulee

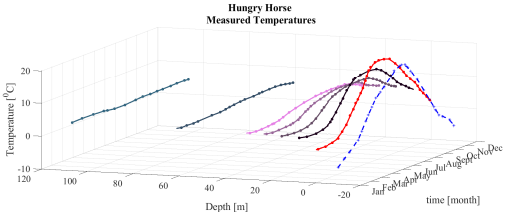

(e) Hungry Horse

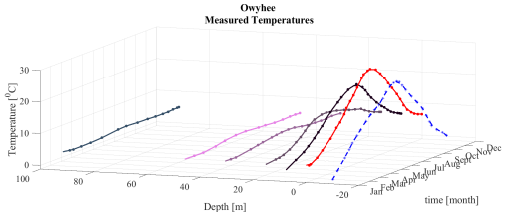

(f) Owyhee

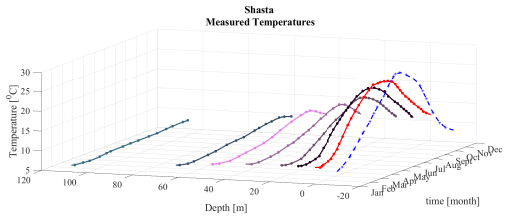

(g) Shasta

Figure B.5: Digitized data from Figure B.4

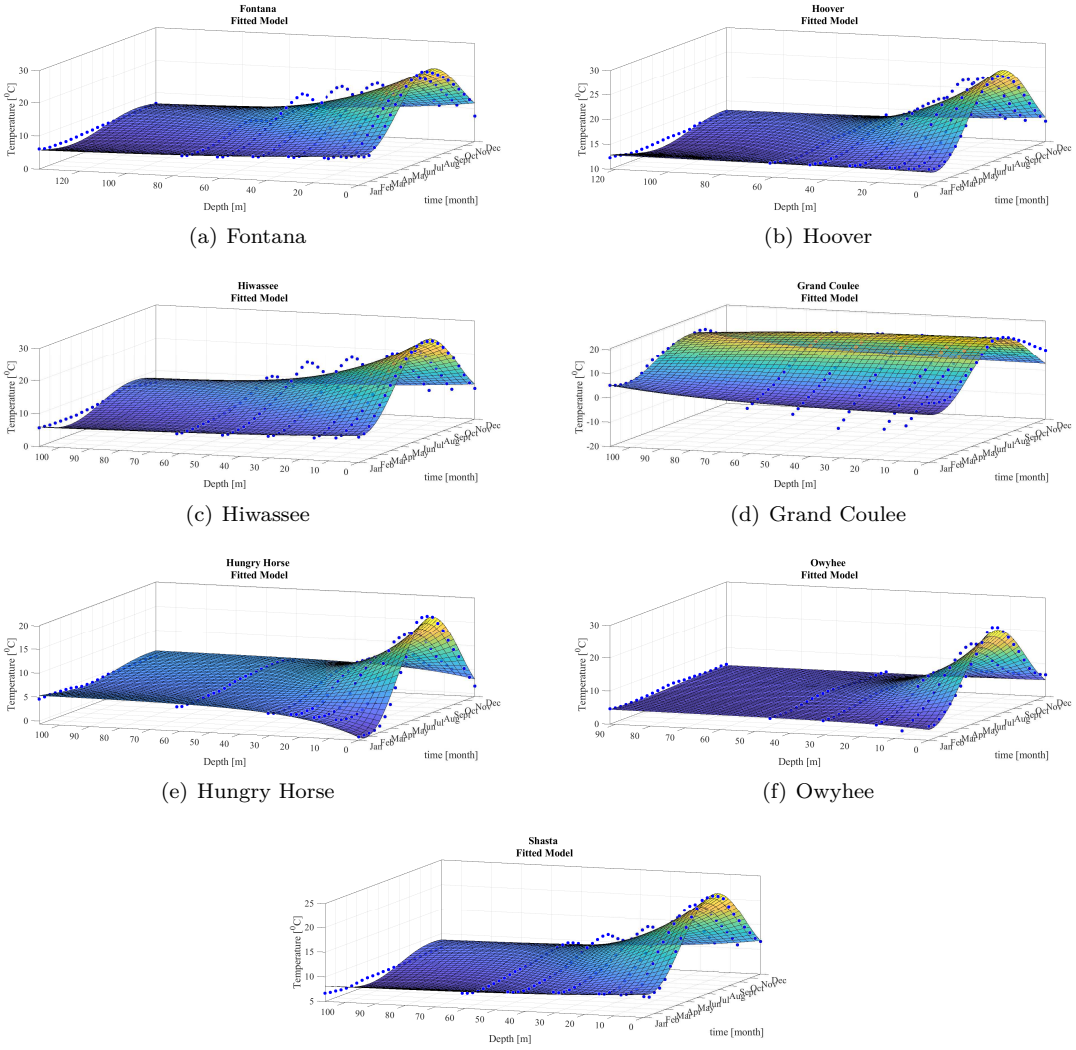

(a) Fontana

(b) Hoover

(c) Hiwassee

(d) Grand Coulee

(e) Hungry Horse

(f) Owyhee

(g) Shasta

Figure B.6: Fitted dam temperatures from (Model II) Figure B.5

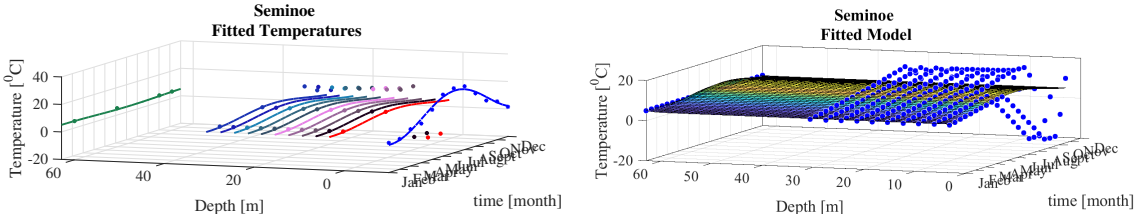

Figure B.7: Fitted dam temperature (from model II) for Seminoe

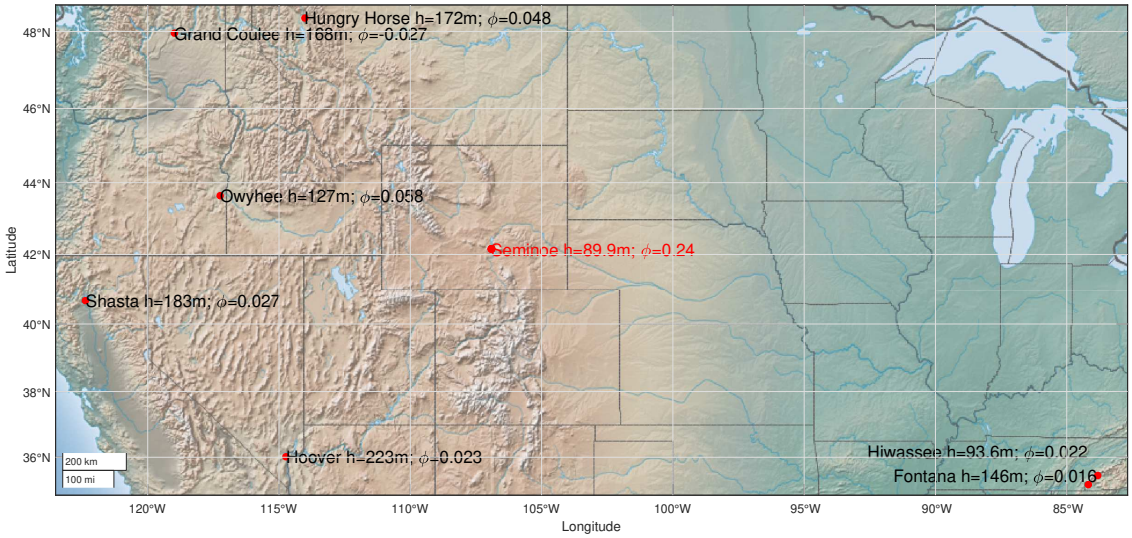

Figure B.8: Dam map

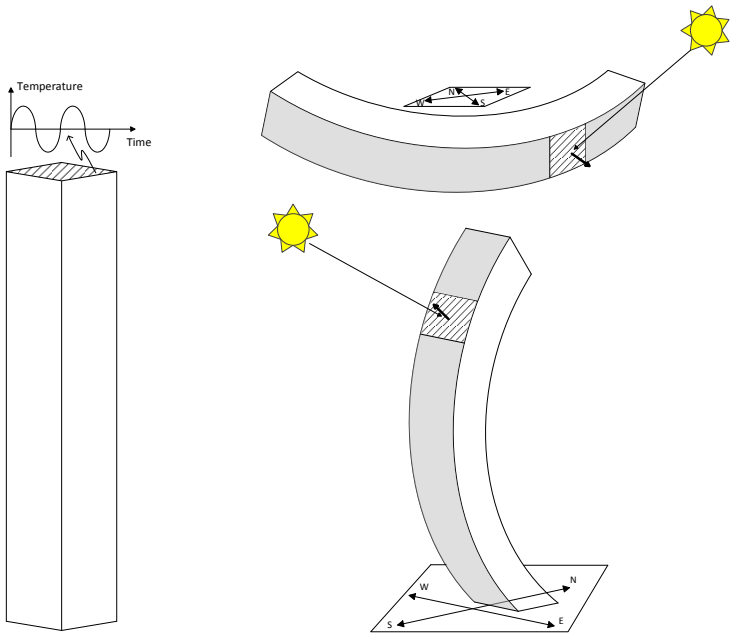

(a) Straight Column (b) Curved Column

Figure B.9: Thermal analysis results of constant temperature applied at the end of the column

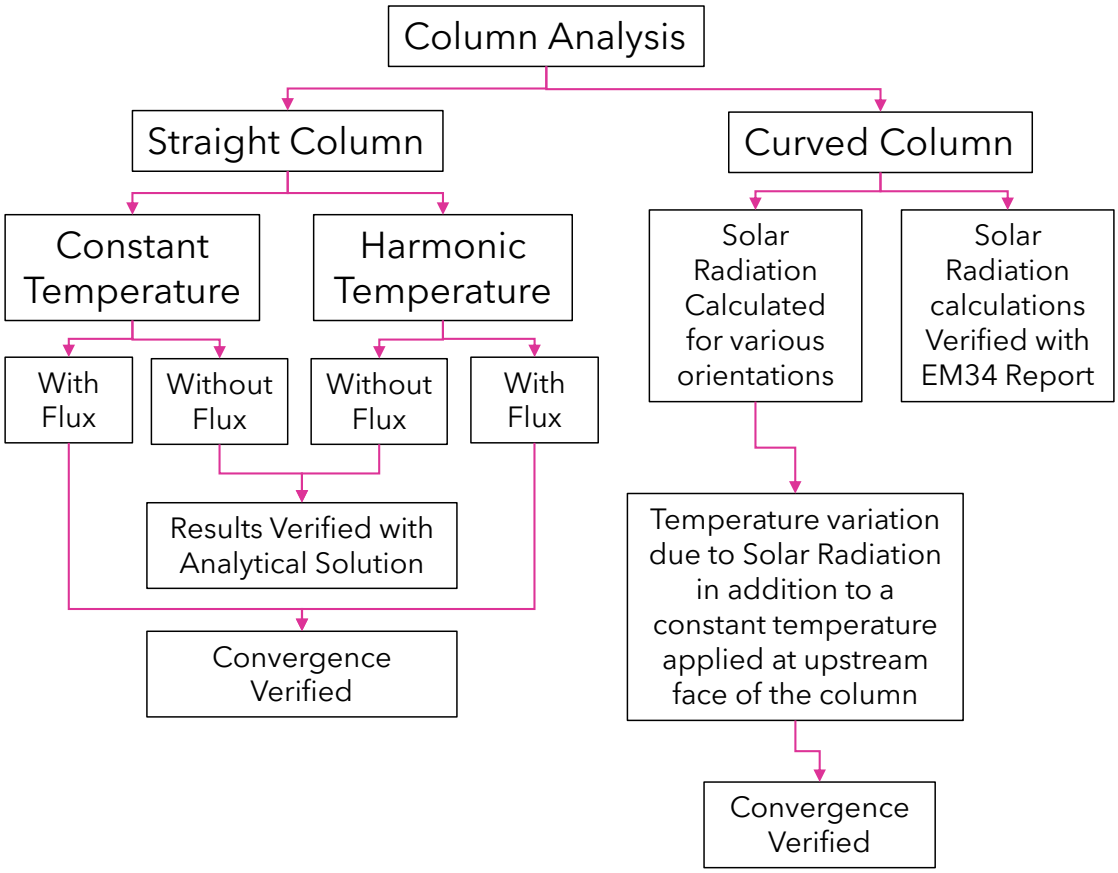

Figure B.10: Verification procedure

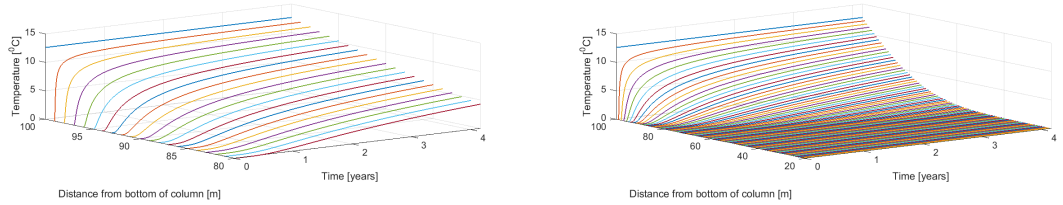

(a) analytical Solution (b) Merlin Solution

Figure B.11: Thermal analysis results of constant temperature applied at the end of the column

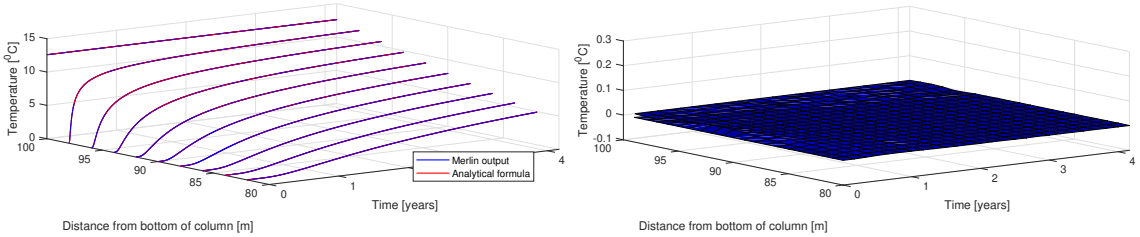

(a) Analytical vs. Merlin Solution (b) Difference of 2 solutions

Figure B.12: Comparison of Analytical and Merlin solutions of constant temperature applied at the end of the column

B.2.2.1.2 Harmonic In order to have a more realistic simulation in this section the previously discussed constant temperature is replaced with a harmonic temperature ($T = -12.6\sin(\frac{2\pi}{12}t)$), plotted in figure B.13, varying with a sine function throughout the year. In figure B.14 the oscillation of temperature within 4 years is shown for Merlin and analytical solutions. It is shown that the temperature can travel almost about 15 [m] through the length of the column and its intensity is reduced within this distance. Figure B.15 also, suggests a good match between the analytical and Merlin solutions for applied harmonic temperature which underlines the accuracy of the finite element code.

B.2.2.1.3 Stability Condition evaluation In order to evaluate the effect of CFL condition in convergence of the thermal analysis, the analysis is conducted considering 2 different time steps. As shown in table B.1 the time step is once considered to be equal to 0.1[month] in which $\frac{\mu\Delta t}{h^2} = 0.435$ which is less than $\frac{1}{2}$ and therefore conforms to the CFL condition. Then, The time step is increased to 1 [month] keeping the mesh size h constant, $\frac{\mu\Delta t}{h^2} = 4.35$ and becomes greater than $\frac{1}{2}$ which in turn does not conform to the CFL condition. figure B.16 shows the results of these 2 analyses compared to the analytical solution. As seen the difference of the analytical and Merlin solutions, although decreasing, lasts for CFL non-conforming analysis after 4 years.

Results show that the difference between the analytical and Merlin solutions are greater in Non-conforming analysis. In other words, failing to conform to the CFL condition had resulted in a delay in the convergence of the analysis.

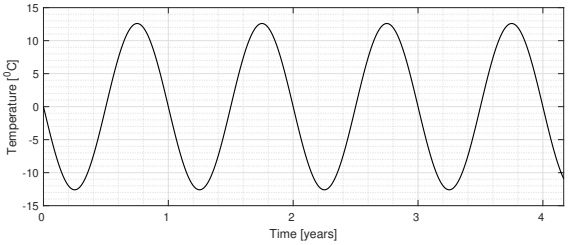

Figure B.13: Applied harmonic temperature

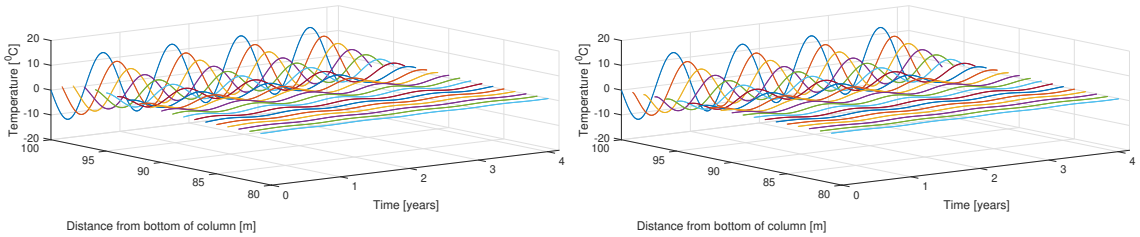

(a) analytical Solution (b) Merlin Solution

Figure B.14: Thermal analysis results of harmonic temperature applied at the end of the column

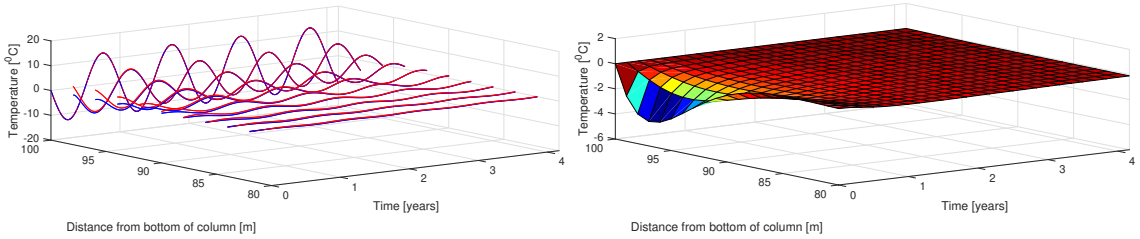

(a) Analytical vs. Merlin Solution (b) Difference of 2 solutions

Figure B.15: Comparison of Analytical and Merlin solutions of harmonic temperature applied at the end of the column

Table B.1: CFL conforming and non-conforming conditions

	$\mu\ [m^2 mo^{-1}]$	$\Delta t[mo]$	$h[m]$	$\frac{\mu \Delta t}{h^2}$
Case1	4.35	0.1	1	0.435
Case2	4.35	1	1	4.35
Case3	4.35	2	1	8.7

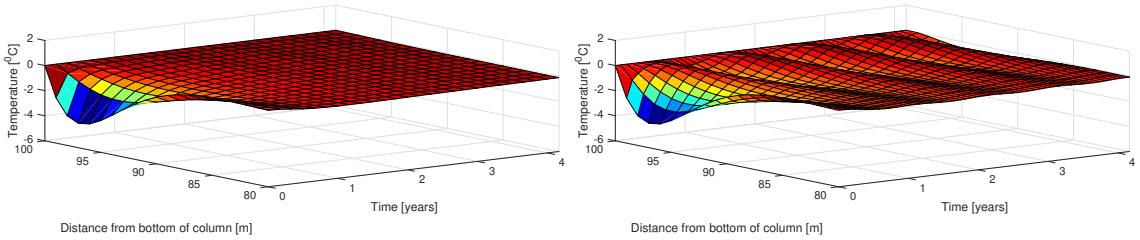

(a) Difference of 2 solutions, CFL Conforming (b) Difference of 2 solutions,CFL Non-conforming-Case 2

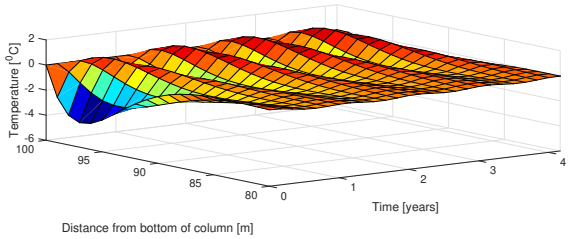

(c) Difference of 2 solutions,CFL Non-conforming-Case 3

Figure B.16: Comparison of results of CFL condition conforming and non conforming thermal analysis with harmonic temperature applied at the end of the column

B.2.2.2 Flux

In reality the temperature transfer from surrounding fluid cannot be simulated by applying the temperature directly to a material. In other words, there is a heat convection between the fluid and material and should be taken into account. In this study the fluid is considered to be air and, thus, the air-concrete film coefficient is used to apply the temperature using a flux rather than direct application. Therefore, the aforementioned constant and harmonic temperatures are repeated here to assess the effect of heat flux.

B.2.2.2.1 Constant Results for the heat flux with a constant temperature of 12.6 $[^oC]$ is shown in figure B.17.

B.2.2.2.2 Harmonic In this section the heat flux of a harmonic temperature is evaluated. Figure B.15 shows the Merlin solutions for the thermal analysis of column under harmonic temperature

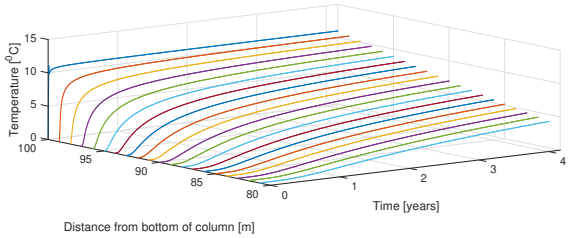

Figure B.17: Thermal analysis results of constant water temperature using flux applied at the end of the column

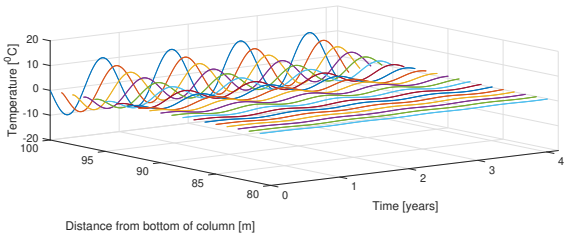

Figure B.18: Thermal analysis results of harmonic water temperature using flux applied at the end of the column

B.3 Solar radiation

In order to investigate the effect of solar radiation, a curved column presented in figure B.19, is first considered as an arch located at the upstream face of the Seminoe and then once again it is studied as a cantilever at the same location which is shown in figure B.19. In this study only the location and the orientation of Seminoe with respect to the south is used for solar radiation calculations and therefore the existence of water is omitted for the cantilever and solar radiation is calculated through the whole height of the column as this might be the case for other dams. As previously stated the model is a $1[m] \times 1[m] \times 100[m]$ concrete column and there are 100 elements through it's length. For the solar radiation study, only the elements on the convex side of the column were assumed to receive the solar radiation as they are facing the South. Studying the arch and cantilever will let us investigate both the effect of orientation and inclination of the surface in the received amount of solar radiation. Because the column has a curvature, the arch elements each have different orientations with respect to the South direction and cantilever elements each have different inclinations with respect to horizon, therefore, will receive different amount of solar radiations. Figure B.20 shows the temperature variation due to solar radiation through the length of the column within a year for both arch and cantilever. As seen in the figure, in the arch, the temperature increase is maximum at the center of the arch which is facing the South direction almost directly. As for the cantilever also the maximum tempertaure increase happens at the top of the cantilever as it is inclined upward and in turn receives the maximum direct solar radiation throughout the whole year. The temperature increase due to solar radiation is then added to the constant temperature of $12.6[^oC]$, which is the constant term of the air temperature at the Seminoe location, and thermal analysis is conducted using Merlin. The temperatures through the central axis of the column is shown in figure B.21 for about 3 years which is showing good stability even after a year. It should be noted that the distance between mesh elements that the information is expected to travel is $0.5[m]$ herein and therefore, in order to conform to the CFL condition, the analysis time step was set to $0.02[month]$. Figure B.22 is showing the procedure to calculate the temperature due to solar radiation to be applied on the curved column.

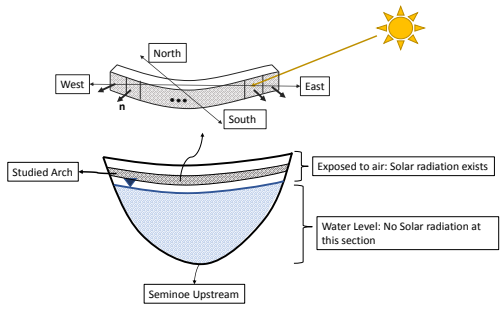

(a) Arch

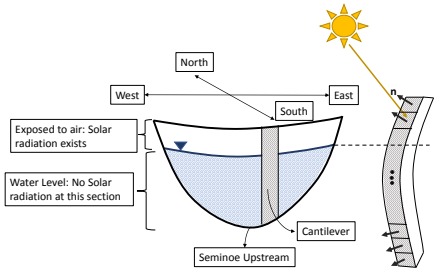

(b) Cantilever

Figure B.19: Studied arch and cantilever located at upstream Seminoe

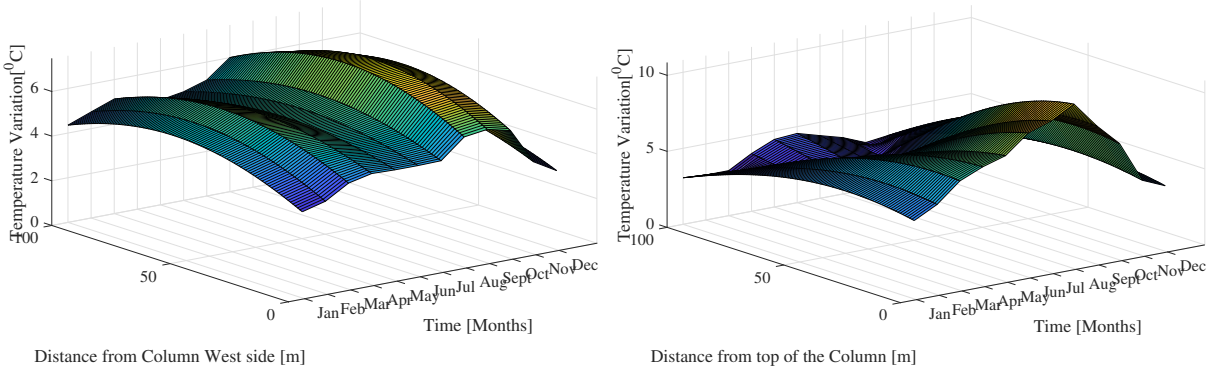

(a) Arch (b) Cantilever

Figure B.20: Temperature variation due to solar radiation throughout the curved column within 1 year

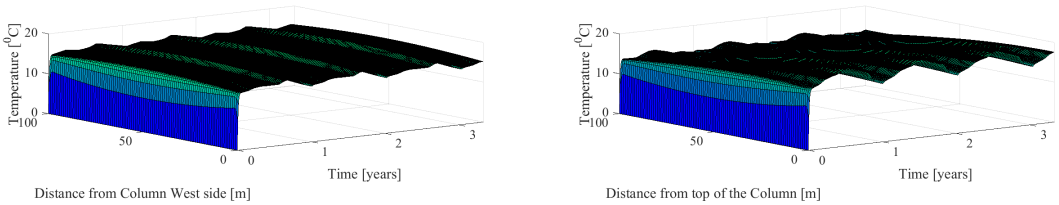

(a) Arch (b) Cantilever

Figure B.21: Thermal analysis result for nodes on the central axis of the curved column considering solar radiation effect

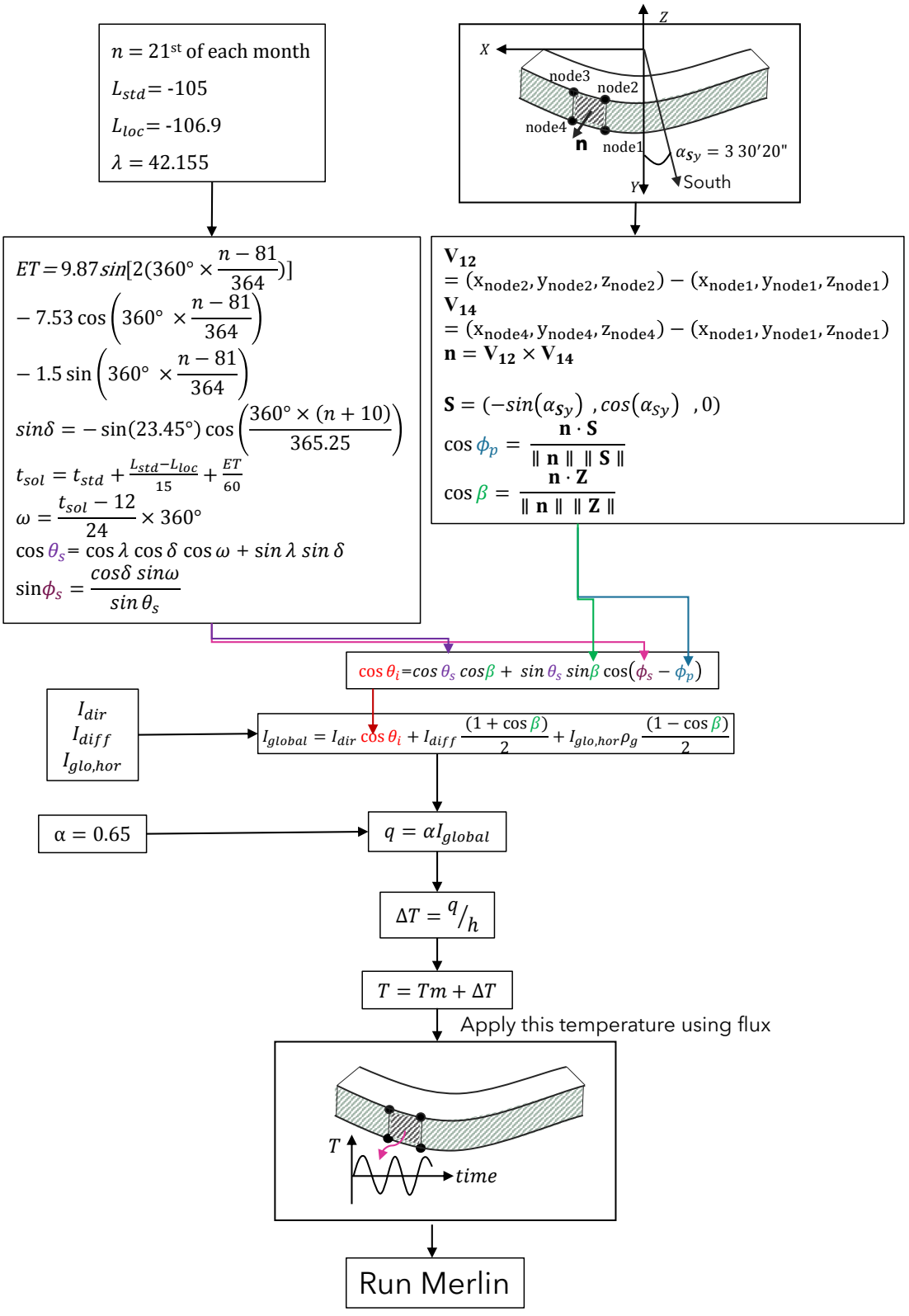

Figure B.22: Solar radiation calculation procedure for curved column

B.4 Conclusion

This chapter presented the smaller scale of the main thermal analysis to be conducted in the subsequent chapters. As described in this chapter, the thermal analysis of a single straight column was conducted using constant and harmonic temperatures applied directly to the top of the column and results compared to the numerical solution. Once the results validated the finit element method by showing a good match between the finite element and numerical solution, the stability of the solution was then assessed and thermal analysis was conducted using film coefficients to apply the temperatures to get closer to the real situation. In the next section, the purpose was to validate the solar radiation calculation presented in previous chapter, and therefore, two curved cantilever and arch were studied to determine their temperatuer increase due to solar radiation for which the results are shown and discussed.

Appendix C

Verification Study for Pool and Concrete Temperatures

Table C.1: Temperature data fitting

	a	b	c	ϕ	Method I	Method II
			Fontana			
Top	17.7415	-9.49679	0.70389	0.015827	0.902	0.994
Bot	5.612374	1.833289	8.823558			
Air	14.08135	9.601167	4.390997			
			Hoover			
Top	20.01634	-7.83074	0.714605	0.022716	0.936	0.984
Bot	12.04701	-1.22955	5.073473			
Air	23.07812	-12.0916	7.539764			
			Hiwassee			
Top	18.8469879	-11.0046	0.8444	0.02161	0.912	0.953
Bot	6.302679	-3.10449	12.13985			
Air	14.18313	10.17568	4.402833			
			Grand Coulee			
Top	9.224278	-10.6	0.645757	-0.02681	0.67548	0.78859
Bot	8.848105	-5.29629	19.1146			
Air	10.43781	-12.3562	1.258763			
			Hungry Horse			
Top	9.465751	-10.1285	0.694353	0.047607	0.933082	0.964424
Bot	4.733725	-0.93688	5.089331			
Air	6.051459	-11.8553	-5.05113			
			Owyhee			
Top	14.45718	-11.3601	0.977942	0.057675	0.965436	0.969316
Bot	4.37022	-0.3687	5.535384			
Air	11.16966	-11.0676	1.300982			
			Shasta			
Top	17.07467	-7.7792	0.75023	0.027206	0.910388	0.960983
Bot	7.115839	-1.81833	5.165946			
Air	17.13336	-9.66453	1.184623			

Table C.2: Temperature data fitting for Seminoe

	a	b	c	ϕ	Method I	Method II
			Seminoe			
Top	-10.6406	-30.2534	9.053441	0.237732	-0.024	0.596
Bot	-0.60584	-12.9162	2.650509			
Air	12.58733	-12.6138	0.974763			

Appendix D

Benchmark Problems for AAR FEA Code Validation

Abstract

Before a finite element code is used to perform AAR analysis, it is critical that it be first validated.

The RILEM international Committee on Diagnosis & Prognosis of AAR Affected Structures *has issued a series of benchmark problems. This chapter, taken from (***saouma-tc259***) is a enunciation of those problems.*

The analyses of these problems by the finite element code, Merlin, used in this report, will be reported in the next appendix.

D.1 Introduction

A number of structures worldwide are known to (or will) suffer from chemically induced expansion of the concrete. This includes not only the traditional alkali aggregate reaction (also known as alkali silica reaction) but increasingly delayed ettringite formation (DEF)[1].

There are three components to the investigation of structures suffering from such an internal deterioration: a) Chemo-physical characterization focusing primarily on the material; b) Computational modeling of the evolution of damage and assessing the structural response of the structure; and c) managing the structure, (**fasseu2003**).

When focusing on the second aspect, the ultimate objective is to make a predictive assessment of the structural condition and its significance under accidental or extreme scenarios, raising numerous considerations: a) Would future operation and serviceability be affected?, b) Would safety be compromised at some point in time?, and c) How will degradation and structural significance evolved over time. Answering those questions require predictive capabilities that are best addressed through numerical simulation (usually finite element analysis) accounting for the structure's inherent complexities. Assessing the capabilities of current finite element models to perform reliable are predictive structural assessment of ASR-affected concrete structure is the subject of the benchmark proposed in this chapter.

[1]It is well known that DEF is often associated with AAR, however it is increasingly observed that it can occur by itself in massive concrete structure subjected to early age high temperature and under high relative humidity (above 95%).

The assessment of finite element codes has been partially performed within the ICOLD International Benchmark Workshops on Numerical Analysis of Dams, and only limited discussion about AAR within the European project Integrity Assessment of Large Concrete Dams[2], NW-IALAD were conducted. Nevertheless a rigorous and rational assessment of existing codes capabilities remain to be conducted. This observation was recently strengthened by a benchmark study about shear walls subjected to AAR before being tested under reverse cyclic loading. For the sake of practice, models calibration of large structures should ideally be based on the inherently limited past inspection data, including permanent deformations of a dam's top of the spillway, or surface cracking maps for reinforced concrete. In the field of science and engineering, sound extrapolation and prediction of future degraded states rely on the validation of sophisticated numerical tools and softwares.

To date, finite element models of ASR-affected concrete structures are yet to be validated within a formal and rather systematic framework. The objective of the proposed benchmark is perceived by its authors as the initial step toward developing a formal approach recognized by the profession.

Although the authors are fully cognizant of the complexity of reactive transport phenomenons occurring in alkali-silica concrete, and their effects on damage development and residual expansion, connecting microstructural evolution and structural significance is considered beyond the scope of this study. The proposed study is focused on the interactions of temperature, relative humidity, chemically induced expansion, and mechanical loading.

The proposed benchmark includes two sets of problems, the first on material-scale concrete specimens, and the second, at the structural scale. The material-scale problems have been conceived to test the specific capabilities (strengths and deficiencies) of the benchmarked models to capture the effects of environmental factors and loading, individually or concurrently.

The description of the tests and the mandatory format for participant to reports their results are described hereafter. Test problems are presented with increasing complexity and difficulty with only a limited number of output parameters (generally only one). It is believed such a gradual validation of the constitutive models is needed and provides adequate validation to complex simulation of large-scale aging structures such as hydro-electric concrete dams and nuclear power plants's concrete containment subjected to either static and dynamic loading.

D.2 Objectives

This document is submitted by the authors to the Civil Engineering community for the assessment of finite element codes which can perform a "modern" simulation of reactive concrete-induced expansion.

The study includes two parts, the first addresses material modeling, and the second structure modeling. For the material modeling each study is split in two parts: a) parameter identification for the constitutive model (through calibration of the model with provided laboratory test results); and b) predictive capabilities.

[2]The sixth (Salzburg) and the eighth (Wuhan) benchmarks invited participants to analyze Pian Telessio and Poglia dams respectively. There was no submission to the former, and only two for the second.

D.3 Important Factors in Reactive Concrete

Assuming that the final residual swelling of the reactive concrete is known, and based on experimental and field observations, indications are that the following factors[3] should be considered in the finite element analysis of a structure:

1. Environmental Conditions of the concrete
   (a) Temperature
   (b) Humidity
2. Constitutive models
   (a) Solid concrete (tension, compression, creep, shrinkage)
   (b) Cracks/joints/interfaces.
3. Load history
4. Mechanical Boundary Conditions
   (a) Structural Arrangement
   (b) Reinforcement
   (c) Anchorage

D.4 Test Problems

Table D.1 describes the 11 problems defined. Participants do not have to consider all of them and may select only those appropriate for their finite element code.

Table D.1: List of Benchmark Problems

No.	Description
P0	Textual description of finite element code/models
	Material Response
P1	Constitutive model
P2	Capturing drying and shrinkage
P3	Capturing creep
P4	Effect of Temperature
P5	Effect of RH
P6	Effect of confinement
	Structural Response
P7	Internal reinforcement
P8	Reinforced concrete beam
P9	Dam (simplified)
P10	Reinforced concrete panel expansion
P11	Nuclear containment vessel (Simplified)

D.4.1 Units

For all problems use: m, sec., MN, and MPa.

[3]There is no general agreement on the importance of all these parameters, the list is intended to be inclusive of all those perceived by researchers to be worth examining.

D.4.2 P0: Finite Element Model Description

This very first section should include up to five pages of description of the model adopted in this particular order:

Constitutive Model

1. Basic principles of the model and its implementation.
2. Nonlinear constitutive model of sound or damaged concrete (clarify)
   (a) Instantaneous response (elasticity, damage, plasticity, fracture and others)
   (b) Delayed response (creep and shrinkage)
3. Effect on the chemically induced expansion by
   (a) Moisture
   (b) Temperature
   (c) Stress confinement
4. Effect on the mechanical properties of concrete by
   (a) Expansion
   (b) Shrinkage and creep

Finite Element Code Features

1. Gap Element
2. Coupled hydro-thermo-mechanical
3. Others

D.4.3 Materials

In light of the preceding list of factors influencing AAR, the following test problems are proposed.

D.4.3.1 P1: Constitutive Models

At the heart of each code is the constitutive model of concrete. This problem will assess the code capabilities to capture the nonlinear response in both tension and compression.

It should be noted that in some codes, (**sellier2009combination**) the constitutive model is tightly coupled (in parallel) with the AAR expansion one (modeled as an internal pressure), in other, (**saouma-aar-1**) it is more loosely coupled (in series) with the AAR (modeled as an additional strain).

D.4.3.1.1 Constitutive Model Calibration Perform a finite element analysis of a 16 by 32 cm concrete cylinder with f'_c, f'_t and E equal to 38.4 MPa, 3.5 MPa and 37.3 GPa respectively[4]. Traction is applied on the top surface, and a frictionless base is assumed. Make and state any appropriate assumption necessary, use the following imposed strain histogram:

$$0 \rightarrow 1.5\frac{f'_t}{E} \rightarrow 0 \rightarrow 3\frac{f'_t}{E} \rightarrow 1.5\varepsilon_c \rightarrow 0 \rightarrow 3\varepsilon_c \tag{D.1}$$

where $\varepsilon_c = -0.002$. If needed, the fracture energy G_F in tension and compression are equal to 100Nm/m^2 and 10,000 Nm/m^2 respectively.

[4]These parameters should be used in all subsequent test problems.

D.4.3.1.2 Prediction Repeat the previous analysis following an AAR induced expansion of 0.5%, you may use the experimentally obtained degradation curve, by (**ise92**) and published by **capra03empty citation**, Fig. D.1

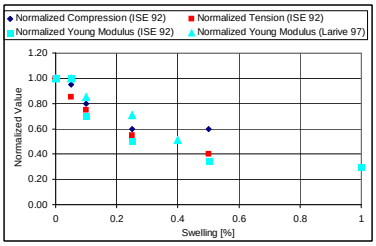

Figure D.1: Deterioration of AAR affected concrete (**capra03**)

Prediction should highlight concrete mechanical properties degradation in terms of ASR evolution; in particular: Young modulus, tensile and compressive strengths.

D.4.3.2 P2: Drying and Shrinkage

For some structures not necessarily under water (such as bridges or certain hydraulic structures), drying shrinkage strains may be of similar order of magnitude as the AAR induced ones. As shown in Fig. D.2 one must consider various cases of drying and shrinkage, reactive and non reactive concrete, and at relative humidities ranging from a low 30% to a fully saturated environment, and sealed or not. There are a total of 6 potential cases of interest:

a. Non reactive concrete at 30% RH
b. Reactive concrete at 30% humidity
c. Non Reactive concrete sealed specimen
d. Non Reactive concrete under water.
e. Reactive Concrete, sealed cylinder.
f. Reactive concrete under water. Note that this is not identical to a 100% RH if leaching is to be accounted for.

which will be analyzed in P2 and P5

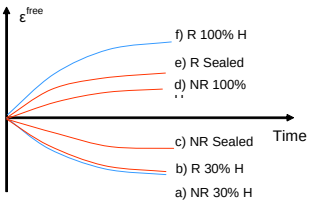

Figure D.2: Drying and Shrinkage test Cases

D.4.3.2.1 Constitutive Model Calibration For calibration purposes, the parameters can be fitted using a 16 by 32 cm cylinder to perform the following analyses: a, c, and d with respect to the temporal

variation of mass (Fig. D.3(a)) and longitudinal strain (Fig. D.3(b)). For initial condition, assume an initial saturation of 0.85, and $T(t=0) = 38°\text{C}$

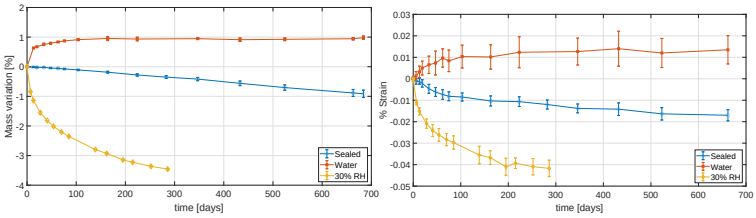

(a) Mass variations (b) Strain Variation

Figure D.3: Non reactive concrete under various RH conditions; (**multon06**)

D.4.3.2.2 Prediction Using the parameter determined from the previous section, repeat the same analysis with the temporal annual variation of external RH for the cylinder shown in Fig. D.4.

$$RH(\text{week}) = \frac{RH_{\max} - RH_{\min}}{2} \sin\left(2\pi \frac{t-16}{52}\right) + \frac{RH_{\max} + RH_{\min}}{2} \tag{D.2}$$

where $RH_{\max}$ and $RH_{\min}$ are equal to 95% and 60% respectively, and $T(t=0) = 20°\text{C}$. The model response

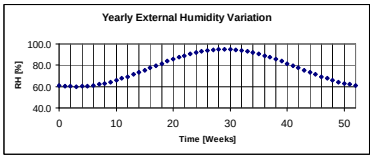

Figure D.4: Humidity variation

should first exhibit a negative strain due to shrinkage and then a positive strain due to water absorption until 30 weeks and finally new shrinkage until 52 weeks.

D.4.3.3 P3: Basic Creep

There is strong experimental and field indications that creep plays a dominant role in the irreversible long term deformation concrete subjected to constant load. Its effect must be accounted for to properly extract the AAR expansion. This may be explained through biaxially or triaxially loaded elements where swelling is restricted in one direction while free to occur on the other(s). Therefore, in the AAR constrained direction creep deformation will be predominant. This is more likely to occur in arch dams.

D.4.3.3.1 Constitutive Model Calibration For a 13 by 24 cm cylinder subjected to 10 and 20 MPa axial compression, plot the longitudinal and radial displacements. You may calibrate your model on the experimental curve shown in Fig. D.5.

D.4.3.3.2 Prediction Using the previously determined parameters, repeat the same analysis for the axial load history shown in Fig. D.6. During the first 16 first weeks, the model should exhibit negative strain due to creep. The load increase at the 16th week should imply an instantaneous strain followed by

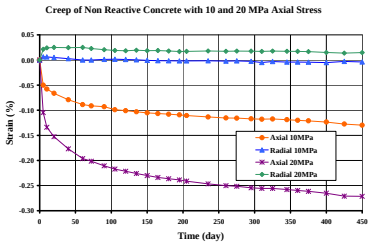

Figure D.5: Creep in non-reactive concrete under sealed condition for different axial stress; (**multon06**)

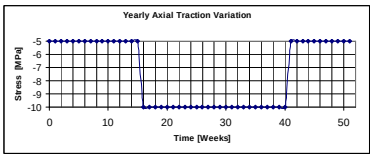

Figure D.6: Stress variation

creep until the 40th week. Then, partial creep recovery should be observed during the first days following unloading.

D.4.3.4 P4: AAR Expansion; Temperature Effect

All chemical reactions are thermodynamically driven. Reactive concrete expansion varies widely with temperature ranges usually encountered in the field or laboratories. Hence, it is of paramount importance that the kinetics of the reaction captures this dependency.

D.4.3.4.1 Constitutive Model Calibration Perform the finite element analysis of a 13 by 24 cm cylinder under water, free to deform at the base and undergoing a free expansion, and for $T = 23^o$C and 38°C. Fit the appropriate parameters of your model with Fig. D.7 obtained by **larive1998LCPCempty citation**.

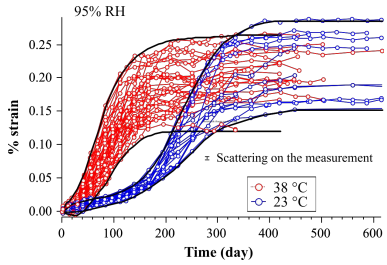

Figure D.7: Free expansion from Larive's tests;(**larive1998LCPC**)

D.4.3.4.2 Prediction Repeat the previous analysis using the variable internal annual temperature variation

$$T(\text{week}) = \frac{T_{\max} - T_{\min}}{2} \sin\left(2\pi \frac{t-16}{52}\right) + \frac{T_{\max} + T_{\min}}{2} \tag{D.3}$$

where $T_{\max}$ and $T_{\min}$ are equal to 25°C and 0°C respectively, as shown in Fig. D.8. Use $RH(t=0) = 100\%$ and $T(t=0) = 10°\text{C}$.

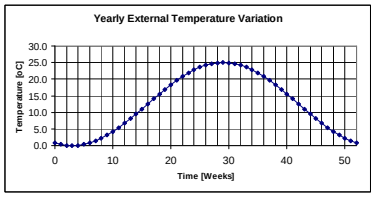

Figure D.8: Temperature variation

As the dependence of ASR characteristic times to temperature is exponential, the predictions should be highly non linear. ASR rate should be very slow down during cold period and accelerate during hot period without in a nonlinear response.

D.4.3.5 P5: Free AAR Expansion; Effect of RH

Relative humidity plays a critical role in the expansion of AAR affected concrete. It is well established (**poole92**) that expansion will start for a RH at least equal to 80%, and will then increase with RH (RH^8 is a widely accepted formula). For external bridge structures and some dams this can be critical.

D.4.3.5.1 Constitutive Model Calibration Using a 16 by 32 cm cylinder, and assuming a temperature of 38°C, fit the appropriate parameters for mass and vertical strain variation of reactive concrete as shown in Fig. D.9(a) and D.9(b) respectively. Use $RH(t=0) = 85\%$.

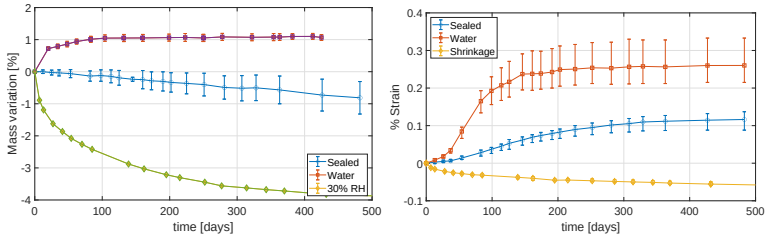

(a) Mass variation (b) Strain Variation

Figure D.9: Reactive concrete under various RH conditions;(**multon2005structural**)

D.4.3.5.2 Prediction Repeat previous analysis using the RH variation shown in Fig. D.4.

ASR rate should be increased during high saturation and decreased during dry periods.

D.4.3.6 P6: AAR Expansion; Effect of Confinement

It has long been recognized that confinement inhibits reactive concrete expansion, (**charlwood92**), (**leger96**) and most recently (**multon06**). This test series seeks to ensure that this is properly captured by the numerical model.

D.4.3.6.1 Constitutive Model Calibration For a 13 by 24 cm cylinder, and assuming a temperature of 38°C, analyze the following test cases (all of which consist of sealed specimens):

P6-a. No vertical stress, no confinement (Free swelling), Fig. D.10(a).

P6-b. Vertical stress of 10 MPa, no confinement, Fig. D.10(b).

P6-c. No vertical stress, concrete cast in a 5 mm thick steel container, Fig. D.10(c).

P6-d. Vertical stress of 10 MPa and concrete cast in a 5 mm thick steel container, Fig. D.10(d).

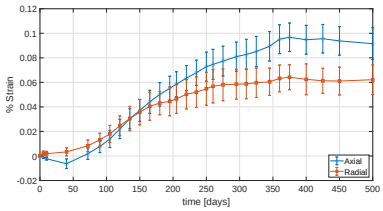

(a) No vertical stress, no confinement (free swelling)

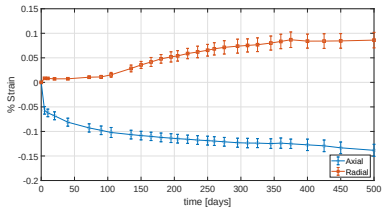

(b) 10 MPa vertical stress, no confinement;

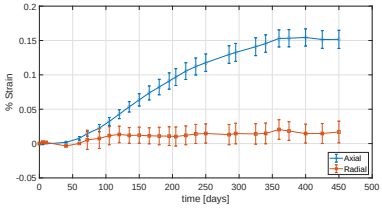

(c) Vertical stress of 10 MPa and concrete cast in a 5 mm thick steel container;

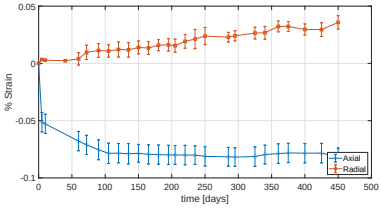

(d) Vertical stress of 10 MPa and concrete cast in a 5 mm steel container;

Figure D.10: Expansions in terms of confinements (**multon06**)

In all cases, plot both the axial and radial strains.

D.4.3.6.2 Prediction Repeat the analysis with the vertically imposed stress histogram shown in Fig. D.6.

With such compressive loading, ASR expansion should not be observed in the axial direction. However, creep should be the main cause of negative strain. In radial direction, ASR expansion should be higher than for stress-free expansion.

D.4.4 Structures

D.4.4.1 P7: Effect of Internal Reinforcement

D.4.4.1.1 Description Internal reinforcement inhibits expansion and AAR induced cracking would then align themselves with the direction of reinforcement as opposed to the traditional "map cracking". This test problem seeks to determine how the numerical model accounts for this, especially when cracking (thus a nonlinear analysis is needed) occurs.

Analyze the cylinder shown in Fig. D.11 under the same condition (free expansion, 38°C, 100% RH), for the same duration with a single internal reinforcing bar of diameter 12 mm in the center, and E=200,000 MPa and f_y =500 MPa.

D.4.4.1.2 Prediction Determine longitudinal strain in the rebar and the longitudinal and radial strains on the surface of the concrete cylinder. In both cases values are to be determined at mid-height.

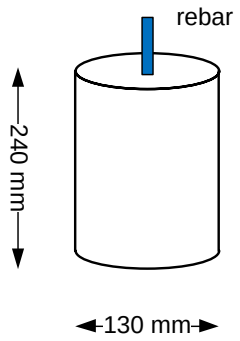

Figure D.11: Concrete prism with internal reinforcement

Expansion should be reduced along the reinforcement and compressive stresses should develop orthogonally. Small modification of expansion should be observed in the directions perpendicular to steel bar. If evaluated, cracking should be parallel to the reinforcement.

D.4.4.2 P8: Reinforced Concrete Beams

D.4.4.2.1 Description The mechanical behavior of two concrete beams, studied by S. Multon during his Ph.D. works at LCPC, is proposed. One beam is damaged by ASR during two years of exposure in a 38°C environment and differential water supply, leading to differential ASR expansion within the structures (**multon2003evaluation**). The other made with non-reactive aggregates was stored in similar conditions. Namely, the effects of the ASR development have been quantified in a 4-points bending test of the beams, resulting in a lot of data among which the residual stiffness and the flexural strength of both reactive and non-reactive beams. The objective is to simulate the evolution of the two beams during the two years of tests, and to finish by a simulation of beam failure in four points bending, Fig. D.12.

Material characteristic are the same then in tests P1 to P6, therefore, the LCPC performed tests at several dates since the fabrication. Results are given in Table D.2. During the 2-years aging phase, beams were placed on simple bearings along the geometrical mid-height (span of 2.8 m): steel bars were embedded at mid-height of the structure. During the 4-point bending test, beams were simply supported on the lower face (span of 2.75 m).

In the present benchmark only beams P4 and P6, Fig. D.12, have to be simulated.

Table D.2: Reinforced Concrete beam mechanical properties

	28 days	180 days	2 years	
	Reactive Concrete			
E	37,300	30,100	34,600	MPa
f_c	38.4	41.2	43	MPa
f_t	3.5	3.4	3.8	MPa
	Non-Reactive Concrete			
E	38,700	37,800	38,700	MPa
f_c	35.5	40.4	43	MPa
f_t	3.6	3.2	3.7	MPa

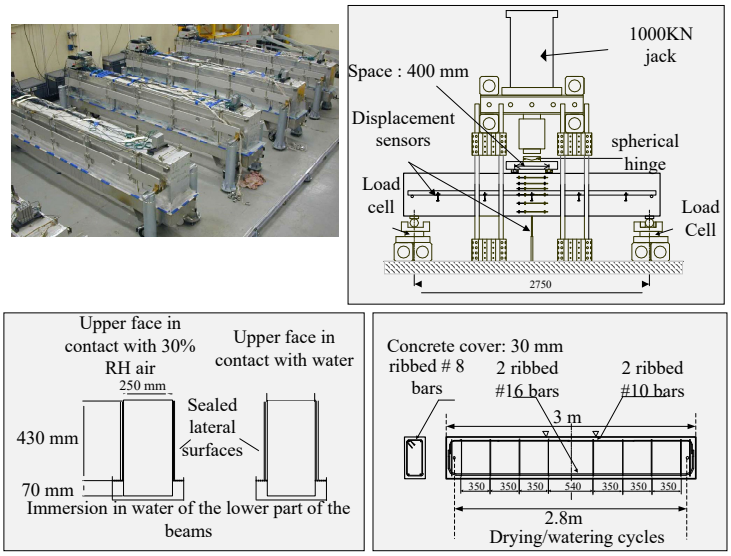

Figure D.12: Multon's Beams

As AAR depends on humidity, a humidity profile must be fitted, in order to consider effect of saturation on the reaction. In order to fit the drying-humidification cycle, the mass evolutions of the beams are given below.

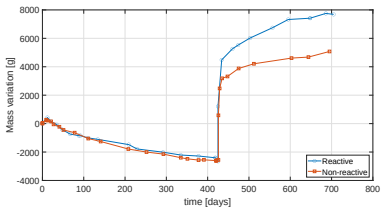

Figure D.13: Mass variation of the beams

Initial saturation of the beam is 0.85, temperature is constant and equal to 38°C. The concrete porosity is around 16% (15% at the bottom and 17% at the top of the beam).

D.4.4.2.2 Prediction

- The first objective is to find a realistic humidity profile compatible with the mass variation history given in figure D.13.
- The second objective is to predict the deflection of each beam, at mid span, versus time
- The third objective is the evolution of stress versus time, in the bottom longitudinal reinforcement #16, at mid span.
- The last stage consists in simulating for the two beams a four point bending test schematized in Fig. D.12. Participants have to provide the Force-deflection curve until failure of each beam.

Numerical results can be compared to experimental results presented in (**multon2003evaluation**) to assess precision of the model.

D.4.4.3 P9: AAR Expansion; Idealized Dam

D.4.4.3.1 Description This next test problem assesses the various coupling amongst various parameters as well as the finite element code and its ability to simulate closure of joint. A common remedy for AAR induced damage in dams is to cut a slot in the structure (**newell1999fontana**; **caron2003slot**; **gilks03**; **metalssi2014modeling**). This will relieve the state of stress, and allow the concrete to expand freely. However, at some point concrete swelling will result in a contact between the two sides of the slot. Hence, this problem will test the model ability to capture this important simulation aspect as well.

Consider the reduced dam model shown in Fig. D.14 with the following conditions: a) lateral and bottom faces are all fully restrained; b) front back and top faces are free; c) slot cut at time zero, total thickness 10 mm; d) concrete on the right is reactive, and concrete block on the left is not reactive; e) hydrostatic pressure is applied only on the right block.

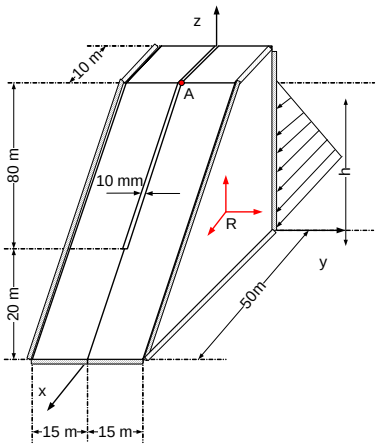

Figure D.14: Idealized dam

D.4.4.3.2 Prediction Using the fitting data of P6, and an friction angle of 50° for concrete against concrete, and zero cohesion, consider two cases:

- Homogeneous field of internal temperature (20°C), relative humidity (100%), and an empty reservoir.
- Transient field of external temperature Fig. D.8, relative external humidity Fig. D.4, and pool elevation variation Fig. D.15 given by where ELmax and ELmin are equal to 95 and 60 respectively.

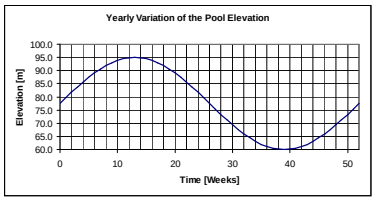

Figure D.15: Yearly variation of pool elevation

For both analysis, the specified temperature and relative humidity is the one of the concrete surface. Zero flux condition between dam and foundation. Reference base temperature of the dam is 20^oC.

- x, y, z displacements of point A.

- Fx, Fy and Fz resultant forces on the fixed lateral face versus time (25 years). Assume the typical yearly variations of external air temperature and pool elevation shown in Fig. D.8 and D.15 respectively.

This model seeks to capture: a) general finite element program capabilities in modeling the joint response; b) ease (or difficulty in preparing the input data file for a realistic problem; and c) coupling of the various parameters.

$$EL(\text{week}) = \frac{EL_{\max} - EL_{\min}}{2} \sin\left(2\pi \frac{t}{52}\right) + \frac{EL_{\max} - EL_{\min}}{2} \tag{D.4}$$

where $EL_{\max}$ and $EL_{\min}$ are equal to 95 and 60 respectively.

The slot cutting and subsequent joint closure due to ASR expansion reflect the high nonlinearity of the FE calculation. In this case, modelling should capture stress release caused by cutting and subsequent contact of the surfaces without numerical convergence problems. Of primordial importance will be the stress redistribution in the dam through the various phases.

D.4.4.4 P10: Expansion of RC Panel With or Without Lateral Confinement

This section has been prepared with the assistance of Nolan Hayes, Ammar Abd-Elssamd and Qiang Gui from the University of Tennessee, Knoxville.

The University of Tennessee, Knoxville (UTK), under U.S. Department of Energy (DOE) subcontract managed by Oak Ridge National Laboratory (ORNL), have been performing large scale laboratory testing of confined and unconfined concrete blocks (simulating a typical reinforced concrete member found in light water reactor nuclear power plants).

The objective of this benchmark test case is to perform predictive numerical simulations of two large-scale reinforced concrete blocks (with different boundary conditions) and compare the simulation results with the already collected monitoring data.

D.4.4.4.1 Description

Geometry The laterally-confined reinforced concrete reactive specimen, referred to as *CASR* ("C" for confined), is cast inside a rigid steel frame while a similar reinforced concrete reactive specimen, referred to as *UASR* ('U', for unconfined) is allowed to expand without lateral restraints. A third specimen, non-reactive, referred to as *CTRL*, for control, is also not subjected to lateral restraints (**hayes2018monitoring**). See summary in Table D.3

All three specimens of dimensions, $136'' \times 116'' \times 40''$ (length, width and height; x-y-z axis), i.e., 3.453 m × 2.946 × 1.016 m, Fig. D.16 are reinforced near the top and the bottom faces by two welded layers of orthogonal rebars: (22) #11 bars (1.41" nominal diameter, cross section area: 1006 mm^2), (10) in one direction and (12) in the perpendicular direction, placed in horizontal planes – See Fig. D.16(d) for layout. Rebars are made of standard carbon steel. Square plate heads (4" × 4" × 1", i.e., 10.16 cm × 10.16 cm × 2.54 cm) are welded to the rebar extremities. The concrete cover, in the least distance to the concrete outer surface, is 3" (7.62 cm). There is no reinforcement in the third, i.e.,

Table D.3: Characteristics of the three specimens

ID	Label	Confined	Reactive
1	CASR	Yes	Yes
2	UASR	No	Yes
3	CTRL	No	No

vertical, direction, to the exception of (6) #11 debonded rebar spacers placed inside of pipes to allow free vertical expansion during the test.

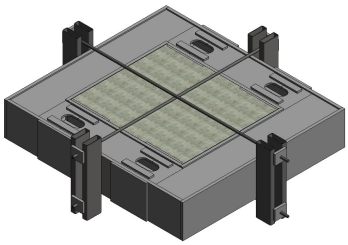

(a) Computer rendering of the confined specimen (CASR)

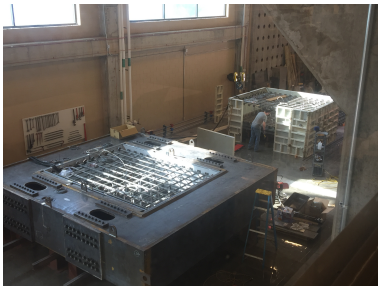

(b) Form construction in UTK Civ. Env. Eng. high bay

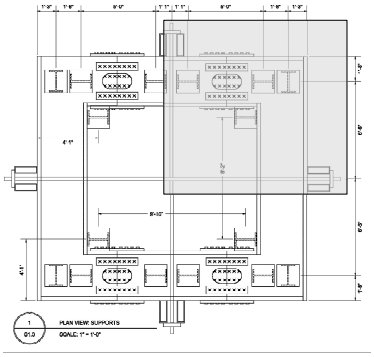

(c) Confined specimen layout – Top view. (Shaded area indicating symmetries)

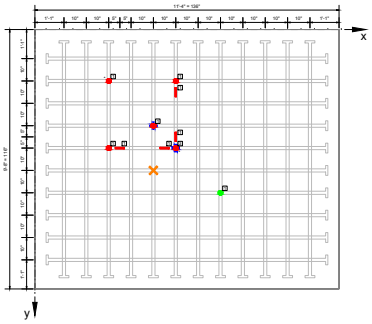

(d) Reinforcement layout – Top view. Bottom and top reinforcement layout are identical.

Figure D.16: Reinforced concrete panel test problem (**hayes2018monitoring**)

Steel Confinement Frame The steel plate girder frame was designed with the primary goal of maximizing stiffness in bending. In order to achieve this goal, 3" thick plates, height 3'4", were chosen as flanges to the plate girder. These flanges are connected by three 2" thick web plates, length 2'10". All steel was manufactured from A572 Grade 50 steel plate. Design of splice plate connection not provided here is available upon request.

In order to reduce frictional effects between the steel frame and the concrete specimen, a single layer (thickness: 1.5 mm) of high-density polyethylene (HDPE) was introduced at the interface, providing a low steel-HDPE friction coefficient estimated by the vendor around 0.3 and unilateral contact conditions.

Additional Post-tensioned system Four threadbar post-tension bars (2 in each direction, 2.5 inches dia.) manufactured by DYWIDAG-Systems International (DSI) were installed in September 2016, in order to increase the confining force, if necessary. It is initially just slightly tightened to avoid "slack", and has remained, as of today.

Casting and Curing Casting took place July 23rd 2016. In an attempt to mitigate potential crack sources other than ASR, the formworks were insulated by placing rigid foam sheathing insulation with an R-value of three around the side and on top of the specimens, shortly after pouring. The insulation was placed with edges overlapping and secured in place with tape and plastic wrap.

All formworks were removed on August 4, 2016. Each large specimen and concrete cylinder, for further materials testing, was covered with wet burlap to prevent moisture loss. The burlap was periodically moistened as required to keep the concrete surfaces wet.

A few days after casting, the bottom support is removed, and the concrete block is vertically supported by four $18'' \times 18''$ (45.7 cm $\times$ 45.7 cm) corner plates. Plates are directly supporting the specimens on the concrete surface. The estimated steel-concrete friction coefficient is $\approx$0.6.

Operation A modular environmental chamber was designed by Norlake Scientific with the initial primary goals for temperature and humidity control being 100^{o}f $\pm$ 2^{o}f (38^{o}C $\pm$ 1^{o}C) and 95% $\pm$ 5%. The chamber was initialized for full operation early morning August 19, 2016.

The chamber is periodically shutdown for inspection on a average frequency of 2 days per month. During shutdowns, the average temperature and RH are about $\approx 77^{o}$f (25^{o}C) and 60% (transient of about 4 hours). After the shutdown period, the chamber is restarted and and the temperature and humidity return to the original set points within 6 hours.

Target mix design The mix design has been extensively investigated at the University of Alabama, and the one retained, including a reactive and a control mix, is shown in Table D.4 with 1" (25 mm) maximum size aggregate (MSA) composed of Green schist – muscovite, chlorite, quartz, Na-feldspar, K-feldspar, calcite, and, cristobalite.

In this mix, only the coarse aggregate is reactive. A 50% sodium hydroxide solution (NaOH) is used to increase the alkali loading of the reactive mix to 5.25 kg.m^{-3}, and a 30% lithium nitrate solution (LiNO3) is used at 150% of the manufacturerś recommended dosage to mitigate ASR for the control mix.

Table D.4: Target mix design . Aggregate quantities are for oven-dry material. Water quantities assume aggregates in saturated-surface dry (SSD) condition. $^{(*)}$ To limit the early-age temperature below $\approx 65^{o}$C, about 70% of the water was added to the mix as ice cubes.

Materials	Quantity, kg.m^{-3} (lb.yd^{-3})	
	Reactive	Control
Coarse Aggregate	1180 (1988.8)	1180 (1988.8)
Fine Aggregate	728 (1226.6)	728 (1226.6)
Cement	350 (590)	350 (590)
Water$^{(*)}$	175 (295)	175 (295)
w/c	0.5	0.5
NaOH solution	9.8 (16.6)	-
$LiNO_3$ solution	-	11.9 (20.03)

Mechanical properties 28 days mechanical properties compressive and tensile strengths, and the elastic modulus are shown in Table D.5, D.6 and D.7, respectively along with their mean and standard deviations.

Table D.5: Reported 28 days compressive strengths f'_c (MPa)

Specimen Type	AVG	STD
CASR	22.2	2.07
UASR	20.7	1.17

CASR: Confined Reactive Specimen

UASR: Unconfined Reactive Specimen

A representative 28 days stress-strain curve is shown in Fig. D.17.

Table D.6: Reported 28 days tensile strengths f'_t (MPa)

Specimen Type	AVG	STD
CASR	2.70	0.215
UASR	2.13	0.044

CASR: Confined Reactive Specimen
UASR: Unconfined Reactive Specimen

Table D.7: Reported 28 days elastic modulus E_c (GPa)

Specimen Type	AVG	STD
CASR	34.5	3.03
UASR	34.4	2.22

CASR: Confined Reactive Specimen
UASR: Unconfined Reactive Specimen

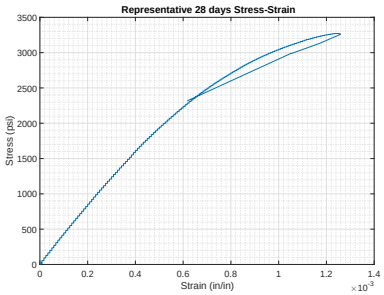

Figure D.17: Stress Strain curve (28 days)

Shrinkage Shrinkage has been measured in the CTRL specimen. The datapoints for the shrinkage curve are shown in Table D.8.

Table D.8: Provided shrinkage curve data

Measured Shrinkage	
Age (Days)	Shrinkage
5	-0.0031%
10	-0.0104%
20	0.0162%
30	-0.0178%
40	-0.0185%
50	-0.0190%
60	-0.0194%
100	-0.0214%
200	-0.0245%
300	-0.0275%

Expansion curves obtained from earlier material testing Expansion curves were obtained by Pr. E. Giannini, at the University of Alabama (UA), while testing different aggregates-forming concrete. The concrete blocks, $300 \times 300 \times 600$ mm, are stored in UA climate chamber at 38°C and 95%RH, shown in Fig. D.18, and their expansion was periodically monitored using DEMEC points.

Data are tabulated in Table D.9 and shown in Fig. D.19(a) where the vertical expansions were taken over a 150 mm gauge length, and longitudinal expansions (same direction as longitudinal) were taken

Figure D.18: Concrete expansion block tested by Prof. E. Giannini

over a 500 mm gauge length. It should be noted that the reported mean (or average) corresponds to the average of all the experimental values.

Table D.9: Provided expansion curve data

Calculated Expansions		
Age (Days)	Average Exp.	STD
6	0.000%	0.0000%
40	-0.004%	0.0045%
68	0.000%	0.0031%
87	0.012%	0.0081%
103	0.020%	0.0091%
117	0.028%	0.0103%
138	0.045%	0.0193%
152	0.057%	0.0250%
170	0.070%	0.0307%
190	0.088%	0.0382%
220	0.103%	0.0440%
304	0.146%	0.0634%
312	0.157%	0.0733%
350	0.165%	0.0729%
371	0.174%	0.0782%
459	0.192%	0.0885%
504	0.197%	0.0903%

Recorders/sensors location Recorder[5] locations are shown as follows:

Embedded KM strain transducer (KM-100B) , referred as *strain gauges*, gauge length 100 mm, in Fig. D.19(b) and Table D.10.

Resistive strain gauges General purpose resistive strain gauges (gauge length: 1.52 mm) were attached to the reinforcing bars in the specimens. These sensors are attached to the top and bottom of the rebar in the select locations to measure rebar strain. The location of resistive strain gauges of interest are shown in Fig. D.19(b) and Table D.10.

Long gauges fiber-optics-based deformation sensors (SofO, gauge length $\approx$ 1.0–1.5 m with location) measure (1) the vertical deformation between the bottom and top rebars layers, and, (2) horizontal deformation at the bottom surface as illustrated and tabulated in Fig. D.20 and Table D.11

Test duration Casting occurred July 23rd 2016. Assuming testing will end April 19, 2019, it is requested to model a total duration of 1,000-days.

[5]In a finite element analysis, point from which we determine computed values are commonly referred to as "recorders"

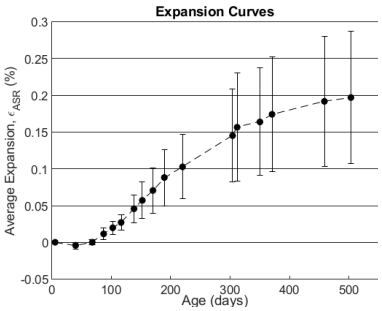

(a) Laboratory measured expansion. Error bars: standarddeviation.

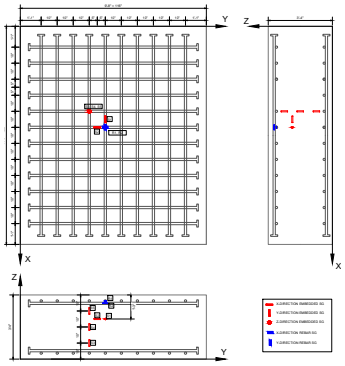

(b) Location of internal concrete gauges

Figure D.19: Recorded expansion

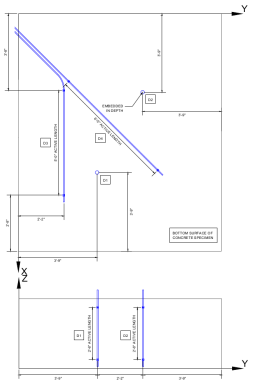

Figure D.20: Location of deformation sensors

D.4.4.4.2 Predictions Plot for both specimens, CASR and UASR, as a function of time (increments of one month) the following model outputs:

1. Vertical displacements at D1
2. Concrete strain at S1, S2, S3, S4 and S5.
3. Reinforcement strains at R1 and R2

Numerical results can be compared to experimental data published in (**hayes2018monitoring**).

D.4.4.5 P11: AAR Expansion of Nuclear Containment Vessel Followed by Earthquake

D.4.4.5.1 Description Ultimately, codes should be able to analyze nuclear containment vessel structures suffering from AAR under dynamic excitation.

Table D.10: Strain gauges location points. 'S' refers to KM embedded sensors, while 'R' refers to resistive strain gauges placed directly on the rebars.

		Coord. [inches]			Coord. [meter]		
ID	Dof	x	y	z	x	y	z
S1	1	58	53	25	1.473	1.346	0.635
S2	2	63	48	25	1.600	1.219	0.635
S3	3	53	43	10	1.346	1.092	0.254
S4	3	53	43	20	1.346	1.092	0.508
S5	3	53	43	30	1.346	1.092	0.762
R1	1	63	53	36.375	1.600	1.346	0.924
R2	2	63	53	34.875	1.600	1.346	0.886

Table D.11: Deformation sensor location points

		Start Coord. [inches]			End Coord. [inches]			Start Coord. [meter]			End Coord. [meter]		
ID	Dof	x	y	z	x	y	z	x	y	z	x	y	z
		Coord. inches			Coord. [meter]								
D1	3	91	45	4.25	91	45	35.75	2.311	1.143	0.108	2.311	1.143	0.908
D2	3	45	71	4.25	45	71	35.75	2.311	1.143	0.108	2.311	1.143	0.908
D3	1	45	26	0	104	26	0	1.143	0.660	0	2.642	0.660	0
D4	1-2	38.75	28.75	0	89.75	79.75	0	0.984	0.730	0	2.280	2.026	0

Accordingly, a much simplified geometry, inspired by **nureg6706empty citation**, is adopted. Fig. D.21(a) shows the dimensions as well as the key material parameters. Note that the mat foundation and the walls only are subjected to AAR, the dome is not.

Total reinforcement is 1% vertically, and 0.5% circumferentially. Reinforcement in each direction is to be split in two layers, each 10 cm from the wall. Ignore reinforcement of the dome, however triple the elastic modulus of the concrete. Steel elastic modulus is 200 GPa, and yield stress 250 MPa.

For added clarity, the boundary conditions, and the expansion curve is shown in Fig. D.21(b). Only gravity and AAR loads are first considered. Note that the AAR expansion is assumed to follow Larive's curve (**larive98**)

$$\varepsilon(t) = \varepsilon^{\infty} \frac{1 - \exp(-\frac{t}{\tau_c})}{1 + \exp\left(-\frac{(t-\tau_l)}{\tau_c}\right)} \tag{D.5}$$

D.4.4.5.2 Prediction

Two sets of analyses are required:

D.4.4.5.3 Static

Though an axisymmetric analysis is possible, it is highly recommended that a 3D one (using 180° segment) be performed. Plot

1. Horizontal displacement of point A (Δ_x) versus time (increments of one month).
2. Maximum (positive) principal stress ($\sigma_{(1)}$) in the wall versus time.
3. Crack profiles at $t = [5, 10, 20, 30]$ years

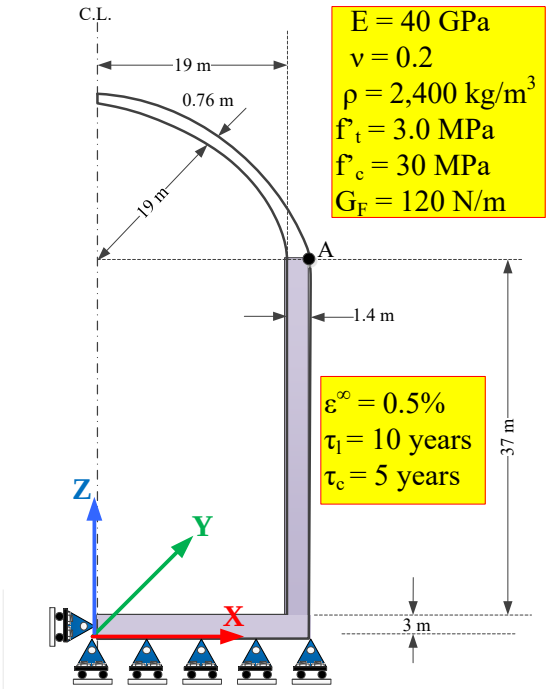

(a) Geometery and Material Properties

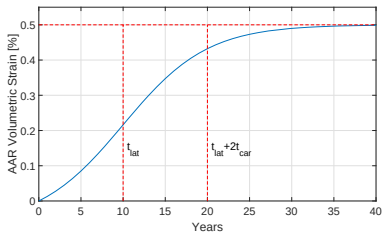

(b) Expansion Curve

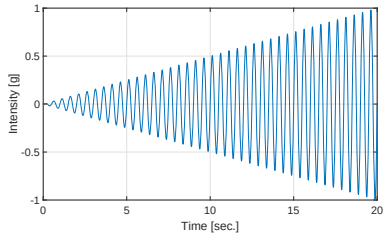

(c) Expansion Curve

Figure D.21: Characteristics of the NCVS

D.4.4.5.4 Dynamic

Perform a 3D dynamic analysis, for a harmonic intensifying dynamic excitation, shown in Fig. D.21(c), assumed to occur at age $t = 20$ years. Assume a 5% Rayleigh damping. Report the following:

1. Time of failure (may be defined when the analysis failed to converge).
2. Time displacement curves for point A starting with the AAR displacement that occurred at time 20 years, until failure (as defined by the user) occurs.
3. Maximum (positive) principal stress ($\sigma_{(1)}$) in the wall versus time.
4. Deformed shapes and crack profiles at 1 sec. increment (starting with $t = 0$) until reported failure.

Results should capture the expansion trends with particular emphasis on the confining effects of the base-mat and dome. The dynamic analysis should capture crack localization,localized failures. Indicate to which extent soil-structure interaction have been accounted for, and whether rocking has been prevented. Dynamic analysis should be a restart from the static analysis resulting in already damaged structure.

D.5 Conclusion

Given that ASR is already a prevalent problem worldwide and that even more are likely to be identified in the near-distant future, it is of the utmost importance that proper numerical tools are available to offer a diagnosis and prognosis.

For a credible prediction, those tools ought to be first validated through the analysis of simple experimental tests to determine if separate and identifiable phenomena can indeed be captured.

Only, once these tools have been validated through material testing, then they ought to be assessed through the analysis of structural components where many separate phenomenon interplay.

Then, and only then, should those tools be deemed (to various degrees) capable of providing engineers with credible set of predictions.

Analysts are encouraged to summarize their findings, determined where the model succeeded and where it filed to capture the intended response and possibly provide an explanation.

Finally, it should be noted that the authors have placed a very high bar to reach in these benchmark problems. Hence, it is supposed that probably not a single finite element code can successfully analyze all problems hereby presented, however strength and limitation should be always identifiable.

Appendix E

Validation of Merlin for AAR Studies

Abstract

Before a finite element code is used to perform AAR analysis, it is critical that it be first validated.

The RILEM international Committee on Diagnosis & Prognosis of AAR Affected Structures *has issued a series of benchmark problems. This chapter is the contribution of the authors in such a study (***saouma-tc259***).*

E.1 Finite Element Model Description

The AAR model of the author is an uncoupled one, that is the constitutive model is in no way affected by the AAR which itself is considered to be an initial strain (akin of temperature), which grafts itself on the mechanical one. It is implemented in (**merlin**), and a complete "validation" of the code with the RILEM benchmark is separately published(**merlin-aar**). This section will describe first the AAR model yielding to the expression of the AAR strain tensor which is accounted for.

E.1.1 AAR Model

E.1.1.1 Premises

Two different aspects of mathematical modeling of AAR in concrete may be distinguished: 1) The kinetics of the chemical reactions and diffusion processes involved, and 2) The mechanics of fracture that affects volume expansion and causes loss of strength, with possible disintegration of the material (**bazant00a**).

The proposed model (**saouma-aar-1**), (**saouma-aar-book**) is driven by the following considerations:

1. AAR is a volumetric expansion, and as such can not be addressed individually along a principal direction without due regard to what may occur along the other two orthogonal ones.
2. Kinetics component is taken from the work of (**larive98**; **ulm00**).
3. AAR is sufficiently influenced by temperature to account its temporal variation in an analysis.
4. AAR expansion is constrained by compression, and is redirected in other less constrained principal directions.This will be accomplished by assigning "weights" to each of the three principal directions.
5. Relatively high compressive or tensile stresses inhibit AAR expansion due to the formation of micro

or macro cracks which absorb the expanding gel.

6. High compressive hydrostatic stresses slow down the reaction.
7. Triaxial compressive state of stress reduces but does not eliminate expansion.
8. Accompanying AAR expansion is a reduction in tensile strength and elastic modulus.

E.1.1.2 Expansion Curve

One of the most extensive and rigorous investigation of AAR has been conducted by (**larive98**) who tested more than 600 specimens with various mixes, ambiental and mechanical conditions. Not only did the author conduct this extensive experimental investigation, but a numerical model has also been proposed for the time expansion of the concrete. In particular, a thermodynamical based model for the expansion evolution is developed, and then calibrated with the experimental data, Figure 2.7(b).

$$\xi(t,\theta) = \frac{1 - e^{-\frac{t}{\tau_c(\theta)}}}{1 + e^{-\frac{(t-\tau_l(\theta))}{\tau_c(\theta)}}} \tag{E.1}$$

where τ_l and τ_c are the latency and characteristic times respectively. The first corresponds to the inflexion point, and the second is defined in terms of the inter-subsection of the tangent at τ_L with the asymptotic unit value of ξ. In a subsequent work, (**ulm00**) have shown the thermal dependency of those two coefficients:

$$\begin{array}{rclcrcl} \tau_l(\theta) & = & \tau_l(\theta_0)\exp\left[U_l\left(\frac{1}{\theta}-\frac{1}{\theta_0}\right)\right]; & & U_l & = & 9,400 \pm 500K \\ \tau_c(\theta) & = & \tau_c(\theta_0)\exp\left[U_c\left(\frac{1}{\theta}-\frac{1}{\theta_0}\right)\right]; & & U_c & = & 5,400 \pm 500K \end{array} \tag{E.2}$$

expressed in terms of the absolute temperature ($\theta^o K = 273 + T^o C$) and the corresponding activation energies. U_l and U_c are the activation energies minimum energy required to trigger the reaction for the latency and characteristic times respectively. To the best of the authors knowledge, the only other tests for these values were performed by (**scrivener05**) who obtained values within 20% of Larive's, and dependency on types of aggregates and alkali content of the cement has not been investigated. Hence, in the absence of other tests, those values can be reasonably considered as representative of dam concrete also.

E.1.1.3 Volumetric Expansion

Hence, the general (uncoupled) equation for the incremental free volumetric AAR strain is given by

$$\dot{\boldsymbol{\varepsilon}}_V^{AAR}(t) = \Gamma_t(f_t'|w_c,\sigma_I|COD_{max})\Gamma_c(\overline{\sigma},f_c')g(h)\dot{\xi}(t,\theta)\,\boldsymbol{\varepsilon}^{\infty}|_{\theta=\theta_0} \tag{E.3}$$

where COD is the crack opening displacement, $\xi(t,\theta)$ is a sigmoid curve expressing the volumetric expansion in time as a function of temperature and is given by Eq. E.1, $\boldsymbol{\varepsilon}^{\infty}$ is the laboratory determined (or predicted) maximum free volumetric expansion at the reference temperature θ_0, Figure 2.7(b).

The retardation effect of the hydrostatic compressive stress manifests itself through τ_l. Hence, Eq. E.2 is expanded as follows

$$\tau_l(\theta,\theta_0,I_\sigma,f_c') = f(I_\sigma,f_c')\tau_l(\theta_0)\exp\left[U_l\left(\frac{1}{\theta}-\frac{1}{\theta_0}\right)\right] \tag{E.4}$$

where

$$f(I_\sigma,f_c') = \begin{cases} 1 & \text{if } I_\sigma \geq 0. \\ 1 + \alpha\frac{I_\sigma}{3f_c'} & \text{if } I_\sigma < 0. \end{cases} \tag{E.5}$$

and I_σ is the first invariant of the stress tensor, and f'_c the compressive strength. Based on a careful analysis of (**multon2003evaluation**), it was determined that $\alpha = 4/3$. It should be noted, that the stress dependency (through I_σ) of the kinetic parameter τ_l makes the model a truly coupled one between the chemical and mechanical phases. Coupling with the thermal component, is a loose one (hence a thermal analysis can be separately run), $0 < g(h) \leq 1$ is a reduction function to account for humidity given by

$$g(h) = h^m \tag{E.6}$$

where h is the relative humidity (**capra98**). However, one can reasonably assume that (contrarily to bridges) inside a dam $g(h) = 1$ for all temperatures.

$\Gamma_t(f'_t|w_c, \sigma_I|COD_{max})$ accounts for AAR reduction due to tensile cracking (in which case gel is absorbed by macro-cracks).

$$\text{Smeared Crack} \begin{cases} \text{No} \quad \Gamma_t = \begin{cases} 1 & \text{if} \quad \sigma_I \leq \gamma_t f'_t \\ \Gamma_r + (1-\Gamma_r)\gamma_t \frac{f'_t}{\sigma_I} & \text{if} \quad \gamma_t f'_t < \sigma_I \end{cases} \\ \text{Yes} \quad \Gamma_t = \begin{cases} 1 & \text{if} \quad \text{COD}_{max} \leq \gamma_t w_c \\ \Gamma_r + (1-\Gamma_r)\gamma_t \frac{w_c}{\text{COD}_{max}} & \text{if} \quad \gamma_t w_c < \text{COD}_{max} \end{cases} \end{cases} \tag{E.7}$$

where γ_t is the fraction of the tensile strength beyond which gel is absorbed by the crack, Γ_r is a residual AAR retention factor for AAR under tension. If an elastic model is used, then f'_t is the the tensile strength, σ_I the maximum principal tensile stress. On the other hand, if a smeared crack model is adopted, then COD_{max} is the maximum crack opening displacement at the current Gauss point, and w_c the maximum crack opening displacement in the tensile softening curve (**wittmann88**).

Concrete pores being seldom interconnected, and the gel viscosity relatively high, gel absorption by the pores is not explicitly accounted for. Furthermore, gel absorption by the pores is accounted for by the kinetic equation through the latency time which depends on concrete porosity. The higher the porosity, the larger the latency time.

Γ_c in turns accounts for the reduction in AAR volumetric expansion under compressive stresses (in which case gel is absorbed by diffused micro-cracks) (**multon2003evaluation**):

$$\Gamma_c = \begin{cases} 1 & \text{if} \quad \overline{\sigma} \leq 0. \quad \text{Tension} \\ 1 - \frac{e^\beta \overline{\sigma}}{1+(e^\beta - 1.)\overline{\sigma}} & \text{if} \quad \overline{\sigma} > 0. \quad \text{Compression} \end{cases} \tag{E.8}$$

$$\overline{\sigma} = \frac{\sigma_I + \sigma_{II} + \sigma_{III}}{3f'_c} \tag{E.9}$$

Whereas this expression will also reduce expansion under uniaxial or biaxial confinement, these conditions are more directly accounted for below through the assignment of weights.

E.1.1.4 AAR Strain Redistribution

The third major premise of the model, is that the volumetric AAR strain must be redistributed to the three principal directions according to their relative propensity for expansion on the basis of a weight which is a function of the respective stresses. Whereas the determination of the weight is relatively straightforward for triaxial AAR expansion under uniaxial confinement (for which some experimental data is available), it is more problematic for biaxially or triaxially confined concrete.

Given principal stress vector defined by $\sigma_k, \sigma_l, \sigma_m$, weights are assigned in function of the three principal

stresses, Figure E.1. These weights will control AAR volumetric expansion distribution.

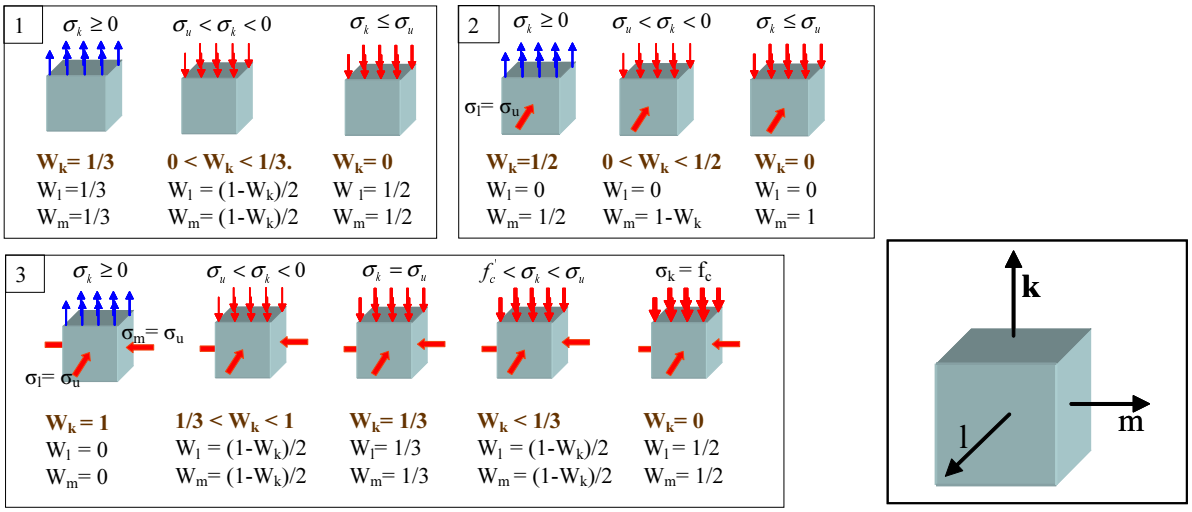

Figure E.1: Weight of Volumetric AAR Redistribution in Selected Cases

It should be noted that the proposed model will indeed result in an anisotropic AAR expansion. While not explicitly expressed in tensorial form, the anisotropy stems from the different weights assigned to each of the three principal directions.

E.1.1.5 Degradation

This deterioration being time dependent, a time dependent model that mirrors the expansion is adopted.

$$E(t,\theta) = E_0 \left[1 - (1-\beta_E)\,\xi(t,\theta)\right] \tag{E.10}$$

$$f_t'(t,\theta) = f_{t,0}' \left[1 - (1-\beta_f)\,\xi(t,\theta)\right] \tag{E.11}$$

where E_0 and $f_{t,0}'$ are the original elastic modulus and tensile strength, β_E and β_f are the corresponding residual fractional values when ε_{AAR} tends to $\varepsilon_{AAR}^{\infty}$.

E.1.2 Concrete Constitutive Models

Whereas our AAR model could be coupled with any (including linear elastic) constitutive model, the last one in Merlin is based on a fracture-plastic one for concrete continuum (smeared crack model) and on a fracture mechanics based one for discrete cracks.

The structural model, has two constitutive models: a) one for distributed failures (smeared crack model) implemented in the spirit of plasticity **cervenka99empty citation**; and b) one for discrete cracks implemented in the spirit of "Fracture Mechanics" (**saouma96efm2**).

E.2 P1: Constitutive Model

E.2.1 Problem Description

As previously mentioned, Merlin's constitutive model is completely disassociated from AAR's, and is first tested in this section. Hence, P1 seeks to capture the nonlinear response of concrete when subjected to a load history covering both tension and compression. Simulation is conducted for a 16×32 cm cylinder shown in Figure E.2 (same mesh will be used for all test problems).

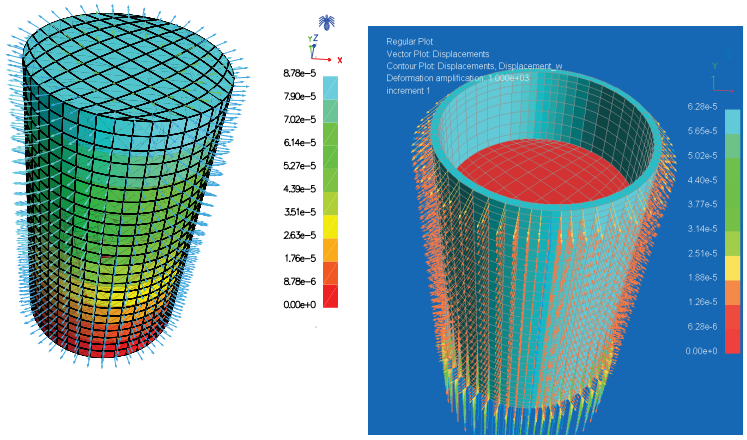

(a) Mesh of concrete cylinder

(b) Mesh of concrete cylinder and steel jacket

Figure E.2: Finite element model for concrete cylinders

E.2.2 Simulations

Two simulations are conducted, the first without AAR, and for a strain history given by

$$0 => 1.5\frac{f'_t}{E} => 0 => 3\frac{f'_t}{E} => 1.5\epsilon_c => 0 => 1.5\epsilon_c \tag{E.12}$$

and the second for an identical strain history which is however preceded by a AAR expansion.

Figure E.3 plots the load-displacement curve at the top of the cylinder. In both cases, the curve load-displacement at the top of the cylinder surface is plotted. The AAR expansion vs time is also plotted.

First, we observe the model nonlinear response with a peak compressive strength of about -38 Mpa, and an onset of nonlinearity of about -13. MPa. The tensile strength of 3.5 MPa is also reduced by the specified $\beta_t = 0.4$ to about 1.4 MPa, and finally the elastic modulus degradation of β_E is also clearly captured.

E.3 P2: Drying and Shrinkage

Problem was not addressed as our finite element code does not have a hygral model. This can be partially alleviated by having layers of concrete with reduced expansion on the surface to account for drying shrinkage.

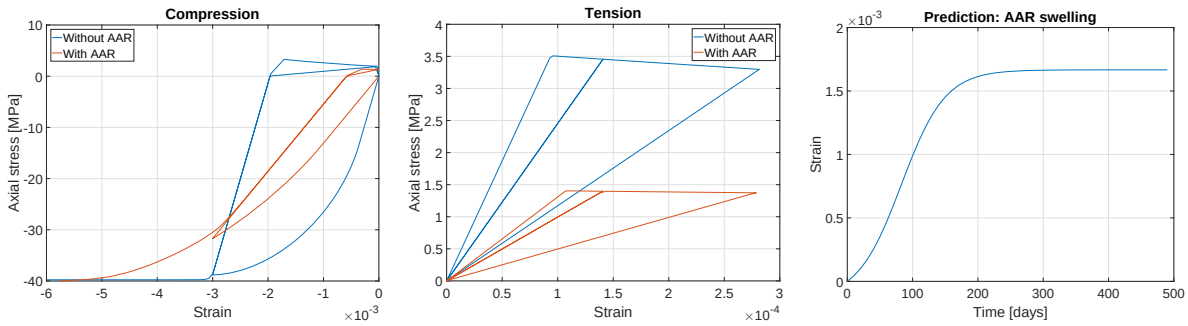

(a) Compression (b) Tension (c) AAR Swelling

Figure E.3: Results of Constitutive Model

E.4 P3: Creep

In the absence of an explicit creep model in Merlin, creep is indirectly accounted for through a time varying creep coefficient ($\Phi(t)$) as follows:

$$\sigma(t) = \frac{E_0}{1+\phi}\varepsilon(t) \Rightarrow \phi(t) = \frac{E_0\epsilon(t)}{\sigma(t)} - 1 \tag{E.13}$$

and at each time step the young modulus is modified according to

$$E(t) = \frac{E_0}{1+\phi(t)} \tag{E.14}$$

E.4.1 Simulations

Using a time varying creep coefficient calibrated from Fig. D.5, a 13×24 cm cylinder concrete cylinder is investigated for the stress variation shown in Fig. D.6.

Traction was applied on the frictionless top of the cylinder.

In Figure E.4(a) we examine numerical and experimental axial strain:

- In the absence of creep, the experimental (a) and numerical (b) results without creep are reasonably close and in the absence of an axial compressive stress they are highest.
- Amongst experimental results, largest swelling is (a) (no compressive stress), followed by (c) and (e) (with axial stresses of -10 and -20 MPa respectively).
- Amongst numerical predictions, in descending order of expansion: (b) with no axial stresses followed by (c), (d), and (f), where the corresponding axial stresses are 0, -10 and -20 MPa respectively.

In Figure E.4(b) the -2 MPa stress is still too low to overcome the AAR expansion, and thus it is the only case where a positive strain takes place. For stresses higher than -10 MPa, the AAR is zero and the combined elastic and AAR strain are thus well into the negative range, while for -5 and -10 MP the net axial strain is almost nil.

In Figure E.4(c) we examine the radial strain. In this axi-symmetric problem, we note that, with an imposed axial stress of -10 and -20 MPa, both experimental and numerical strains are about equal to 2.5 $\times 10^{-3}$ which is half ε^{∞} thus reinforcing the notion that AAR's strain redistribution (or anisotropic expansion) observed by experimentalists and the author's model. Then the smaller the imposed axial stress, the smaller the final radial AAR's strain is, and it would be about equal to ε^{∞} when there is no creep.

In Figure E.4(d) we examine the radial strain in this axi-symmetric problem, we note that both experimentally and numerically they are about equal to 2.5×10^{-3} which is half ε^{∞}, thus reinforcing the notion of AAR's strain redistribution (or anisotropic expansion) observed by researchers and embedded in the author's model. It should be noted that the radial strain is also mildly affected by the Poisson's radial expansion.

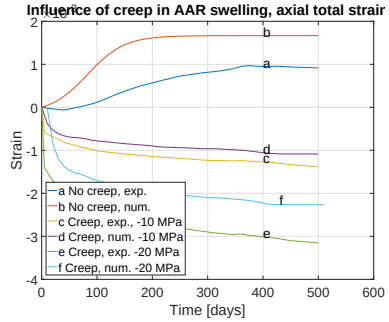

(a) Influence of creep in AAR swelling, axial total strain

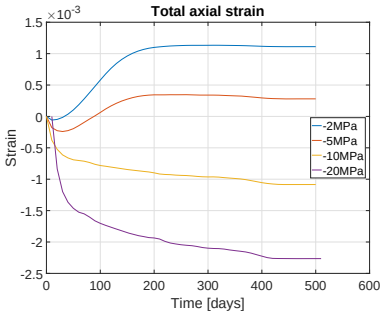

(b) Total axial strain (numerical)

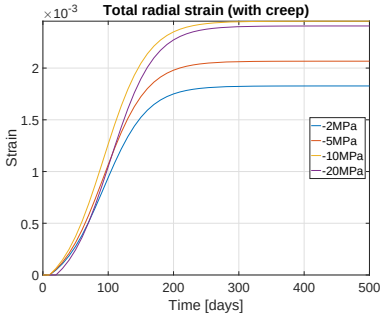

(c) Total radial strain with creep (numerical)

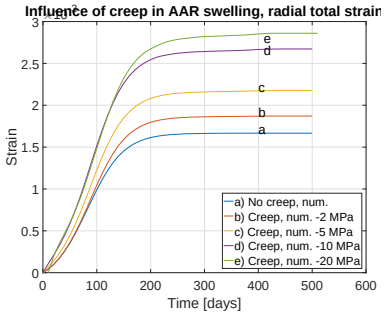

(d) Influence of creep in AAR swelling, radial total strain

Figure E.4: Numerical results of calibration for Creep; Part 1

We then examine each stress value separately. In Figure E.5(a), -2 MPa shows that the effect of creep is almost nil. The largest expansion is radially (between third and half of ε^{∞} and the lowest is also radially (less than third of ε^{∞}). Creep has no influence on the axial strain which is still positive (that is the expansion is larger than the elastic/creep contraction), nor on the radial strain, which is still positive too (that is the expansion is larger than the Poisson's effect due to the elastic/creep contraction).

Figure E.5(b) the stress is now -5 MPa, and observations are the same as for the preceding case of -2 MPa; however, the larger imposed stress accentuate them.

Figures E.5(c) and E.5(d) corresponds to the axial strain under -10 MPa, (c) with axial strains and (d) with radial strains. Curves (a) and (b) in Figure E.5(c) shows that the creep doesn't have any impact on the vertical strain, which is correct: there is not supposed to be any AAR's expansion in the direction if the stress exceeds -10 MPa. Curve (c) gives the total strain without creep, so this is the elastic strain (once again, there is no AAR's strain here). Finally, curves (d) and (e) show numerical and experimental strain in axial direction, they are reasonably close.

For Figure E.5(d), we note that creep doesn't have any impact, except through Poisson's effect. Note that we reach half of ε^{∞} i.e. 2.5×10^{-5}.

Figures E.5(e) and E.5(f) correspond to the axial strain under -20 MPa, (e) with axial strains and (f) with radial strains. Same conclusions can be made as with -10 MPa: creep doesn't have any impact on AAR

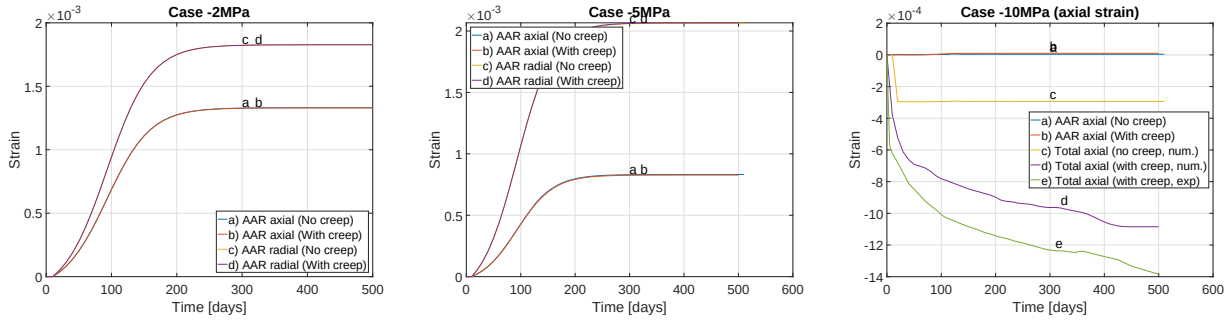

(a) Case -2MPa (b) Case -5MPa (c) Case -10MPa (axial strain)

(d) Case -10MPa (radial strain) (e) Case -20MPa (axial strain (f) Case -20MPa (radial strain)

Figure E.5: Numerical results of calibration for Creep, part 2

strains, except through Poisson's effect.

Finally, a prediction for the response of a cylinder subjected to an time varying axial stress shown in Figure E.6(a) is performed. Using an average of the two $\phi(t)$ (corresponding to -10 and -20 MPa), response is shown in Figure E.6.

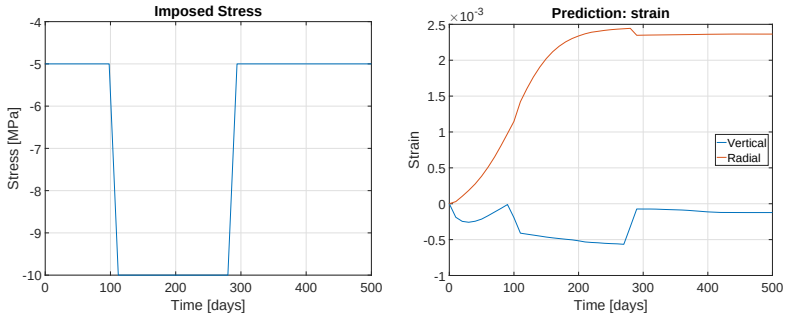

(a) Imposed Stress (b) Axial and radial strains

Figure E.6: Numerical results of prediction

First, the vertical elastic strain, compounded by creep decreases down to a minimum of about -2.5×10^{-4} at about 20 days. At that point, AAR's expansion rate is almost nil, smaller than the contraction due to creep, and thus the strain decreases. Then the AAR's expansion starts, and the strain is increasing again, AAR's expansion is starting to overcome the elastic strain.

Then the axial stress is increased from -5 to -10 MPa, and the elastic strain compounded with creep

causes a further contraction. At -10 MPa, the AAR axial expansion is completely inhibited (and redirected in the radial direction), and all strain increase is solely due to creep. When the stress is again dropped from -10 to -5 MPa there is a rebound, and from that point onward both creep contraction and (reduced) AAR's expansion are at work. However, at that point, the propensity for AAR has been exhausted, and mst of it occurred along the radial direction (which is close to 2.5×10^{-3} at the end), so it cannot compensate for the elastic strain. In the radial direction, we observe an opposite behavior. First, due to the basic AAR's expansion in this direction, plus the redirected AAR's expansion between 100 and 300 day, and finally because of Poisson's effect.

E.5 P4: AAR Expansion; Temperature Effect

E.5.1 Simulations

Three simulations are performed:

Validation : By simulating the free expansion at 23^oC and 38^oC for which Figure D.7 shows the experimental data (the large variability should be noticed).

Prediction for a harmonic temperature variation given by

$$T(days) = \frac{T_{max} - T_{min}}{2} \sin(2\pi \frac{t/7 - 16}{52}) + \frac{T_{max} + T_{min}}{2} \tag{E.15}$$

Where T_{max} and T_{min} are 25^0C and 0^oC respectively, Figure D.8.

Figure E.7(a) shows the predicted expansion versus time for the two temperature. As anticipated, expansion is much faster at the higher temperature. Furthermore, the numerically predicted AAR strain are close to the experimentally obtained one from which critical data was calibrated (ε^{∞}, τ_{lat} and $\tau char$), Figure D.7.

Results for the prediction are shown in Figure E.7(b). The harmonic thermal strain ($\epsilon_{th} = \alpha.\Delta T$) is first given, and the one caused by AAR is simply given by $\epsilon_{AAR} = \epsilon_{total} - \epsilon_{th}$.

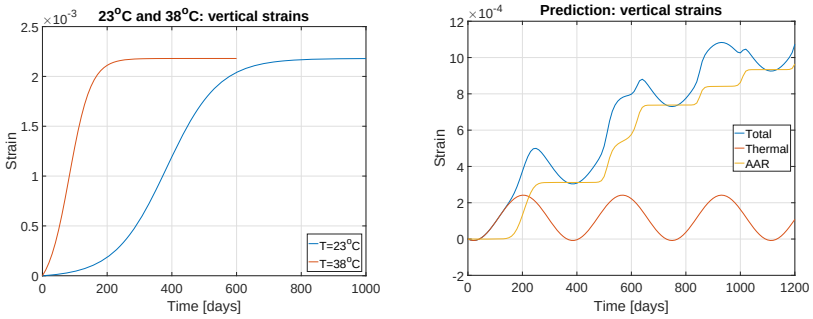

(a) Vertical strains at 23^oC and 38^oC

(b) Predicted response to an harmonic temperature variation

Figure E.7: Numerical results for calibration and prediction for the effects of temperature

We note that the AAR strain is flat for low temperature (and thus the plateau), and the total strain increases with time due to the combined effects of AAR expansion and temperature. The decreases are driven by the decrease in the temperature.

E.6 P5: Free AAR Expansion; Effect of RH

Adopting the model of (**capra98**), the variation of RH is acounted as follows:

$$\varepsilon^{RH} = RH^m \varepsilon^{100\%} \tag{E.16}$$

where m is determined to equal 8 through a regression analysis of experimental data.

E.6.1 Simulations

Again, three simulations have been performed:

Calibration Two analyses with an external relative humidity of 100 and 30 percent using the experimental dataset of **multon2003evaluationempty citation**, as shown in Figures D.9(a) and D.9(b), respectively.

The impact of RH on AAR swelling has been modeled as a modification of the final volumetric AAR strain according to the equation: $\epsilon^{AAR}(t) = \epsilon^{AAR}_{\infty}.RH^8(t)$. A constant relative humidity of 80% will thus lead to multiplying the final volumetric AAR strain by 0.17.

The factor 8 however, has not yet been well established, which led to simulating the Prediction case using three different values of this factor: 7, 8, and 9.

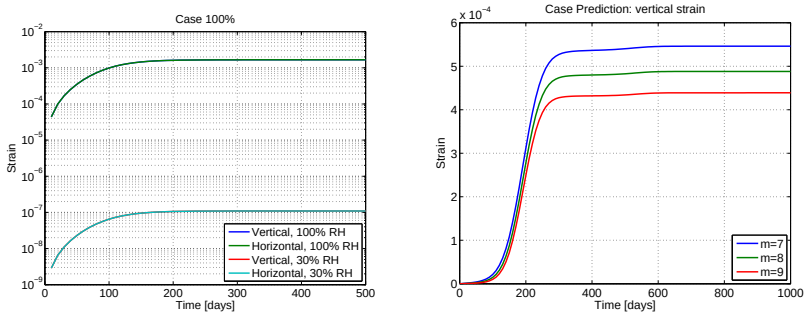

(a) Expansion in terms of RH

(b) Effect of the variation in m

Figure E.8: Calibration: Effect of Relative Humidity

The results of the first simulation are shown in Figure E.8(a) for expansion in terms of RH; as expected at 30% RH, expansion is practically nil. Figure E.8(b) shows the effect of factor m on this expansion: the higher the exponent value, the lower the level of expansion. Let's point out that in this case, no attempt was made to calibrate input data with experimental results, and the final AAR-induced strain was set to 0.5% just like in most of the previous simulations.

E.7 P6: AAR Expansion; Effect of Confinement

E.7.1 Simulations

Five simulations are performed:

Calibration Based on Multon's thesis in which four cases are considered:

- a) Free expansion, no confinement.

- b) -10 MPa vertical stress, no confinement.
- c) Free expansion, confinement.
- d) -10 MPa vertical stress, confinement

Prediction for the variable stress history with confinement.

Confinement is provided by a 5mm steel cylindrical jacket inside which the concrete is cast.

Numerically, concrete and steel are separated by an interface element which allows for axial deformation, and which allows for the steel to act as a confinement.

For the calibration, concrete axial and radial strains are shown in Figure E.9(a), whereas the steel strains are shown in Figure E.9(b). Examining the concrete strains, and in descending strain order, we observe that:

1. (b) Radial, -10 MPa, no confinement. Since AAR is inhibited in the axial direction by the -10 MPa axial stress, it is entirely redirected in the radial direction. The AAR's strain is about 15×10^{-4} corresponding to a total volumetric AAR strain of 30×10^{-4} which is approximately equal to the specified $\varepsilon^{\infty} = 28.8 \times 10^{-4}$.
2. (c) Axial, free with confinement. In this case it is the radial expansion which is inhibiting the expansion, and hence it is redirected in the free axial one. As expected the magnitude is about twice.
3. (a) Axial and radial, free no confinement; they are both equal to approximately 9×10^{-4} at 350 days. This is indeed one third of the specified $\varepsilon^{\infty} = 0.288\%$ since we have an unconstrained isotropic expansion.
4. (d) -10 MPa confinement radial; Following an initial increase due to Poisson effect, some swelling occurs but is partially inhibited.
5. (c) Radial free confinement; unlike previous case, there is no initial strain, and a gradual increase in swelling. Swelling is reduced as most of it occurs in the axial direction.
6. (d) -10 MPa axial confinement the initial compressive strain corresponds approximately to the elastic one (σ/E or 2.7 $\times 10^{-4}$, then as a result of AAR swelling it rebounds (specially that due to confinement, it can only expand axially).
7. (b)-10 MPa axial no confinement; -10 axial confinement the initial compressive strain corresponds approximately to the elastic one (σ/E or 2.7 $\times 10^{-4}$ however since there is no confinement all the AAR expansion is redistributed in the radial direction (contrarily to the preceding case).

As to the steel radial strains they reflect the gradual AAR's induced (swelling) radial strains in the confining jacket.

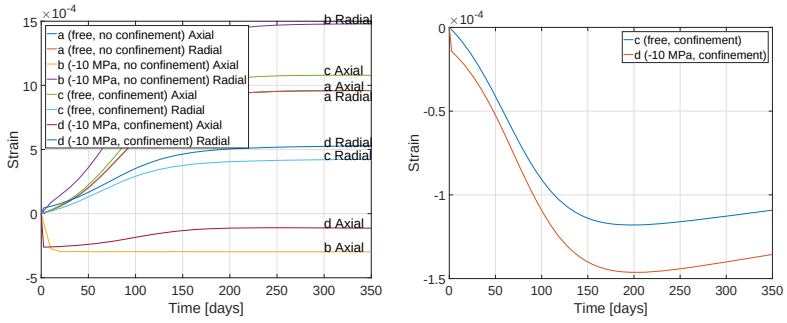

(a) Calibration, concrete axial and radial strains

(b) Calibration, steel radial strains

Figure E.9: Calibration; Effect of confinement

As to the prediction, Figure E.10(a) shows the applied stress history, and Figure E.10(b) the corresponding

strains. Concrete undergoes an initial elastic axial deformation due to the -5 MPa traction, then it expands due to the AAR. When the -10 MPa traction is applied, there is an elastic strain, and at that point the AAR is practically nil as the concrete is axially subjected to a stress equal to the threshold limiting value. When the -10 MPa is dropped to -5 MPa, there is again an elastic "rebounding" and the AAR is nil as it has been exhausted by that time.

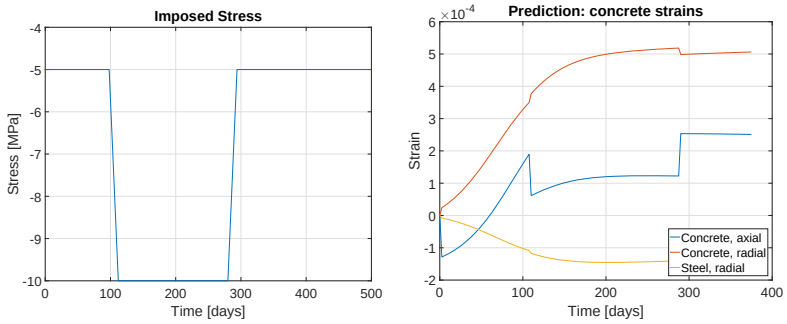

(a) Imposed Stress (b) Axial and radial strains

Figure E.10: Prediction; Effect of confinement

The concrete radial strain is primarily driven by AAR (Poisson effect is shown but almost negligible). Though partially constrained by the steel jacket, expansion is mostly in the radial direction in this case since axial expansion is constrained. Finally, the steel radial strain reflects the concrete time dependent expansion.

E.8 P7: Effect of Internal Reinforcement

Internal reinforcement inhibits expansion and AAR induced cracks would then align themselves with the direction of reinforcement as opposed to the traditional "map cracking", (**mohammed03**).

Concrete is modeled by its nonlinear constitutive model, and a linear elasto-plastic model is used for the steel.

Figure E.11 provides some snapshots of the mesh, and note that at about 5 mm away of the rebar, its effect on the AAR is almost nil. The steel axial stress is quite small, $\simeq 0.063$ MPa.

Concrete strains, Figure E.11 are indeed restrained in the axial direction, and most of the expansion is in the radial. $\varepsilon_{axial} + 2\varepsilon_{radial} = (0.35 + 2(0.85)) \times 10^{-3} = 20.5 \times 10^{-4}$ which is approximately equal to the specified ε^{∞}.

E.9 P8: Reinforced Concrete Beam

Not modeled, as Merlin does not have a hygral model.

E.10 P9: AAR Expansion; Idealized Dam

Using the fitting data of P6, and an friction angle of 50^o for concrete against concrete, and zero cohesion, we consider two cases:

Slot Cut Simulation Performed on a 2D mesh.

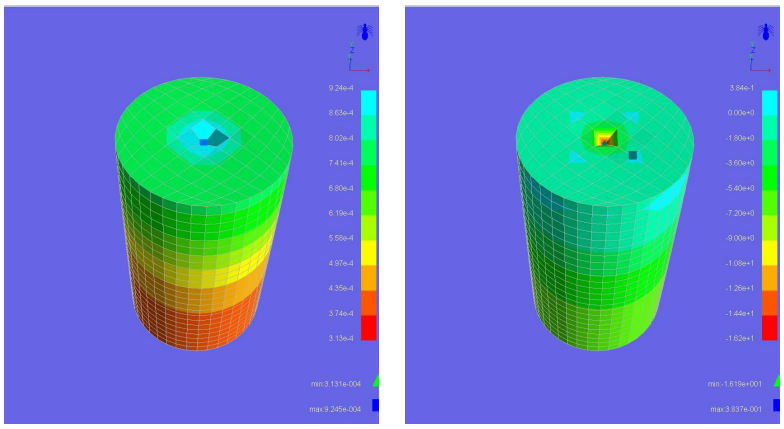

(a) Axial strain (b) Axial stress

Figure E.11: Effects of reinforcement on AAR

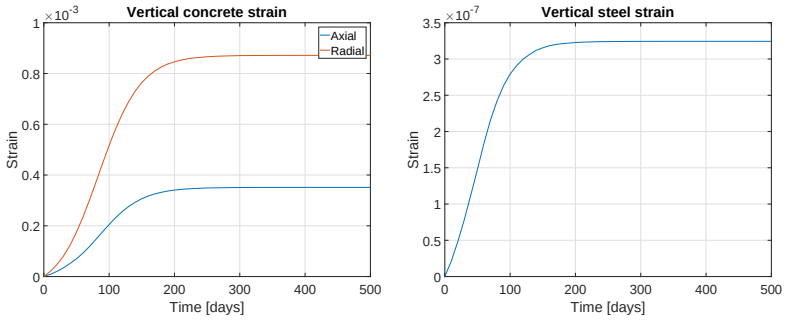

(a) Concrete (b) Steel

Figure E.12: Effect of Internal Reinforcement

Slot cut closure performed on a 3D mesh.

E.10.1 2D Slot Cut

A "proof of concept" approach was followed to capture the impact of a slot cut in a 2D nonlinear analysis (both concrete and joint) with dimensions corresponding to those of the Benchmark.

The model is shown in Fig. E.13(a) and consists of four parts: a) a non reactive concrete on the left; b) reactive concrete on the right; c) a volume defining the slot inside the reactive concrete; and d) a zero thickness joint element between the first and third group.

Results are shown in Fig. E.13(b) and clearly show that the following essential features were captured following the slot cut: a) there is a drastic decrease in the original 10 mm slot as the concrete is allowed to more freely expand; and b) there is a decrease in the resulting lateral force exercised by the concrete expansion. On the other hand, should there have been no slot cut, then the gap would remain essentially the same, however the lateral confining force would keep on increasing.

For both analysis, the specified temperature and relative humidity is the one of the concrete surface. Zero flux condition between dam and foundation. Reference base temperature of the dam is 20^{o}C.

1. x, y, z displacements of point A.

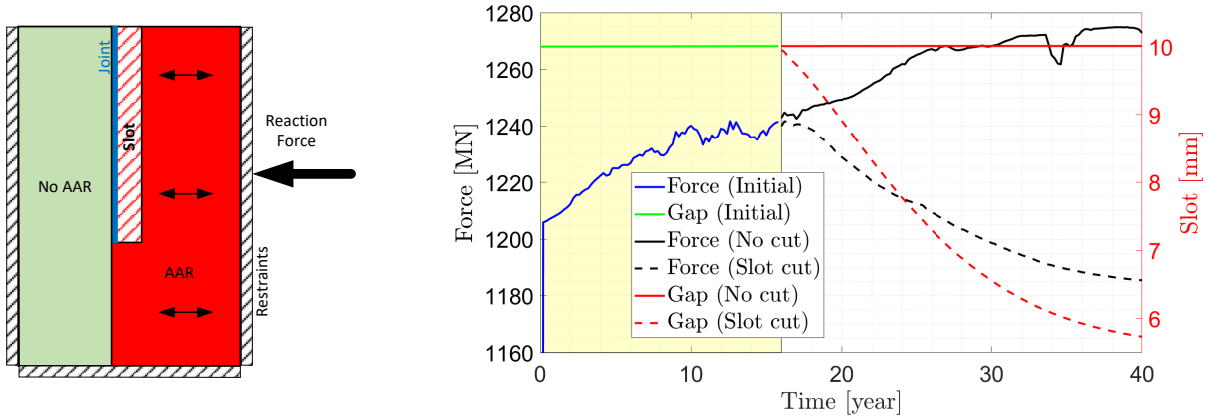

(a) Schematic (b) Results

Figure E.13: Simulation of slot cut in a dam

2. F_x, F_y and F_z resultant forces on the fixed lateral face versus time (25 years). Assume the typical yearly variations of external air temperature and pool elevation shown in Figures D.8 and D.15, respectively.

This model seeks to capture: a) general finite element program capabilities in modeling the joint response; b) ease (or difficulty in preparing the input data file for a realistic problem; and c) coupling of the various parameters.

E.10.2 3D Simulation of Post-Cut Gap Closure

The 3D mesh of the model of Figure D.14 is shown in Figure E.14.

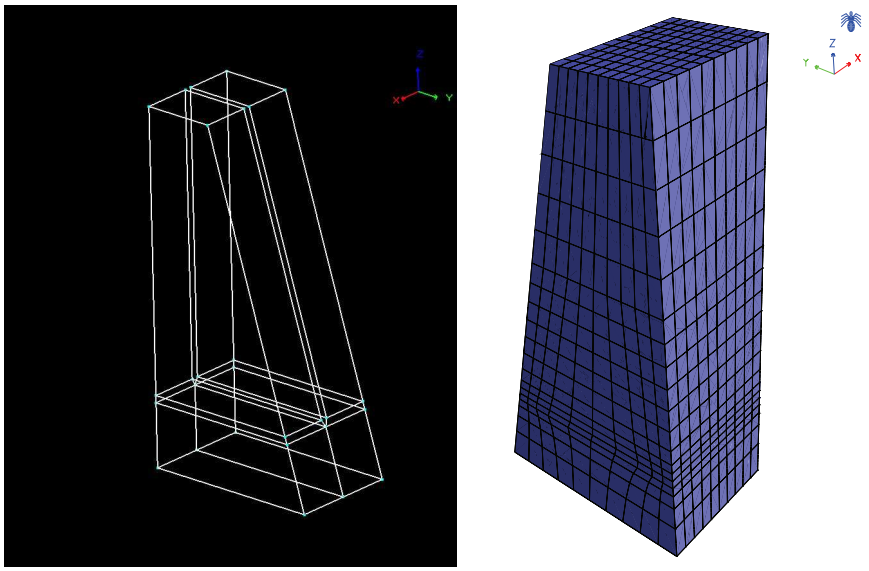

(a) 3D finite element mesh outline (exagerated slot width) (b) 3D finite element mesh

Figure E.14: 3D Finite element mesh

In this first analysis, the dam is subjected only to AAR, and for the 10 mm slot, with AAR, we seek to determine the slot thickness in terms of time (as it is reduced by AAR), Figure E.15(a) and the corresponding contact stresses, Figure E.15(b).

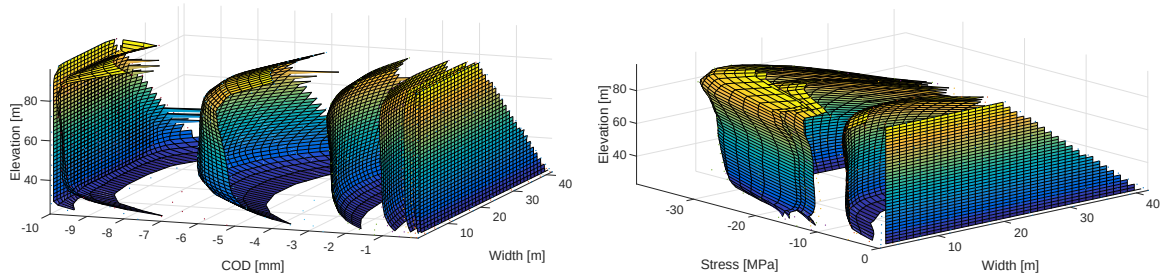

(a) Slot thickness for time: 0.167, 1.67, 3.33, 5, 6.67, 8.33, 10 and 11.67 years

(b) Slot normal stresses for time: 8.33, 11.67, 15, 18.33 and 121.67 years

Figure E.15: 3D response of a dam subjected to AAR

From these plots, we conclude that

1. The slot is initially completely open (COD=0), and gradually the COD reaches -10 mm which is precisely the thickness of the slot. At that point, the interface element is activated, and there can be no more expansion.
2. The concavity of the surfaces is to be noted. There is more expansion in the center than on the edges. Eventually the expansion is entirely uniform and we have a nearly full contact at -10 mm.
3. Similarly, there is less expansion on the top than in the bottom.
4. The bottom has also reduced expansion due to the problem formulation as it is constrained to the bottom concrete.
5. Similarly, the stresses are zero in the beginning as there is no contact.
6. Gradually the stress increase, and we observe the same concavity as the one noted for the COD. In other words, stresses are much higher in the center than on the edges.
7. The concavity remains present even after many years, stresses will be higher in the central part than on the edges.

From these observations, we conclude that we were we able to capture the "true" response of the slot, to anticipate the time of closure and to map the corresponding stresses. A salient observation is that the COD/stress state can be quite complex, and thus great care should be exercised in planning for and after slot cutting.

E.11 P10: Reinforced Concrete Panel

Full disclosure: this analysis was undertaken as part of a sponsored project, and a probabilistic based analysis was performed (**ornl-3**). Only results of the deterministic one are reported.

Six different analyses were performed, Table E.1 with a finite element mesh composed of 1,001 nodes and 720 quadrilateral elements, Figure E.16(a). Two sets of reinforcements are modeled at the top and the bottom of the specimen. In the Merlin finite element software, the rebars can be modeled easily by defining the the start and end nodes. Then, Merlin automatically applies the mesh on the rebars. The finite element mesh of the rebars for the panel is shown in Figure E.16(b).

Table E.1: Different types of the models for the panel

ID	Reinf.	Loading	BC on xz plane	BC on yz plane	Material model
P1	No	ASR	x=y=z=0	x=y=z=0	Linear Elastic
P2	No	ASR	x=y=0	x=y=0	Linear Elastic
P3	Yes	ASR	x=y=z=0	x=y=z=0	Linear Elastic
P4	Yes	ASR	x=y=0	x=y=0	Linear Elastic
P5	Yes	ASR	x=y=z=0	x=y=z=0	Non-Linear
P6	Yes	ASR	x=y=0	x=y=0	Non-Linear

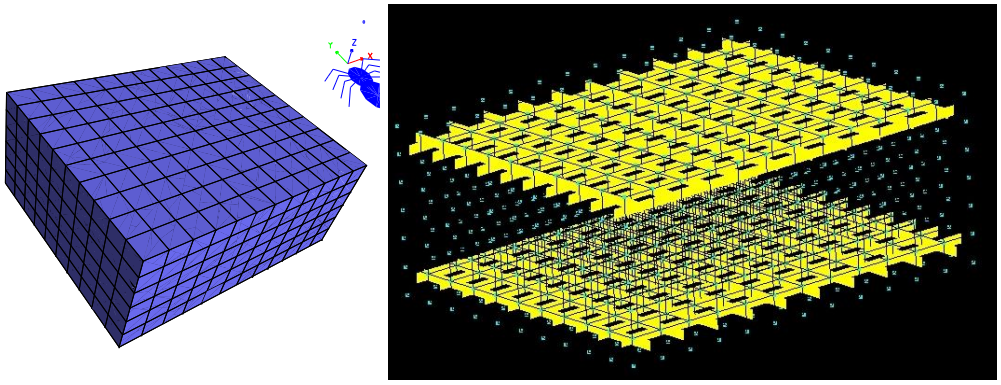

(a) Mesh (b) Reinforcement mats

Figure E.16: Details of the finite element mesh

In all models, the panel is experienced only the ASR expansion and no external load (directly or indirectly) is applied to the panel. The models are expected to expand only in z direction. Figure E.17 compares the un-deformed and deformed shape of the panel under two boundary conditions explained in Table E.1. Based on Figure E.17, restricting the side-walls in all three directions leads to expansion of the panel z direction. In this condition, the maximum deformation belongs to the middle point in the upper and lower faces. On the other hand, this figure shows the condition in which the side-walls are only restricted in x and y directions (not z). In this condition the model has a uniform expansion in both +z and -z direction. Considering the symmetry of the panel, in both boundary models the panel shows the same responses along the positive and negative z axis.

In order to investigate the structural responses of the panel, two index points in the center of the panel. The first is on the top surface and the other in the middle of the thtickness.

Figure E.18 shows the progressive failure of the panel model P5 under ASR expansion. As seen, the cracking first starts at the Inc = 109 at the corners of the panel (where is higher stresses is expected). Also, the starting increment (109) corresponds to the previously discontinuity in the stress time histories of the concrete and reinforcement.The cracking is first propagate along the two opposite corner of the panel (it is symmetry). Another set of cracks appear in the center of the panel (around the Index-2) at Inc = 184. This corresponds to the stress reduction in Index-2at practically the same increment.

E.11.1 ASR + Shear Load

The first six models are only based on ASR expansion. Those are followed by P7 to P17 based on different combination of linear/nonlinear models and applied incremental displacement load (to impose a shear load).

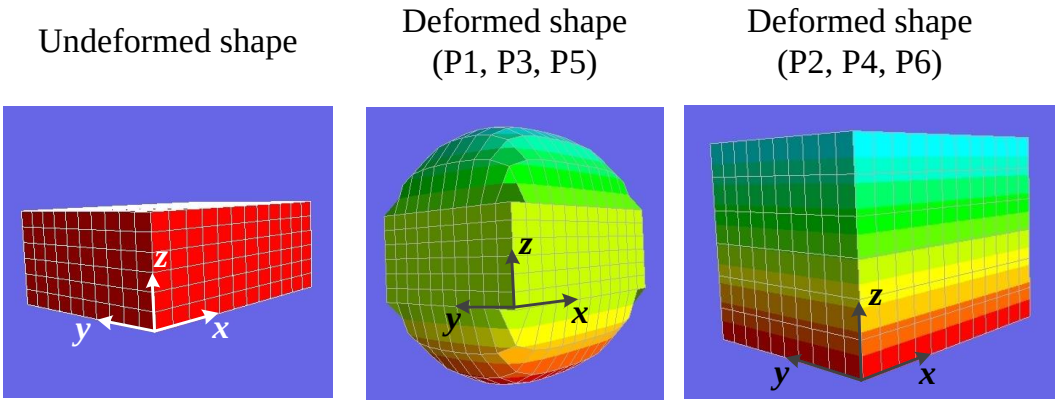

Figure E.17: Comparison of the deformed and un-deformed shapes of the panel

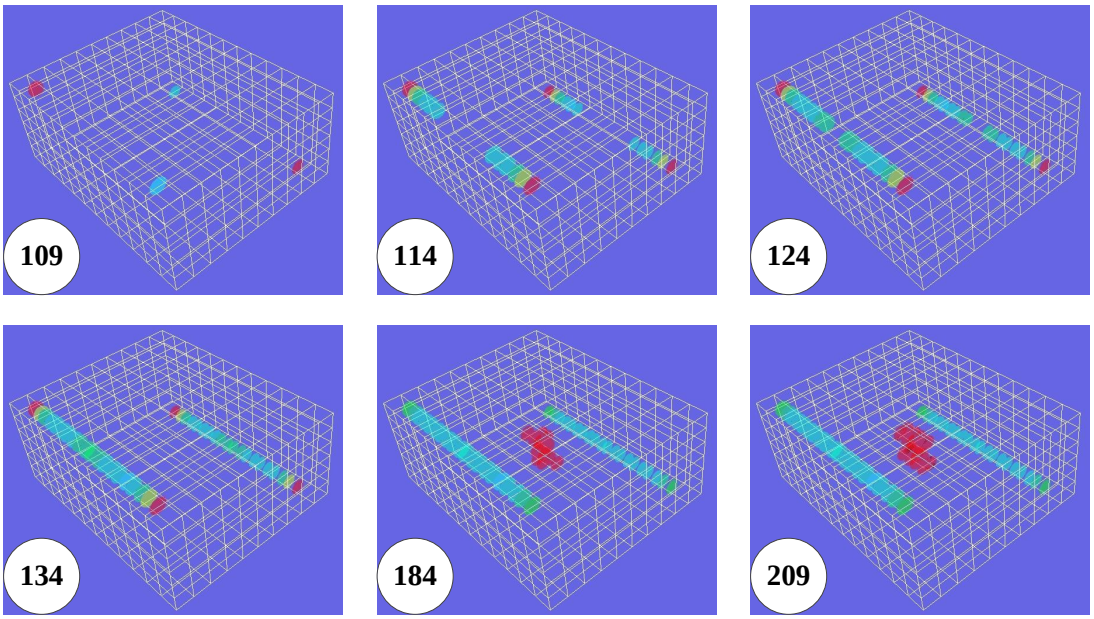

Figure E.18: progressive failure in panel model p5 ($_{x^-:(0,0,0);\ x^+:(0,0,0);\ y^-:(0,0,0);\ y^+:(0,0,0)}$) under asr expansion

Models P7 to P12 all are based on linear elastic concrete, with and without reinforcement effect (not studied here). P13, P14 ad P15 are based on nonlinear concrete model (smeared crack model), in the presence of reinforcement, and different boundary conditions. P13 is, in fact, the reference model for this group (no ASR expansion is applied). P14 and P15 are different in the boundary conditions applied under the ASR expansion. P14's BC is identical to P5 and the one in P15 is similar to P6.

Figure E.19 shows the load-displacement curve of three cases. As seen, the load-displacement curve is nonlinear in all cases (nonlinear material assumption). Based on this figure, the initial slope of the P13 is more than P14 and P15, showing that the initial ASR expansion leads to softening of the panel (due to cracking). There is a discontinuity in the capacity curve of the panel P13 at $\Delta = 2.14$ mm. This point

corresponds to the initiation of the first set of the cracks in the diagonal form. There is not such a sudden jump or reduction in two other curves (P14 and P15) because they already experienced some cracking before applying the incremental displacement.

The capacity curve of the panel P14 is more than the P13, while the capacity curve of the P15 is less than P13. Both the P14 and P15 experience ASR expansion and some cracking before applying the incremental displacement. The differences of the capacity curves can be attributed to the boundary conditions applied in the ASR part. In the panel P14, full confinement of the model under ASR expansion make the panel strength. Based on Figure E.18, the panel does not have critical cracking under ASR expansion. Also, most of the cracking is concentrated at the center which experience lower tensile stresses under incremental divorcement. On the other hand, panel P15 was free to expand along its thickness and thus had more cracked elements initially (before applying the incremental displacement). Therefore, this model has a lowest capacity curve among the three cases.

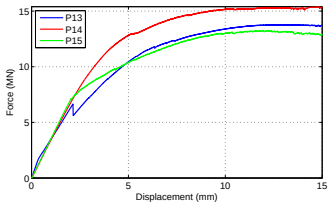

Figure E.19: Load-displacement curve for the Panel P13, P14 and P15

Figure E.20 shows the progressive failure mode of the panel model P13 under incremental displacement. As seen, the cracking starts at the upper right corner of the panel and then lower left corner. These two points correspond to the high tension area. The cracking proceeds in vertical direction along the walls. Then, a sudden diagonal cracked area appears in the panel which is believed to be the main failure mode. At this time, the crack pattern looks like “N” letter. Further cracking develops around this main path.

Figure E.21 shows the progressive failure mode of the panel model P14 under incremental displacement. The cracking of the panel at the last increment of the ASR expansion is taken as an initial condition for the incremental displacement. As seen, the failure mode in this model is completely different from P13 (the reference model). Considering initial cracking at the center of panel, the rest of the cracks propagate in the diagonal form in both directions. It makes the crack pattern looks like “X” letter. Further cracking develops around this main path.

Figure E.22 shows the progressive failure mode of the panel model P15 under incremental displacement. The cracking of the panel at the last increment of the ASR expansion is taken as an initial condition for the incremental displacement. Based on this figure (and having in mind the boundary conditions of the P15 under ASR expansion), it can be seen that the panel experience almost a uniform cracking along its thickness under ASR expansion. This failure mode is completely different from P13 (the reference model) and P14 (the other ASR-affected model). It is not possible to define a specific failure mode in this model, because even under the incremental displacement the model has more or less uniform cracking (or opening of already cracked elements).

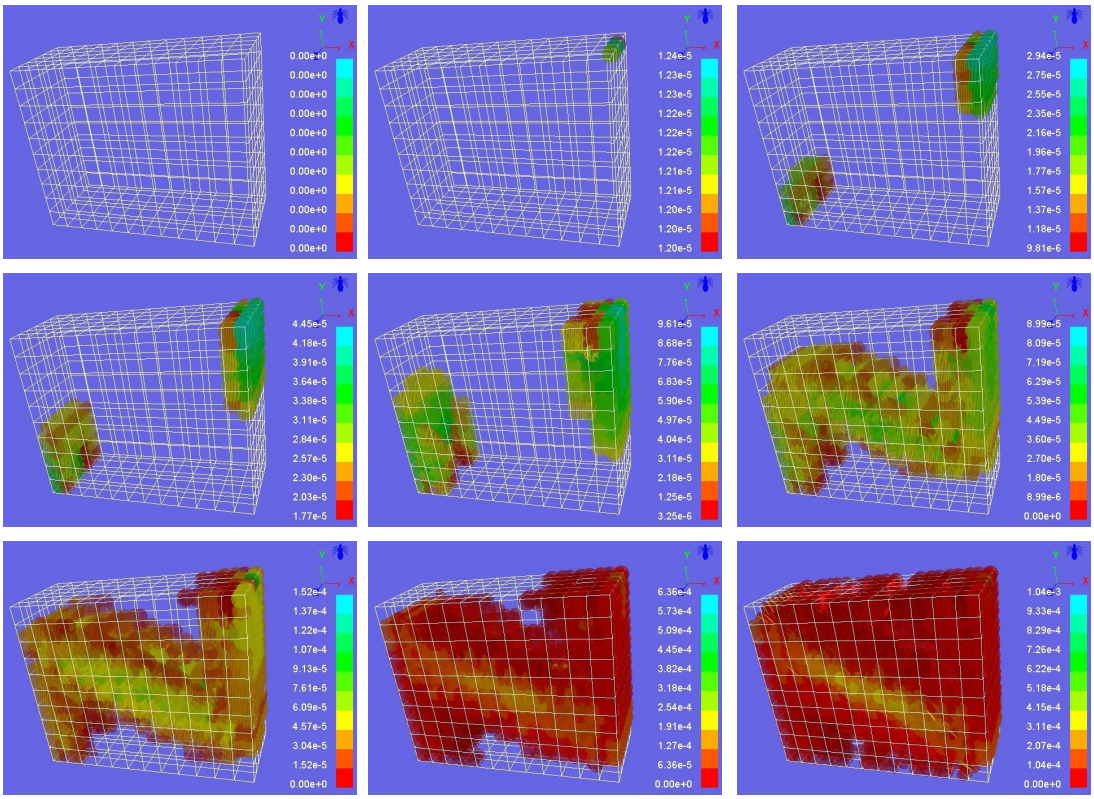

Figure E.20: Progressive failure of the panel P13 under incremental displacement

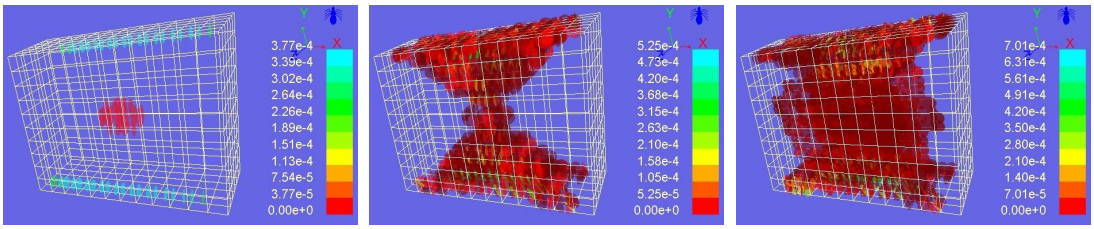

Figure E.21: Progressive failure of the panel P14 under incremental displacement

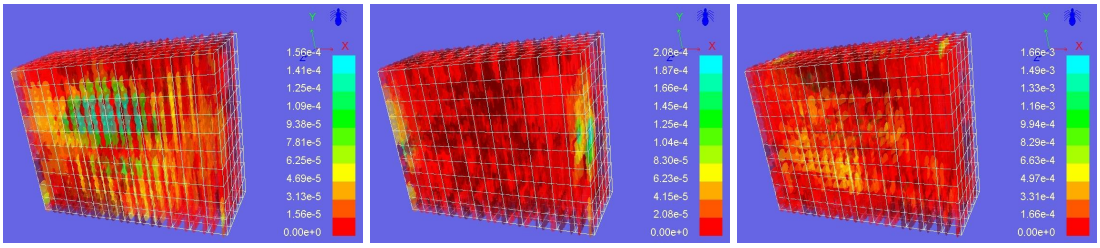

Figure E.22: Progressive failure of the panel P15 under incremental displacement

E.12 P-11: Nuclear Containment Structure

This last analysis addresses the last benchmark problem, however there are some minor suble differences: 1) we used dynamic intensifying acceleration function (so-called ETAF), while the benchmark is based on static intensifying load; and 2) we used the results of six ETAFs to reduce the uncertainty and dependency to external load while the benchmark is deterministic.

Again, full disclosure: this analysis was also performed within the context of an NRC sponsored research and has been separately published in (**saouma-nrc-report-fea**) and (**Saouma2019Seismic**).

The structure will be first subjected to 40 years of ASR expansion followed by multiple seismic excitation (with or without ASR induced damage), and results will be compared with the response of the NCVS subjected to the same seismic excitations but without prior ASR expansion (Figure E.23 B, C, and A respectively).

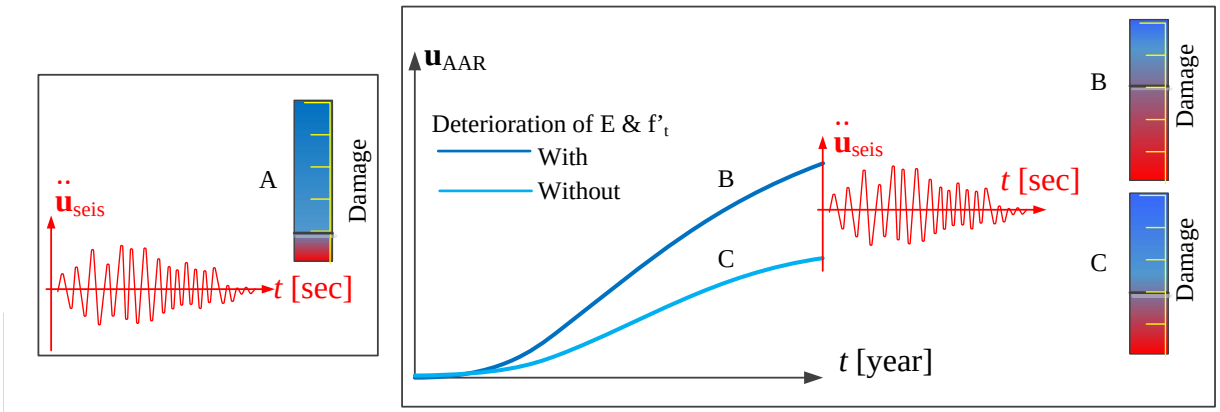

Figure E.23: Three scenarios of investigation: A: No ASR; B: ASR with 40% damage; and C: ASR without Damage.

The selected and partially buried NCVS is schematically shown in Figure E.24(a). Note that only the concrete underneath the soil level will be subjected to ASR (as a result of the high relative humidity likely to be present in the surrounding foundation).

The potential secondary stresses induced by the uplift forces (caused by the eccentricity of the resulting inertial force), Figure E.24(b), will be mitigated by the insertion of cohesive based joint elements (**saouma96efm2**) where necessary. A 3D continuum model, Figure E.24(c) is prepared. Reinforcement is modeled as "smeared" by altering the stiffness matrices of those continuum elements they cross. A 0.5% reinforcement was assumed in both directions.

It is assumed that the NCVS operates for 40 years during which it undergoes a relatively mild total expansion of 0.3% uniformly distributed over the "contaminated" zone as an additional internal strain.

Accompanying this expansion are two levels of concrete degradation zero and 30% reduction of E and f'_t after 40 years. The 40 years expansion is simulated in two weeks increments assuming a constant temperature and RH. The external average temperature at the site is estimated to be 11^oC (external face of NCVS), the internal temperature is in turn estimated to be 25^oC. Hence, an average mean yearly temperature of $(25 + 11)/2 = 18\ ^oC$ is assumed. Note that in a more refined analysis, the temperature distribution across the wall should be considered, and monthly average temperatures should also be refined.

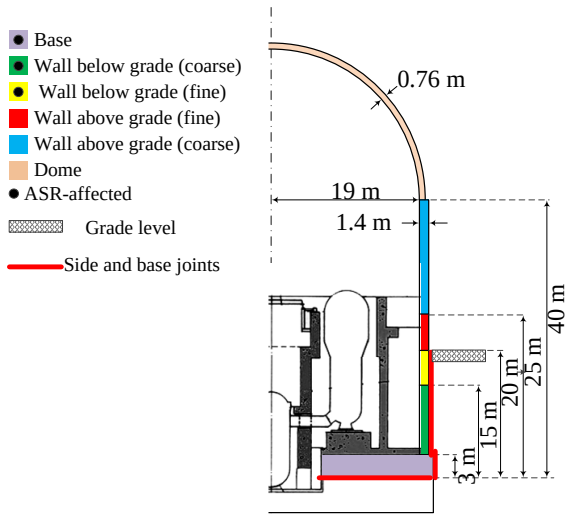

(a) Geometry and dimensions

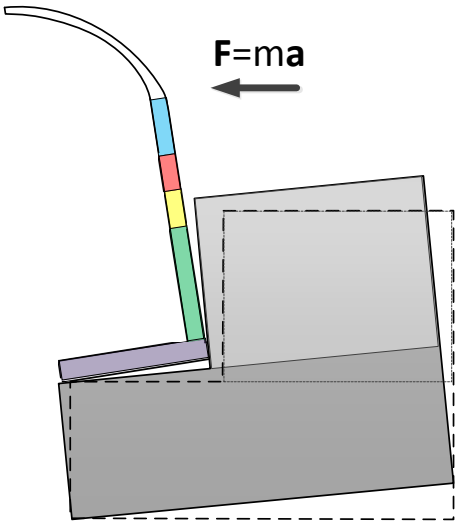

(b) Potential uplift modeled by joint elements

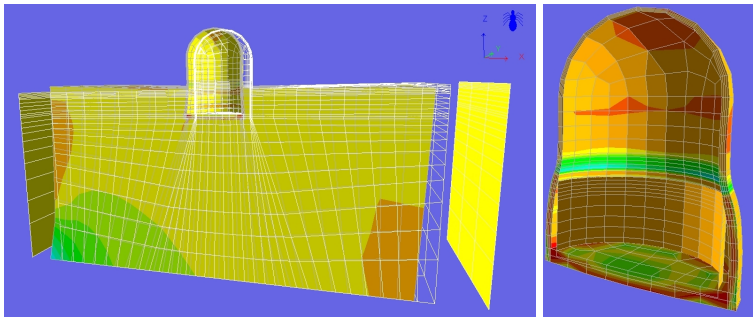

(c) Half 3D model with lateral viscous dampers and container mesh (with ASR expansion)

Figure E.24: Geometry, material groups, role of joint elements, and finite element mesh

Rock (both the foundation and lateral) is assumed to be linear elastic. Interface joints are placed around and below the NCVS to capture potential uplift of lateral separation of the container from the adjacent rock.

Six different randomly generated ETAFs were used. Schematically, all the ETAFs are analogous as they are all based on a random white noise.

Three sets of analyses were performed: 1) Static + ASR, 2) Static + Dynamic, and 3) Static + ASR + Dynamic (100 for the stochastic ground motions, and three for each of the six ETA).

E.12.1 Static + ASR Analyses

In this first analysis, 40 years of ASR in the NCVS is simulated. Figure E.26(a) shows swelling of the container along with a closeup on the concrete-rock separation. Clearly ASR expansion interacts with the structure in what may be *a priori* counter-intuitive: a) the mat expands in a concave shape due to the structural constraints of the cylindrical vessel, Figure E.26(b)-1; b) the wall pushes against the adjacent rock, but is constrained by both the base mat and the upper portion of the enclosure not subjected to expansion, Figure E.26(b)-2, causing strong curvature, joint opening, and ensuing stress discontinuities; and c) sliding of the NCVS itself, Figure E.26(b)-3. Furthermore, the evolution of concrete cracks is shown in

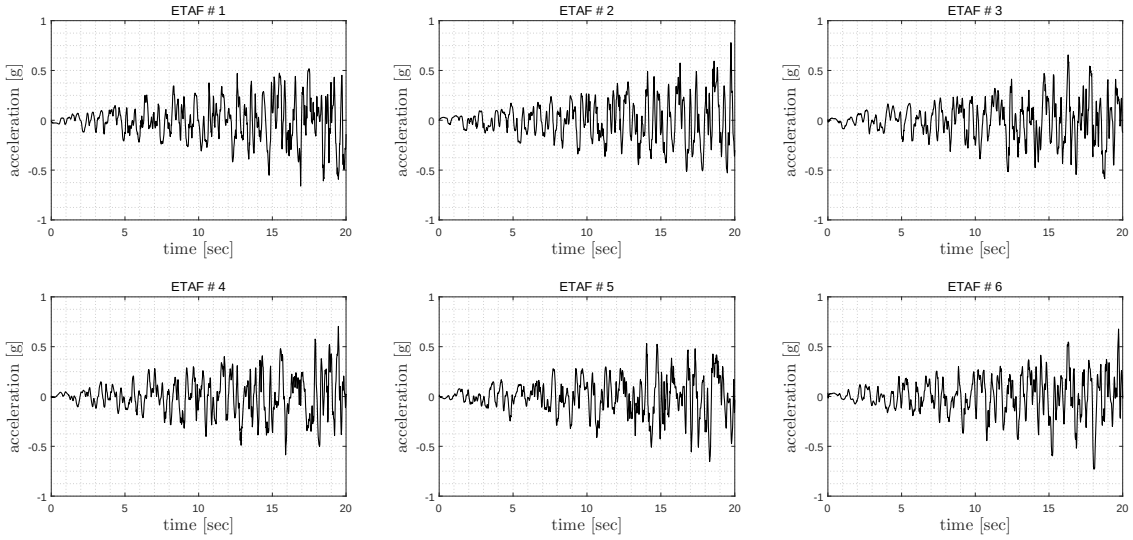

Figure E.25: Six adopted ETF

Figure E.26(c). It should be noted that cracking starts at the central region of the mat base and along a ring on the wall next to soil level.

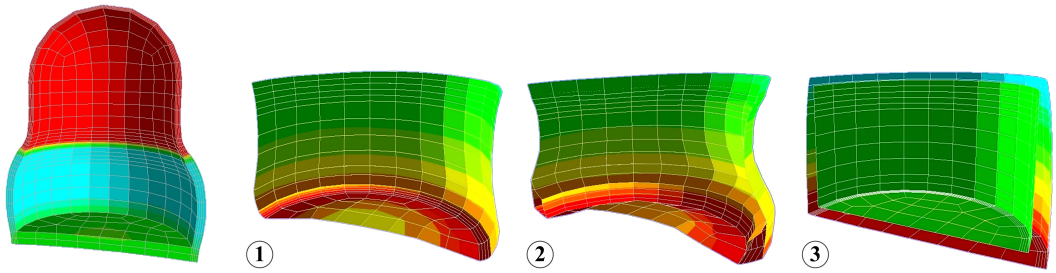

(a) Swelling of contaminated zone

(b) Evolution of joint opening/sliding due to ASR

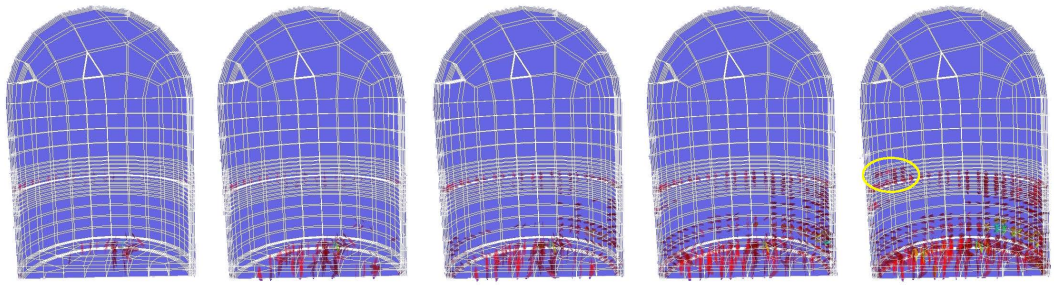

(c) Internal crack propagation (left to right)

Figure E.26: Response of NCVS under static + ASR analysis after 40 years

E.12.2 Impact of ASR on Capacity Curves

Impact of ASR on the structural response of the NCVS can now be ascertained by comparing "Static + Seismic" with "Static + ASR + Seismic" for displacement and stresses for six different ETA functions. Three

sets of simulations are compared: a) Static + dynamic analysis (Referred to Dyn. in the plots); b) Static + ASR with degradation of f'_t and E over time + dynamic analysis; and c) Static + ASR (without material degradation) + dynamic analysis.

Displacements: The absolute value of the (horizontal) displacements corresponding to peaks in (the six) ETAFs is first extracted.The mean of those six ETAFs for each of three assumptions are computed, Figure E.27(a). These are ramping curves as the dynamic acceleration is indeed defined as a linearly increasing one. To better grasp the impact of ASR, results are normalized with respect to the one without ASR (dynamic only), Figure E.27(b). The deviations are time-dependent and, as expected, model with ASR degradation is much more impacted than the one without. On average, and for this case study, ASR with degradation results in ∼20% change, whereas the one without has ∼8% variation with respect to the "Dyn. only" model. If material degradation is ignored (which is an erroneous abstraction) displacements are still lower than those cases without ASR, but greater than ASR with degradation. Note that discrepancy with respect to the case without ASR starts at around 9 s (i.e., until this point the ASR had little impact on deformation). The impact of ASR (with and without degradation) is time-dependent due to the complexities of the internal stress states induced by it or resulting from the seismic excitation, Figure E.27(b).

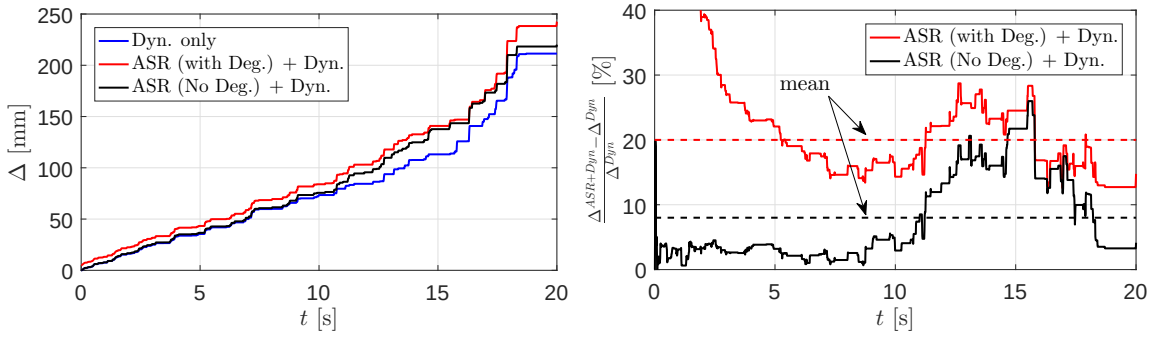

(a) Displacement profile at the top

(b) Displacements normalized and mean differences

Figure E.27: ETA-based displacements and the mean differences

Stresses: Time history of maximum principal stresses are recorded. The ASR affected responses result in higher stresses than those without degradation, and additional substantial damages will be induced by the ASR (with internal damage accounted for). At the base, Figure E.28(a), maximum principal stresses are positive (cracking) and attenuate with time. Stresses are at first low when ASR dominates, but then suddenly increase with a localized damage at time $\simeq$ 17 sec. At the grade elevation, Figure E.28(b), stresses are much higher without ASR, and then gradually decrease with no indication of failure. Note that the tensile strength is 3.1 MPa. On the other hand, in the presence of prior ASR expansion, the stresses are negative, and a sudden localized failure appears at t= 14 sec. For a point above grade, Figure E.28(c), stresses are higher in the absence of ASR and there is indication of a localized failure at t = 15 s. In the presence of ASR, the failure is delayed to about 17 sec. Finally, at the base of the dome, Figure E.28(d), the ASR stresses are substantially higher than without and localized failure occurs around 17 s. For this case, ASR has reduced the stresses at the base, but substantially increased them at the base of the dome. Indeed, stress attenuation with time is the direct result of a nonlinear analysis where upon cracking there is a substantial stress redistribution resulting in localized stress reduction.

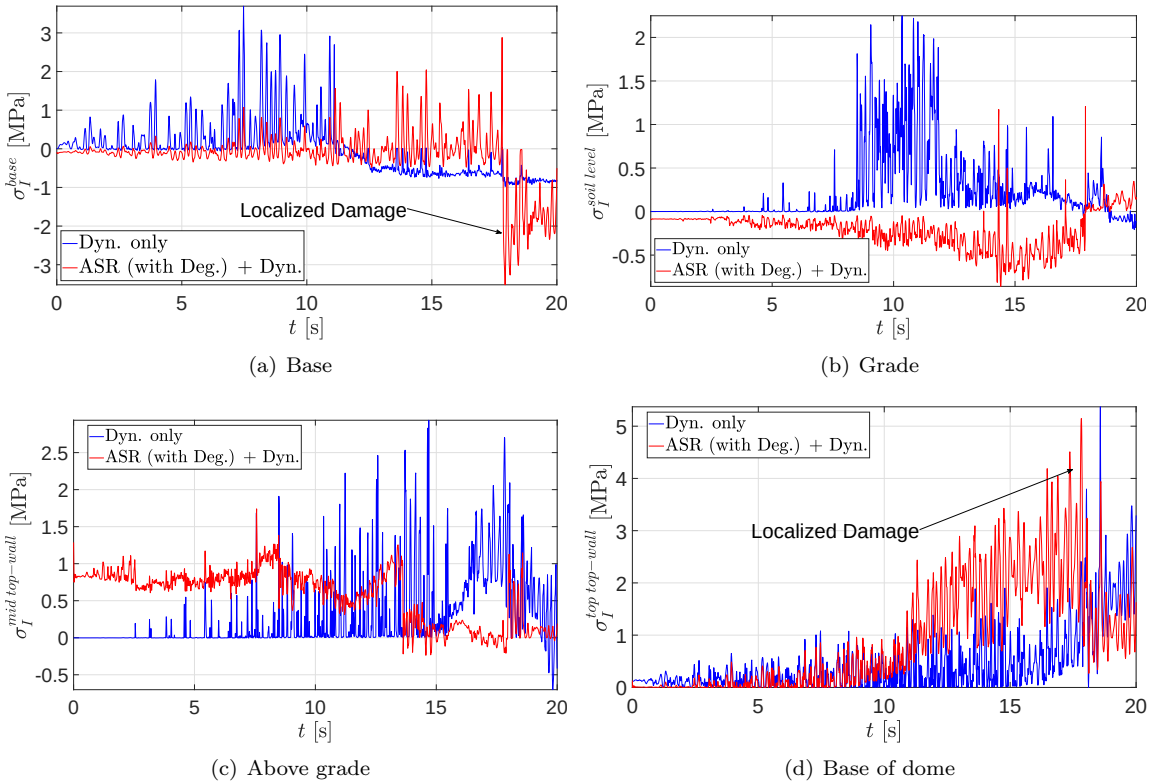

(a) Base (b) Grade

(c) Above grade (d) Base of dome

Figure E.28: Principal stresses capacity curves

Cracking: of the structure is shown Figure E.29 at different times. In general, the crack pattern of ASR affected models are different and the previous observations are qualitatively confirmed by the crack profiles. Indeed, the damage index (DI), ratio of the cracked sections to the total area, is highest when ASR (with damage) preceded the seismic excitation. The ASR has a much higher impact of that portion of the NCVS below grade than above (where no ASR is modeled).

The sound NCVS experiences the major cracks at the soil level at about 12.8 s, while at the corresponding time the ASR-affect NCVS had already some major cracks though all the top-wall. Results of ETA analysis prove that "endurance" of the NCVS is reduced when it is subjected to initial ASR.

E.13 Acknowledgments

The assistance of Mr. Antoine Tixier in the analyses of P1-P8 is gratefully acknowledged.

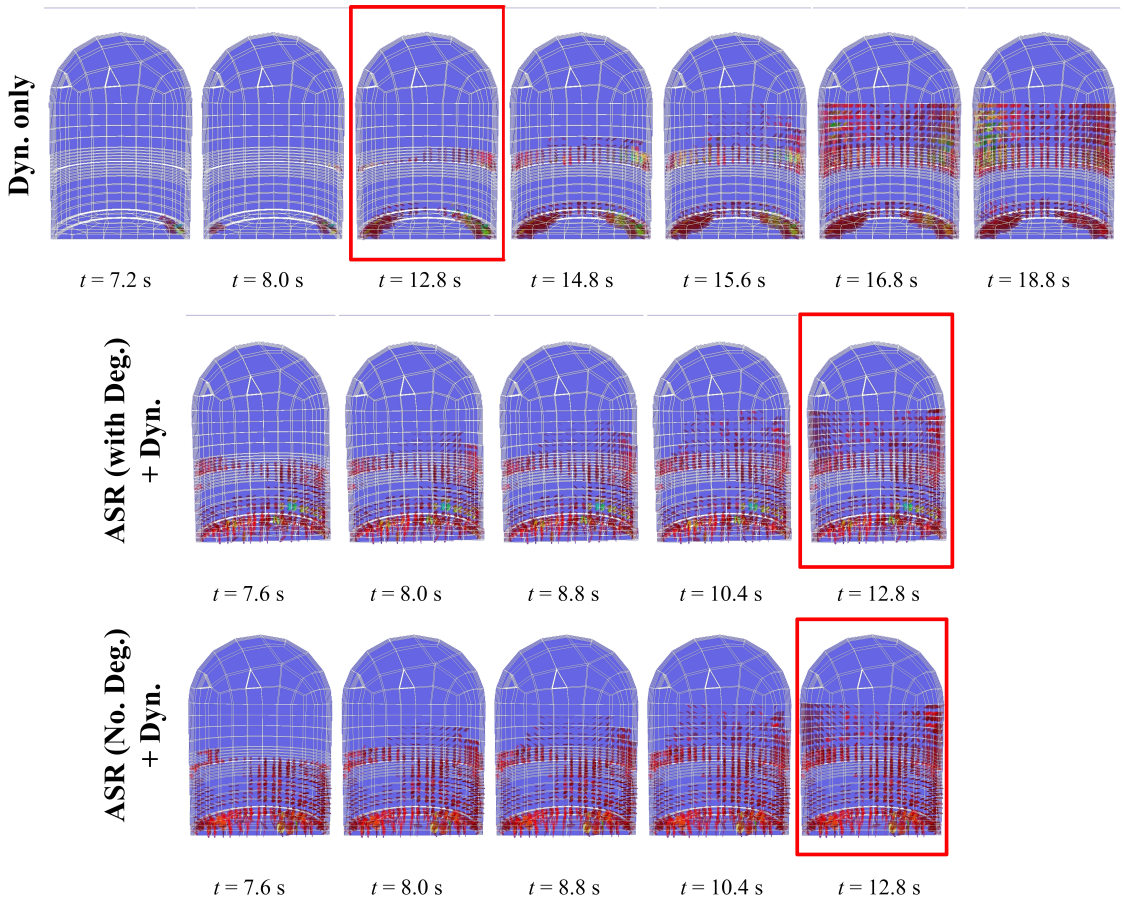

Figure E.29: Crack profile from a sample ETA simulation at identical time steps

Appendix F

Complementary Figures

Abstract

In the course of this research, multiple secondary figures were generated. It was deemed preferable to include them in this report so as not to confuse reading of the report with too many of them.

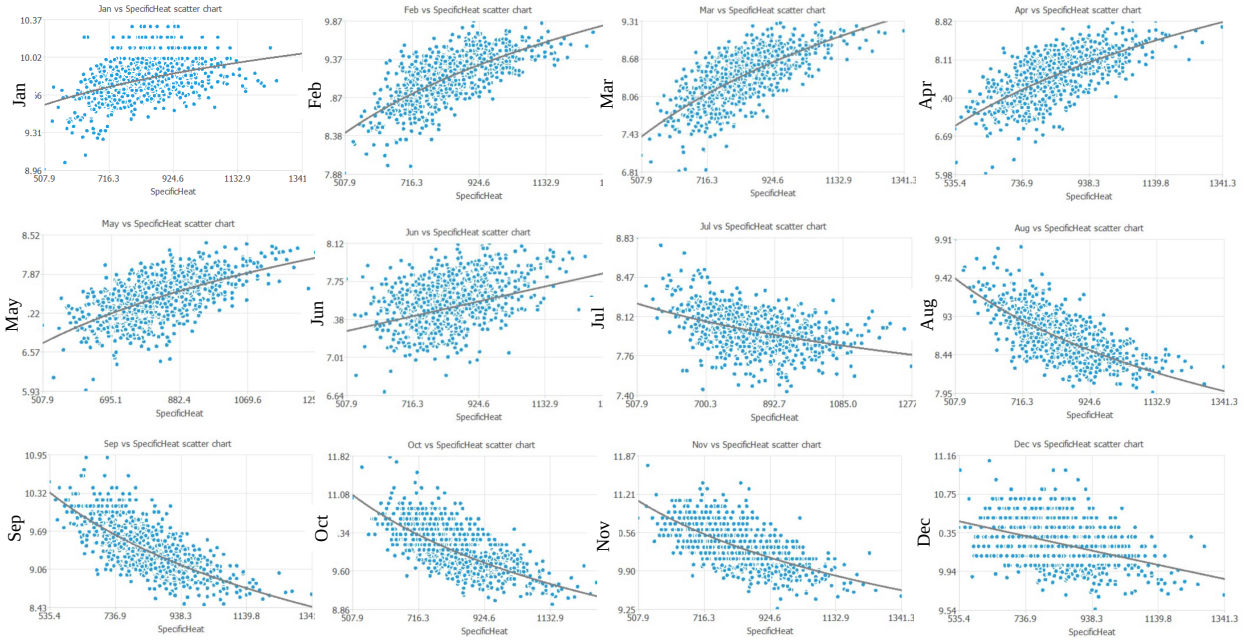

Figure F.1: Monthly specific heat correlation coefficients at node 944 (PoI)

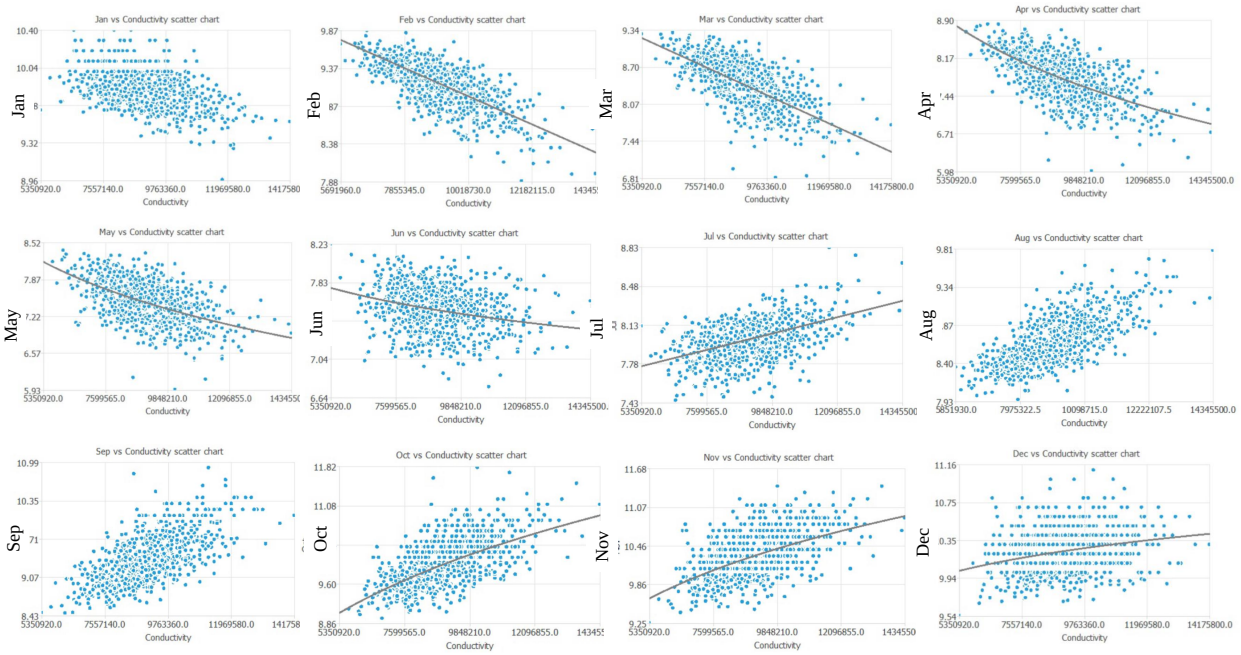

Figure F.2: Monthly conduction correlation coefficients at node 944 (PoI)

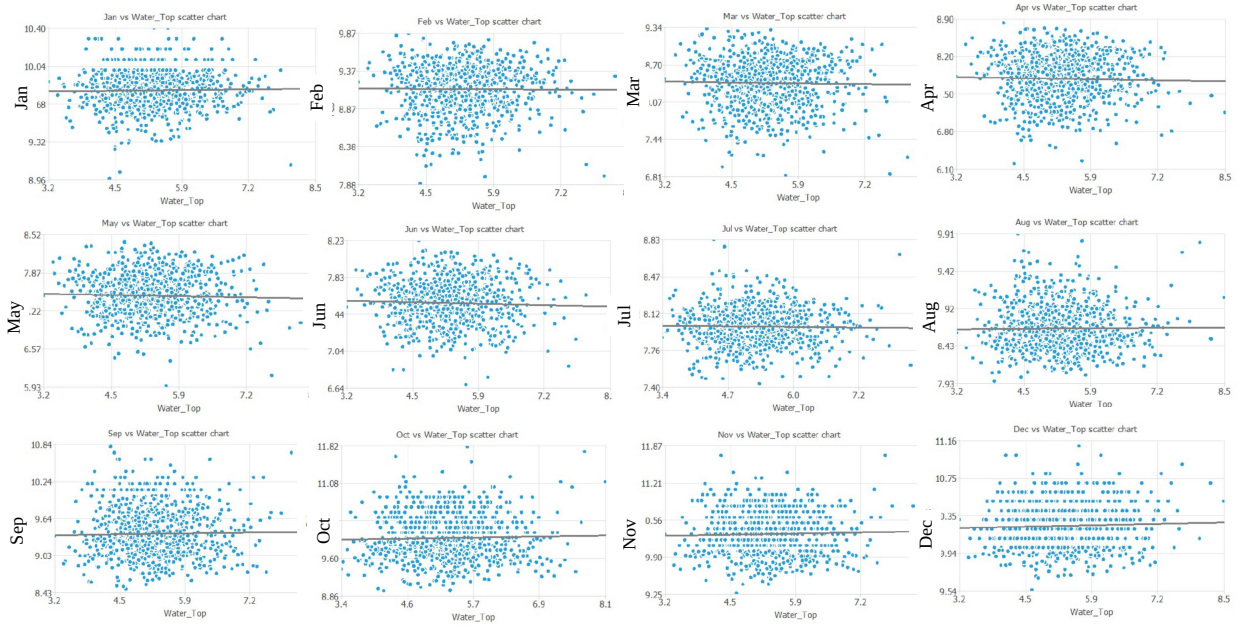

Figure F.3: Monthly top water temperature correlation coefficients at node 944 (PoI)

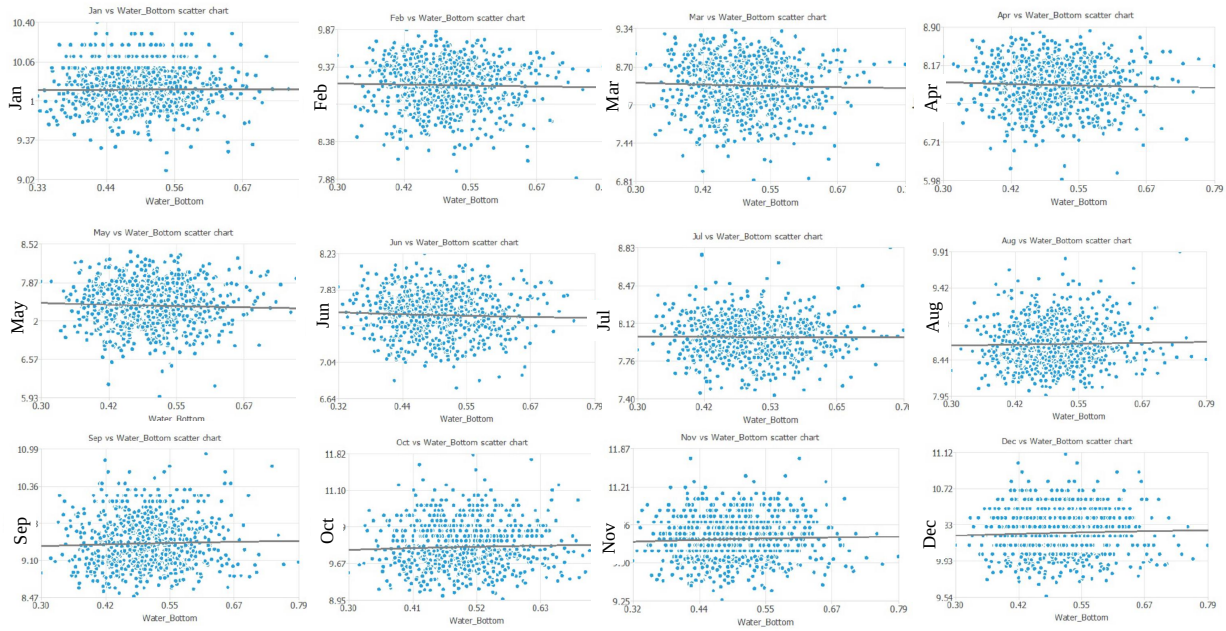

Figure F.4: Monthly bottom water temperature correlation coefficients at node 944 (PoI)

Appendix G

Tabulation of Selected and Referenced Seminoe Recorded Data

Abstract

In the course of this research, multiple sets of data had to be examined, tabulated and examined. Those are reported in this appendix, and we should note that not all of them were actually used in the investigation.

G.1 Geophysical

Table G.1: Summary of Data Collected for Geophysical Investigation (**hatch**)

Hole No.	**Block**	**Proposed Depth (ft)**	**Depth of Geophysical Log (ft)**				
			Sonic	**BOR** Den/Cal	**SES** Den/Cal	**Optical**	**Acoustic**
DH 09-1	L	35	32.1	32.2	33.8	34.7	34
DH 09-2	K	75	71.7	71	73.4	74.4	74.2
DH 09-3	G	125	122.9	122.6	124.2	125.2	125.4
DH 09-4	E	75	73.6	73	75.2	76.1	76.2
DH 09-5	C	34	34.1	34	35.5	36.3	36.3

G.2 Irreversible displacements

G.2.1 Pendulum Based

Table G.2: T_3B Measurements (**Seminoe-Crest-Displ**)

Date	Deflection	Settlement	Date	Deflection	Settlement
Date	(cm)	(cm)	Date	(cm)	(cm)
3/17/2020	21.8	-7.5	9/10/2002	14.0	-4.0
9/19/2019	22.3	-7.6	4/12/2002	11.6	-3.4
4/24/2019	23.2	-7.9	10/6/2001	12.2	-3.7
9/27/2018	22.9	-7.6	4/17/2001	12.2	-3.7
3/20/2018	22.6	-7.6	4/4/2000	10.4	-3.0
10/4/2017	23.2	-7.0	9/23/1999	-	-3.7
4/5/2017	20.4	-	4/16/1999	10.4	-2.7
3/13/2017	-	-7.3	9/9/1998	11.3	-3.4
9/21/2016	22.3	-7.6	4/29/1998	10.1	-3.0
9/24/2015	22.9	-	9/15/1997	11.6	-3.0
9/23/2015	-	-7.3	4/25/1997	10.4	-2.7
3/27/2015	21.0	-7.0	9/27/1996	11.0	-2.7
9/15/2014	21.0	-7.0	3/22/1996	9.1	-2.4
3/24/2014	20.6	-6.5	9/26/1995	10.1	-2.4
9/24/2013	20.1	-	4/4/1995	9.4	-1.8
9/17/2013	-	-6.4	9/9/1994	10.4	-2.1
3/27/2013	18.3	-6.1	4/1/1994	9.8	-1.5
9/21/2012	20.4	-6.4	10/5/1993	9.8	-1.5
3/29/2012	18.0	-5.8	4/2/1993	-	-0.6
9/13/2011	19.8	-6.4	9/22/1992	8.5	-1.2
4/1/2011	18.0	-5.5	3/26/1992	8.2	-0.6
9/28/2010	19.2	-5.8	9/19/1991	8.8	-0.9
3/15/2010	18.6	-5.8	4/23/1991	7.0	-0.3
10/2/2009	18.6	-5.8	9/11/1990	7.6	-0.3
5/4/2009	17.7	-	11/28/1989	-	-
4/14/2009	-	-5.2	10/19/1989	7.0	-
10/27/2008	18.9	-5.2	4/26/1989	5.8	-
4/23/2008	18.0	-4.9	9/19/1988	7.3	-
9/12/2007	18.3	-5.2	6/1/1988	5.5	-
4/9/2007	16.5	-4.9	9/21/1987	5.2	-
9/18/2006	-	-4.9	4/7/1987	3.7	-
4/3/2006	15.5	-4.3	10/30/1986	4.6	-
9/1/2005	16.2	-4.9	4/22/1986	3.7	-
4/1/2005	13.7	-4.3	4/11/1985	1.8	-
9/23/2004	15.5	-4.3	10/30/1984	3.4	-
3/23/2004	14.0	-4.0	4/16/1984	0.9	-
12/4/2003	14.3	-3.4	7/27/1982	0.3	-
4/2/2003	12.8	-4.0	3/26/1982	2.4	-
			7/2/1979	1.2	-

G.2.2 Plumbline based

Table G.3: Plumbline measurements of upstream face (**lung2012**)

Depth	**Elev**	**St. 2+18**		**St. 3+04**		**St. 4+60**	
m	**m**	**2002**	**2012**	**2002**	**2012**	**2002**	**2012**
0.0	1939.7	0.0	0.0	0.0	0.0	0.0	0.0
1.5	1938.2	9.7	17.5	33.3	39.6	22.4	23.9
3.0	1936.7	9.7	20.6	54.1	65.0	42.9	49.3
4.6	1935.2	28.7	44.5	73.2	88.9	50.8	62.0
6.1	1933.7	54.1	69.9	100.1	119.1	71.4	84.1
7.6	1932.1	73.2	106.4	127.0	147.6	76.2	92.2
9.1	1930.6	100.1	133.4	146.1	171.5	87.4	106.4
10.7	1929.1	115.8	155.7	163.6	195.3	108.0	128.5
12.2	1927.6	119.1		173.0		125.5	
13.7	1926.0	127.0		182.6		147.6	
15.2	1924.5	150.9		196.9		149.4	
16.8	1923.0	166.6		203.2		152.4	

G.2.3 Extensometer

Table G.4: Extensometer (**hatch**)

ID	**Location**	**Gauge length (cm)**	**Annual Length Change (mm/yr)**	**Annual Growth Rate (μstrain/yr)**
TE-1	Station 0+83	450.19	0.70	156
TE-2	Station 1+85	459.33	0.76	166
TE-3	Station 2+51	465.73	0.91	196
TE-4	Station 3+10	465.43	0.91	196
TE-5	Station 3+34	465.89	0.91	196
TE-6	Station 3+77	468.33	0.91	195
TE-7	Station 4+60	464.82	0.46	98
TE-8	Station 5+30	463.14	0.30	66

G.2.4 Joint meters

G.3 Concrete properties

G.3.1 1975 Cores

Table G.5: Joint Meter Summary

Joint Meter	Location	Relative Movement Direction	Annual Movement (mm/yr)
JT-4	Upstream crack above water	Vertical Shear (up/down)	-0.10
JT-5	Upstream crack above water	Longitudinal (open/close)	0.13
JT-6	Upstream crack movement	Horizontal Shear (in/out)	0.05
JT-7	Downstream control		0.00
JT-8	Downstream crack movement	Vertical shear (up/down)	0.076
JT-9	Downstream crack movement	Longitudinal (open/close)	0.00
JT-10	Downstream crack movement	Shear (in/out)	0.051

Table G.6: 1975 Modulus oF Elasticity (**Brandon75**)

		MOE(Gpa)	
Spec	depth (m)	E_s 1st cycle	E_s 2nd cycle
DH-1	1.6	10.3	11.1
DH-1	7.8	16.1	17.1
DH-1	8.5	15.7	17.6
DH-1	15.2	22.1	23.4
DH-1	16.9	14.8	16.9
DH-2	2.3	14.8	15.9
DH-2	3.7	12.8	14.0
DH-2	5.2	11.0	12.5
DH-2	11.9	15.6	17.0
DH-2	13.8	14.4	13.1
DH-2	16.9	11.2	12.7

Table G.7: 1975 Compressive Strength, (**Brandon75**)

Loc	depth (m)	f'_c (Mpa)	Rupture Mode (in order of occurrence)
DH-1	0.4	39.6	Shear, breakout
DH-1	1.6	17.8	Bond slip, breakout
DH-1	5.4	33.4	Breakout, splitting
DH-1	7.8	48.1	Shear
DH-1	8.5	41.8	Splitting, breakout
DH-1	8.7	38.1	Splitting, breakout
DH-1	9.4	39.2	Shear
DH-1	12.7	40.1	Shear, breakout
DH-1	14.2	43.2	Shear
DH-1	15.2	35.0	Splitting, breakout
DH-1	15.3	34.4	Splitting, breakout
DH-1	16.9	38.9	Splitting shear, breakout
DH-2	2.3	30.5	Bond slip, breakout
DH-2	3.7	40.9	Shear, breakout
DH-2	4.7	35.6	Splitting, shear
DH-2	5.2	29.1	Bond slip, breakout, splitting
DH-2	6.5	43.7	Shear
DH-2	8.2	51.4	Shear
DH-2	11.9	38.9	Breakout, shear
DH-2	13.2	43.0	Shear
DH-2	13.8	26.8	Breakout, splitting
DH-2	15.9	34.1	Splitting, shear
DH-2	16.3	39.9	Shear, breakout
DH-2	16.9	29.3	Breakout, splitting

Notes, Significance of Rupture Mode:

1. Shear, as typical mode, gave higher strengths.
2. Breakout of rock pebbles affected strength and development of shear.
3. Splitting observed in 50 percent of tests, affected strength to minor or major degree.
4. Bond slip, of interior rock pebble.

Table G.8: 2003 Core Testing Results (**hatch**)

Hole No. **No.**	**Depth** **(m)**	**Elevation** **(m)**	f'_c **(MPa)**	R **(GPa)**	ν **-**
DH03-01 vertical		1,938.3	12	-	-
		1,936.5	17	13	0.31
		1,935.5	16	8	0.23
		1,934.4	24	11	0.27
		1,934.0	26	16	0.30
		1,932.0	26	-	-
		1,931.4	22	11	0.25
		1,930.3	23	15	0.25
		1,929.7	26	13	0.52
		1,928.7	20	11	0.24
		1,928.2	23	-	-
		1,926.6	32	14	0.19
		1,926.1	30	19	0.20
		1,921.9	30	19	0.14
		1,920.5	30	20	0.25
		1,918.8	33	27	0.19
		1,916.6	37	19	0.17
	Average		**25**	**16**	**0.25**
DH03-02 vertical		1,938.0	9	-	-
		1,937.4	19	8	0.48
		1,935.9	20	9	0.30
		1,935.1	22	10	0.29
		1,934.4	20	7	0.14
		1,931.8	29	11	0.13
		1,929.2	39	17	0.23
		1,928.3	24	11	0.24
		1,925.5	23	-	-
		1,924.1	33	12	0.16
		1,919.8	28	10	0.25
		1,916.8	37	27	0.35
	Average		**25**	**12**	**0.26**
DH03-03 horizontal	3.7	1,883.7	29	26	0.28
	6.6	1,883.7	37	25	0.21
	8.9	1,883.7	33	37	0.26
	Average		**33**	**29**	**0.25**
DH03-04 DH03-04A horizontal	0.3	1,880.9	44	18	0.30
	4.0	1,880.9	36	29	0.29
	6.7	1,880.9	37	22	0.16
	8.7	1,880.9	40	28	0.23
	Average		**39**	**24**	**0.25**

Table G.9: 2009 Test results (**hatch**)

Hole No.	Block No.	Depth Interval (m)		f_c (MPa)	E (GPa)	μ	f_t (MPa)	f_s (MPa)
DH 09-1	L	0.00	3.05	19.10	5.58	0.24	-	-
DH 09-2	K	3.05	7.62	23.17	10.96	0.24	0.46	1.69
DH 09-3	G	7.62	15.24	26.27	12.76	0.26	0.52	2.10
DH 09-4	E	15.24	22.86	32.34	14.82	0.20	0.50	1.93
DH 09-5	C	22.86	38.10	34.27	18.27	0.16	0.70	2.45
		Average		28.61	12.96	0.23	0.55	2.10

Table G.10: 2013 Test results (**hatch**)

Hole No.	Station Station	Depth (m)	Block No.	Depth (m)	Interval (m)	f_c (MPa)	E (GPa)	ν	f_t (MPa)	f_s (MPA)
DH 13-1	5+29	10.85	L	0.00	3.05		8.55	0.30	-	-
DH 13-2	4+80	22.86	K	3.05	7.62		10.48	0.24	0.41	1.62
DH 13-3	2+98	38.10	G	7.62	15.24	22.55	9.58	0.24	0.48	1.83
DH 13-4	2+28	22.59	E	15.24	22.86	28.27	12.20	0.23	0.62	2.00
DH 13-5	1+23	10.64	C	22.86	38.10	35.99	18.13	0.24	1.03	1.72
				Average		25.03	11.86	0.24	0.55	1.93

Table G.11: 1980-2003-2013 Compressive Strength (**hatch**)

		1980		**1998**		**2003**		**2009**		**2013**	
Depth		**El**	f'_c	**El**	f'_c	**El**	f'_c	**El**	f'_c	**El**	f'_c
(m)		**(m)**	**(MPa)**	**(m)**	**(MPa)**	**(m)**	**(MPa)**	**(m)**	**(MPa)**	**(m)**	**(MPa)**
		-	-	-	-	1,938.2	10.1	-	-	-	-
0.0	3.0	1,937.5	19.2	1,937.4	18.5	1,937.4	19.0	1,937.4	19.1	-	
		1,936.9	26.9	1,936.9	28.5	-	-	-	-	1,936.6	18.5
Avg		**1,937.2**	**23.0**	**1,937.1**	**23.5**	**1,937.8**	**14.5**	**1,937.4**	**19.1**	**1,936.6**	**18.5**
		1,935.3	28.8	1,935.4	28.6	1,935.8	18.0	-	-	1,935.5	19.2
		-	-	-	-	1,935.1	21.8	1,935.0	24.5	1,934.7	19.2
		1,934.0	25.2	1,934.1	32.5	1,934.3	23.0	1,934.3	25.4	1,934.3	23.2
3.0	7.6	-	-	-	-	-	-	1,933.7	17.4	1,933.4	20.9
		1,932.7	29.0	-	-	-	-	1,932.8	23.8	-	
		-	-	-	-	1,931.9	27.3	1,931.8	22.1	1,931.8	20.1
		1,931.5	32.1	1,931.2	25.7	1,931.4	22.0		-	-	
Avg		**1,933.4**	**28.8**	**1,933.6**	**29.0**	**1,933.7**	**22.4**	**1,933.5**	**22.6**	**1,934.0**	**20.5**
		-	-	-	-	1,930.3	22.7	1,930.6	28.8	1,930.5	21.6
		-	-	1,930.2	21.4	1,929.7	25.9	1,929.9	22.5	1,930.1	25.4
		-	-	-	-	1,929.0	29.2	1,928.9	21.0	1,929.3	20.0
		-	-	1,928.6	17.8	-	-	-	-	1,928.7	19.2
7.6	15.2	1,927.8	25.2	-	-	1,928.2	23.3	1,928.1	26.8	1,927.8	23.6
		-	-	1,926.4	34.1	1,926.6	31.5	1,926.8	27.2	1,926.6	29.5
		-	-	-	-	1,925.8	26.3	1,925.5	31.2	1,925.7	21.8
		-	-	-	-	-	-	-	-	1,925.0	26.2
		-	-	1,923.7	34.3	1,924.1	33.4	1,923.6	30.0	1,923.7	24.6
Avg		**1,927.8**	**25.2**	**1,927.2**	**26.9**	**1,927.7**	**27.5**	**1,927.6**	**26.8**	**1,927.5**	**23.6**
		-	-	-	-	-	-	-	-	1,922.5	18.3
		1,921.7	43.5	-	-	1,921.9	30.3	1,921.8	32.7	1,922.0	27.4
		-	-	-	-	1,920.2	29.1	1,920.7	34.5	1,920.5	27.4
15.2	22.9	-	-	-	-	-	-	-	-	1,919.7	36.3
		-	-	-	-	1,918.8	33.1	1,918.9	32.1	1,918.4	27.4
		-	-	-	-	-	-	1,918.1	23.7	-	-
		-	-	-	-	1,916.7	36.9	1,916.6	32.8	1,916.5	31.2
Avg		**1,921.7**	**43.5**			**1,919.4**	**32.4**	**1,919.2**	**31.2**	**1,919.9**	**28.0**
		1,915.6	42.4	-	-	-	-	1,915.3	31.2	1,915.8	33.5
		-	-	-	-	-	-	-	-	1,914.8	40.8
		-	-	-	-	-	-	1,913.9	34.5	-	-
		-	-	-	-	-	-	-	-	1,913.4	36.0
		-	-	-	-	-	-	1,911.6	36.7	1,911.2	37.1
		-	-	-	-	-	-	1,910.4	35.4	1,910.1	36.3
22.9	38.1	-	-	-	-	-	-	1,908.6	28.2	1,907.9	36.1
		-	-	-	-	-	-	1,907.1	39.9	1,906.8	33.4
		-	-	-	-	-	-	1,905.3	29.7	1,905.1	29.6
		-	-	-	-	-	-	1,903.7	32.7	1,903.5	38.5
		-	-	-	-	-	-	1,902.4	36.6	1,902.5	36.7
		-	-	-	-	-	-	1,901.1	32.3	1,901.0	37.8
Avg		**1,915.6**	**42.4**	-	-	-	-	**1,907.9**	**33.7**	**1,908.4**	**36.0**

Table G.12: 1980-2003-2013 Elastic Modulus (**hatch**)

		1980		**1998**		**2003**		**2009**		**2013**	
Depth		**El**	E	**El**	E	**El**	E	**El**	E	**El**	E
(m)		**(m)**	**(GPa)**	**(m)**	**(GPa)**	**(m)**	**(GPa)**	**(m)**	**(GPa)**	**(m)**	**(Pa)**
0.0	3.0	1,937.5	8.62	1,937.4	12.20	1,937.4	7.79	1,937.4	5.58		
		1,936.9	12.96	1,936.9	14.41					1,936.7	8.55
Avg		**1,937.2**	**10.82**	**1,937.1**	**13.31**	**1,937.4**	**7.79**	**1,937.4**	**5.58**	**1,936.7**	**8.55**
3.0	7.6	1,935.3	13.79	1,935.4	12.00	1,935.8	10.20			1,935.5	9.58
		-	-	-	-	1,935.1	10.48	1,935.1	14.13	1,934.9	6.41
		1,934.0	14.89	1,934.1	19.93	1,934.3	11.45	1,934.3	8.48	1,934.3	10.96
		-	-	-	-	-	-	1,933.7	12.55	1,933.7	13.93
		1,932.7	12.20	-	-	-	-	1,932.8	7.72	-	-
		-	-	-	-	1,931.9	10.55	1,931.8	11.45	1,931.9	9.79
		1,931.5	13.31	1,931.2	15.03	1,931.4	10.55	-	-	-	-
Avg		**1,933.4**	**13.58**	**1,933.6**	**15.65**	**1,933.7**	**10.62**	**1,933.5**	**10.89**	**1,934.1**	**10.14**
7.6	15.2	-	-	-	-	1,930.3	14.96	1,930.6	10.20	-	-
		-	-	1,930.2	9.86	1,929.7	13.44	1,929.9	13.10	1,930.1	8.76
		-	-	-	-	1,929.0	14.20	1,928.9	8.96	1,929.4	11.58
		-	-	1,928.6	8.34	-	-	-	-	1,928.7	5.65
		1,927.8	23.30	-	-	1,928.2	11.65	1,928.1	12.48	1,927.7	9.03
		-	-	1,926.4	19.65	1,926.6	13.72			1,926.6	9.72
		-	-	-	-	1,925.8	14.69	1,925.5	19.10	1,925.7	11.58
		-	-	-	-	-	-	-	-	1,925.0	10.00
		-	-	1,923.7	14.82	1,924.1	12.34	1,923.7	10.62	1,923.7	9.17
Avg		**1,927.8**	**23.30**	**1,927.2**	**13.17**	**1,927.7**	**13.58**	**1,927.8**	**12.41**	**1,927.1**	**9.45**
15.2	22.9	-	-	-	-	-	-	-	-	1,922.5	15.10
		1,921.7	26.61	-	-	1,921.9	18.55	-	-	1,922.0	14.07
		-	-	-	-	1,920.2	15.24	1,920.8	16.48	1,920.6	11.72
		-	-	-	-	-	-	-	-	1,919.7	11.65
		-	-	-	-	1,918.8	27.37	-	-	1,918.5	12.55
		-	-	-	-	-	-	1,918.1	12.76	-	-
						1,916.7	18.00	1,916.6	12.07	1,916.5	11.31
Avg		**1,921.7**	**26.61**	-	-	**1,919.4**	**19.79**	**1,918.5**	**13.79**	**1,920.0**	**12.76**
22.9	38.1	1,915.6	23.30	-	-	-	-	1,915.3	17.17	1,915.8	10.89
		-	-	-	-	-	-	-	-	1,914.8	22.27
		-	-	-	-	-	-	-	-	1,913.4	14.20
		-	-	-	-	-	-	1,911.6	16.48	1,911.2	14.13
		-	-	-	-	-	-	1,907.2	22.20	1,906.8	21.37
		-	-	-	-	-	-	-	-	1,905.1	15.44
		-	-	-	-	-	-	-	-	1,903.5	19.86
		-	-	-	-	-	-	1,902.4	17.37	1,902.5	22.41
		-	-	-	-	-	-	-	-	1,901.0	22.89
Avg		**1,915.6**	**23.30**	-	-	-	-	**1,909.1**	**18.34**	**1,908.2**	**18.13**

G.3.2 Shear Strength

Table G.13: Combined Intact Shear Properties within the Normal Stress Range (**Erdogan2010**)

	Measured values				Reclamation Database
AAR	Low	Medium	High	All Combined	No AAR
c, MPa	0.00	0.00	0.00	0.00	0.00
Φ, deg	36.7	42.0	58.1	56.2	53
R^2	0.21	0.96	0.87	0.31	0.48

G.4 Overcoring

Table G.14: Overcoring test results (**hatch**)

Hole #	Run #	X (m)	Y (m)	Z (m)	σ_{max} (MPa)	σ_{min} (MPa)	α^* Deg.	E (GPa)	Node #
				Vertical					
	1			56.96	0.83	0.40	-27.1	18.9	
	1A			56.96	0.91	0.44	-27.1	20.8	
	2			54.67	1.44	-0.15	77.1	18.3	
DH03-01	3	-51.6	70.4	53.85	1.48	-0.73	81.2	17.7	
	4			52.14	0.48	-0.93	88	31.0	
	5			50.64	1.35	-0.41	70.9	20.8	
	6			49.12	1.59	-0.43	85.5	25.2	
	2			54.63	0.99	-0.21	101.8	15.4	
DH03-02	3	48.3	71.3	53.65	0.76	-0.49	72.2	14.4	
	4			52.23	0.88	-0.34	78.7	16.0	
	5			49.22	0.90	-0.71	80.5	18.5	
				Horizontal					
	1			68.67	4.78	1.61	91.7	26.7	
DH03-03	2	??	??	65.63	5.56	0.95	90.7	33.5	
	3			64.24	3.20	0.31	100.9	34.7	
	4			62.65	2.48	0.70	92.2	33.2	
	1			68.85	4.13	0.84	59.5	34.4	
	2			68.27	4.08	2.88	61	33.9	
DH03-04A	3	??	??	65.65	2.92	1.00	67.4	33.2	
	4			64.25	1.58	0.23	64.9	31.8	
	5			62.76	1.33	0.45	71.2	29.1	

* Direction of σ_{max}

G.5 Temperatures

G.5.1 Air

Table G.15: Air temperature (**hatch**)

Month	**Jan**	**Feb**	**Mar**	**Apr**	**May**	**Jun**	**Jul**	**Aug**	**Sep**	**Oct**	**Nov**	**Dec**
T°C	-5.4	-5.0	-2.4	2.1	7.3	12.8	17.7	19.3	15.9	9.9	3.0	-2.9
$T^{\circ}_{Radiation}$C	-0.9	0.8	2.6	5.8	9.8	14.0	18.5	20.9	19.6	15.6	9.1	2.4

G.5.2 Water

Table G.16: Water temperature (**hatch**)

Depth (m)	**Jan**	**Feb**	**Mar**	**Apr**	**May**	**Jun**	**Jul**	**Aug**	**Sep**	**Oct**	**Nov**	**Dec**
0.0	3.9	3.9	4.4	-	-	12.2	17.2	22.2	20.0	15.6	12.8	8.9
1.6	5.6	6.1	6.7	-	-	11.7	16.1	21.7	20.0	15.6	12.2	8.3
4.6	6.7	7.2	7.2	-	-	10.0	14.4	18.9	19.4	15.0	11.7	8.3
7.7	6.9	7.5	7.5	-	-	9.4	11.7	12.2	13.3	14.4	11.7	8.3
19.8	7.2	7.8	7.8	-	-	8.9	10.0	10.6	11.1	10.6	11.1	8.3
35.1	7.2	7.8	7.8	-	-	8.9	8.9	8.9	9.4	9.4	9.4	8.3
80.8	7.8	8.3	8.3	-	-	8.3	8.3	8.3	8.3	8.3	8.3	8.3

Table G.17: Water Temperatures(^{o}C) at different elevations for Seminoe Dam during 5 months in 2018

Seminoe - Water Column Temperature.xlsx						
		February	June	October	November	December
Elevation(m)	Depth(m)	36.08(Days)	155.75(Days)	274.29(Days)	309.66(Days)	337.16(Days)
1935.78	3.05	12.8			10.2	5.3
1932.74	6.1	2.3			10.1	5.3
1929.69	9.1	2.2	15.9	16.2	10.1	5.3
1926.64	12.2	2.1	13.9	15.9	10.1	5.3
1923.59	15.2	2.1	13.7	15.8	10.1	5.3
1920.54	18.3	2.1	13.5	15.8	10.1	5.3
1917.50	21.3	2.1	13.2	15.8	9.9	5.3
1914.45	24.4	2.1	12.3	15.8	9.9	5.3
1911.40	27.4	2.1	10.7	15.8	9.9	5.3
1908.35	30.5	2.1	10.2	15.8	9.9	5.3

Appendix H

Additional Uncertainty Quantification Results

Abstract

The uncertainty quantification (UQ) study was conducted with 50, 100, and 200 analyses. We have retained results of the last one in the report, and this chapter will simply report the figures associated with the 50 and 100 analyses UQ studies.

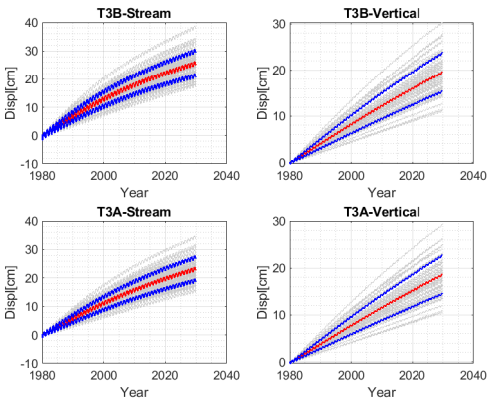

(a) 50 Analysis

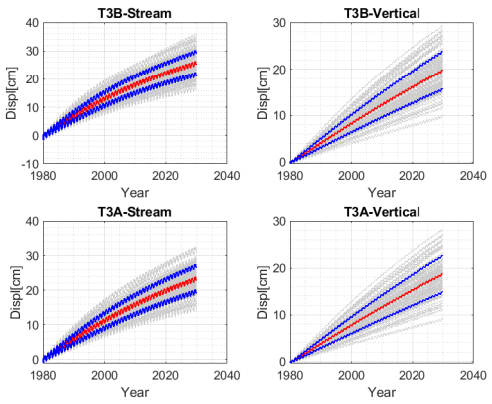

(b) 100 Analysis

Figure H.1: Crest Displacements (Stream and vertical directions)

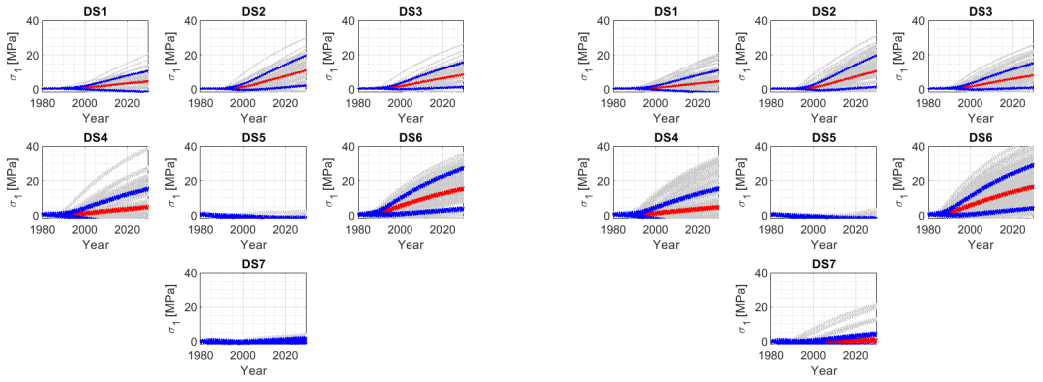

(a) 50 Analysis (b) 100 Analysis

Figure H.2: Maximum Principal Stress; Downstream

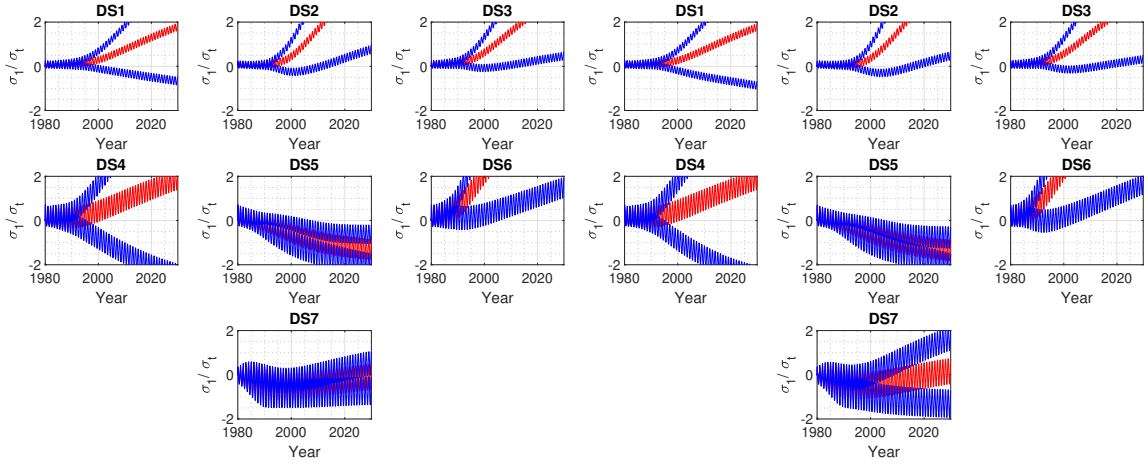

(a) 50 Analysis (b) 100 Analysis

Figure H.3: Ratio of Maximum Principal Stress to Tensile Strength; Downstream

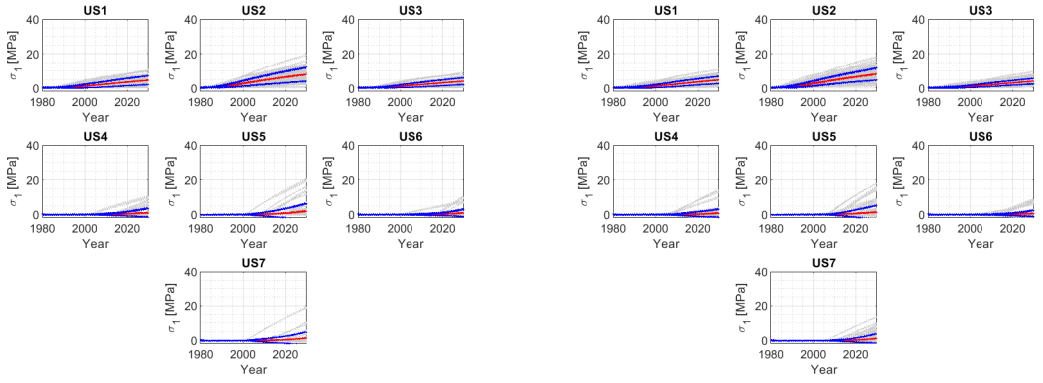

(a) 50 Analysis (b) 100 Analysis

Figure H.4: Maximum Principal Stress; Upstream

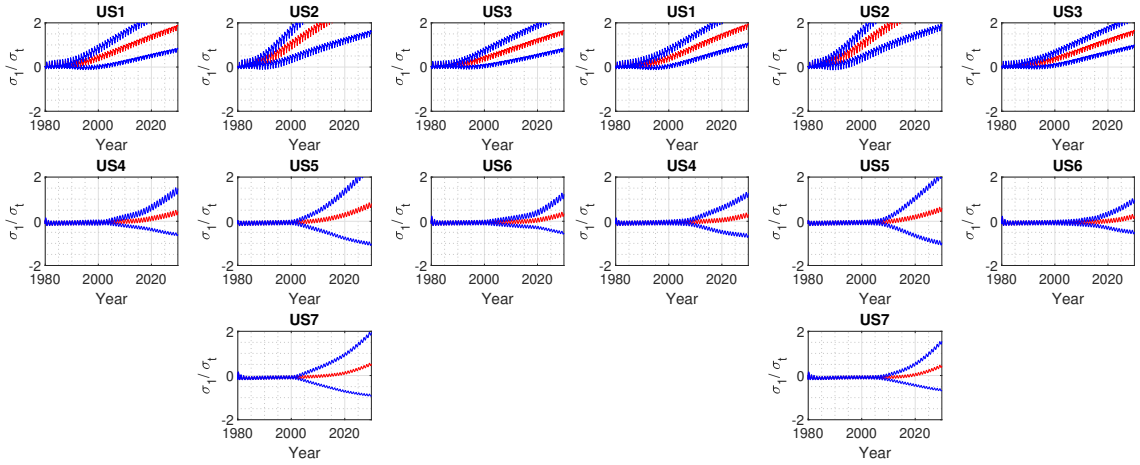

(a) Analysis 50 (b) Analysis 100

Figure H.5: Ratio of Maximum Principal Stress to Tensile Strength; Upstream

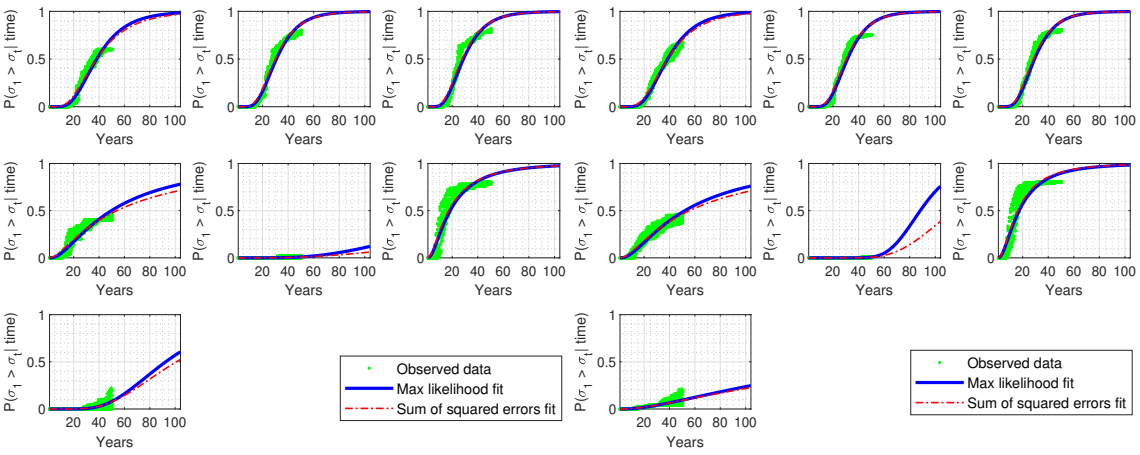

(a) 50 Analysis (b) 100 Analysis

Figure H.6: Probability of Exceedance; Downstream

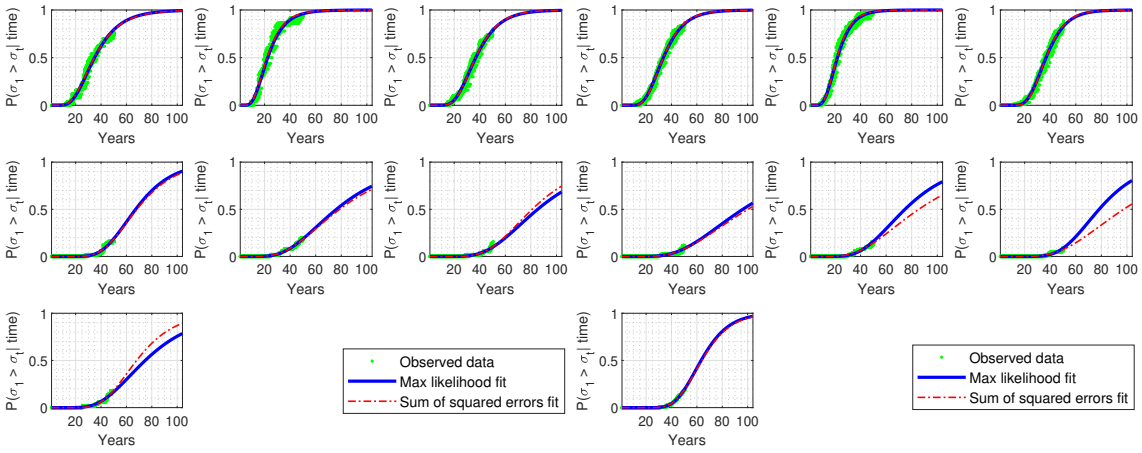

(a) Analysis 50 (b) Analysis 100

Figure H.7: Probability of Exceedance; Upstream

Appendix I

Modeling Dam-Foundation

Abstract

Modeling of the foundation proved to be slightly problematic. At first the presence of the first massive concrete placement was ignored, and given the (typical) deformed shape of the arch dam, this would have resulted in joint openings in the downstream face.

Reclamation commented that this was not observed, and the first massive concrete placement ensured that there would be no slip nor rotation at the base. Hence, all the analyses in the report accounted for this massive concrete placement (modeled by drastically increasing the joint properties at the base of the dam).

This appendix, however reports the results previously obtained for academic interest as this may indeed occur in other arch dams suffering from AAR. So far the illustrated results were based on the assumption

of the full rock-concrete bond below the dam. However, this might not be the case for other arch dams. Therefore, the analysis results assuming a rock-concrete joint below the dam are presented in this chapter. the crack opening displacements at the bottom of the dam is shown in figure I.1 using 6 nodes in a row from upstream to downstream in order to assess the potential for the uncontrolled release of water. As seen the the crack is closing on the upstream side while opening on the downstream which denies the likelihood of the release of water from bottom of the dam.

Figure I.2 also demonstrates the same finding for 7 different time steps and at 6 different locations suggesting that the crack opening displacement is close to zero at the upstream and greater at the downstream and is increasing with time. This observation suggests the deformations as shown in figure I.3. In other words the dam is tilting towards the upstream resulting in the opening of the crack on the downstream side. The angles β and α can be a rough indication of the dam tilt which are also plotted in figure I.4.

The 200 analysis shows that the mean value of the rotation of the dam wall is greater than the mean of the dam bottom rotation while these 2 values are approaching to each other with time. At the end of the analysis the mean value of the α and β are about 0.0035 and 0.0015 radians.

In addition to the crack opening on the downstream side of the dam, the abovementioned figure is also supporting the fact that sliding is occuring at the bottom of the dam as plotted in figure I.5. Since in the finite element model, the joint elements have finite stiffness to prevent closure there are negative displacements reported In figure I.1.

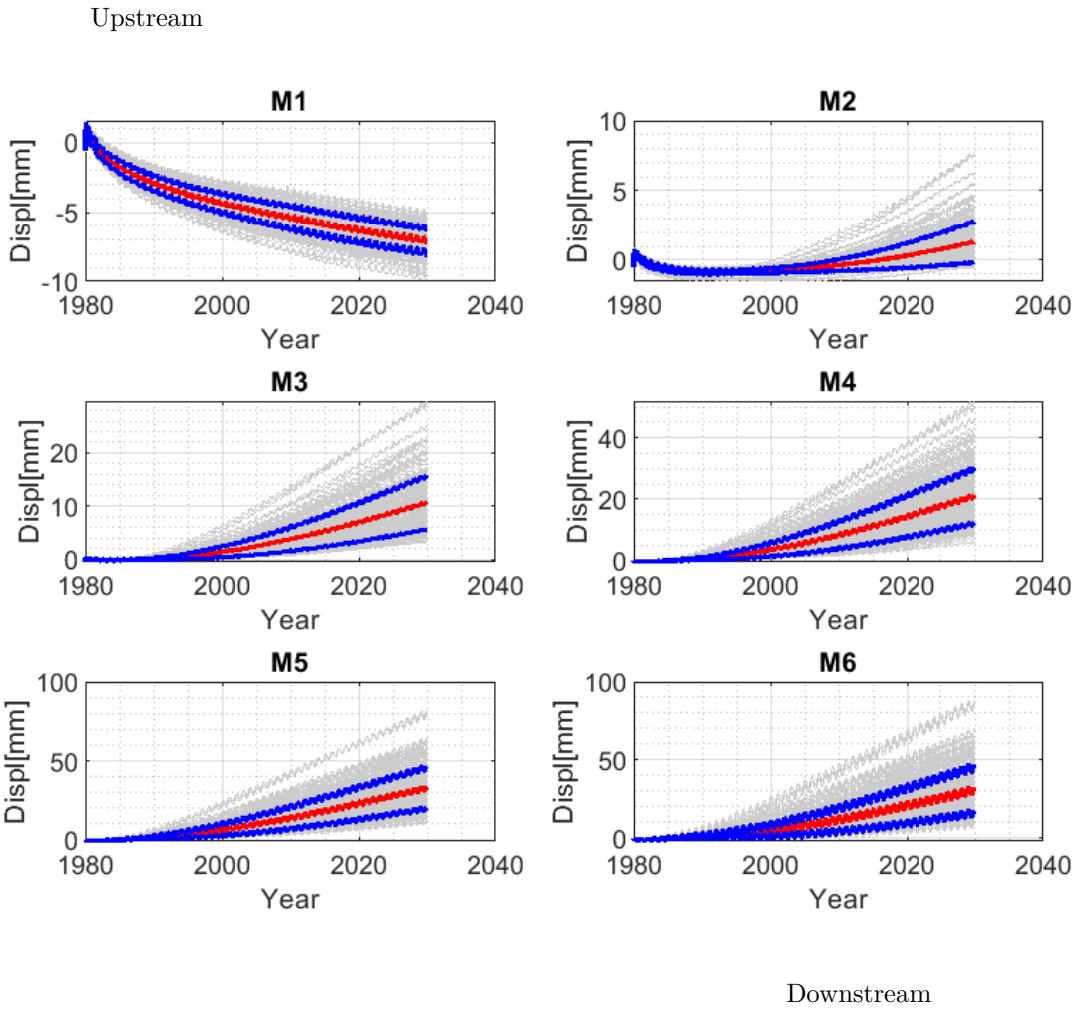

Figure I.1: Concrete Rock interface crack opening displacements for 6 nodes from upstream to downstream for all increments

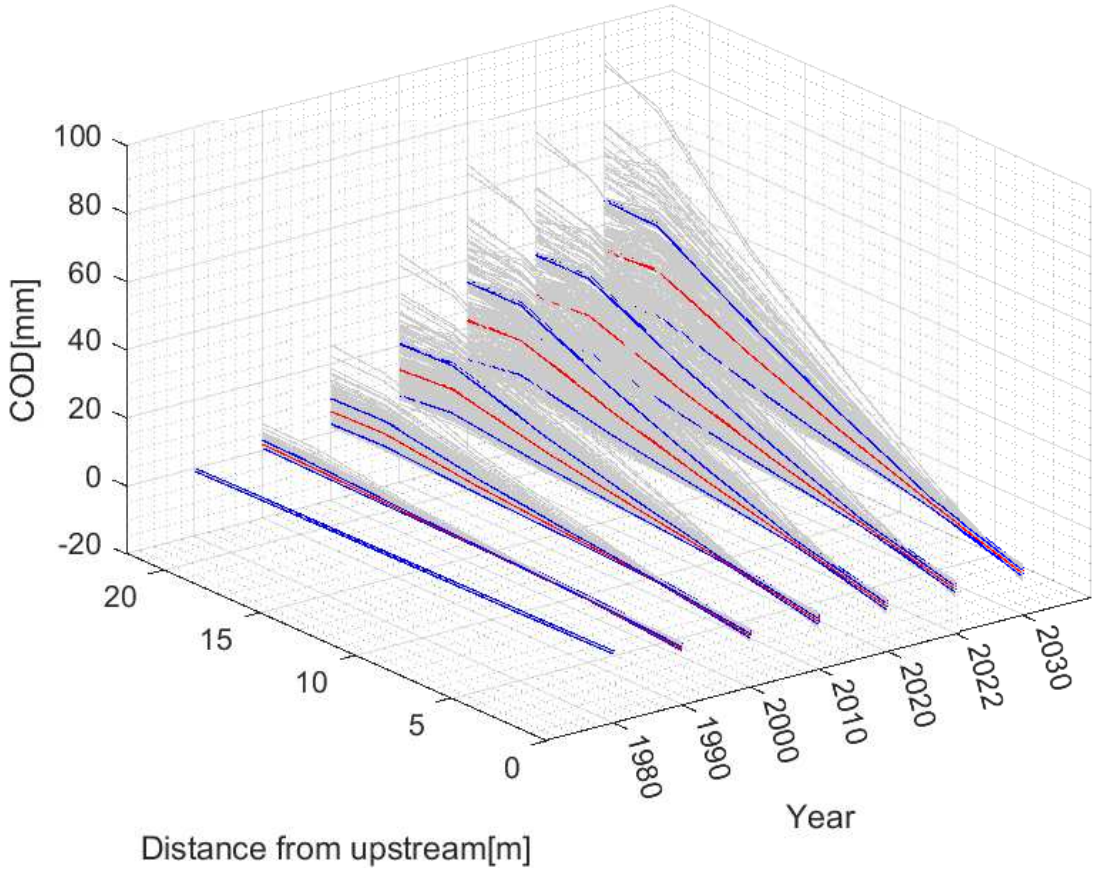

Figure I.2: Concrete Rock interface crack opening displacements for 6 nodes from upstream to downstream for 5 different increments

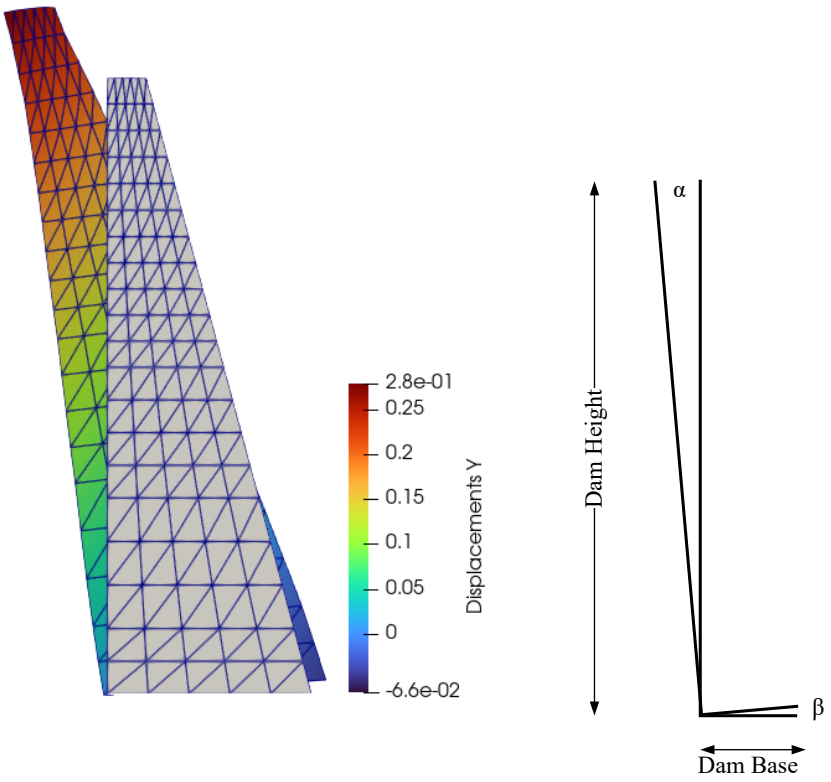

(a) as Modeled

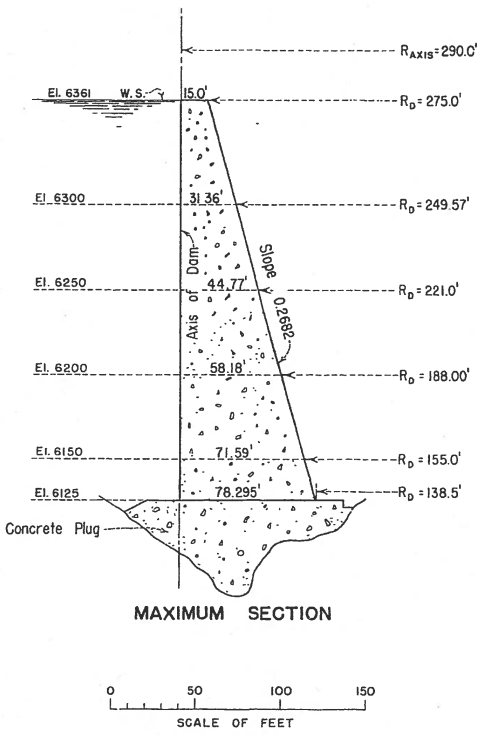

(b) Real model

Figure I.3: Dam tilts

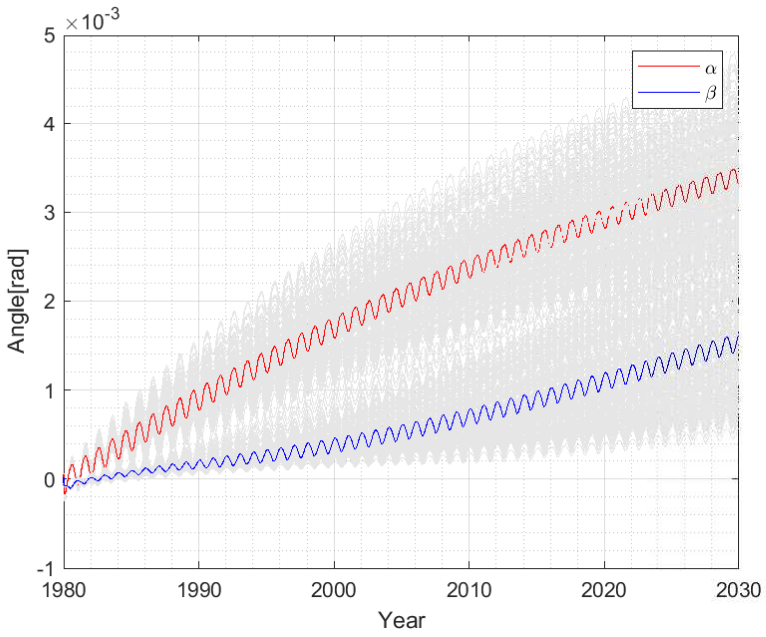

Figure I.4: angles

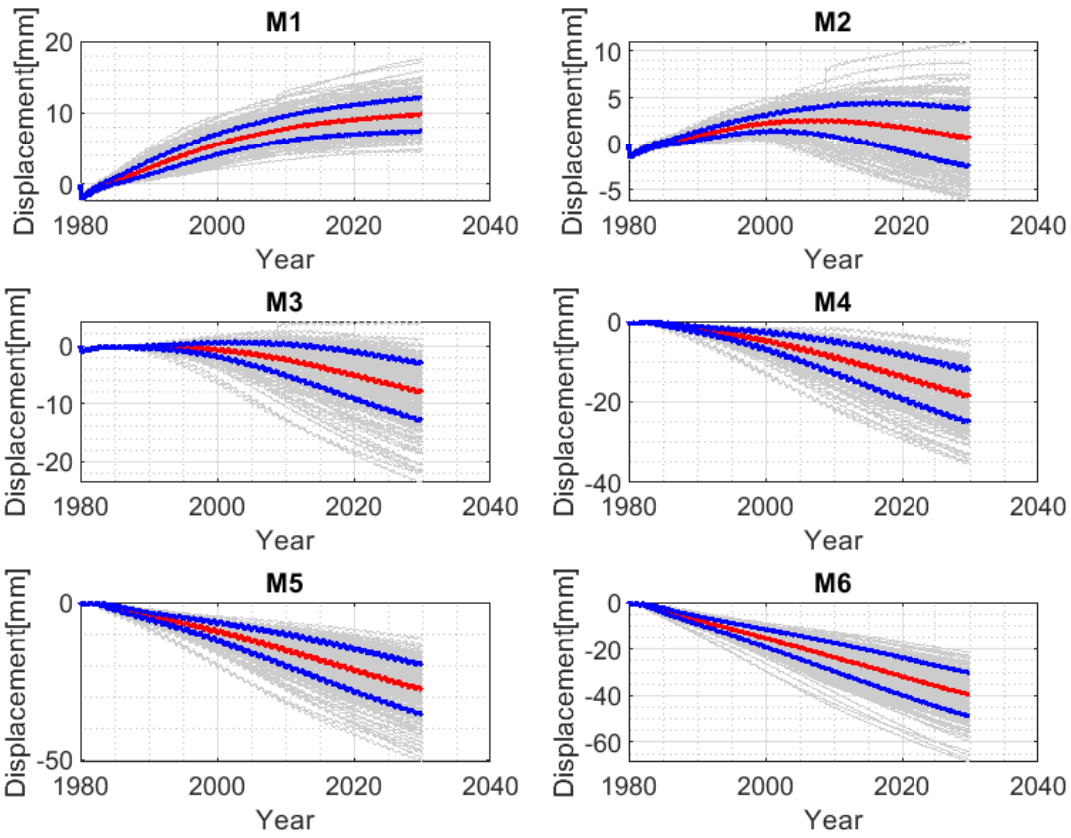

Figure I.5: Sliding; (+ve) Upstream